SYNTHESIS AND CHARACTERIZATION OF MECHANICALLY ALLOYED NANOSTRUCTURED Al-Fe

Thesis

Submitted in partial fulfillment of the requirements for the degree of

DOCTOR OF PHILOSOPHY

By

RAJATH HEGDE

DEPARTMENT OF METALLURGICAL AND MATERIALS ENGINEERING

NATIONAL INSTITUTE OF TECHNOLOGY KARNATAKA,

SURATHKAL, MANGALORE-575025

KARNATAKA INDIA

JULY 2013

NATIONAL INSTITUTE OF TECHNOLOGY KARNATAKA, SURATHKAL

DECLARATION

I hereby declare that the Research Thesis entitled **SYNTHESIS AND CHARACTERIZATION OF MECHANICALLY ALLOYED NANOSTRUCTURED Al-Fe** which is being submitted to the **National Institute of Technology Karnataka, Surathkal** in partial fulfillment of the requirements for the award of the Degree of **Doctor of Philosophy in Metallurgical and Materials Engineering** is a bonafide report of the research work carried out by me. The material contained in this Research Thesis has not been submitted to any University or Institution for the award of any degree.

MT06F04 **RAJATH HEGDE**

(Register Number, Name & Signature of the Research Scholar)

Department of Metallurgical and Materials Engineering

Place: NITK-Surathkal

Date:15.07.2013

NATIONAL INSTITUTE OF TECHNOLOGY KARNATAKA, SURATHKAL

CERTIFICATE

This is to certify that the Research Thesis entitled **SYNTHESIS AND CHARACTERIZATION OF MECHANICALLY ALLOYED NANOSTRUCTURED Al-Fe** submitted by **RAJATH HEGDE (Register Number: MT06F04)** as the record of the research work carried out by him, is accepted as the Research Thesis submission in partial fulfillment of the requirements for the award of degree of Doctor of Philosophy.

Research Guide
(Name and Signature
with Date and Seal)

Chairman - DRPC
(Signature with Date and Seal)

ACKNOWLEDGEMENT

The work on this dissertation has been exciting, instructive, and cognitive. Without help, support, and encouragement from several persons, it would have been much more difficult to finish this research work.

First of all, I would like to thank my supervisor, Prof. Dr A.O. Surendranathan for his support and constant help provided during the entire research work. I especially wish to thank Prof. Dr K. Rajendra Udupa whose encouragement and guidance made my thesis work possible. I am grateful for him to have accepted my candidature for pursuing PhD studies in the department initially. Thanks are also due to Prof. Dr K. Narayan Prabhu, head of the department for providing the necessary infrastructure to carry out the research work. I would also like to thank Prof. Dr P. Prasad Rao in introducing me to the faculty members of Deakin University, Australia to carry out my research experiments. I owe my thanks to Prof. Dr Jaganath Nayak of the department for useful discussions on XRD. I wish to thank Dr Udaya Bhat for giving me valuable information about TEM characterization and Dr Ravishankar for helping me with SEM operation and training. My special thanks to Prof. Dr Shivakumar, and Prof. Dr S.M. Kulkarni for their valuable suggestions as RPAC members. I thank all the non teaching staff members of the department for extending enthusiastic support towards my research work. Some of them whose names I would like to mention here are Mrs Sharmila, and Vinaya, Mr Vasanth, Mr Giriappa, Mr Sundar. Mr Lokesh, and Mr Babu.

I would also like to mention SAIF IITB Mumbai, ACMS Lab IIT Kanpur, and Materials Department, IISc, Bangalore for providing TEM, VSM and XRD facilities. My special thanks to Prof. Vikram Jayaram and Mr Krishnamurthy from the IISc for letting me use their research facilities.

I would like to extend special thanks to Prof. Dr Cui'e Wen for selecting me as an overseas researcher to undertake PhD studies at the institute for technology research and innovation (ITRI), GTP, Waurn Ponds, Deakin University, Australia. Thanks for selecting, sponsoring and providing me with the necessary infrastructure to carry out research work at the state of the art research facility. Prof. Cui'e was supervising and advising me beyond the scientific part of my life over a year, which helped me to become the person and the specialist I am now. I would also like to thank Prof. Dr Peter Hodgson director of ITRI for short listing me and making my stay comfortable as a overseas PhD researcher. I also owe special thanks to my senior colleagues Dr Yuncang Li, Dr Qing Li, Robert Pow, Dr Nikki, Dr Andrew Sulliavan electron microscopist, Mohan and Katrina for metallography preparations. I would like to thank all my fellow PhD students, Ling Li, Rishabh Bhargava, Arwa, Joni Zhou, Eileen, Rijesh, and other co-workers of the Institute for the nice years

spent together: coffee breaks, business trips, conferences, and mutual help. I am very grateful to Dr. Rimma Lapovok for that invaluably useful and intensive time I spent at Materials Engineering department at Monash University, Clayton campus in Melbourne, Australia for ECAP-BP work. I also thank Mr Hans, the legendary German baker for providing me accommodation to stay in his house for the entire duration of my stay in the city of Geelong. I also thank my house mate and fellow researcher at ITRI Jiangting for helping me to get accustomed to the Australian environment.

I am also grateful to Prof. Dr Alexandra Khvan at the State Technological University (MISIS), Moscow, Russian Federation, for providing me an opportunity to travel and stay in the cities of Moscow and St' Petersburg for presenting my research paper at the international scientific-technical conference on modern problems of physical metallurgy of non ferrous alloys.

I would like to thank my wife Beena, my daughter Supravika and my son Skanda, I had to stay away from them for nearly seven long years to pursue my PhD and through these years, they have been a constant source of encouragement to do quality research work without once distracting me from my vision.

This research would not have been possible without the sacrifices made by two most important people in my life, my father and my mother. Though my father is no more now, I would like to dedicate this research work to both of them.

ABSTRACT

Elemental powders of Al and Fe with an atomic composition of 50 % each were mechanically alloyed in a high energetic planetary ball mill. Tungsten carbide milling media (MM) were utilized for ball milling. The milling vial was filled with toluene liquid to prevent contamination of the milled products from the milling media and atmosphere. Ball milling duration extended upto 185 hours; characterization of the milled powder was carried out by X-ray diffractometer (XRD), differential scanning calorimetry (DSC), vibrating sample magnetometry (VSM), scanning electron microscopy (SEM) and transmission electron microscopy (TEM). The major objectives of characterization were to investigate phase transformation, morphology and topography, structural changes, determination of particle size and magnetic properties of the ball milled powders. Crystallite size was reduced to 86 nm at the end of one hour of ball milling and to 12 nm at the end of 65 hours of milling time. Simultaneously, mechanical alloying (MA) has occurred with the formation of Fe rich BCC Fe (Al) solid solution whose lattice parameter was 0.29316 nm at the end of 185 hours of ball milling duration. During the course of ball milling, slight amorphisation was observed at higher duration of ball milling time (> 125 hours). Heating the ball milled powders in the calorimeter showed the transition to ordering from a near ideal solid solution. The decrease (122 to 76.5 emu/gm) in saturation magnetization (M_S) was due to progressive alloying of Al in Fe, moreover, powder samples ball milled for ≤ 20 hours of milling duration exhibited soft magnetic properties (coercivity, $H_C \leq 125$ Oe) and the remaining ones were magnetically hard (H_C >125 Oe). Transition to intermetallic compound from solid solution has induced paramagnetic behavior when ball milled powders were heated beyond 520 ^{0}C. Further, ball milled powder (185 hours of milling time) was compacted, sintered and annealed, due to which annealed compact started exhibiting a fully ordered (long range order, LRO, parameter 'S' of 0.7) structure. Such an ordered compact was subjected to plastic deformation by various compressive stresses for a very short duration of time. The highly ordered compact transformed into a fully disordered (LRO, 'S' = 0.20) structure when plastically deformed with stresses ≥ 4 GPa. Increase in compression stresses caused crystallite size refinement, increased hardness and M_S in the deformed compact.

In another set of experiments, the role of milling media (MM) was investigated. Elemental powders of Al and Fe with an atomic % of 50 each were ball milled in high energetic planetary ball mill utilizing stainless steel MM. The milling vial was filled with argon inert gas to avoid atmospheric and MM contamination of the milled products. Milling was carried out for a maximum duration of 400 hours. It was inferred that Longer duration of milling was required to achieve MA, crystallite size refinement and amorphisation to certain extent using stainless steel MM compared to that of ball milling with tungsten carbide MM. Metastable amorphous solid solution of Fe (Al) was found to be formed at the end of 400 hours of milling time which has a

lattice parameter of 0.2934 nm, crystallite size refinement to the tune of 5 nm and lattice strain of 2.215%. Equilibrium phases (AlFe/$AlFe_3$ intermetallics) have precipitated when metastable amorphous solid solution was thermally activated in the temperature range of 500 ^{0} to 700 ^{0}C. Ball milled powders exhibited soft magnetic properties with the sole exception of powder milled for 300 hours which behaved as a hard magnetic material. M_S of 400 hour ball milled powder was 21.37 emu/gm. Ferromagnetism at room temperature decreased notably with increase in temperature reaching a paramagnetic phase in the temperature range of 620 ^{0} to 720 ^{0}C for most of the ball milled powders. Transmission electron microscopy (TEM) with selected area diffraction pattern (SADP) images has authenticated the XRD results of indexing, the presence of amorphous phase and nanocrystalline domain which appeared to be less than 20 nm.

Further, ball milled powders which have been mechanically alloyed using stainless steel MM was consolidated to bulk pellet form using equal channel angular pressing with back pressure (ECAP-BP). Such pellets have been characterized by XRD, optical microscopy (OM), SEM, nanoindentation, TEM, DSC, VSM and texture analysis. Slight increase in crystallite size (13.4 nm) occurrred as a result of elevated temperature consolidation; though back pressure assisted ECAP-BP consolidation has decreased the diffusion coefficient thereby restricting the grain boundary mobility. Depending on the consolidation temperature and back pressure, either transitional (not fully ordered) AlFe alloy or a combination of AlFe/$AlFe_3$ intermetallics coexisted in a few pellets. Pellets consolidated at higher temperature (450 ^{0}C) and back pressure (480 MPa) possessed better densification compared to those pellets processed at lower temperatures and back pressures. Metallurgical events like grain refinement, nucleation of nanopores, and precipitation of second phase particles were noted from SEM images of the pellets. Mechanical properties at the nano level measured by load induced nanoindentation are dominated by the local phase composition rather than the bulk mechanical properties of the pellets. Intermetallic phases provided greater nanohardness and elastic modulus values than those regions where transitional alloy and elemental phases were present. In addition, finer crystallite sizes in the nano level in the pellets promote higher nanohardness and elastic modulus. Comparision between the magnetic parameters of ball milled powders and ECAP-BP consolidated pellets, M_S of the pellets is lower while H_C is higher with most of the pellets possessing hard magnetic properties. Steep increase in LRO 'S' (0.45 to 0.85) and similar decrease in lattice parameter (0.28987 nm to 0.2882 nm) beyond 450 ^{0}C caused a transition to paramagnetic ($\leq$ 2 emu/gm) behavior in the pellets. In addition to ECAP-BP consolidation, powders ball milled in stainless steel MM were consolidated by compaction followed by sintering in a nitrogen atmosphere. Sintered compacts exhibited coarser crystallites (120 nm) and reduced lattice strain (0.232 %) compared to ball milled powders and ECAP-BP consolidated pellets. Larger lattice parameter (0.2949 nm) of AlFe intermetallic is noted in addition to the presence of AlN and traces of Al, Fe and Fe_4N phases in the sintered

compacts. However, stronger texture (Maximum Intensity of 703.500) coupled with the presence of AlFe intermetallic and AlN phases caused sintered compacts to possess higher mechanical properties than the ECAP-BP processed pellets.

In another set of experiments, elemental powders of Al and Fe (initial composition of 90 atomic % and 10 atomic % respectively) were ball milled in argon atmosphere using stainless steel milling media. Milling caused Al lattice dilation to the tune of 0.4088 nm forming Al rich solid solution (Al (Fe)) resulting in crystallite size refinement to as low as 6 nm. Quantitatively, 9 % of unalloyed Al was present after 400 hours of ball milling duration. Due to amorphous structure, distinct glass transition temperature prior to crystallisation and a narrow supercooled liquid like region could be observed in all the powder samples. Hard magnetic properties ($H_C \geq 294.10$ Oe) with low M_S (≤ 8.432 emu/gm) were observed in all the ball milled powders. Appearance of grain boundaries, dislocations and amorphous structure was evident from the TEM analysis.

Further, the ball milled powders (Al_{90}-Fe_{10} category) were consolidated by ECAP-BP as well as by compaction and sintering. Metastable Al rich solid solution transformed into a stable $Al_{76}Fe_{24}$ compound of monoclinic structure in all the pellets due to consolidation of the ball milled powders. DSC analysis indicated the slight amorphous structure in the pellets. Pellets exhibited soft magnetic ($H_C \leq 107.63$ Oe) properties with a very low paramagnetism M_S (≤ 0.6582 emu/gm). Pellets with excellent bonding between the particles were produced with a low back pressure (300 MPa) and temperature (450 ^{0}C), which is much lower than the sintering temperatures. Nanosized grain boundaries, amorphous and $Al_{76}Fe_{24}$ compound phases were distinctly visible in the SEM-FEG micrographs of the pellets. Sintered compacts exhibited crystalline phases of $Al_{76}Fe_{24}$ compound, AlN and unalloyed Al. Larger quantity (74 %) of $Al_{76}Fe_{24}$ crystallized in the 400-h sintered compact, although the lattice dilation of Al in the 250-h sintered compact was to the tune of 0.4109 nm. Maximum size of the crystallites in the sintered compact was 135 nm, which was much larger than that of ECAP-BP consolidated pellets (D = 11 nm). Among all the consolidated materials of both the categories (Al_{50}-Fe_{50} and Al_{90}-Fe_{10}), 400-h sintered compact of Al_{90}-Fe_{10} system possessed strongest texture (Maximum intensity of 6556.00), coupled with highest nanohardness and elastic modulus caused by larger quantities of $Al_{76}Fe_{24}$ intermetallic and AlN phases.

The present investigation unambiguously brings out the fact that mechanical alloying followed by consolidation in different modes (ECAP-BP and sintering) and conditions produces nanomaterials with spectrum of structure and properties from which a choice of industrial product can be developed.

KEY WORDS: Ball milling; Mechanical alloying; AlFe alloys; ECAP-BP; Nanostructured

TABLE OF CONTENTS

LIST OF FIGURES

LIST OF TABLES

NOMENCLATURE

Symbol	Description
MA	Mechanical alloying/Mechanically alloyed
MM	Milling media
SPS	Spark plasma sintering
ECAP-BP	Equal channel angular pressing with back pressure
HPT	High pressure torsion
HIP	Hot isostatic pressing
SPD	Severe plastic deformation
HP	Hot pressing
FAPAS	Field activated pressure assisted sintering
Al_{50}-Fe_{50}	Aluminium 50 atomic % and iron 50 atomic %
Al_{90}-Fe_{10}	Aluminium 90 atomic % and iron 10 atomic %
XRD	X-ray diffraction
DSC	Differential scanning calorimeter
VSM	Vibrating sample magnetometer
SEM	Scanning electron microscope
FEG	Field emission gun
TEM	Transmission electron microscope
SE	Secondary electrons
BSE	Back scattered electrons
EDS	Energy dispersive x-ray spectroscopy
SADP	Selected area diffraction pattern
WC	Tungsten carbide
SS	Stainless steel
LRO	Long range order
CSRO	Chemical short range order
SRO	Short range order
NNAPB	Nearest neighbour anti phase boundary
APB	Anti phase boundary
ECAE	Equal channel angular extrusion
ECAC	Equal channel angular compaction
UFG	Ultra fine grained
H	Magnetic field

M	Magnetization
M_S	Saturation magnetisation
H_C	Coercivity
M_R	Remanent magnetisation
B	Magnetic flux density
M	Magnetic permeability (4π x 10^{-7} H/m)
χ	Susceptibility
C	Curie constant
BPR	Ball to powder weight ratio
h/hr	Hour
a	Lattice parameter
D	Crystallite size
II	Integrated intensity
d	Inter planar spacing
S	Super lattice/LRO Parameter
F	Fundamental
Å	Angstrom
K_α	Wavelength of Cu radiation
λ	Wavelength of x-ray
hkl	Miller indices
θ	Bragg angle
FCC	Face centred cubic
BCC	Body centred cubic
F	Structure factor
P	Multiplicity factor
K	Scherrer constant
FWHM	Full width at half maximum (β)
ε	Lattice microstrain
μ	Linear absorption coefficient
μ/ρ	Mass absorption coefficient
ρ	Density
d_P	Penetration depth
I	Intensities of the diffracted beam
I_O	Intensities incident x-ray beam
ω_{Fe}	Weight fraction of Fe
ω_{Al}	Weight fraction of Al

H	Nano hardness
E	Elastic modulus
OP-S	Oxide Polishing Suspensions
OM	Optical microscopy/micrographs
T_S	Temperature of the sample
T_R	Temperature of the reference
T_C	Curie temperature
Oe	Oersted
ht	Height
P	Load
Tg	Glass transition temperature
Tx	Onset temperature of crystallization
Tp	Peak temperature of the crystallization reaction
Eqn	Equation

CHAPTER 1: INTRODUCTION

Over the last two decades, **Al-Fe** binary and multi component alloys have been extensively investigated for possible applications in areas like mechanical, structural, magnetic and aerospace domains (Stoloff N. S. et al. 2000). The AlFe intermetallic compound possesses excellent properties like good strength at intermediate temperatures, high specific stiffness, and corrosion resistance at elevated temperatures even in hostile atmospheres like oxidizing, carburizing and sulphidising one. In addition, they possess low thermal conductivity, high specific strength and relatively high electrical resistivity (Krasnowski M, Kulik T. J. 2007, Krasnowski M. et al 2006, Nogueira R. N, and Schon C. G. 2005). Thus, these properties make the AlFe compound very attractive for structural applications and defense industries in addition to aerospace applications at high temperatures (Froes F. H. et al. 1992). In addition, coarse grained Al-Fe has excellent soft magnetic properties with higher resistivity for application at elevated temperatures (upto 500^0 C) (German R. M. 1994). Further, AlFe intermetallic compounds are lighter than steel and Ni-based alloys making them attractive substitutes for stainless steel and Ni-based super alloys (Krasnowski M., Kulik T. J. 2007). Al alloys with Al content greater than 50 atomic percent have shown promising features like good ductility and high strength (Asgharzadeh H. et al. 2011, Lee K. J. and Woo K. D. 2011). However, practical limitation as far as application of this alloy in its cast form is concerned is its low toughness at room temperature and limited workability (McKamey C. G. et al. 1991). A new class of Al-based alloys which are in the forefront of research activities are the nanocrystalline ones. Reducing the grain size to nano range (< 100 nm) brings about far superior physical and mechanical properties compared to coarse (≥ μm) grained counterparts (Padmanabham K. A. 2001, Pfullmann T. H. et al. 1996). Nevertheless, there has been a lot of research on Al-Fe system possessing equilibrium state, whereas non-equilibrium state of this alloy has had very few research analyses. Nanostructured intermetallics cannot be produced by conventional methods, but can be synthesized with homogeneous structure and composition by non conventional processing (Krasnowski M., Matyja H. 2001) techniques followed by appropriate heat treatment.

Rapid solidification techniques of synthesizing metastable phases in Al-Fe systems have been reported earlier (Nayak S.S. et al. 2008, Badan B. et al. 1996, Nayak S.S. et al. 2011). Solid solubility extension limits, formation of amorphous and quasicrystalline phase and crystallization of intermetallics by melt spinning (Badan B. et al. 1996, Nayak S.S. et al. 2011) in Al-Fe system have been investigated and reported. Non-equilibrium synthesis technique of mechanical alloying (MA) in Al-Fe binary systems too has been reported (Nayak S.S. et al. 2010, Nayak S.S. et al. 2006, Sasaki T. T. et al. 2009). Compared to rapid solidification process, mechanical alloying is

far easier and in some systems it is the only process of producing amorphous phase. Moreover, it is also capable of obtaining wider composition range of amorphous phase in the alloy (Suryanarayana C. 2001). Technique of reinforcing with carbide during mechanical alloying of Al-Fe system has already been reported (Yoritoshi Minamino. et al. 2004). A few papers have been devoted to the MA of these two and three metals in a nitriding fluid (Miki M. et al 1995, Krasnowski M., Kulik T. 2003 and Krasnowski M, Matyja H. 2001). However, MA of elemental Al and Fe by high energetic ball milling in different milling media has been explored to a wider extent in this research work.

Mechanical alloying by high energetic ball milling is largely a non-equilibrium process resulting in metastable structures and phases from elemental powder particles at or near room temperature. Such an alloyed powder shows variety of stable and metastable nanocrystalline/amorphous structures (Lu L. and Lai M.O. 1998, Suryanarayana C. 2001). Due to the formation of nanostructure, properties such as high hardness, ductilisation of brittle materials and enhanced diffusivities (2009) are observed paving the way for increased applications of such materials. Al-Fe nanoparticles obtained by ball milling process are influenced by milling media (MM) which enables a balance between fracture and welding and induces the refinement of powder particles. Milling characteristics, which influence the particle size are vial and ball material, rotation speed of the vial, balls to powder weight ratio and milling atmosphere. The role of MM can be quite complex because in addition to preventing the occurrence of excessive welding of the aluminium powder particles it can also react with aluminium during milling leading to the formation of aluminium oxide (JCPDS 1999) phase. In addition, improper selection and control of MM and its parameters can cause Cr, W and C contamination in Al alloys during milling. Various metallurgical events and magnetic behavior which occur during ball milling in different milling media have been captured in this research work to an extent to which other research works have not reported.

Certain categories of amorphous Al alloys exhibit several superior properties that are not observed in crystalline alloys (Tavoosi M. et al. 2012). Amorphous alloys have largely been produced in the form of powders by MA or atomisation, thin ribbons by melt spinning and wires (Hong S. J. et al. 1999) with minute diameter. Application of such amorphous alloys is limited largely due to the size constraints of powders, ribbons and wires. Moreover, due to the low glass forming abilities of Al alloys there is very limited research reports on the synthesis of amorphous alloy powder and consolidation to bulk form.

Consolidation of mechanically alloyed powder to bulk form is a challenging task due to strain hardening of alloyed powder during ball milling. In addition, ball milling induces nanocrystalline

and amorphous structure in the synthesised powder. Retaining the nanocrystalline and amorphous structures in the consolidated form is critical from the point of view of the application of such bulk materials. Thus, these materials exhibit enhanced mechanical, structural and magnetic properties compared to their microstructured equivalent (Murty B. S. and Ranganathan S. 1998). Nanoparticles are prone to contamination but show peculiar thermal stability during consolidation at high temperature and pressure. The major challenge is in the form of rapid grain growth during consolidation of nanoparticles at elevated temperature. Obviously, temperature and pressure are important parameters which assist in the formation of fully dense, high purity and desired grain size in the consolidated bulk material. In addition, severe shear stresses and strains are desirable to effectively demolish pores and cracking of surface oxide layers.

In order of increasing shear effectiveness during consolidation, various consolidating processes listed are; spark plasma sintering (SPS), uni-axial hot pressing, direct extrusion, high speed sintering, equal channel angular pressing (ECAP) and high pressure torsion (HPT). However, consolidation by hot pressing, hot extrusion and SPS requires high temperature; as such it will lead to recrystallization, grain growth and brittle structure. Consolidation of powder by hot isostatic pressing (HIP) requires evacuation cycle coupled with hermetical sealing and attaining a high temperature in the range of 850 to 950 ^{0}C for 2 to 4 hours. However, the presence of residual porosity and contamination of the compacts at elevated temperature is a setback for HIP process. HPT and ECAP are also known as severe plastic deformation (SPD) methods. As an alternative process, SPD methods provide consolidation of mechanically alloyed powders relatively at lower temperatures and high pressure compared to conventional sintering and other consolidation techniques. Nevertheless, interesting metallurgical events such as phase changes, inhibition of grain growth, crystallization to intermetallic phases, and retention of amorphous and qauscicrystalline phase could evolve during SPD consolidation of milled powder. HPT is a fairly simple technique consisting of simultaneous application of high pressure and torsion in consolidating nanosized powders, preserving the nanostructure or amorphous phase in the bulk samples. Unfortunately, HPT allows one to obtain ultrafine-grained samples with very small size, which makes it difficult for studying and renders it impossible for practical applications. Combination of cold pressing followed by hot extrusion, hot pressing (HP), HIP and SPS consolidation techniques have been reported by Omori M. (2000). Various types of amorphous Al-based alloys have been synthesized by rapid quenching of liquid or vapour, solid state reactions (Inoue A. 1998) and melt spinning (Perepezko J. H. et al. 2000). Further, warm pressing, warm extrusion, explosive compaction techniques (Kim Y. B. et al. 2004, Esaki H. et al. 1989, Sung-Chul Lim. et al. 2007 and Jozef Miskuf. et al. 2009) of consolidation of amorphous powder have been investigated and reported. The consolidation technique best suited to retain nanoscale grain

size seem to be pulse electric discharge sintering (Kolesnichenko V. G. et al. 2012) followed by HP (Krasnowski M., Kulik T. J. 2007). Combination of hot consolidation techniques like HPT and field activated pressure assisted sintering (FAPAS) have been attempted to consolidate the MA powder to bulk form (Viswanathan V. et al. 2006 and Bernard F. et al. 2004). However, the maximum size of the resulting bulk Al alloys has been limited to a large extent is the major drawback of this technique.

ECAP with back pressure (BP) is an inexpensive and simple consolidation technique compared to other methods. In which, a range of high back pressure and lower working temperature are effectively utilized in compacting and plastically deforming the powder. In addition, the mechanical properties of bulk Al-Fe alloys can be improved by introducing AlN during consolidation of mechanically alloyed powders. Thus, research concerning the formation of nitride by hot consolidation (sintering) of mechanically alloyed Al-Fe powder in a nitrogen environment is scarce. So, the consolidation by ECAP with BP is a promising technique which is worth exploring in addition to sintering in a nitrogen atmosphere.

Present research explores ball milling of elemental Al and Fe which initiates mechanical alloying. Further, the research concentrates on consolidation of mechanically alloyed powders by ECAP-BP as well as compaction followed by sintering. Various metallurgical events which occur during ball milling and consolidation have been captured and reported. Further, magnetic, mechanical and structural properties including texture during the processing have been analysed and reported. Characterization in every stage of the process is carried out.

1.1 Scope and Objectives

1) To mechanically form an alloy from the elemental powders of Al and Fe using high energetic planetary ball mill in both Al_{50}-Fe_{50} and Al_{90}-Fe_{10} systems with different milling media (MM).
2) To investigate the role of MM, which play an important role in the process of fracture of individual powder particles, comminution and mechanical alloying of elemental powders.
3) Investigate the various metallurgical events which occur during ball milling by X-Ray Diffraction (XRD), Differential Scanning Calorimeter (DSC) and electron microscopy (SEM & TEM).
4) To analyse the ball milled powder for magnetic properties at room temperature and elevated temperature.
5) To consolidate mechanically alloyed powder by equal channel angular pressing with back pressure (ECAP-BP). Here, the intention is to preserve the non-equilibrium metastable phases and structures in the consolidated pellets generated possibly during milling.
6) To characterise the ECAP-BP processed pellets by XRD, DSC, metallography, vibrating sample magnetometer (VSM) and nanoindentation. Explore the possibility of texture formation during consolidation process.
7) To investigate the structural, magnetic and nano-hardness transition in bulk annealed AlFe compacts as a function of plastic deformation.

These research objectives have a wide range of scopes;

1) Alloy production by MA occurs almost at room temperature which can have advantages over high temperature synthesis.
2) Research work could pave the way for successful commercial implementation of ECAP-BP process as a powder metallurgy consolidation method, hitherto used exclusively as an extrusion process.
3) Combination of MA and ECAP-BP consolidation process of synthesizing alloyed bulk material could be an alternative for traditional manufacturing processes like melting and casting.
4) Compared to hot isostatic pressing (HIP), ECAP-BP consolidation is economical because the approach does not include evacuation, encapsulation and sintering stages.

5) The research also focuses on consolidating the ball milled powders by compaction and pressureless sintering in nitrogen atmosphere. An attempt to introduce nitrides in the bulk material could have huge impact on the mechanical as well as structural properties.
6) Further, the research makes an effort to achieve the above said objectives by synthesizing ultra fine grained bulk Al-Fe alloy pellets/compacts with optimized Fe content. Such that the bulk product would become as light as possible for various applications in aerospace and defense purposes as soft and hard magnetic materials.

1.2 Organisation of the Thesis

The thesis comprises of six chapters, the section briefly describes the main features of each chapter as follows:

Chapter 1 gives an introduction to Al-Fe alloys, various research processes used to synthesize mechanically alloyed powders as well as consolidation of the ball milled powders. Identifies areas requiring research, lists the scope and objectives of the research study and briefly describes the proposed investigations to be carried out.

Chapter 2 provides literature review of various methodologies used to synthesize nanostructured Al-Fe alloy powder and consolidation of such powders into bulk form. Provide descriptions regarding magnetic materials and their properties. Synthesis methods, like mechanical alloying by ball milling, consolidation of powder by equal channel angular pressing with back pressure (ECAP-BP), compaction and sintering are presented. Characterization techniques like X-ray diffraction (XRD), electron microscopy, differential scanning calorimeter (DSC), vibrating sample magnetometer (VSM), nanoindentation and metallography are described.

Chapter 3 covers experimental details carried out in this research work like ball milling, ECAP-BP, compaction, sintering and annealing, deformation by compression and nanoindentation. Characterization experiments like XRD, DSC, electron microscopy, VSM, metallography and optical microscopy are explained in details. Determination of structural parameters, phase identification, magnetic properties and bulk sample preparations for transmission electron microscopy and metallography are dealt. X-ray penetration depth for Al-Fe alloys has been calculated. Specification of various equipments used and the location where these experiments were carried out are also mentioned.

Chapter 4 presents results, analysis and discussions pertaining to material of Al_{50}-Fe_{50} system (50 atomic % each). Chapter is divided into two categories based on the type of milling media (MM)

used. First, WC and toluene MM is used to ball mill elemental powders, further the milled powders are consolidated by compaction, sintering and annealing and subsequently deformed. Second, stainless steel MM is used to ball mill elemental powders, further the milled powder is consolidated by two routes, i) by ECAP-BP and ii) by compaction and sintering. Each of the two categories of milled powder and consolidated bulk samples are subjected to various characterisation techniques to investigate, phase transformation, structural, magnetic, mechanical, morphological and topography investigations and the results have been reported.

Chapter 5 presents results, analysis and discussions pertaining to material of Al_{90}-Fe_{10} system (90 atomic and 10 atomic % respectively). In this section, ball milling is carried out in stainless steel milling media and subsequently milled powders have been consolidated by two routes, i) by ECAP-BP and ii) compaction and sintering. Material characterization analysis has been carried out at every stage of the experiments for assessing phase transformation, structural, magnetic, mechanical, morphological and topography investigations and the results have been reported.

Chapter 6 gives the conclusions of the whole research work carried out.

CHAPTER 2: LITERATURE REVIEW

Most of the important current techniques used to synthesise ultrafine-grained/amorphous/quasicrystalline alloyed powders with greater emphasis on the Al-Fe binary system is focused. Methods focussing on phase transition during mechanical alloying as a function of ball milling duration and its implications on metallurgical and magnetic events have been surveyed. Further, powder consolidation methods used in synthesising bulk Al-Fe is focused. While characterization techniques used to assess metallurgical, mechanical and magnetic properties of the bulk material are surveyed.

2.1 Synthesis of Al-Fe Alloy Powder from Elemental Powders

A variety of physical and chemical methods have been employed to synthesize nanopowders of metals and alloys. Intermetallic nanoparticles have been prepared by chemical methods such as reduction reaction process (Pithawalla Y. B., Deevi S. 2004). Evaporation methods have been effectively used by researchers to prepare significant quantities of metallic nanoparticles (Siegel R. W. 1993). Magnetron sputtering has been used to synthesize intermetallic nanoparticles, sputtering is advantageous when used for metals and alloys with high melting points (Cherif S. M. et al 2007). The laser vaporization controlled condensation (LVCC) has been used to produce intermetallic nanopowders (Abdelsayed V. et al. 2006) under well-defined conditions of temperature and pressure in a diffusion cloud chamber (Pithawalla Y. B. et al. 2000). Preparation of intermetallic FeAl (20-30 at % Al) nanoparticles by LVCC and characterization of magnetic properties have been reported (Pithawalla Y. B. et al. 2001). Synthesis of Fe-Al nanopins using arc discharge process has been reported (Zhang W. S. et al. 2005). A wide variety of methods including casting, powder metallurgy, hydrogen arc plasma, self-propagation high temperature synthesis (SHS) and mechanical alloying (MA) have been employed for the synthesis of intermetallic compounds (Rafiei M. et al. 2009).

Ball milling of elemental powder causes particle size reduction simultaneously inducing mechanicall alloying. Such a powder processing method is especially suitable for production of those compounds that are difficult to prepare by conventional processes due to high vapour pressure or large differences in melting points of the components. Evolution of powder morphology and phase changes during MA of Fe-Al powder mixtures containing 10–85 atomic percent Al using a low energy ball mill has been reported (Oleszak D. and Shingu P. H. 1997). According to their investigation, alloys containing 10–50 atomic percent Al and 60-85 atomic percent Al resulted in disordered solid solution and amorphous structure respectively. An extended solid solution of Al in Fe was obtained after one hour of ball milling time. However, no

amorphisation occurred even after 32 hours of milling time as reported by Bonetti E. et al (1995). However, thermal treatment of ball milled powder transformed to Fe_3Al intermetallic phase with chemical disorder in $Fe_{75}Al_{25}$ system. While $Al_{50}Fe_{50}$ milled powder transformed to FeAl intermetallic with partial chemical order. Though, MA of Al-Fe system has been previously reported, nevertheless there is still a lot of uncertainity existing with regards to phase formation sequence occurring during ball milling. Thus, further research is necessary during ball milling of elemental powders of Al and Fe. Especially, investigation of phase transformation, topography, morphology, composition variation and magnetic behaviour is necessary.

When ordered Fe-40Al is subjected to ball milling, three types of structural changes occur: nanocrystallisation, loss of long range order (LRO) and destruction of chemical short range order (CSRO) (Negri D. et al. 1999). A new nanostructured system, FeAlB, with high content of boron, was prepared by mechanical alloying in a high energetic ball mill, structural and magnetic properties were investigated (Rico M.M. et al. 2005). In the recent past, there have been reports about MA of Fe-50 atomic percent Al (Oleszak D. and Shingu P. H. 1994. Huang B. et al. 1997. Eelman D. A. et al 1998. Hashii M. 1999). Study of structural and phase transformations taking place during mechanical alloying of Fe-50 at. % Al nano powder mixture in a high energy rate ball mill and during subsequent heating of the milled nano powders have been reported (Krasnowski M. et al. 2006). The disordered Fe (Al) solid solution is the product of the milling process in all the mentioned cases. Fully ordered FeAl phase by MA of Fe-50 at. % Al has been reported, in which, synthesis, microstructure, morphology, thermal stability and thermal behavior of MA nano powders were investigated (Hongwei Shi et al. 2007). Metastable nanocrystalline Fe-66Al solid solution which is ferromagnetic at room temperature was prepared from elemental powders by mechanical alloying using high energy rate ball mill; bulk magnetization studies reveal ferromagnetism at room temperature (Sebastian V. et al. 2007). Magnetic properties and structure of nanocrystalline Fe-Al with Al content between 50 and 90 atomic percent have been reported for low energy rate mechanical alloying of Fe and Al (Jartych E. et al. 1999). The intermetallic Fe_3Al has been successfully synthesized from mixture of Fe and Al powders in a atomic ratio of 72:28 by mechanical alloying. Further, structural evolution and nearest neighbour antiphase boundaries (NNAPBs) during alloying have been investigated (Run-Hua Fan et al. 2005). Disordering of FeAl alloy induces paramagnetic to ferromagnetic transitions (Apinaniz E. et al. 2001). The microstructural, mechanical and magnetic properties of ball milled and annealed Fe-40Al atomic percent (B2) alloys have been studied (Amils X. et al. 1999). Disorder–order (ferro-paramagnetic) transition of mechanically alloyed (MA) Fe-40 atomic percent Al, and dependence of magnetic properties on the milling times and annealing temperatures have been shown (Zeng Q. and Baker I. 2006). Strain-induced ferromagnetism in B2-structured Fe–Al arises mostly from anti-phase

boundary (APB) tubes. Where, groups of moment-bearing Fe atoms with at least three like nearest-neighbours are large enough to be magnetically coupled and behave ferromagnetically (Wu D. et al. 2004).

2.2 Consolidation of Mechanically Alloyed Powder

Severe plastic deformation (SPD) process can be successfully implemented to consolidate ultra fine particles of metals and alloys. Especially, particles with highly metastable phases and structures like nanocrystalline/amorphous powders can be consolidated to bulk form. Additionally, it allows consolidation relatively at lower temperatures thus enabling to retain the metastable phase/structure (Luo P. et al. 2010). Moreover, SPD is most suitable in producing multiphase materials. Bulk ultrafine grained materials can either be consolidated from ultrafine grained nanostructured particles or by refining coarse grain structured bulk material. In the later, which is the refining process, SPD is among the most popular method of producing nanostructured bulk material (Valiev R. Z 2004). In particular, ECAP (Valiev R. Z. and Langdon T. G. 2006) and high pressure torsion (HPT) (Zhilyaev A. P., Langdon T. G. 2008) are successful as refining SPD methods. HIP is the most common compaction process for consolidating alloy powders. Process involves, hermetically sealing after evacuating followed by application of hydrostatic pressure at high temperature within a pressure vessel. Contamination by gaseous impurities and residual porosities are a big concern in the HIP consolidation (Donachie M. J. Jr 2000). SPS is capable of consolidating mechanically alloyed powders at relatively low temperatures and short sintering times. Moreover, the plasma generated facilitates sintering and eliminates surface impurities (Omori M. 2000). Compared to ECAP-BP and HIP, SPS engages much higher temperature, while the onset of crystallization is delayed by adding Y_2O_3 (Thierry Grosdidier et al. 2007). Hot pressing and SPS show a lot of similarities; however the precursor (mechanically alloyed powder) is loaded in a graphite die and a uniaxial pressure is applied during hot pressing. Instead of using an external heating source, pulsed direct current is passed through the precursor held within an electrically conducting pressure die in SPS (Thierry Grosdidier et al. 2006). High pressure torsion (HPT) has been used to consolidate particles to bulk form retaining the nano particle size and non equilibrium structures associated with ball milled powders. The severe shear deformation involved is responsible in obtaining good bonding between the particles and break the surface oxide layer. Thus, consolidation can be achieved comparatively at lower temperatures compared to most SPD methods. However, HPT produces bulk material with small size making it impossible for mechanical testing and for practical applications. Equal channel angular extrusion (ECAE) is capable of producing bulk material retaining the non equilibrium structures (Senkov O. N. et al. 2005). However, it requires compaction and encapsulation of particle and moreover may not produce full density pellets even after multiple passes.

A few research articles have shown successful implementation of back pressure assisted equal channel angular compaction (ECAC) of alloy powder. Pure Al particles were successfully consolidated by ECAC-BP at 100 ^{0}C; full density and good bonding with excellent mechanical properties have been obtained (Xia K., Wu X. 2005). Mechanically alloyed Al particles and carbon black was consolidated by ECAP-BP at 450 ^{0}C, full density was reached after 8 passes (Goussous S. et al. 2009). Mechanically alloyed Al 2024 powder has been densified by conventional sintering and ECAP with and without back pressure to obtain near full density almost at room temperature (Nishtha Gupta et al. 2012). High strength Ti based bulk alloy material was produced by consolidating normal and dehydrided particles using back pressure-ECAP (Xu W. et al. 2008). Phase investigation during heating and cooling two types of Al-Ti alloys consolidated from ball milled and mechanically stir-mixed powders respectively by ECAP-BP at 903 ^{0}K was carried out (Klaus-Dieter Liss et al. 2009). High strength ultrafine nanograined bulk Al was obtained by back pressure assisted ECAP consolidation of ultrafine grained Al powders at 400 ^{0}C (Xu W. et al. 2007). Pure Al particles were consolidated by 50 MPa of back pressure assisted ECAP at 100 ^{0}C, consolidated bulk material was further deformed by four passes through the ECAP die (Xia K. et al. 2007). A new low energy method consisting of ECAP consolidation of elemental Ti and Al powder followed by combustion synthesis has been reported (Morsi K., Goyal S. 2007). Microstructure and mechanical properties of Bulk Al synthesized by ECAP-forward extrusion consolidation has been investigated (Paydar M. H. et al. 2009). Bulk Fe-50Al was synthesized by mechanical alloying followed by sintering which showed the formation of Fe-Al (B) intermetallic (Izadi S. et al. 2010). Al-5 wt % Fe alloy ingots were processed by equal channel angular extrusion with back pressure, solid solubility of Fe in Al, strength, ductility and microhardness were investigated (Stolyarov V. V. et al. 2003). Owing to its high reactivity, SPD-based consolidation processes are perhaps the most suitable for Ti since lower processing temperatures can be used. Despite the advances in the development of the nanopowder preparation methods, problems still remain concerning powder purity, residual porosity of compacts, grain growth during consolidation and retention of non-equilibrium structures/phases, which have not been resolved yet. One promising consolidation technique is the equal channel angular pressing with back pressure (ECAP-BP) as a severe plastic deformation (SPD) method, which enables to produce ultra fine grained (UFG) materials. Especially, when large volume of powder has to be consolidated, ECAP based processes are preferred to those based on HPT and other SPD. However, there is hardly any research done in terms of consolidation of ball milled Al-Fe powder by ECAP-BP. Especially, in the binary alloy system of Al_{50}-Fe_{50} and Al_{90}-Fe_{10} systems, no research reports are available on MA and ECAP-BP consolidation.

In this research work, equal channel angular pressing (ECAP) with back pressure (BP) is utilized to consolidate the mechanically alloyed powder. Moreover, the non equilibrium structures possibly generated during ball milling could be retained in the ECAP-BP consolidated bulk material.

2.3 Magnetic Materials and Properties

Although all materials are influenced greater or lesser by the presence of the magnetic field, but the degree of this influence is the key to classify these materials into ferromagnets, paramagnets, diamagnets, ferrimagnets and antiferromagnets.

The intensity of the magnetic field is represented by H while the number of dipoles per unit volume of a magnetic material is measured by M or Magnetization. The magnetic flux density of a material is the result of the interaction between the applied field and the field produced by the material itself. It is defined as B as presented in the equation 2.1 (SI system):

$$B = \mu (H+M) \qquad \text{Eqn 2.1}$$

Where μ is the magnetic permeability of a vacuum and is equal to $4\pi \times 10^{-7}$ H/m. The amount of magnetization produced in a material under the influence of an external magnetic field is not only measured by M. There is also another factor which is called susceptibility (χ) and is indicator of variation of M with H:

$$\chi = M/H \qquad \text{Eqn 2.2}$$

Magnetic permeability is another parameter which relates the magnetic flux density to the strength of the applied field, and is expressed by:

$$\mu = B/H \qquad \text{Eqn 2.3}$$

Magnetic state of a material is a function of several parameters such as temperature, pressure, applied magnetic field and its geometry; therefore the material may exhibit more than one form of magnetism by varying any of these parameters (Levy J. C. S. 1986). Ferromagnetic materials are used in almost all major technical fields such as electrical and mechanical motors, high-power electromotors, computer and telecommunication industry, magnetic high density recording, navigation, aviation and space operations, automation micromechanics, medicine, sensor techniques, magnetocaloric refrigeration, materials testing and household applications.

2.3.1 Diamagnetic materials

Almost all materials have the tendency to resist the external field and being repelled by it and therefore exhibiting diamagnetic behaviour. When exposed to an external field, these materials produce a magnetization in the opposite direction of the applied field. In diamagnetic materials no unpaired electrons exist, therefore the atoms have no net magnetic moment and the overall magnetization of the material comes from the electrons orbital motions that can be explained as follows: When a material is exposed to an external magnetic field, its electrons experience two forces: The Coulomb attraction to the nucleus and a Lorentz force from the magnetic field. The latter depends on the orbiting direction of the electron. This Lorenz force may cause the electrons to pull away from the nucleus or get them closer to it. According to Lenz's law (Cullity B. D. 1972), the orbital magnetic moments that were aligned opposite to the field would increase and the ones aligned parallel to the field would decrease. As a result, a small bulk magnetic moment opposite to the direction of the magnetic field is created that leads to the repulsion of that material from the field. However it should be noted that all materials undergo this orbital response, but in paramagnetic and ferromagnetic substances, the diamagnetic effect is partly ignored by the stronger influence of the unpaired electrons

2.3.2 Paramagnetic materials

Paramagnetic materials are composed of atoms, with unpaired electrons that cause net magnetic moments. While in the case of paired electrons, the Pauli Exclusion Principle necessitates that the electrons' magnetic moments should be in opposite directions and cancel each other out. When relaxed, the magnetic moments in paramagnetic materials tend to randomly orient with respect to each other, resulting in a net zero magnetization.

However, when exposed to a magnetic field, these moments align toward the field, causing huge positive susceptibilities in the material. It should be noted that due to thermal vibration of atoms, not all atomic moments will have the chance to align toward the field. The relationship between susceptibility and temperature is presented by Currie-Weiss Law (Eqn 2.4):

$$\chi = C/ (T-\theta) \qquad \text{Eqn 2.4}$$

where: C is Curie constant, T is temperature and θ is material constant and is zero for a perfectly paramagnetic material. Figure 2.1 shows the temperature dependence of magnetic susceptibility of paramagnetic, ferromagnetic and ferrimagnetic materials.

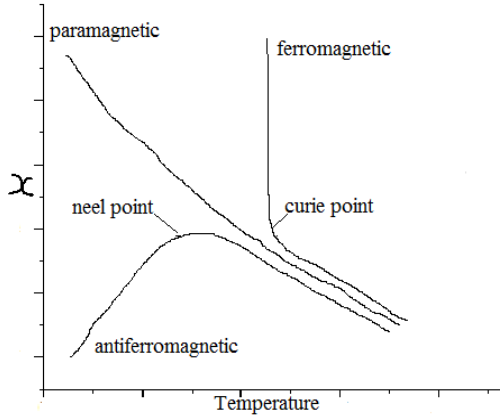

Figure 2.1 Temperature dependent magnetism

2.3.3 Ferromagnetic materials

Ferromagnetic materials are analogous to paramagnetic ones in having unpaired electrons that build up a net magnetic moment in their atom. However in ferromagnetic materials the magnetic moments build powerful internal fields that are strong enough to resist the thermal vibration effect in randomizing them and therefore the magnetic movements align parallel to the atoms surrounding them through exchange interactions and create regions called domains. Apart from the tendency of electrons' intrinsic magnetic moments to be parallel to an applied field, one more factor affects this behaviour. To maintain a lowered energy state, the material maintains the parallel orientation of magnetic moments even when the applied field is removed (Fabrizio M. et al. 2009). Fe, Co and Ni are the three elements that exhibit ferromagnetic property at room temperature. Several compounds and solid solutions can be processed out of these materials, and therefore the number of magnetic materials can be infinite. The susceptibility of these materials is very large in comparison with paramagnetic ones. As seen in Figure 2.1, the overall trend is that the susceptibility decreases with increasing temperature; however it is apparent that after a certain temperature this trend accelerates sharply. This point is called the **Curie** temperature at which thermal vibrations of the atoms overcomes the exchange interaction and beyond this point, the ferromagnetic material becomes paramagnetic. The Curie-Weiss equation is true beyond Curie temperature for ferromagnetic materials.

2.3.4 Antiferromagnetic materials

In antiferromagnetic materials, the exchange interactions present among atoms result in anti parallel magnetic moments in neighbouring atoms (Cullity B. D. 1972). These materials act almost the same way as paramagnetic materials in having no net magnetization. This effect is due to the structure of antiferromagnets, which is composed of two associated sublattices of atoms in which the magnetic alignments are opposite to each other. The characteristic temperature of the

antiferromagnetic (Fig. 2.1) materials is called "Neel temperature" beyond which the magnetic moments of atoms will orient randomly and in fact the material becomes paramagnetic.

2.3.5 Ferrimagnetic materials

Ferrimagnetic materials similar to antiferromagnetic ones, exhibit magnetization at room temperature and saturated domains; however with an unzero net magnetic moments that leads to an overall magnetization which is of course less than it would be for ferromagnetic materials as not all the atoms counteract the dominant direction of magnetization. These types of magnetic materials contain ionic compounds, such as oxides, i.e. magnetite (Fe_3O_4) that belongs to the class of ferrites (Knobel M. et al. 2003).

2.4 Experimental Methods

Experimental methods like mechanical alloying by high energetic ball milling (planetary), metal powder consolidation techniques like ECAP-BP, cold compaction and sintering have been surveyed. Deformation of sintered and annealed material by uniaxial compression and subsequently the techniques for structural, morphological, mechanical, and magnetic characterization are surveyed in this section.

2.4.1 Mechanical alloying (MA)

Mechanical alloying (MA) is a ''top-down'' process belonging to the family of severe plastic deformation techniques. It allows the refinement of a coarse grain powder, with grain diameter of the order of ≈ 50 mm, via cyclic fracture and welding of powder particles. Several types of mills such as standard mills, ball mills, or shaker mills can be used. Ball mills are usually preferred to other types of mills. MA is extremely appealing due to its simplicity and ease of use. A vast diversity of nanocrystalline alloys (e.g., Fe-Co, Fe-Pb, Al-Mg, etc.), including immiscible systems such as Pb-Al and even ceramics can be synthesized by mechanical alloying, which opens a vast range of opportunities for nanocrystalline materials processed by MA. MA technique allows one to overcome problems, such as e.g., large difference in melting points of the alloying components as well as unwanted segregation or evaporation that could occur during melting and casting (2009). A great advantage of this process originates also from the fact that it allows one to obtain materials far from their thermodynamic equilibrium. In particular this processing route has been successful in producing many types of solid solutions, disordered/ordered and amorphous alloys. Nanostructured intermetallic materials can be synthesised by MA as a result of ball milling process.

MA via ball milling is a solid state, dry milling process that leads, through a micro-sandwich morphology, to the mixing of elemental powders and eventual alloy formation. It is a practical processing route for the synthesis of phases or phase mixtures. The process leads to an alloy formation by solid state reactions assisted by severe plastic deformation that occurs during ball milling of elemental powders. This technique has become popular due to its comparatively low cost, great flexibility in the selection of processing parameters, and variety of attainable products. However, a serious problem with the ball milling of fine powders is the susceptibility to contamination from the milling media (balls and vial) or from the gases in the environment, both of which can affect materials properties. Ball milling is associated with long periods of milling times in order to obtain crystallite sizes below 20 nm. This technique modifies the structure and solid solubility limits of alloys and solid solutions and induces lattice strains and phase transformations. The formation of metastable phases and disordering of the lattice through alloying gives rise to interesting structural, mechanical and magnetic properties. This is particularly evident in the case of Al-Fe intermetallic systems. Thus, the limitation of MA process is almost eliminated by choosing a suitable milling media and an inert gas environment which do not contaminate the synthesized ultra fine grained powder.

2.4.1.1 High energetic planetary ball milling

In this section the focus is on ball mill utilising the principles of planetary motion and capable of delivering high impact energy. Such type of ball mills have been used to process elemental powders of Fe and Al. Known as centrifugal or planetary mills (Fig.2.2), these are devices used to rapidly grind materials to colloidal fineness, they develop high grinding energy via centrifugal or planetary action. To grind a sample in this device, the starting particle size should be less than 10 mm, the sample (material) and several balls are placed inside the bowl or jar and the balls to powder weight ratio depends on the type of material being ground and the fineness required. Each jar (vial) is mounted on an independent rotatable platform, thus a set of four grinding jars for the planetary ball mill are arranged in such a way that each moves (Fig. 2.2 red arrow) around its own axis and, in the opposite direction, around (black arrow) the common axis of the sun wheel. The direction of rotation of sun wheel and jars are indicated by arrows. The rotation is at uniform speed and uniform ratios. The result is that the superimposition of the centrifugal force changes constantly (Coriolis motion). The grinding balls describe a semi-circular movement, separate from the inside wall and collide with the opposite surface with high impact energy. The impact and friction forces are the reasons for the impressive size reduction power of the PM 400 machine. Superimposition of centrifugal forces produces grinding ball movements with high pulverization energy. Centrifugal forces acting on the grinding jar wall initially carry the grinding balls in the direction in which the grinding jar is rotating, differences occur between the speed of the grinding

jar wall and the balls, resulting in strong frictional forces acting on the sample. As rotational movement increases, Coriolis forces act on the balls displacing them from the grinding jar walls. Balls fly through the grinding jar interior and impact against the sample on the opposite grinding jar wall (observe the blue balls and arrows in Fig. 2.3, this releases considerable dynamic impact energy. Combination of frictional forces and impact forces cause high degree of size reduction.

Figure 2.2 Retsch PM-400 planetary ball mill, note that the milling chamber contains a disk (sun wheel) with four symmetrically located grinding jars (vials).

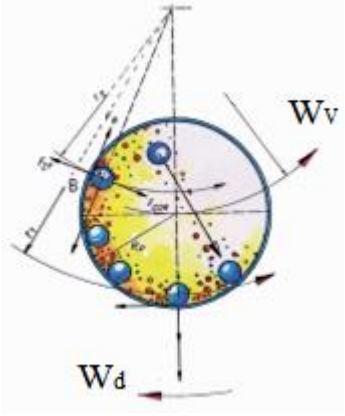

Figure 2.3 Top view of planetary ball mill technology, shows balls and powder motion inside the vial, W_d and W_V are the angular frequencies of the supporting disk and the vials, respectively.

2.4.1.2 Mechanical alloying parameters

Mechanical alloying requires the optimization of several variables in order to achieve alloying of elemental powders with desired grain size. Following are few very important variables which have a bearing on the constitution of the final mechanically alloyed product:

1. Ball milling intensity (Power transferred)
2. Ball milling speed
3. Ball milling time

4. Ball milling media
5. Ball-to-powder weight ratio
6. Extent of filling the vial
7. Ball milling atmosphere
8. Ball milling temperature

Ball milling intensity (I):

Quite often milling intensity I is estimated using an expression (Eqn 2.5) which contains the following variables:

$$I = V\Delta Enf \qquad \text{Eqn 2.5}$$

where ΔE is the dissipated energy in a system containing n balls, 'V' a variable less than unity, whose value depends on the volume occupied by the balls inside the vials, and 'f' the frequency at which the balls are thrown to the opposite walls of the vials, which, in the case of a planetary mill, is a function of the angular frequencies (Fig 2.3) of the supporting disk (sun wheel) and the vials, Wd and Wv, respectively. If we consider the energy dissipation then it can only be dissipated during the impact between the balls and the walls of the vials, ΔE depends on a few intrinsic parameters of the planetary mill, such as the distance between the center of the disk and walls of the vials, and the distance between the center of the disk and the center of the vials (Nogues J. et al. 2006). However, there are other relevant parameters, such as the ball-to-powder weight ratio and the milling time, that play an important role in the amount of energy transferred and, therefore, in controlling the final properties of the milled material.

Ball milling speed:

Faster the mill rotates the higher would be the energy input into the powder. But, depending on the design of the mill there are certain limitations to the maximum speed that could be employed. For example, in a conventional ball mill increasing the speed of rotation will increase the speed with which the balls move. Above a critical speed, the balls will be pinned to the inner walls of the vial and do not fall down to exert any impact force. Therefore, the maximum speed should be just below this critical value so that the balls fall down from the maximum height to produce the maximum collision energy. Another effect of the maximum speed is that at high speeds (or intensity of milling), the temperature within the vial reaches a high value promoting diffusion that is required in the alloying of the elemental powders. Too high a temperature may lead to dynamic recrystallisation, grain growth and contamination of the alloyed powder. A fully amorphous phase was formed in a Ni-Zr powder mixture at high energy of milling whereas a mixture of crystalline

and amorphous phases formed at low and intermediate milling energies (Calka A., Radlinski A. P. 1991).

Ball milling time:

The duration of milling is the most important parameter. The duration is so chosen as to achieve a steady state between the fracturing and cold welding of the powder particles. The duration of milling varies depending on the type of mill used, the intensity of milling, the ball-to-powder ratio, and the temperature of milling. These times have to be decided for each combination of the above parameters and for the particular powder system. But, it should be realized that the level of contamination increases and some undesirable phases form if the powder is milled for times longer than required (Suryanarayana C. 2001). Therefore, it is desirable that the elemental powders are milled just for the required duration so as to obtain alloy formation with grain size reduction to nano level and not any longer.

Ball milling media (MM):

Figure 2.4 shows jars and balls, these grinding media or milling media (MM) are available in different materials namely agate, sintered corundum, zirconium oxide, stainless steel, special steel, and tungsten carbide. Milling sets made from high-performance ceramics, sintered corundum and zirconium oxide with their high abrasion resistance offer a long working life combined with minimal abrasion. Hardened steel, tool steel, hardened chromium steel, tempered steel, stainless steel, WC±Co, and bearing steel are some of the most common types of materials used as MM. In addition to these materials, some special materials (Suryanarayana C. 2001) are used for MM and these include copper, titanium, niobium, zirconia (ZrO_2), yttria stabilized zirconia, partially stabilized zirconia with yttria, sapphire, and silicon nitride (Si_3N_4). Performance and the results depend on the choice of the milling jar and the balls with which it is filled. The selection depends on the sample volume as well as the milled fineness to be achieved and the purity required. Table 2.1 makes it possible to select a suitable mixing configuration, depending on the quantity of the sample and the grain size of the feed material. For coarse size reduction, large balls are used and ultra fineness requires the use of small balls; higher the ball density, higher will be the pulverization energy. Jar and ball material should resist abrasion and facilitate subsequent analysis. It is always desirable, to have the milling vessel and the milling balls made of the same material as the powder being milled to avoid cross contamination. In certain instances, during initial stages of ball milling, the powder being milled gets coated on to the surface of the balls and also gets cold welded. Such a type of coating can be advantageous as it prevents contamination of the powder due to excessive wear of the balls. Coating must be kept to a minimum thickness or else it creates problems like difficulty in detaching the powder and formation of heterogeneous final product. In

order to minimize thick coating and to increase the powder yield, a combination of smaller and larger balls are to be employed, it is possible that different sized balls produce shearing forces that may help in detaching the coated powder.

Figure 2.4 milling media, grinding jars and balls.

Specification and different parts of the milling jar (vial) is shown in the cross sectional view in Figure 2.5. Different parts and specification of the milling vial is indicated in the figure according to numbers, each of these numbers is described as follows:

1. Protective jacket made of stainless steel (for all ceramic, agate and WC jars)
2. Positive O-ring seals on lids
3. The gap between the jar and the edge of the lid simplifies opening
4. Anti-rotation feature, non-slip seating due to exact centering
5. Identification of the grinding jar (item number, material and volume)
6. Space for user labeling (e.g. product being processed)
7. Flanges on the jar and lid facilitate handling

For effective functioning of milling media (MM), the diameter of the ball used as MM, maximum size of the feed material, volume of selected vial (MM) are shown in Table 2.1. Selection of a suitable vial depends on the material to be milled, thus vials made from different materials in composition can be selected for milling certain material. Vials made from different materials, their composition, hardness and density are given in Table 2.2.

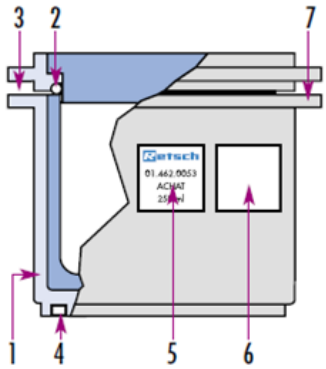

Figure 2.5 specification and details of milling jar (vial).

Table 2.1 specification of milling media

Jars type rated volume	Eff.volume (material and balls)	Max. feed particle size	Recommended ball charge			
			40 mm ϕ	30 mm ϕ	20 mm ϕ	10 mm ϕ
50 ml	5-30 ml	< 3 mm			3 pcs.	10 pcs.
125 ml	15 –80 ml	< 4 mm			6 pcs.	25 pcs.
250 ml	25-150 ml	< 6 mm		5 pcs	12 pcs.	50 pcs.
500 ml	75-300 ml	< 10 mm	4 pcs	8 pcs	20 pcs.	100 pcs.

Table 2.2 material analysis of milling media

Grinding set	**Composition(approx.)**	**Degree of hardness**	**Density kg/m^3**
Agate	99.9% SiO_2	7.0 Mohs	App. 2600
Sintered corundum	99.7% Al_2O_3	9.0 Mohs	App. 3900
Silicon nitride	53.0 % Si, 35.2 % N, 3.5 % I, 2.5 % Al, 0.5 % Mg	HV=1400kg/mm^2=14GPa	3200
Zirconia	97.0% ZrO_2	8.5 Mohs	5700
Stainless steel	84.5 Fe, 13.0% Cr	53HRC=app.HV=5.7GPa	7700
Chrome steel 2	86.0% Fe, 11.5% Cr	60HRC= app.HV=7GPa	7700
Chrome steel 4	84.0% Fe, 13.5% Cr	53HRC=app.HV=5.7GPa	7700
Tungsten carbide	94.0% WC, 6.0% Co	HV=1150kg/mm^2=11.2GPa	14400

The milling time decreases with an increase in the energy of the mill. Fig. 2.6 shows the time required to reach a specific particle size during milling in a planetary ball mill and in an attritor. It is noted that the times are an order of magnitude shorter in the attritor (Thummler F., Oberacker R. 1993). An attritor (a ball mill capable of generating higher energies) consists of a vertical drum with a series of impellers inside it. Set progressively at right angles to each other, the impellers energize the ball charge, causing powder size reduction because of impact between balls, between balls and container wall, and between balls, agitator shaft, and impellers. Some size reduction appears to take place by interparticle collisions and by ball sliding. A powerful motor rotates the impellers, which in turn agitate the steel balls in the drum.

Ball-to-powder weight ratio (BPR):

BPR is an important variable during the milling process, investigators have varied BPR value from as low as 1:1 to as high as 200:1. In a small capacity planetary ball mill, a ratio of 10:1 is commonly used while milling the powder. The BPR has a significant effect on the time required to achieve a particular phase during the milling process. Shorter time is required to achieve an amorphous phase at higher BPR during mechanical alloying of elemental metals in a ball mill. Higher BPR causes an increase in the weight proportion of the balls leading to an increase in the number of collision per unit time, consequently more collision energy is imparted on the powder particles and thus alloying occurs at a more rapid pace. The collision energy generated may cause

an increase in the temperature, thus an amorphous phase formed may crystallize due to substantial rise in temperature.

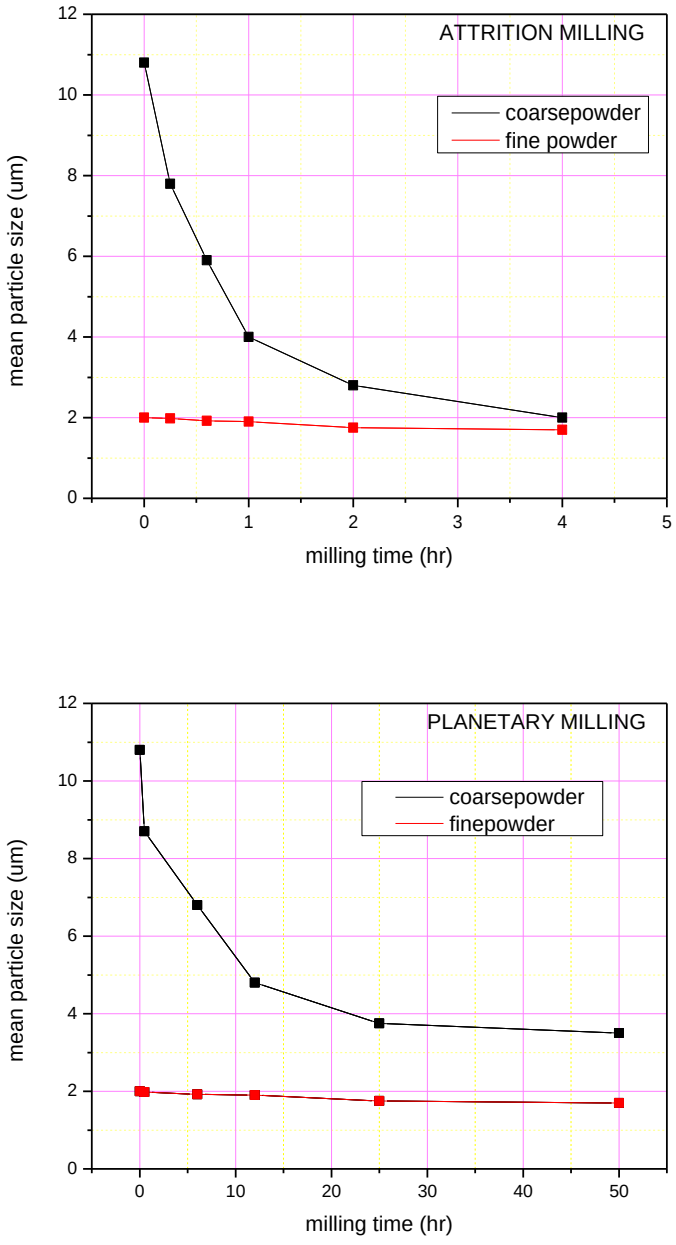

Figure 2.6 attrition milling and planetary milling. Mean particle size as a function of milling time.

Extent of filling the vial:

Elemental metal powders are trapped between the container wall and the impinging balls, thus the collision energy exerted by the balls on the powder causes mechanical alloying and size reduction. Sufficient space must be provided for the balls and powders to move around freely in the milling vial. Filling the milling vial with exact quantity of balls and powder is very critical, too large

quantity in the milling vial will reduce the space necessary to provide free movement for the balls, then the collision energy produced is less. On the other hand, if the quantity of filling is too small then the production rate is low. To obtain the best milling results, generally 50 % of the vial space is left unoccupied.

Ball milling atmosphere:

Mechanical alloying of elemental metal powders by planetary ball milling has to be carried out in certain restricted atmosphere only, if not then the major effect of milling in an open atmosphere is on the contamination of the powder. Powders are milled in vials which have been either evacuated or evacuated and then filled with an inert gas such as argon or helium. High purity argon is the most commonly used gaseous atmosphere to avoid oxidation and contamination during milling. Normally the loading and unloading of the metal powders into the milling vials are done inside atmosphere controlled glove box (Fig. 2.7). Glove box is repeatedly evacuated and refilled with argon gases to facilitate removal and placing of milling vials. It has been reported that milling operations were done in ball mills placed inside an evacuated glove box filled with argon. Ductile materials tend to coalesce by welding. This is typically avoided by adding small quantities of a process control agent such as methanol, ethanol, stearic acid, and paraffin compounds.

Figure 2.7 operation of glove box in an evacuated mode

Ball milling temperature:

Temperature experienced by the metallic/alloy powder during milling is directly dependent on the kinetic energy of the revolving balls inside the milling vial. It has an effect on the constitution of the final product, thus enabling temperature to be an important parameter during the mechanical alloying process. High temperature generated during the process is associated with diffusion, increasing the entropy (higher mobility of the atoms) of the system resulting in the formation of intermetallic phase (due to recovery and recrystallisation). On the other hand, if the temperature generated is low then an amorphous phase would form, mainly due to anti site defects in the structure of the material being milled. It has been reported that the macroscopic temperature of the container and the balls measured by thermocouples was noted to be about 100 ^{0}C. On the other hand, the local (microscopic) temperatures can be very high often exceeding the melting points of some of the component metals. It is quite tough to measure the microscopic temperature during the process because of the dynamic nature of milling; nevertheless some of the investigators have reported the microscopic temperature prevailing during the milling process to be about 590 ^{0}C for NiZr powder. These investigations were estimated by calculating and relating various microstructural parameter changes during the milling process.

2.4.1.3 Mechanism of mechanical alloying

High energetic ball milling imparts repeated flattening, cold welding, fracture and rewelding of elemental powder particles. When two balls collide in a milling jar small quantity of powder particles are trapped between them, typically about 1000 particles with an aggregate weight of approximately 0.2 mg are trapped during each collision. Such collision energy plastically deforms the powder particles leading to work hardening and fracture. The new fractured surfaces are welded together to form a new particle with increased size. During early stages of milling the particles are softer (combination of material being milled are normally ductile to ductile or ductile to brittle) and have more tendencies to weld together to form particles of larger size. A wide range of particle sizes are produced and with some as large as three times bigger than the starting particles. Continued deformation causes work hardening and fracture by the fragmentation of fragile flakes. The fractured flakes generated by such mechanism reduce in size due to the absence of strong agglomerating forces. During this stage of ball milling the tendency to fracture predominates over cold welding. Due to continued collision of the grinding balls, the structure of the particles is refined steadily while the particle size remains unchanged. Consequently, the interlayer spacing decreases while the number of layers in a particle increases. After milling for certain length of time, a balance is attained between the rate of fracture and the rate of welding, thus smaller particles are able to withstand deformation without fracturing and tend to get welded onto the larger particles. At this stage, there is an overall tendency to drive both the large particles

and small particles towards an intermediate size, thus each particle possesses all of the starting ingredients according to the proportions they were mixed together. Particles larger than average size are reduced while those which are smaller than average grow through agglomeration of smaller particles. Moreover, the particles reach saturation in hardness due to the accumulation of strain energy with every impact of ball collision. Thus, it is quite clear that during MA by high energetic ball milling, heavy deformation is introduced into the particles. This is evident by the presence of a variety of crystal defects such as dislocations, vacancies, stacking faults, and increased grain boundaries. Such crystal defects when present enhances the diffusivity of solute elements into the matrix. Further, slight rise in temperature during milling aids in the diffusion mechanism. MA takes place amongst the constituent elements normally at room temperature. The rate of refinement of the internal structure (particle size, crystallite size, lamellar spacing, etc.) is roughly logarithmic with processing time, thus the initial particle size is relatively unimportant. As the ball milling duration varies from a few minutes to a few hours, the lamellar spacing decreases reducing the crystallite size to nano scale as shown in Figure 2.8.

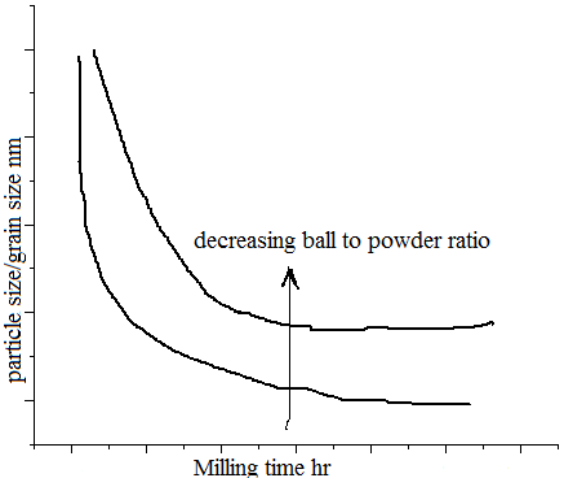

Figure 2.8 particle/crystallite size reduces with increase in milling duration.

2.4.1.4 Solid solubility

It is possible to synthesize stable equilibrium solid solutions and also metastable nonequillibrium supersaturated solid solutions in a binary system by mechanical alloying of elemental powders. During mechanical alloying of elemental (binary system) powder in a ball milling, interdiffusion occurs between the two components resulting in a solid solution. Solid solubility is expected to increase with milling duration as diffusion progresses and reaches a saturation level (Fig. 2.9), beyond which there is no further increase in solubility. This saturation value is termed as solid solubility limit achieved by mechanical alloying during ball milling. In another instance, when a

binary component forms an isomorphous system during mechanical alloying, the lattice parameter of one metal decreases and that of the other increases during milling. Upon reaching steady state conditions the two lattice parameters merge to form an expected lattice parameter (Fig 2.9) of the homogeneous solid solution. During mechanical alloying of elemental powders by planetary ball milling, solid solution formed can be identified and investigated by x-ray diffraction (XRD) pattern. The diminishing and absence of solute peaks in a XRD pattern of a powder sample obtained at a precise milling duration suggests a transition to solid solution and complete dissolution respectively. TEM investigation of mechanically alloyed powder showed nanostructured solute particles in the solvent matrix. Thus it is desirable to use more than one technique to determine accurately the precise solid solubility limits (Suryanarayana C. 2001).

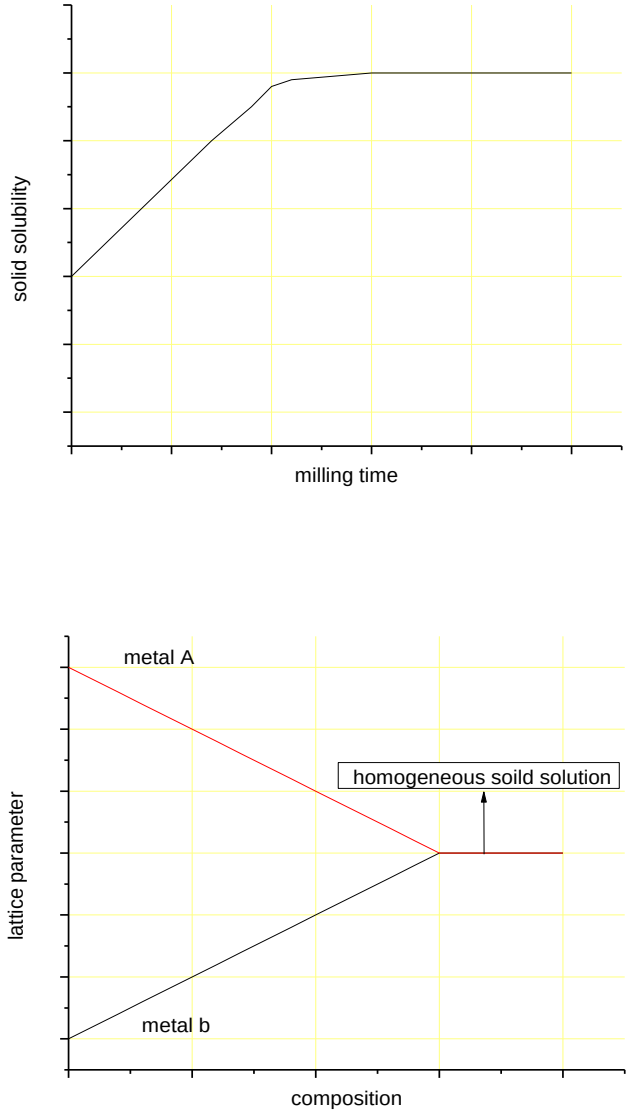

Figure 2.9 solid solubility vs milling time, lattice parameter vs composition.

2.4.2 X-ray diffraction (XRD)

Phase transformation and structural changes during MA and consolidation was investigated by XRD, thus the literature has been surveyed. X-ray diffraction (XRD) has long been used to determine the atomic-scale structure of materials. This technique is based on the fact that the wavelength of x-rays is comparable to the distances between the atoms in crystals.

2.4.2.1 X-ray generation & properties

X-rays are electromagnetic radiation with typical photon energies in the range of 100 eV - 100 keV. For diffraction applications, only short wavelength x-rays (hard x-rays) in the range of a few angstroms to 0.1 angstrom (1 keV - 120 keV) are used. Because the wavelength of x-rays is comparable to the size of atoms, they are ideally suited for probing the structural arrangement of atoms and molecules in a wide range of materials. The energetic x-rays can penetrate deep into the materials and provide information about the bulk structure. A coherent beam of monochromatic X-rays of known wavelength is required for XRD Analysis. Striking a pure anode (target) of a particular metal with high-energy electrons in a sealed vacuum tube generates X-rays (as electrons collide with the atoms in the target, a continuous spectrum of x-rays are emitted) that may be used for X-ray diffraction. By the right choice of metal anode and energy of accelerated electrons, a known wavelength (i.e., energy) or group of wavelengths will dominate the X-rays generated. The high energy electrons also eject inner shell electrons in atoms through the ionization process. When a free electron fills the shell, an x-ray photon with energy characteristic of the target material is emitted. Copper (Cu) X-ray tubes are the most commonly used ones for X-ray diffraction of inorganic materials. The wavelength of the strongest Cu radiation (K_α) is approximately 1.54 angstroms (Å). Other anodes commonly used in X-ray generating tubes include Cr (K_α 2.29 Å), Fe (K_α 1.94 Å), Co (K_α 1.79 Å), and Mo (K_α 0.71 Å). The radiation produced in the tube includes $K_{\alpha1}$, $K_{\alpha2}$, and K_β as the highest energy X-rays and a whole host of lower energy radiation. We generally use the K_α for our analytical work. The K_β radiation is usually removed by use of a filter, a monochromator or an energy-selective detector. The $K_{\alpha2}$ radiation is removed from the X-ray data electronically during data processing. The energy E of a x-ray photon and its wavelength is related by the equation $E = hc/\lambda$, where h is Planck's constant, c the speed of light and λ the wavelength of x-ray.

2.4.2.2 Directing the X-rays on the specimen

Parallel beam of X-rays is directed to the specimen. In most diffractometer systems, as shown in Fig. 2.10, a series of parallel plates (soller slits) arranged parallel to the plane of the diffractometer circle and several scatter and receiving slits (arranged perpendicular to the diffractometer circle) are used to create an incident beam of X-rays that are (approximately) parallel. Soller slits are

commonly used on both the incident and diffracted beam, but this will vary depending on the particular system. The scatter slits (on the incident beam side) may be varied to control the width of the incident beam that impinges upon the specimen and the receiving slits may be varied to control the width of the beam entering the detector. Filters for removing K_β may be located in the beam path on the generator or detector side of the path; a monochromator, if present, is usually located on the detector side between the receiving slit and the detector. The diffractometer with the optical systems that generates a tightly controlled and focused incident beam of X-rays is shown in the sketch in Figure 2.10.

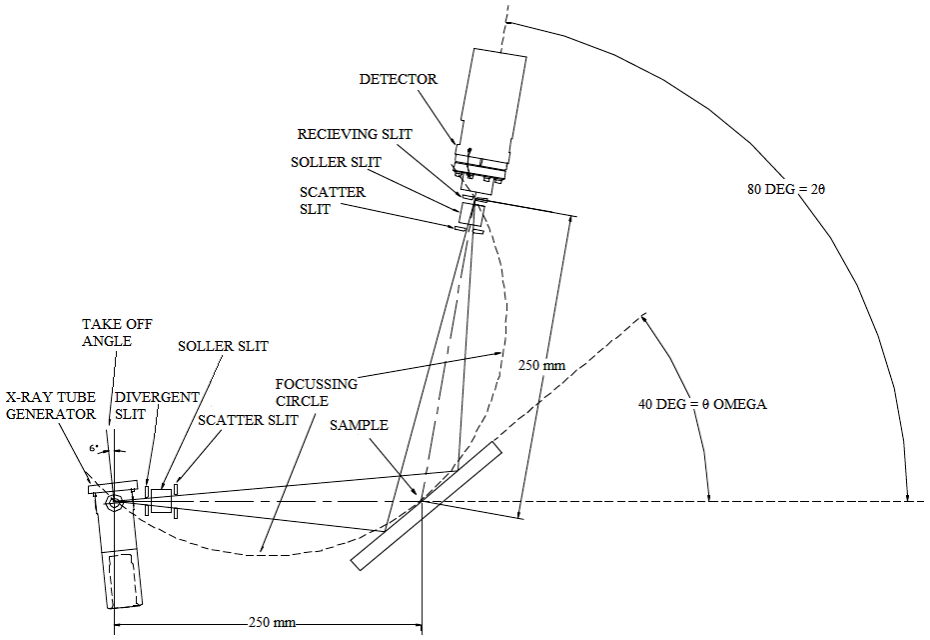

Figure 2.10 XRD optics

2.4.2.3 X-ray diffraction technique and Bragg's law

When a beam of x-rays impinges on a solid material, a portion of this beam will be scattered in all directions by the electrons associated with each atom or ion that lies within the beam's path. Let us now examine the necessary conditions for diffraction of x-rays by a periodic arrangement of atoms. Consider the two parallel planes of atoms A–A' and B–B' in the Figure 2.11, which have the same *h*, *k*, and *l* Miller indices and are separated by the interplanar spacing d_{hkl}. Now assume that a parallel, monochromatic, and coherent (in-phase) beam of x-rays of wavelength λ is incident on these two planes at an angle θ. Two rays in this beam, labeled 1 and 2, are scattered by atoms *P* and *Q*. Constructive interference of the scattered rays 1' and 2' occurs also at an angle θ to the planes, if the path length difference between 1–*P*–1' and 2–*Q*–2' (SQ+QT) is equal to a whole number, *n*, of the wavelength. Thus, the condition for diffraction is given in equation 2.6.

$n\lambda = SQ+QT$ Eqn 2.6

$n\lambda = d_{hkl} \sin\theta + d_{hkl} \sin\theta$ Eqn 2.7

$n\lambda = 2d_{hkl}\sin\theta$ Eqn 2.8

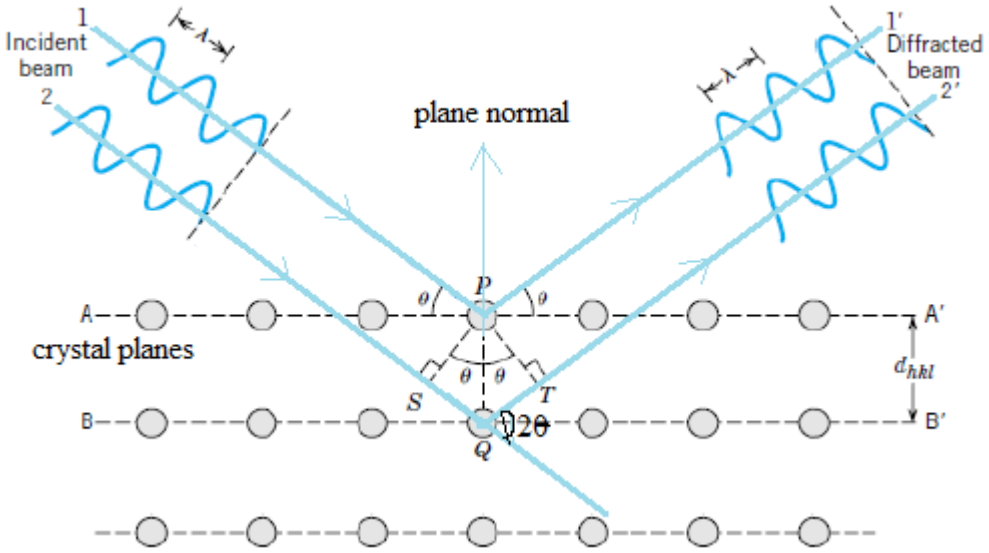

Figure 2.11 Wave length (λ) of X-Ray, incident beam and diffracted beam, periodic arrangement of atoms, crystallographic planes and Bragg angle (2θ).

The equation. 2.7 and 2.8 are known as **Bragg's law;** *n* is the order of reflection, which may be any integer (1, 2, 3 . . .) consistent with sinθ not exceeding unity. Thus, The Bragg equation relates x-ray wavelength and interatomic spacing with the angle of the diffracted beam (2θ) as shown in Figure 2.11. If Bragg's law is not satisfied, then the interference will be non constructive in nature so as to yield a very low intensity diffracted beam. The magnitude of the distance between two adjacent and parallel planes of atoms (i.e., the interplanar spacing d_{hkl}) is a function of the Miller indices (*h, k,* and *l*) as well as the lattice parameter (a). For example, for crystal structures that have cubic symmetry, the interplanar spacing 'd' is given by equation 2.9.

$$d = \frac{a}{\sqrt[2]{h^2+k^2+l^2}}$$ Eqn 2.9

in which *a* is the lattice parameter. Relationships similar to equation 2.9, but more complex, exist for the other six crystal systems. Bragg's law and its equation (Eqn 2.8), is a necessary but not sufficient condition for diffraction by real crystals. It specifies when diffraction will occur for unit cells having atoms positioned only at cell corners. However, atoms situated at other sites (e.g., face and interior unit cell positions as with FCC and BCC) act as extra scattering centers, which can produce out-of-phase scattering at certain Bragg angles. The net result is the absence of some of

the diffracted beams that, according to equation 2.8, should be present. For example, for the BCC crystal structure, $h + k + l$ must be even if diffraction is to occur, whereas for FCC, h, k, and l must all be unmixed (either odd or even).

2.4.2.4 Powder diffraction

Powder XRD (X-ray Diffraction) is perhaps the most widely used x-ray diffraction technique for characterizing materials. As the name suggests, the sample is usually in a powder form, consisting of fine grains of single crystalline material to be studied. The technique is also used widely for studying particles in liquid suspensions or polycrystalline solids (bulk or thin film materials). X-rays diffracted from a powder/polycrystalline sample produce a continuous ring called the 'debye ring' as shown in the Figure. 2.12, when the crystallites are randomly oriented and sufficient crystallites are present in the sample. In a linear diffraction pattern, the detector scans through an arc that intersects each Debye cone at a single point; thus giving the appearance of a discrete diffraction peak as shown in the Figure. 2.12.

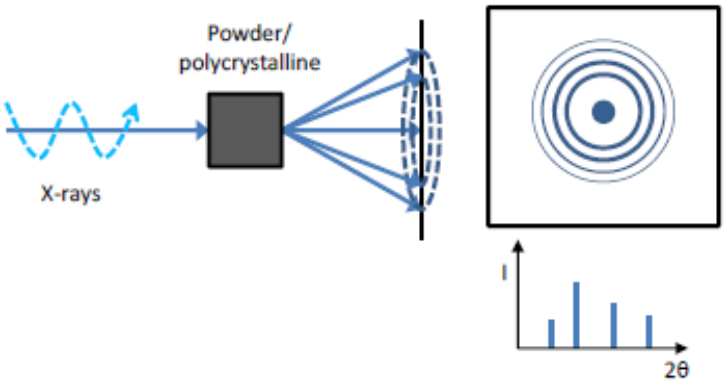

Figure 2.12 X-ray pattern obtained from a polycrystalline sample

2.4.2.5 Diffraction techniques

Diffraction technique, in which a powdered or polycrystalline specimen is employed, consists of many fine and randomly oriented particles that are exposed to monochromatic x-radiation. Each powder particle (or grain) is a crystal, and having a large number of them with random orientations ensures that some particles are properly oriented such that every possible set of crystallographic planes will be available for diffraction. Powder diffractometers come in two basic varieties: θ-θ in which the X-ray tube and detector move simultaneously or a θ-2θ in which the X-ray tube is fixed, and the specimen moves at ½ the rate of the detector to maintain the θ-2θ geometry. Panalytical x-ray diffractometer utilized for this research work at the Deakin University is a θ-2θ system; the "angle" of the diffraction (recorded as 2θ by convention) is related to the interplanar spacing, d, by the Bragg law, and the intensity of the diffraction maximum (peaks) is related to the strength of

those diffractions in the specimen. Basically diffractometer is an apparatus used to determine the angles at which diffraction occurs for powdered specimens; its features are represented schematically in the Figure 2.13. Powder specimen S in the form of a flat plate is supported such that rotations about the axis labeled O is possible; this axis is perpendicular to the plane of the page. The monochromatic x-ray beam generated at point 'T' impinges the specimen 'S' and gets diffracted, the intensities of the diffracted beam is detected at 'C'. X-ray source (located at T), the specimen 'S' and the detector assembly 'C' are all coplanar. Detector assembly mounted on a moving carriage is capable of rotating about the axis 'O'; its angular position in terms of 2θ is marked on a graduated scale. Rotations of the detector assembly 'C' and the specimen holder 'S' are synchronized in such a way that a rotation of the specimen through θ is accompanied by a 2θ rotation of the detector, this ensures the angle of incidence (θ) and the angle of reflections (2θ) are according to Bragg's law. Collimators are incorporated within the beam path to produce a well-defined and focused beam. Utilization of a filter provides a near-monochromatic beam. As the detector moves at constant angular velocity, a recorder automatically plots the diffracted beam intensity (monitored by the counter in the detector assembly) as a function of 2θ; 2θ is termed the diffraction angle, which is measured experimentally. Figure 2.14 shows a Bragg diffraction pattern of a polycrystalline sample recorded by a diffractometer using a specialized software. The high-intensity (counts) peaks (also known as Bragg peaks) result when the Bragg diffraction condition is satisfied by some set of crystallographic planes.

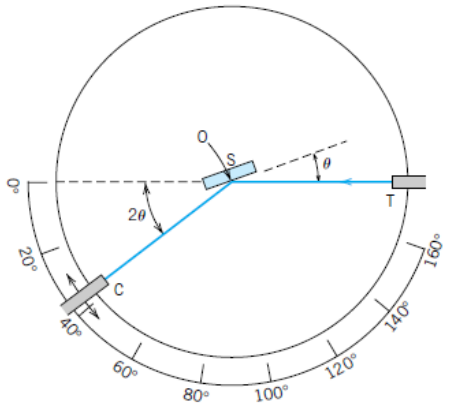

Figure 2.13 Diffractometer (θ-2θ)

A polycrystalline sample contains thousands of crystallites. Therefore, all possible diffraction peaks can be observed. For every set of planes, there will be a small percentage of crystallites that are properly oriented to diffract (the plane perpendicular bisects the incident and diffracted beams) as shown in the Figure 2.14. Basic assumptions of powder diffraction are that for every set of

planes there are an equal number of crystallites that will diffract and that there is statistically relevant number of crystallites, not just one or two.

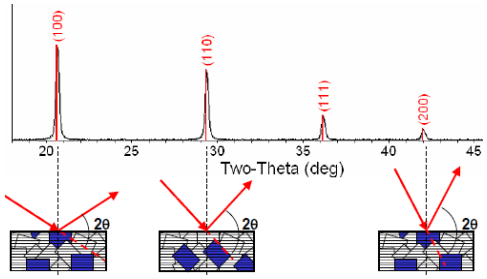

Figure 2.14 diffractions from different crystallographic planes

2.4.2.6 Indexing

Knowledge of the crystal structure is a prerequisite to understand the phenomena such as alloy formation and phase transformations. Indexing the pattern involves assigning the correct Miller indices to each peak in the diffraction pattern. These peaks are also referred to as reflections. It is important to note that correct indexing is done only when all the peaks in the diffraction pattern (Fig. 2.15) are accounted for and no peaks expected for the structure are missing from the diffraction pattern. The interplanar spacing 'd', the distance between adjacent planes in the set (hkl) of a material with a cubic structure and lattice parameter 'a' are obtained from the equations (2.10, 2.11 and 2.12).

$1/d^2 = (h^2+k^2+l^2)/a^2$ Eqn 2.10

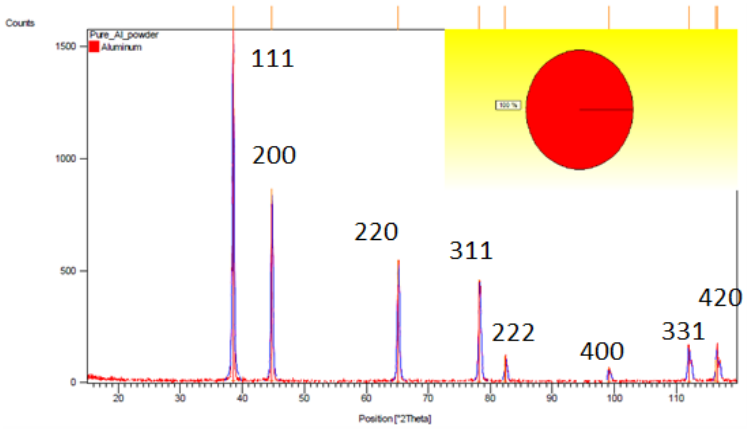

Figure 2.15 XRD pattern of pure Al powder

Squaring the Bragg equation, we obtain

$\lambda^2 = 4\, d^2 \sin^2\theta$, hence $d^2 = \lambda^2 / 4 \sin^2\theta$ Eqn 2.11

$\sin^2\theta = \lambda^2 (h^2+k^2+l^2) / 4a^2$ Eqn 2.12

In the equation 2.12, $\lambda^2/ 4a^2$ is constant for any one pattern, we note that $\sin^2\theta$ is directly proportional to $h^2+k^2+l^2$, as θ increases, planes with higher Miller indices will diffract. The Bravais lattice is identified by noting the systematic presence or absence of reflection in the diffraction pattern, according to these rules; the $h^2+k^2+l^2$ values for the different cubic lattice follow the sequence as indicated in the Table 2.3.

Table 2.3 selection rules for the presence or absence of reflections

$h^2+k^2+l^2$	hkl	bcc	fcc
1	100	-	-
2	110	√	-
3	111	-	√
4	200	√	√
5	210	-	-
6	211	√	-
7	Nil	-	-
8	220	√	√
9	221& 300	-	-
10	310	√	-
11	311	-	√
12	222	√	√
13	320	-	-
14	321	√	-
15	Nil	-	-
16	400	√	√
17	410& 322	-	-
18	411or 330	√	-
19	331	-	√
20	420	√	√

Note:

1) When diffraction is present for unmixed hkl values (all odd or all even), then it can be concluded that the Bravais lattice is **FCC**.
2) When reflections are present for h+k+l = even, then the Bravais lattice is BCC.

The Bravais lattice and the crystal structure are identified from the sequence of $h^2+k^2+l^2$ values in the diffraction pattern. Thus, the XRD pattern (Fig.2.15) has been indexed and the phase identified as Al is shown in the Table 2.4.

Table 2.4 indexed elemental Al peaks

peaks	2θ	$\sin^2\theta$	$\sin^2\theta/\sin^2\theta_{min}$	$h^2+k^2+l^2$	hkl	Crystal structure
1	38.52	0.1088	1 x 3	3	111	FCC
2	44.76	0.1450	1.33 x 3	4	200	FCC
3	65.14	0.2898	2.66 x 3	8	220	FCC
4	78.26	0.3983	3.66 x 3	11	311	FCC
5	82.47	0.4345	3.99 x 3	12	222	FCC
6	99.11	0.5792	5.32 x 3	16	400	FCC
7`	112.03	0.6876	6.32 x 3	19	331	FCC
8	116.60	0.7238	6.65 x 3	20	420	FCC

2.4.2.7 Intensities in X-ray powder patterns

The relative intensities of Bragg diffraction peaks in x-ray powder patterns is given by the following equation 2.13.

$I = IFI^2 P (1+\cos^2 2\theta / \sin^2\theta \cos\theta) A(\theta)e^{-2M}$ Eqn 2.13

In the equation 2.13, the definition of various parameters are as follows:

1) F is the structure factor.
2) I is the relative integrated intensity.
3) P is the multiplicity factor arising from the fact that in a powder some planes occur more frequently than others.
4) In parentheses is the Lorentz-polarization factor which combines three effects, one arising from the polarisation of the X-ray beam, and the other two from the geometry of the apparatus.
5) A is the absorption factor accounting for the fact that scattering at low angles will involve more transmission and will be absorbed more than scattering at high angles.
6) e^{-2M} is a temperature factor to compensate for a change in atomic scattering factor: as the temperature increases, the size of the atom increases.

2.4.2.8 Crystallite size

Crystallite size refers to the size of the diffracting unit, which may or may not correspond to the grain size in a polycrystalline sample, or to the particle size in a powdered sample. The scherrer equation (2.14) given below relates peak width to crystallite size.

$$\beta = {}^{K \times \lambda}/_{D \times cos\theta}$$ Eqn 2.14

Where β (= $\beta_{1/2}$) is the width in radians at an intensity equal to half the maximum intensity of the peak profile (FWHM) as shown in the Fig. 2.16, β has to be corrected for instrumental broadening. Note that β is an angular width in terms of 2θ and not θ and not a linear width. D is the average crystallite size measured in a direction perpendicular to the surface of the specimen. K is the Scherrer constant (=0.94). One of the reasons for peak broadening is crystallite size reduction as shown in the Fig. 2.17. This method can give correct values only if proper corrections for instrumental and strain broadening have been made. However, as we are interested only in following the trend of change of crystallite size with milling conditions, this simple technique is acceptable.

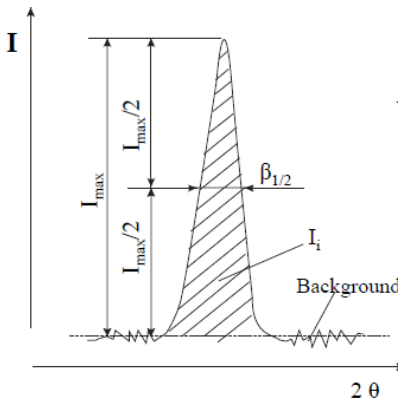

Figure 2.16 to determine half the maximum intensity of peak profile (FWHM)

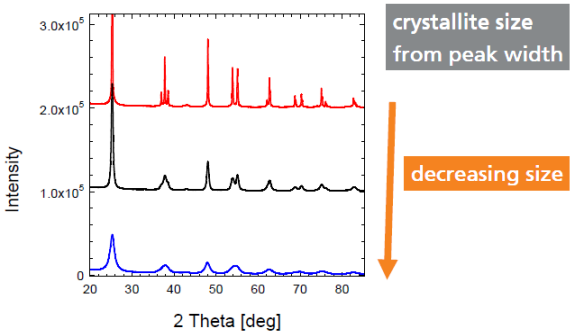

Figure 2.17 crystallite size as a function of peak width (FWHM).

2.4.2.9 Microstrain

Lattice strain (microstrain) arises from displacement of the unit cells about their normal positions (Fig. 2.18) often caused by large deformation resulting in dislocations, surface restructuring, lattice vacancies, interstitial and substitutional solid solutions. Such strains are more common in nano crystalline materials. The peak broadening due to microstrain is assumed to vary as follows:

$\beta_{STRAIN} = \varepsilon 4 tan\theta$ Eqn 2.15

Where β_{STRAIN} is the full width at half maximum (FWHM) of a Bragg reflection excluding instrumental broadening, ε, is the effective lattice microstrain, and θ the Bragg angle. Microstrain (ε) is quantified as follows:

$\varepsilon = \Delta d/d$ Eqn 2.16

d is the interplanar spacing and Δd is the maximum extreme deviation from d, thus ε is the upper limit of the microstrain. However, it is more appropriate to use the root mean square of the microstrain $(\varepsilon^2)^{1/2}$, which is related to microstrain in the following way

$\varepsilon = 1.25\ (\varepsilon^2)^{1/2}$ Eqn 2.17

X-ray peak broadening due to crystallite size is inversely proportional to cosθ and that due to

lattice strain is proportional to tanθ. Thus, by combining these two equations (Eqn 2.14 and 2.15) one gets an equation for the total broadening (after subtracting the instrumental broadening) as follows:

$$\beta = \frac{0.94\,\lambda}{DCos\theta} + 4\varepsilon\, tan\theta \qquad \text{Eqn 2.18}$$

Equation 2.18 is rewritten as follows:

$$\beta\, Cos\theta = \frac{0.94\,\lambda}{D} + 4\varepsilon\, Sin\theta \qquad \text{Eqn 2.19}$$

When βcosθ is plotted against sinθ, a straight line (Fig. 2.19) is obtained with the slope as 'ε' and the intercept as 0.94 λ / D. From these, one can calculate the crystallite size, D and the lattice strain ε.

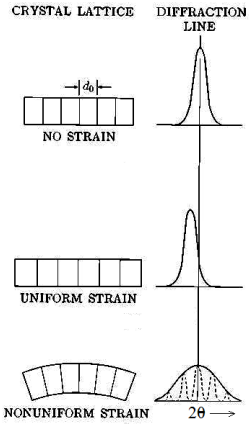

Figure 2.18 effect of lattice strain on debye line width and diffraction peak position.

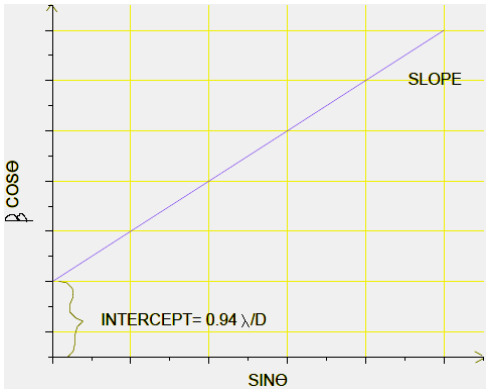

Figure 2.19 graphical method to determine crystallite size

2.4.2.10 X-ray penetration

The X-rays penetrate (Fig. 2.20) the sample to certain extent; therefore it is necessary to have an infinitely thick sample because the contribution to the intensity from the rear side of the sample is negligible. Investigations have shown that when a beam of x-ray is incident on powder /

polycrystalline sample, there will be a fractional decrease in the intensity of the diffracted beam because of absorption from the diffracting sample. The fractional decrease in intensity, I, of an x-ray beam as it passes through the specimen before diffraction is directly proportional to the distance 'x' traversed in the sample and can be written as follows:

$$-\frac{dI}{I} \alpha\, dx \quad \text{or} \quad -\frac{dI}{I} = \mu\, dx \qquad \text{Eqn 2.20}$$

where μ is known as the proportionality constant or the linear absorption coefficient and is dependent on the density of the sample, and the wavelength of the X-rays. Integrating the Equation 2.20 gives equation 2.21:

$$\frac{I}{Io} = \exp(-\mu x) \text{ or } \frac{I}{Io} = \exp(-\frac{\mu}{\rho})\rho x \qquad \text{Eqn 2.21}$$

Where μ/ρ and ρ are known as mass absorption coefficient and density of the sample, I and I_O are the intensities of the diffracted (after travelling a distance χ) and incident x-ray beam respectively in the above equation.

Suppose the mass absorption coefficient of an alloy (material containing more than one element) is to be determined then the μ/ρ of an alloy is defined as the weighted average of the μ/ρ of its constituent elements. If the alloy is FeAl, then ω_{Fe} and ω_{Al} are the weight fractions of Fe and Al in the alloy and $(\mu/\rho)_{Fe}$ and $(\mu/\rho)_{Al}$ their mass absorption coefficients, then the mass absorption coefficient of FeAl alloy is given by the following equation 2.22;

$$(\frac{\mu}{\rho})_{FeAl} = (\frac{\mu}{\rho})_{Fe}\, \omega_{Fe} + (\frac{\mu}{\rho})_{Al}\, \omega_{Al} \qquad \text{Eqn 2.22}$$

The penetration depth d_P is determined when the intensity of the diffracted beam is 1% of the incident beam (ie., transmission factor $I/I_O = 0.01$)

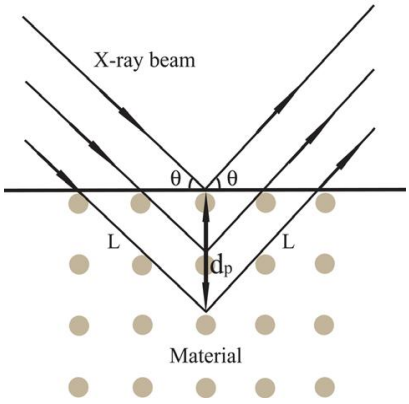

Figure 2.20 penetration depth (dp) of x-rays

Equation (2.23) is used to determine the penetration depth and is derived geometrically by using the optical path of the x-ray during a Bragg diffraction (shown in Fig. 2.11)

$$d_P = L \sin\theta = -\frac{\ln(0.01)}{2(\mu/\rho)\rho}\sin\theta \qquad \text{Eqn 2.23}$$

Therefore, from the equation (2.23) we can clearly state that the x-ray penetration depth depends on mass absorption coefficient and density of the sample in question and the Bragg angle.

2.4.3 Texture measurement (pole figure)

Texture is the distribution of crystallographic orientations of a polycrystalline sample. A sample in which these orientations are fully random is said to have no texture. If the crystallographic orientations are not random, but have some preferred orientation, then the sample has a weak, moderate or strong texture. The degree is dependent on the percentage of crystals having the preferred orientation. Texture is seen in almost all engineered materials, and can have a great influence on material properties. Thus, texture is defined as the orientation distribution of all crystallites of a polycrystalline material with respect to a well known sample orientation. The importance of a texture is given by two facts. First the anisotropy of polycrystalline materials influences their behaviour with thermo mechanical processing, such as forging, extruding, rolling, annealing, etc. Depending on the crystal structure, each individual crystal that forms the polycrystalline aggregate shows anisotropic properties and consequently the orientation distribution of the crystallites has a great influence on the anisotropy of the whole material. Secondly more than 90% of all crystalline materials have a preferred orientation of their crystallites. Texture can be determined by various methods. Some of them allow a quantitative analysis of the texture; others are only qualitative. Among the quantitative techniques, the most widely used is X-ray diffraction using texture goniometers, followed by EBSD-method (electron backscatter diffraction) in scanning electron microscopes. Qualitative analysis can be done by Laue photography, simple X-ray diffraction or with the polarized microscope. Neutron and synchrotron high-energy X-ray diffraction allow access to textures of bulk material and in-situ analysis, whereas laboratory x-ray diffraction instruments are more appropriate for thin film textures.

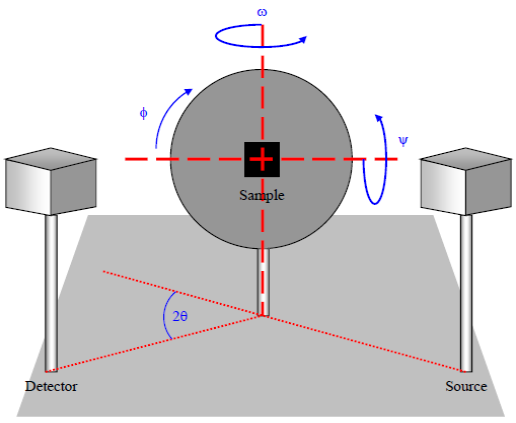

Figure 2.21 schematic representation of a texture measurement

A texture measurement is also referred to as a pole figure as it is often plotted in polar coordinates consisting of the tilt and rotation angles with respect to a given crystallographic orientation. A pole figure is measured at a fixed scattering angle (constant'd' spacing) and consists of a series of Φ - scans (in- plane rotation around the center of the sample) at different tilt or Ψ (azimuth) angles, as illustrated in Fig. 2.21.

2.4.4 Long range order (LRO)

In a binary system consisting of two different atoms A and B, when cooled below a critical temperature, the A atoms arrange themselves in an orderly periodic manner on one set of atomic site and likewise the B atoms on another set of atomic sites. Such a system is then said to be ordered or possess superlattice. When the periodic arrangement of A and B atoms persists over a very large distance in the crystal, it is known as "long range ordering" as shown in Fig. 2.22. If the ordered system is heated above the critical temperature, then the atomic arrangement of A and B atoms in a crystal structure is random, thus disordering state prevails in the system at the cost of ordering.

FeAl alloys exhibit order-disorder transitions; they may exist in an intermediate state where the degree of ordering is not complete. In an atomically ordered state (B2-phase), FeAl alloy possesses BCC structure in which Al atoms occupy cube corner positions while the Fe atoms are present in the body centred site. In a disordered phase (A2-phase), Al atoms could be positioned in Fe site and similarly Fe atoms occupy Al sites (cube corner) due to intermixing of atoms caused by various processes like ball milling and plastic deformation. It has been reported that 10 % of Fe atoms should be present in Al sites to preserve the stoichiometry of the alloy. FeAl alloy structure is shown in the Fig. 2.22; blue colored atom in the centre represents Fe while the pink colored atoms positioned in the cube corner sites represent Al atoms.

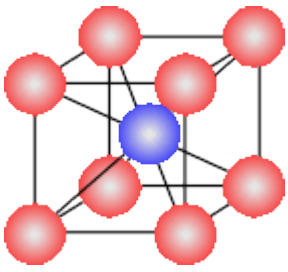

Figure 2.22 ordered AlFe BCC structure

Long range order parameter 'S' is given by the following equation (2.24)

$S = (r_A – F_A) / (1-F_A)$ Eqn 2.24

In the above equation, 'S' is the long range order parameter, r_A is the fraction of 'A' sites occupied by the right atoms, ie A atoms. F_A is the fraction of A atoms in the alloy. As an example consider the FeAl alloy system in which 25 Fe atoms and 75 Al atoms have combined together, at an intermediate state in the alloy system three atoms of Fe have occupied cube corner positions (Al sites). Assuming Fe atoms as 'A' atoms, we obtain the following relation for long range order.

$$S = \frac{\frac{22}{25} - \frac{25}{100}}{1-0.25} = 0.84 \qquad \text{Eqn 2.25}$$

Value of 'S' is 0.84 which indicates a high degree of long range order, S=1 indicates complete ordering while complete randomness or disorder in a system is prevalent when S=0. Thus, 'S' describes the degree of long range order. The above equation can also be rewritten as follows,

$$S = X_{Fe} - W_{Fe} / Y_{Fe} \qquad \text{Eqn 2.26}$$

X_{Fe} – atomic concentration of Iron in the alloy

W_{Fe}- fraction of Al sites occupied by Fe atoms

Y_{Fe}- probability of Fe site in the alloy

2.4.4.1 Effect of order-disorder transition on X-ray diffraction

Shift in the positions of atoms during transition to disorder from order creates a change in the crystal symmetry. Change of crystal symmetry between order and disorder phases can be observed by XRD, since symmetry is lowered in ordered phase, XRD pattern of such a phase exhibits peaks known as super lattice in addition to the fundamental peaks. Fundamental peaks are present in both ordered and disordered phase and show up at the same positions. By calculating the structure factor of various crystal structures, we can easily differentiate the superlattice peaks from that of the fundamental peaks and also determine the lattice planes (hkl) of the superlattice reflection. Consider the FeAl alloy which possesses BCC crystal structure, the following relations for structure factor and atomic scattering factor are deduced

$$F_{hkl} = \sum_1^N 1 f_n e^{2\pi i(hu+kv+lw)} \qquad \text{Eqn 2.27}$$

Structure factor value F_{hkl} exists for diffraction from each set of planes (hkl), where the unit cell contains N atoms each with atomic scattering factor f_n, and fractional coordinates (uvw)

For disordered phase the following reflection conditions prevail:

1) $F = f_{Al} + f_{Fe}$ fundamental reflections are present for (h+k+l = even) 110, 200, 220, 222, 310 etc,,
2) F = 0 No reflections are possible for (h+k+l = odd) 100, 111, 210, 300 etc,,
3) For ordered phase the following reflection conditions prevail:
4) $F = f_{Al} + f_{Fe}$ fundamental reflections are present for (h+k+l = even) 110, 200, 220, 222, 310 etc,,

5) $F = f_{Al} - f_{Fe}$ superlattice reflections are present for (h+k+l = odd) 100, 111, 210, 300, 311 etc,,

In the above conditions, F is the structure factor, f_{Al} is the atomic scattering factor of Al atom and f_{Fe} is the atomic scattering factor of Fe atom.

2.4.5 Scanning electron microscopy (SEM)

The scanning electron microscopes are scientific instruments that use a beam of highly energetic electrons to examine objects on a very fine scale. This examination can yield information about the topography (surface features of an object), morphology (shape and size of the particles making up the object), composition (the elements and compounds that the object is composed of and the relative amounts of them) and crystallographic information (how the atoms are arranged in the object) on a local scale. The spatial resolution is better than that of the optical microscope although not quite as good as the transmission electron microscope (TEM). The SEM has an extremely large depth of focus and is therefore well suited for topographic imaging; the instrument is made up of two main components, the electronic console and the electron column. The electronic console provides control knobs and switches that allow for instrument adjustments such as filament current, accelerating voltage, focus, magnification, brightness and contrast. The Jeol and Supra make are state of the art electron microscopes that use a computer system in tandem with the electronic console. All of the primary controls are accessed through the computer system using the mouse and keyboard. The image that is produced by the SEM is viewed/saved on the computer monitor.

Figure 2.23 shows various components of the electron column, the lower portion of the column is called the specimen chamber. The electron column is where the electron beam is generated under vacuum, focused to a small diameter, and scanned across the surface of a specimen by electromagnetic deflection coils. The secondary electron detector is located above the sample stage inside the specimen chamber. Specimens are mounted and secured onto the stage which is controlled by a goniometer.

Electron gun: Located at the top of the column (Figure 2.23) is the source of electrons. There are three main types of electron guns, the tungsten hair pin, the lanthanum hexaboride (L_aB_6) and the field emission. In the conventional electron gun, a V- shaped filament made of L_aB_6 or tungsten is enclosed (held) within the wehnelt cap (refer Figure 2.24) which controls the number of electrons leaving the gun. In a field emission gun (FEG), filament is usually tungsten with a tip of less than 100 nm. A potential difference is established between an anode and the cathode (filament tip), resulting in an electric field which is concentrated at the tip (extraction voltage) facilitating electron emission. The potential difference between the filament tip and a second grounded anode (FEG) determines the accelerating voltage of the gun. The higher the accelerating voltage the

faster the electrons travel down the column and the more penetrating power they have. FEGs produce much higher source brightness than in conventional guns (electron current > 1000 times), better monochromaticity, but requires a very good vacuum (~10^{-7} Pa).

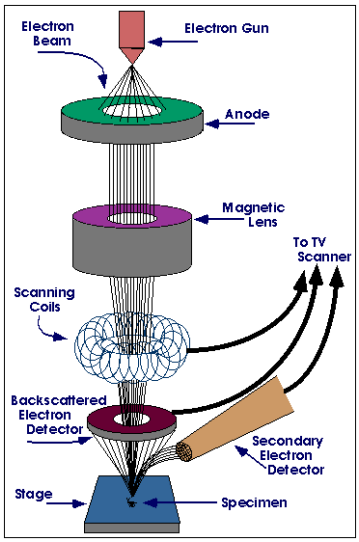

Figure 2.23 Schematic illustration of scanning electron microscopy.

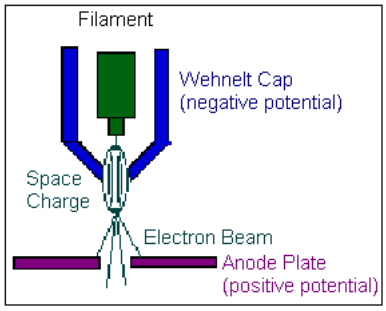

Figure 2.24 filament located within the wehnelt cap.

Condenser Lenses: After the beam passes the anode it is influenced by two condenser lenses that cause the beam to converge and pass through a focal point. What occurs is that the electron beam is essentially focused down to 1000 times its original size. Accelerated voltage in tandem with the condenser lenses is primarily responsible for determining the intensity of the electron beam when it strikes the specimen (Bob Hafner 2007).

Apertures: Different apertures are found in the electron column. The function of these apertures is to reduce and exclude extraneous electrons in the lenses. The final lens aperture (available in15µm, 30µm 60µm etc.,) located below the scanning coils determines the diameter or spot size of the beam at the specimen. The spot size on the specimen will in part determine the resolution and depth of field. Decreasing the spot size will allow for an increase in resolution and depth of field with a loss of brightness (Bob Hafner 2007).

Scanning System: Images are formed by rastering the electron beam across the specimen using deflection coils inside the objective lens. The stigmator or astigmatism corrector is located in the objective lens and uses a magnetic field in order to reduce aberrations of the electron beam. The electron beam should have a circular cross section when it strikes the specimen however it is usually elliptical thus the stigmator acts to control this problem (Bob Hafner 2007).

Vacuum system: A high vacuum pressure of at least $5x10^{-5}$ Torr (for FEG it is $5x10^{-7}$) is required for a variety of reasons (Bob Hafner 2007) that are mentioned as follows;

- The current that passes through the filament rises the filament temperatures to around 2700 ^{0}K. A hot tungsten filament will oxidize and burn out in the presence of air at atmospheric pressure.
- The column optics to operate properly requires a fairly clean, dust-free environment.
- Air particles and dust inside the column can interfere and block the electrons from reaching the specimen in the sample chamber.

In order to provide adequate vacuum inside the column, a vacuum system consisting of two or more pumps is utilized.

2.4.5.1 Electron beam-specimen interaction

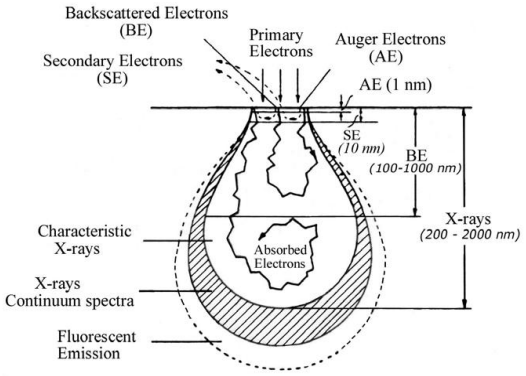

Figure 2.25 transitions of primary or incident electrons.

When an electron beam interacts with the atoms in a sample (material or specimen), individual incident electrons undergo two types of scattering - elastic and inelastic. In the elastic, when an electron beam penetrates into the sample, part of these primary electrons will be immediately reflected back due to the interaction with the atomic nuclei of the sample and without any significant changes in kinetic energy and velocity (< 1eV). These reflected electrons are called back scattered electrons (BSE) and they have energies in the range of 15 to 30 keV, depending on the primary beam energy. The production of backscattered electron varies directly with the specimen's atomic number, thus they are utilized in obtaining information on composition as

heavier elements backscatter more; elements with a higher atomic number will be seen brighter in the resulting image. In addition, these backscattered reflections are used to obtain information on the topographical aspects of the surface (specimen) because the intensity of these reflections depends on the angle between the primary beam (incident) and the surface of the sample. The backscattered reflection (signal) usually comes from a depth of upto1μm as shown in the Figure. 2.25.

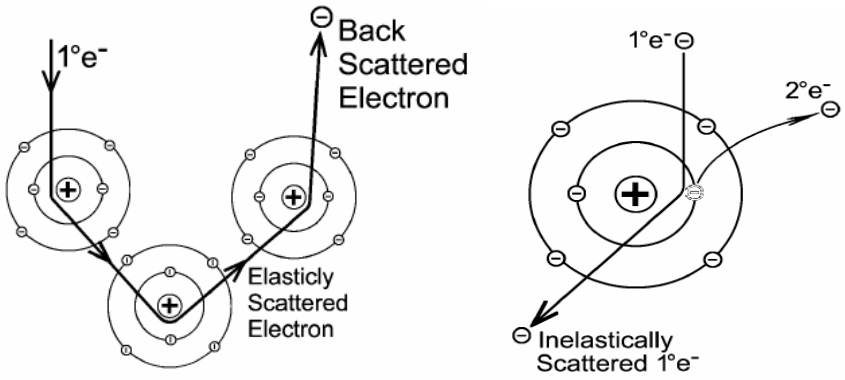

Figure 2.26 Elastic and inelastic scattering.

In the case of inelastic scattering, a beam of electron interacts with the electric field of a specimen atom electron resulting in a transfer of energy to the specimen atom and a potential ejection of an electron from the specimen atom as a secondary electron (SE). SE possesses energy levels of less than 50eV. The escape depth of SE is approximately 5-50 nm, the Figure 2.26 shows schematically the production of BSE and SE.

If the vacancy due to the creation of a secondary electron is filled by an electron from a higher level shell (oribital), an x-ray characteristic of that energy transition is produced. The escape depth of x-rays is in the range of 200 to 2000 nm (refer Figure 2.25), thus x-ray signals originate much deeper into the specimen surface than those reflections (signals) described above. The EDS (energy dispersive x-ray spectroscopy) x-ray detector (also known as EDAX or EDX) measures the number of x-rays emitted versus their energy, energy of x-ray is characteristic of the element from which x-ray was emitted. Thus EDS is most often used in the qualitative elemental analysis to determine which elements are present and their relative abundance.

2.4.6 Transmission electron microscopy (TEM)

Electron-Specimen interaction is what makes Electron Microscopy possible (Bettina Voutou, Eleni-Chrysanthi Stefanaki 2008). The interactions observed on the top side of the diagram (refer the Figure 2.27) are utilized when examining thick or bulk specimens (SEM) while on the bottom side are those examined in thin or foil specimens (TEM).

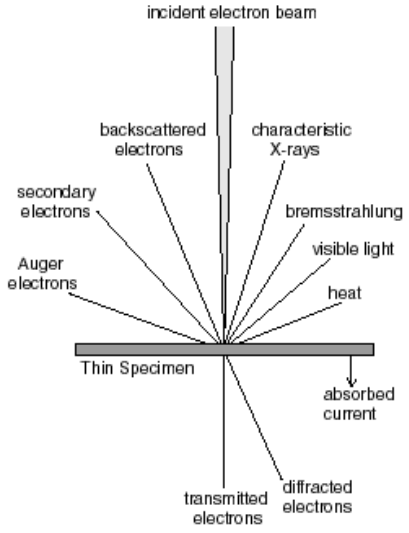

Figure 2.27 schematic illustrations of transmitted electrons.

2.4.6.1 Interactions of electron beam-specimen

TEM exploits three different interactions of electron beam-specimen; unscattered electrons (transmitted beam), elastically scattered electrons (diffracted beam) and inelastically scattered electrons. When incident electrons are transmitted through the thin specimen without any interaction occurring inside the specimen, then the beam of these electrons is called transmitted electrons. The transmission of unscattered electrons is inversely proportional to the specimen thickness. Specimen area that is thick will have fewer electron transmissions through them resulting in dark appearance, while thin specimen allows more electron transmission through them and thus will appear lighter. When incident electrons are scattered (deflected from their original path) by atoms in the specimen elastically (no loss of energy), these scattered electrons (follow Bragg's law) are then transmitted through the remaining portions of the specimen.

All incident electrons have the same energy (thus wavelength) and enter the specimen normal to its surface as shown in the Fig. 2.27. Incidents beam of electrons that are scattered by the same atomic spacing will be scattered by the same angle. These scattered electrons can be brought together (collated) using magnetic lenses to form a pattern of spots; each spot corresponding to a specific atomic spacing (hkl plane). This pattern can then yield information about the orientation, atomic arrangements and phases present in the area being examined.

Beam of incident electrons which are scattered inelastically by the specimen atoms, loses their energy during the collision (interaction). Such scattered electrons are transmitted through the rest of the specimen and are a source for providing information on composition or elemental analysis (electron energy loss spectroscopy) and Kikuchi bands.

2.4.6.2 Imaging mode

A transmission electron microscope is made up of two or three condenser lenses (Fig. 2.28) to focus the electron beam on the sample, an objective lens to form the diffraction in the back focal plane and the image of the sample in the image plane. Some intermediate lenses magnify the image or the diffraction pattern on the screen. If the sample is thin (< 200 nm) and made up of light chemical elements, the image presents a very low contrast when focused. To obtain an amplitude-contrasted image, an objective diaphragm is inserted in the back focal plane to select the transmitted beam (and possibly a few diffracted beams): the crystalline parts in Bragg orientation appear dark and the amorphous parts which are not Bragg oriented appear bright. This imaging mode is called bright field (BF) mode (Fig. 2.29). If the diffraction is constituted by many diffracting phases, each of them can be differentiated by selecting one of its diffracted beams with the objective diaphragm. To do that, the incident beam must be tilted so that the diffracted beam is put on the objective lens axis to avoid off-axis aberrations (Fig. 2.29). This mode is called dark field (DF) mode. The BF and DF modes are used for imaging materials to nanometer scale.

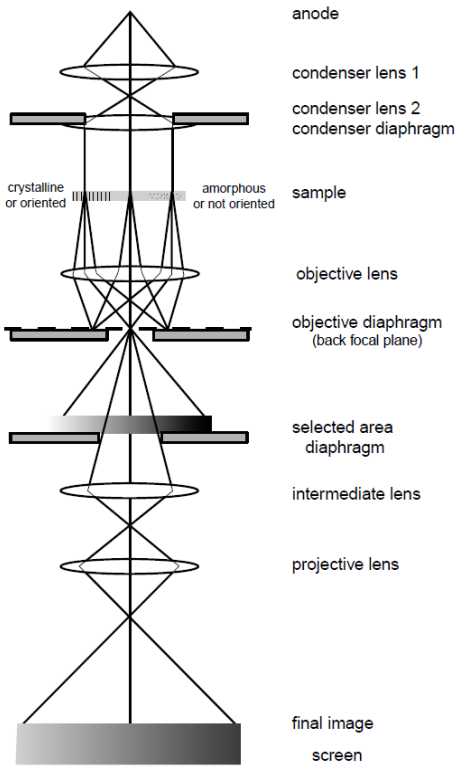

Figure 2.28 Schematic illustration of the working principle of transmission electron microscopy.

The selected area diaphragm is used to select only one part of the imaged sample for example a particle or a precipitate. This mode is called selected area diffraction pattern (SADP). The spherical aberrations of the objective lens limit the area of the selected object to a few hundred

nanometers. Nevertheless, it is still possible to obtain diffraction patterns of a smaller object by focusing the electron beam with the projector lenses to obtain a small spot size on the object surface (2-10 nm). The spots of SADP become circular (rings) whose radius depends on the condenser diaphragm, this is known as microdiffraction (Fig. 2.30). SADP and microdiffraction provide information about lattice symmetry and interplanar spacing (by using Bragg law), which is utilized in identifying the relevant phase.

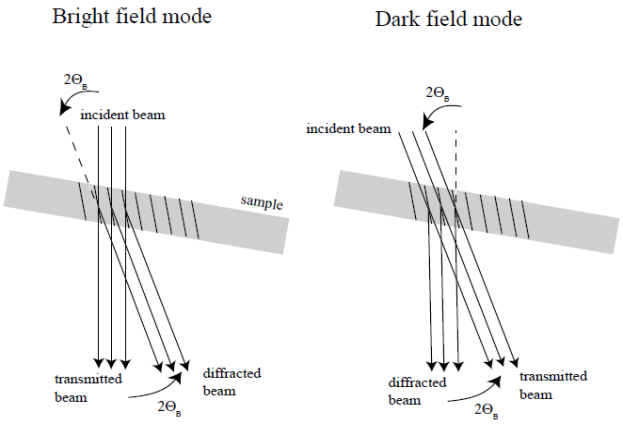

Figure 2.29 Bright and dark field image mode.

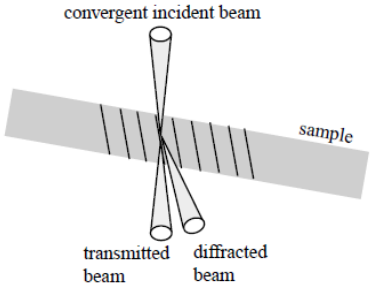

Figure 2.30 Principle of obtaining selected area diffraction pattern (SADP)

2.4.7 Compaction

Compaction enables the forming of loose metal powders into the required size and shape with sufficient strength to withstand till sintering is completed. Cold compaction is done without the application of heat; loose powders are converted into required shape with sufficient strength to withstand ejection from the die and subsequent sintering process.

2.4.7.1 Uniaxial compaction

This technique involves the application of external pressure to compact the loose powder particles; application of pressure is uniaxial. Process involves the compaction of loose powder in a die using hydraulic press, thus giving rise to densification. The mechanism of densification depends on the material and structural characteristics of powder particles. Figure 2.31 shows a uniaxial compaction process involving different stages: charging the powder mix, applying the load using a

single top punch, compaction, removal of the load by retracting the punch and finally ejecting the green compacts. Powder compaction depends on the flow of powder particles past one another while interacting with each other and with the die punch. In addition to this, it also depends on the deformation of particles. When compaction pressure is applied, rapid densification occurs due to particle movement and rearrangement resulting in improved packing. Further increase in pressure leads to elastic and plastic deformation resulting in locking and cold welding of particles, thus at this stage of compaction it is observed from figure (2.31) that large increase in pressures are seen to affect small increase in density. Considering the fact that the particles have a size on the order of approximately 10–100 nm, the number of interparticle contacts will be clearly higher in the case of nanoparticle powder compared to that of coarse grain powders. Hence, the motion of particles via sliding is more difficult in the case of nanoparticle powder due to friction. Before the powder is transferred to the die cavity, it is mixed with the following additives to achieve specific properties:

1) Lubricants: to reduce the particle-die friction.
2) Binders: to obtain sufficient strength before sintering.
3) Deflocculants: to improve the flowability of powder during die cavity filling.

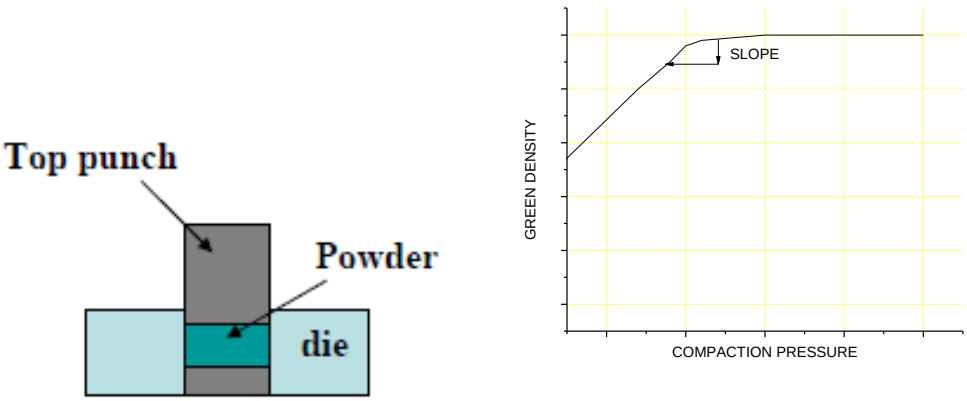

Figure 2.31 uniaxial compaction process and green density as a function of compaction pressure.

2.4.7.2 Uniaxial compression loading

Material response to the application of different mechanical loading depends on the mechanical properties of that material. When materials are subjected to different loading conditions (compression, tensile, shear etc), the effects of such load on the resulting mechanical and magnetic properties are quite interesting.

In a compression test, specimen is subjected to a continuously increasing uniaxial compressive load until it fractures. Load and displacement (Δl) are recorded at a certain deformation velocity. The result of a compression test is a load-displacement curve, which is normally converted into a (compressive) stress (σ)-strain (ε) relation as follows:

$\sigma = P / A$ Eqn 2.28

P is the load on the sample with an original (zero stress) cross sectional area (A), the engineering strain, ε, is defined as

$$\varepsilon = (l - l_O) / l_O = \Delta l / l_O \quad \text{Eqn 2.29}$$

Where l is the gauge length at a given load, and l_O is the original (zero stress) length. During the deformation there are two stages namely elastic and plastic deformation. Elastic deformation is a temporary deformation, completely recovered when the load is removed. The elastic region of the stress-strain curve is the initial linear portion. Plastic deformation is permanent deformation and is not recovered when the load is removed, although a small elastic component is recovered. Plastic region of the stress-strain curve is the nonlinear portion generated once the total strain exceeds its elastic limit. Yield strength is a convenient indication of the onset of plastic deformation.

2.4.8 Differential scanning calorimetry (DSC)

Differential scanning calorimeter (DSC) is based on thermo analytic technique, the technique measures the difference in the amount of heat required to increase the temperature of a sample (S) and a reference (R) material as a function of temperature as shown in Fig. 2.32. The sample and the reference are maintained at identical temperatures throughout the experiment in an environment which may consist of heating or cooling at a controlled rate. The temperature during the DSC analysis is designed such that the sample holder temperature increases linearly as a function of time. The reference material should have a well defined heat capacity over the entire range of temperature to be scanned during the experiment. The ideal reference material is a substance with the same thermal mass as the sample, but with no thermal events (no physical or chemical transition) over the entire temperature range of interest. The thermal mass is the product of the mass and the heat capacity. When the sample undergoes solid to liquid transition during heating, more heat is absorbed by the sample to increase its temperature at the same rate as the reference material. Thus the sample undergoes endothermic phase transition, likewise, when the sample undergoes exothermic process like crystallization, it requires less heat to raise its temperature at the same rate as the reference. By observing the difference in heat flow during endothermic and exothermic processes of the sample, DSC is able to determine the amount of heat flow between the sample and the reference during such transition. DSC experimental results are plotted on a graphical representation of heat flow versus temperature as shown in the figure 2.32. Exothermic reactions of the sample are shown either by a positive or negative peak depending on the kind of technology used in the experiment. The curve shown in the figure (2.32) is used to calculate the enthalpies of the transitions that occurred during the experiment. The enthalpy of the transition is expressed by the following equation (2.30):

$$\Delta H = K A \quad \text{Eqn 2.30}$$

Where Δ H is the enthalpy of the transition, K is the calorimetric constant, and A is the area under

the curve. Calorimetric constant will vary from one instrument to another and is determined by analyzing a well characterized sample whose enthalpy of transition is well known. The DSC analysis of a sample, obtained during heating at a selected heating rate, provides information on the temperature ranges for the different reactions in addition to yielding the typical thermal peaks (as shown in the Figure 2.32) which are characteristic of the reactions occurring during the processing.

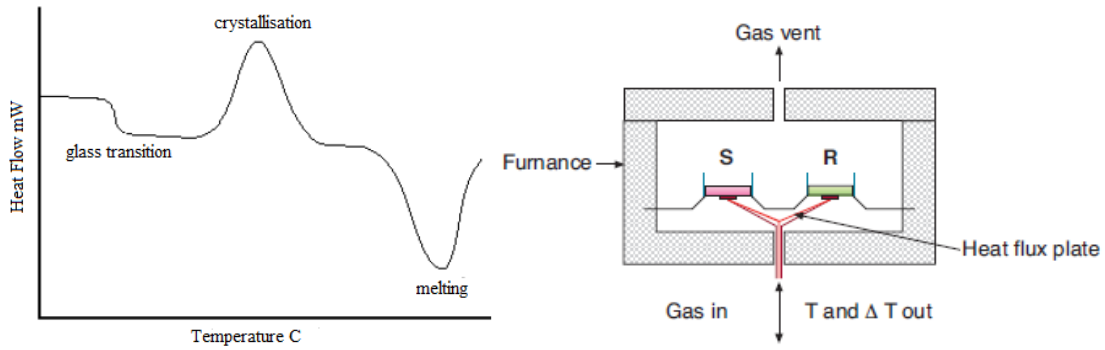

Figure 2.32 left) typical features of a DSC curve and right) schematic c/s of DSC

2.4.9 Nanoindentation

Nanoindentation is an important technique in probing the mechanical behaviour of materials at small scales; the most common use of this technique in our research is for the measurement of hardness and elastic modulus. Nanoindentation is also known as a depth sensing technique operates in the submicron range with nanometer resolution. The test involves indenting the specimen with a very low load using a highly precision instrument as shown in the schematic diagram (Fig. 2.33), which records the load and penetration depth continuously. Separate load and depth linear variable differential transformer (LVDT) sensors are used, the load LVDT measures the deflection of accurately ground support springs to which is attached the indenter shaft. The depth LVDT measures the absolute displacement of the indenter shaft with respect to the load frame. In this system the load is applied to the indenter shaft via a system of leaf springs by the expansion of a load actuator. When the indenter contacts the sample, the springs deflect and this deflection is measured using a force LVDT (linear variable differential transformer). A separated depth LVDT measures the displacement of the indenter shaft relative to the frame of the instrument.

Mechanical properties can be derived from the load-penetration depth curve shown in the figure (2.34) obtained for a nanoindentation test. The resulting load-penetration depth curve typically shows an elastic-plastic loading followed by an elastic unloading. The three sided Berkovich indenter was used in the present research, the contact depth is given by the equation (2.31);

$h_c = h_{max} - \varepsilon \frac{Pmax}{dp/dh}$ Eqn 2.31

where P_{max} is the maximum load, h_c the contact depth at which the cross sectional area (A) is taken to calculate the hardness. Peak indentation depth is denoted by h_{max} and includes elastic and plastic deformation. The depth at which the applied loads become zero on unloading is the final indentation depth denoted by h_r and represents the plastic deformation. Slope of the tangent of the load-penetration depth curve during the unloading cycle is denoted by dp/dh. The factor ε depends on the indenter shape (for Berkovich indenter, ε ≈ 0.75). Once h_c is determined, area of contact (A= c/s area) is determined from the geometry of the indenter, for a Berkovich indenter;

$A=24.49\ h_c^2$ Eqn 2.32

Elastic modulus (E) and hardness (H) are calculated from the following equations (2.33);

$E = \frac{dp}{dh}\frac{\sqrt{\Pi}}{\sqrt{2A}}$ and $H = \frac{P}{A}$ Eqn 2.33

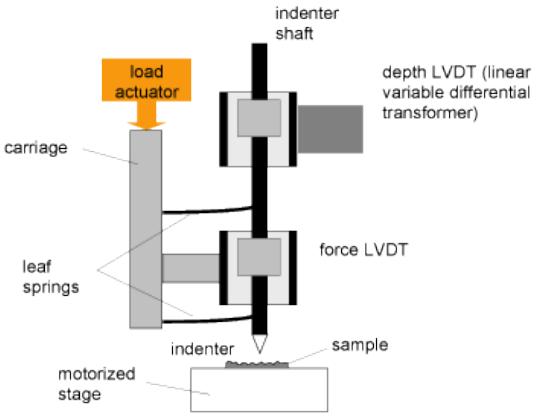

Figure 2.33 Sketch showing the nanoindenter with various actuating mechanisms

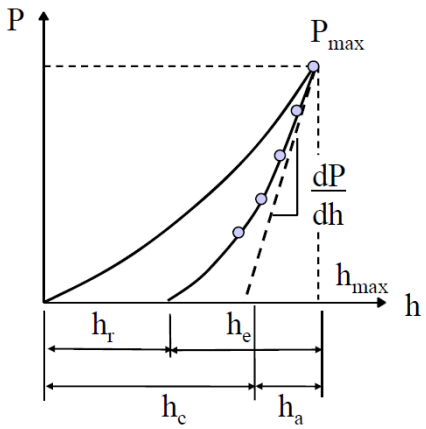

Figure 2.34 load as a function of penetration depth.

2.4.9.1 Specimen preparation

Largest influence on the quality of nanoindentation test data is the condition of the surface of the specimen and also on the way in which it is mounted for testing. A typical indentation into a bulk material is usually of the order of 200 to 500 nm. The theoretical basis of the above contact equation assumes a perfectly flat surface, any irregularities in the surface profile will cause scatter in the readings. Thus cleaning and polishing are very important in obtaining accurate and precision readings.

2.4.10 Vibrating sample magnetometer (VSM)

The working principle of VSM is based on the Faraday's Law of induction, according to which the voltage induced (*V*) in an electrical circuit is proportional to the rate of change of magnetic flux (φ) linking the circuit. This relation can be demonstrated by the following equation (2.34);

$V = -N d\varphi / dt$ Eqn 2.34

where *N* is the number of loops in the electrical coil and dφ/dt is the rate of change of magnetic flux. As magnetic induction $B = \varphi/A$ (*A* is the cross-sectional area of the coil), the above equation can also be written as Eqn 2.35

$V = -NA\, dB/dt$ Eqn 2.35

Accordingly, the change of magnetic induction can be obtained by measuring the electrical voltage (or current) induced. In VSM, the sample is placed in a constant magnetic field as shown in figure 2.35. Vibration of the sample results in the change of magnetic flux through the pick-up coils positioned close to it. A voltage is therefore induced and measured using a lock-in amplifier. This voltage is proportional to the magnetic moment of the sample. Essentially, the VSM (shown schematically in Fig. 2.35) measures the difference of magnetic induction between one region of space with the sample and another without the sample, thus allowing calculation of the magnetic moment, M.

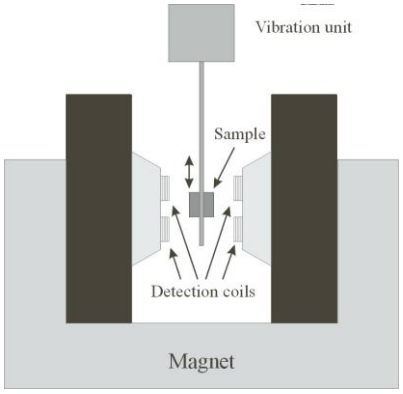

Figure 2.35 Principle of operation of VSM

The VSM, shown schematically in Fig. 2.35 and utilized for this research, employs an electromagnet which provides the magnetizing field (DC), a vibrator mechanism to vibrate the sample in the magnetic field, and detection coils (4 coils) which generate the signal voltage due to the changing flux emanating from the vibrating sample. The output measurement displays the magnetic moment M as a function of the field H.

2.4.11 Consolidation by ECAP

Severe plastic deformation of coarse grained solid metals is extensively done by equal channel angular pressing (ECAP) to refine the grains. The solid metals are extruded by multiple pass through the die, thus ECAP is generally an extrusion process used to process solid metals. However, ECAP with back pressure has been used to consolidate metallic powders (Senkov O. N. et al. 2005 and Xia K., Wu X. 2005).

2.4.11.1 Fundamental parameters in ECAP

The ECAP procedure is a metal flow process operating in simple shear and characterized by several fundamental parameters such as the strain imposed in the die, the slip systems operating during the pressing operation and the consequent shearing patterns present within the as-pressed pellets. Taken together, these various processes define uniquely the precise nature of the pressing operation; all of these parameters (mentioned below) play a critical role in determining the nature of the UFG structure introduced by ECAP.

1. The strain imposed in ECAP
2. The processing routes in ECAP
3. Influence of the channel inner angle, Φ
4. Influence of the channel outer angle of curvature, ψ
5. Influence of the pressing speed
6. Influence of the pressing temperature
7. Influence of a back-pressure

2.4.11.2 Equal channel angular pressing with back pressure (ECAP-BP)

ECAP-BP consists of a vertical entrance channel with a forward pressing plunger (punch) and a horizontal exit channel with a back plunger providing a constant back pressure during pressing, as shown in the Fig. 2.36. The two channels intersecting at 90^0 with a sharp corner has the same circular cross section, the velocity of the forward pressure is controlled by the computer. The forward plunger pushes the sample forward through the shearing plane while the horizontal plunger provides a constant back pressure to the sample. Heating elements are present in the die which enables to conduct ECAP-BP process at different elevated temperatures. Thermocouples

mounted close to the intersection of the channels provide the prevailing temperature of the process. It has been shown that there is no gap between the specimen and the die due to the presence of back pressure and the deformation mode is a simple shear. By applying the forward pressure and maintaining a constant back pressure, powder is compacted in the vertical channel and deformed due to shear strain as the powder is forced into the horizontal channel predominantly under compressive load. Initial compaction in the vertical channel is similar to uniaxial compression.

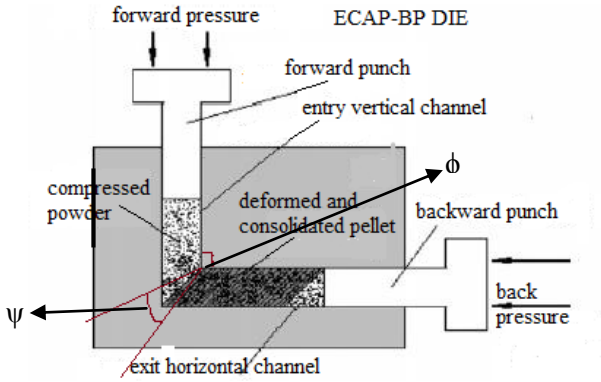

Figure 2.36 sketch showing the critical components and the principle of operation.

The net strain obtained during the process depends on the inner and outer angle as defined by Iwahashi Y. et al 1997.

$$\varepsilon_N = \frac{N}{\sqrt{3}}\{2cot\left(\frac{\phi}{2}+\frac{\psi}{2}\right)+\psi\, cosec\left(\frac{\phi}{2}+\frac{\psi}{2}\right)\} \quad \text{Eqn 2.36}$$

In the equation 2.36, ε_N is the equivalent strain after N passes, ϕ: channel inner angle, ψ: channel outer angle as shown in Fig. 2.36.

2.4.12 Metallography study

Metallography has been the study of the microscopic structure of metals and alloys using optical metallographs, electron microscopes or other surface analysis equipment. More recently, as materials have evolved, metallography has expanded to incorporate materials ranging from electronics to sporting good composites. By analyzing a material's microstructure, its performance and reliability can be better understood. Thus metallography is used in materials' development, incoming inspection, production and manufacturing control, and for failure analysis; in other words, product reliability. Metallography (Metallographic hand book 2010 and www.struers.com) or microstructural analysis includes, but is not limited to, the following types of analysis:

1. Grain size
2. Porosity and voids
3. Phase analysis
4. Dendritic growth
5. Cracks and other defects

6. Corrosion analysis
7. Intergranular attack (IGA)
8. Coating thickness and integrity
9. Inclusion size, shape and distribution
10. Weld and heat-affected zones (HAZ)
11. Distribution and orientation of composite fillers
12. Graphite nodularity
13. Recast
14. Carburizing thickness
15. Decarburization
16. Nitriding thickness
17. Intergranular fracturing
18. Flow-line Stress

2.4.12.1 Selection of metallographic specimens

The selection of test specimens for metallographic examination is extremely important because, if their interpretation is to be of value, the specimens must be representative of the material that is being studied. The intent or purpose of the metallographic examination will usually dictate the location of the specimens to be studied. Having established the location of the metallographic samples to be studied, the type of section to be examined must be decided. In hot-worked or cold-worked metals, both transverse and longitudinal sections should be studied. Special investigations may require specimens with surfaces prepared parallel to the original surface of the product.

2.4.12.2 Size of metallographic specimens

For convenience, specimens to be polished for metallographic examination are generally not more than about 10 to 25 mm (0.5 to 1.0 in.) square, or approximately 10 to 25 mm in diameter if the material is cylindrical. The height of the specimen should be no greater than necessary for convenient handling during polishing. Larger specimens are generally more difficult to prepare. Specimens that are, fragile, oddly shaped or too small to be handled readily during polishing should be mounted to ensure a surface satisfactory for microscopical study.

2.4.12.3 Cutting of metallographic specimens

An abrasive cut-off blade will produce a smooth surface often ready for fine grinding. This method of sectioning is normally faster than sawing. The choice of cut-off blade, lubricant, cooling conditions, and the grade and hardness of metal being cut will influence the quality of the cut. A poor choice of cutting conditions can easily damage the specimen, producing an alteration of the

microstructure. Generally, soft materials are cut with a hard bond blade and hard materials with a soft bond blade (Table 2.5). Aluminum oxide abrasive blades are preferred for ferrous metals and silicon carbide blades are preferred for nonferrous alloys. Abrasive cut-off blades are essential for sectioning metals with hardness above about 350 HV. Extremely hard metallic materials and ceramics may be more effectively cut using diamond-impregnated cutting blades.

2.4.12.4 Precision wafer sectioning

Precision wafer cutting is used for sectioning very delicate samples or for sectioning a sample to a very precise location. Precision wafering saws typically have micrometers for precise alignment and positioning of the sample and have variable loading and cutting speed control. The ideal cutting fluid for abrasive cutting is one that removes the cutting swarf and degraded abrasive blade material. It should have a relatively high flash point because of the sparks produced during abrasive sectioning.

Table 2.5 cut-off blade selection

Hardness HV	Materials	Abrasive	Bond	Bond Hardness
up to 300	non-ferrous (Al, Cu)	SiC	P OR R	Hard
up to 400	non-ferrous (Ti)	SiC	P OR R	Medium Hard
up to 400	soft ferrous	Al_2O_3	P OR R	Hard
up to 500	medium soft ferrous	Al_2O_3	P OR R	Medium Hard
up to 600	medium hard ferrous	Al_2O_3	P OR R	Medium
up to 700	hard ferrous	Al_2O_3	P OR R&R	Medium Soft
up to 800	very hard ferrous	Al_2O_3	P OR R&R	Soft
> 800	extremely hard ferrous more brittle ceramics tougher ceramics	CBN Diamond Diamond	P OR M P OR M M	Hard Very Hard Extremely Hard

P- Phenolic, R- Rubber, R&R- Resin & Rubber, M- Metal. CBN-Cubic boron nitride

2.4.12.5 Specimen mounting

The primary reasons for specimen mounting are to better hold the part to be ground and polished, and to provide protection to the edges of the specimen. Secondarily, mounted specimens are easily fixed into automated machines or held manually. The orientation of the specimen can also be more easily controlled by fixturing it and then setting it in place via mounting. Metallographic mounting is accomplished by compression mounting the plastic under pressure and temperature.

2.4.12.6 Compression mounting and resins

There are four types of compression mounting plastics used predominantly in the metallographic laboratory. These plastics require the use of a mounting press providing heat (140-180°C) and force (27-30 MPa). Thermosetting plastics can be ejected hot but the best results are obtained when the cured mount is cooled under pressure. Thermoplastic compounds do not harden until

cooled and therefore should not be ejected while hot. Regardless of the resin used, the best results are obtained when the specimen is clean and dry, and the cured mount is cooled under full pressure to below 40 °C before ejection from the press. This will ensure minimal shrinkage gap formation. Compression mounts are quick and easy to produce, requiring several minutes to cure at the appropriate mounting temperature. The better compression mounting machines have heaters which can reach temperatures of at least 200 °C (450 °F). For faster turnaround time, water cooling is essential. There are a variety of compression mounting materials. The two main classes of compression mounting materials are thermoset and thermoplastics. Thermoset resins require heat and pressure to cross-link the polymer and the reaction is irreversible. Thermoplastic, on the other hand, can theoretically be remelted. With the addition of fillers such as graphite or copper, the compression mounting compounds can be made conductive (Fig. 2.37). Conductive mounts (polyfast) are used in scanning electron microscopes (SEM) to prevent the specimen from building up a charge. Conductive mounts are also used for specimens requiring electrolytic etching or polishing.

Figure 2.37 conductive mount (polyfast)

2.4.12.7 Grinding

In most cases, the specimen surface and subsurface are damaged after cutting and sectioning. The depth or degree of damage is dependent on how the material was cut. The purpose of abrasive grinding is to remove this damage and to restore the microstructural integrity of the specimen for accurate analysis. Grinding should start with the coarsest paper, platen or stone capable of flattening the specimen and removing the effects of prior operations, such as sectioning. The subsequent steps should remove the effects of previous ones in a short time. Grinding consists of two stages, planar (rough) and fine. Planar or rough grinding (240 grit and coarser) may be performed on belts, rotating wheels or stones. In some methods, diamond abrasives are used on rigid platens.

Planar grinding may be used to accomplish the following:

1. Flatten an irregular or damaged cut surface.
2. Remove sectioning damage, scale and other surface conditions prior to mounting.
3. Remove substantial amounts of specimen material to reach a desired plane for polishing.
4. Level the mount surface.

In fine grinding, damage to the specimen incurred from the planar or rough grinding step must be removed. The specimen is either ground on successively finer abrasive papers (using water to wash away grinding debris and to act as a coolant) or on a rigid disc or cloth charged with a suitable abrasive. For fine grinding, finer abrasives ranging from 1200 to 2400 grit are used and the abrasive grinding papers employed are SiC. The grinding parameters which affect the preparation of metallographic specimens include grinding/polishing pressure, relative velocity distribution between the specimen and grinding surface, and the direction of grinding/ polishing action relative to the specimen. In general, grinding removal rates are described by Preston's Law. This relationship states that removal rates are proportional to the grinding velocity and applied pressure.

2.4.12.8 Polishing

Scratch and deformation free sufaces are crucial in most metallographic specimen preparations today with modern highly technological materials. The requirements to purity, cleanliness, equal distribution of alloying elements and phases are very important. Thus a final polishing step with an active oxide suspension is often carried out to achieve the necessary surface quality for specimen examination. Mechanical abrasion alone is not sufficient for the final step if a deformation free surface is a must. This has led to the development of suspensions, which remove material through both mechanical and chemical actions. The interaction between mechanical and chemical material removal is the important issue during oxide polishing. Sole mechanical abrasion always results in some kind of deformation, whereas exclusive chemical material removal produces relief between various phases. However, by combining the right abrasive with the correct chemical reagent, superb results can be obtained. Depending on the material to be polished, different abrasives can be used in the Oxide Polishing Suspensions (OP-S). Colloidal Silica (SiO_2) is used as abrasive in OP-S and OP-U. Alumina (Al_2O_3) is used as abrasive in OP-AA and OP-AN. The particles used in the final polishing suspensions usually belong to the submicron range. The active oxide suspensions react chemically with the surface of the specimen, building a reaction layer, which is relatively brittle. The brittle layer is removed by the very small abrasive particles in the suspension. This mechanism is repeated continuously, resulting in a very high material removal. OP-S is a colloidal silica suspension with a pH of 9.8 and a grain size of about 0.04 μm. It is especially suited for polishing of very ductile refractory metals like aluminium, titanium, tungsten,

copper and other materials such as silicon. OP-S can also be used with the addition of reagents, normally used for the etching of the material in question. This increases the chemical activity, thus shortening the actual polishing time. OP-U is a colloidal silica suspension, like OP-S, with a pH of 9.8, but with a slightly different composition, which makes it less aggressive than OP-S. OP-U is used for heterogeneous non-ferrous materials and composites. Different phases are evenly polished, resulting in samples with a very good planeness. OP-AA is an acidic aluminium oxide suspension with a pH of 3. It is especially suited for the final polishing of ferrous metals, Ni-base alloys and ceramics. OP-AN is a neutral aluminium oxide suspension with a pH of 7. It can be used for all materials. OP-AN is an all-round oxide suspension with the possibility of mixing additives to obtain chemical activity. Depending on the materials to be polished, different polishing cloths are used. MD-Nap or DP-Nap is mostly used for softer materials with normal oxide polishing suspension whereas MD-Chem or OP-Chem is better suited for harder materials, and for polishing with active oxide polishing suspension.

2.4.12.9 Etching

Etching is done to optically reveal the microstructural features like phases, grain boundaries, intermetallics, amorphous regions, dislocations, etc. Etching selectively alters the surface of the polished specimen based on composition, crystal structure, stress etc. Most common type of etching metals and alloys is by selective chemical method, numerous chemical formulations have been used for different types of metals and alloys.

2.4.13 Optical microscopy

An optical microscope consists of the following two major basic functions.

I. Creating a Magnified Image of a Specimen
II. Illuminating a Specimen

The function to create a magnified image of a specimen consists of three basic functions of obtaining a clear, sharp image, changing a magnification and bringing into focus. An optical system for implementing these functions is referred to as an observation optical system. Meanwhile, the function to illuminate a specimen consists of three basic functions of “supplying light”, “collecting light”, and “changing light intensity”. An optical system for implementing these functions is referred to as an illumination optical system. In other words, the observation optical system projects a sample (specimen) through an optical system and moreover leads a projected image to eyes. On the other hand, the illumination optical system effectively collects light emitted from the light source and leads the light to a specimen to illuminate it.

2.4.13.1 Principles of optical microscope

An optical microscope creates a magnified image of an object specimen with an objective lens and magnifies the image further more with an eyepiece to allow the user to observe it by the naked eye. Assuming a specimen as AB in the Fig. 2.38, primary image (magnified image) A'B' of inverted real image is created with an objective lens (ob). Next, the eyepiece (oc) is arranged so that primary image A'B' is located closer to the eyepiece than the anterior focal point, then more enlarged erect virtual image A"B" is created as shown in Figure 2.38. Naked eye is put in the eye (pupil) position on the eyepiece barrel to observe the enlarged image. In short, the last image to be observed is an inverted virtual image. As described above, this type of microscope which creates a magnified image by combining an objective lens making an inverted real image and an eyepiece making an erect virtual image is called a compound microscope. The observation optical system in an optical microscope is commonly standardized on this compound microscope. Meanwhile, such type of microscope that directly observes an inverted real image magnified with an objective lens is called a single microscope. A microscopic observation on a TV monitor, recently popularized increasingly, uses the way of directly capturing this inverted real image with a CCD camera, thereby being comprised of a simple microscope optical system.

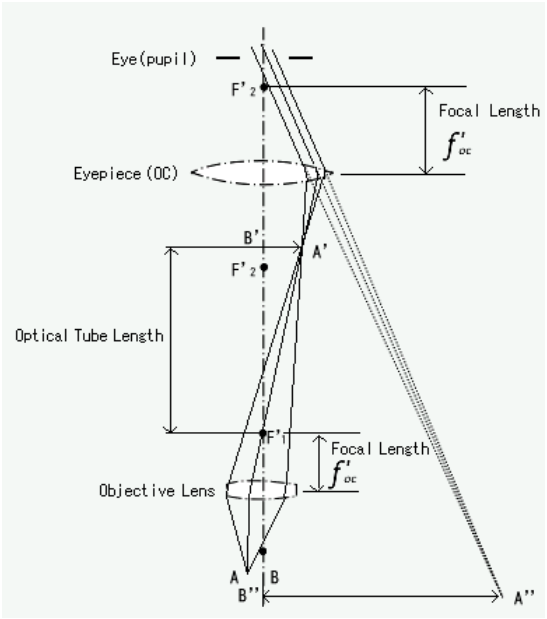

Figure 2.38 schematic illustration of an optical microscope

2.4.14 Sintering process

Sintering is the process by which metal powder compacts are transformed into coherent solids at temperatures below their melting point, under no pressure. Typically, the compact to be sintered is exposed to the relatively high temperature for a duration varying from several minutes to several hours. The powder particles are bonded together by diffusion and other atomic transport

mechanisms. Sintered components are somewhat porous and acquire certain degree of mechanical strength. Traditionally, the sintering process is preceded by a compaction step at low applied pressures in the range of 50 MPa to ≈1 GPa, in order to obtain a green compact with adequate green density. Typically, this compaction process is not optimal in the case of nanocrystalline metals. Indeed, metal nanoparticles exhibit extremely low thermal stability and grain growth would occur during sintering. This would lead to the loss of the nano-features of the material.

The sintering process is significantly governed by the following parameters:

- Temperature and time,
- Geometrical structure of the powder particles,
- Composition of the powder mix,
- Density of the powder compact,
- Composition of the protective atmosphere in the sintering furnace.

Sintering of metal / alloy powder compacts in a continuous sintering furnace is accomplished in four sections. The compacts are initially placed in the preheat zone section of the furnace; the lubricants added to the powder to facilitate the compaction are removed in this section. Compacts which enter the high heat section (Fig 2.39) of the furnace are exposed to the sintering temperature; traces of unalloyed elements in the compacts diffuse into the lattice of higher melting point elements and the particles bond together to form bulk component with less porosity. Sintering process is carried out either in an inert atmosphere or under vacuum. Finally the sintered bulk components are cooled to room temperature below which no atmospheric contamination occurs.

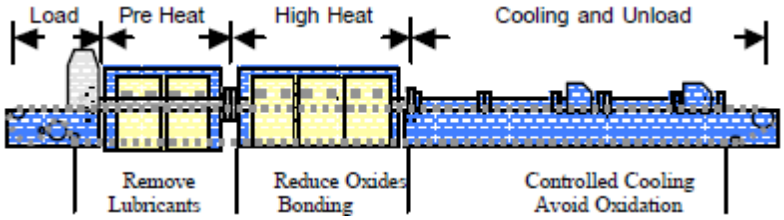

Figure 2.39 various stages of sintering process

CHAPTER 3: EXPERIMENTS

This chapter describes the experimental procedures that have been used to induce mechanical alloying in elemental powders of Al and Fe by means of high energetic ball milling. Further, consolidation of mechanically alloyed (MA) powder by Equal Channel Angular Pressing with Back Pressure (ECAP-BP) and cold compaction followed by sintering are described. Subsequently the experimental procedures for structural, texture, phase transformation/identification, morphological, mechanical and magnetic characterization are described. The chapter has been divided into four major sections, in each section the composition of materials selected, the employed specific experimental set up for material processing, characterization and assessment of properties are concisely presented.

3.1 Materials

Elemental powders of Al and Fe with initial particle size of 60 μm and purity of 99.5 % were mixed in two different atomic compositions for mechanical alloying and consolidation purpose. The first mixture of elemental powders of Al and Fe with an atomic composition of 50 % each is known as Fe_{50}-Al_{50} system. While, the second mixture of elemental powder has an atomic composition of 90 % Al and 10 % Fe and is known as Al_{90}-Fe_{10} system. Each of the two systems of powder is subjected to processing as reported in the following section

3.2 Processing

The processing involved mechanical alloying (MA) by high energetic ball milling process followed by consolidation of the MA powders. Consolidation was done by two different processes, 1) by equal channel angular pressing with back pressure (ECAP-BP) and 2) compaction followed by pressureless sintering.

3.2.1 Mechanical alloying by ball milling

Mechanical alloying is a solid state process involved in alloying of elemental powder, the technique involves in repeated welding, fracturing, and re-welding of mixture of elemental powder particles in a high energetic ball mill. In most cases, this processing route has been successfully utilized to produce many types of solid solutions, materials in non-equilibrium states, disordered and amorphous alloys. Furthermore, mechanical alloying by ball milling reduces the powder particle size by repeated welding and fracturing, thus producing nanocrystalline alloy / solid solution powders. Even though a large variety of milling devices, such as shaker (e.g., Spex mills), attritor or magnetic mills are currently used quite often, this section is focused on planetary ball

mill since planetary ball milling equipment is characterized by their capability to carry out very high energetic processes.

3.2.1.1 High energetic ball milling process

In this section the focus is on ball mill utilising the principles of planetary motion and capable of delivering high impact energy. Retsch PM 400 ball mill (Fig. 3.1) was used to process the elemental powders of Al and Fe of both the systems of materials. The starting particle size (should be less than 10 mm) of elemental powder mixture was 60 μm, several balls and mixture of elemental powders were placed inside the jars according to the required balls to powder weight ratio. The balls to powder weight ratio depends on the type of material being ground and the fineness required. Each jar was mounted on an independent rotatable platform, thus a set of four grinding jars for the planetary ball mill were arranged in such a way that each moved around its own axis and, in the opposite direction, around the common axis of the sun wheel. The rotation was at uniform speed (200 rpm) and uniform ratios. The grinding balls described a semi-circular movement, after which they separated from the inside wall and collided with the opposite surface at high impact energy. Combination of frictional forces and impact forces cause high degree of size reduction in PM 400. Retsch PM-400 with stainless steel milling media and Retsch PM-100 with tungsten carbide milling media were utilised in this research work. The Retsch PM-400 was available at the Institute for Frontier Materials, Deakin University, Waurn Ponds Campus, Geelong, Victoria. Retsch PM-100 was available at the Metallurgical and Materials Engineering Department, NITK, Surathkal, Karnataka, India.

Figure 3.1 high energetic planetary ball mill.

3.2.1.1.1 Ball milling operation

Pure elemental powders of Al and Fe were mechanically alloyed in a high energetic planetary ball mill (Retsch PM-400), the initial compositions of elemental mixture in the two material systems

are reported in section 3.1. Each mixture of elemental powders from the two systems (Fe_{50}-Al_{50} and Al_{90}-Fe_{10}) is subjected to MA as a function of ball milling. Initial particle size and purity of elemental powders was around 60µm and 99.5% respectively. **Stainless steel** jar and balls were used, the ball to powder weight ratio was 10:1. The volume of stainless steel jar was 500 ml, the effective volume of material along with balls was between 150 to 300 ml and 100 pieces of balls of 10 mm diameter was used. The composition of stainless steel jar was 84.5 % Fe and 13.0 % Cr, hardness was 53 HRC while the density was 7700 kg/m^3. Jar and balls were cleaned to remove the coating from previous milling operations, the cleaning involved rotating the jar filled with balls and ethanol, running the ball mill with ethanol solution cleans the balls and the jar from impurities and elements present from the previous milling operations. To minimize oxygen and atmospheric contamination, the milling process (mechanical alloying) was performed in an envelope of **argon** atmosphere. Cleaned stainless steel jars were filled with Elemental powders of Fe and Al in the desired quantity, the jars were closed with air tight lids and argon gas was filled under pressure. Simultaneously the one way release valve was opened to let out the air into the atmosphere so that the jar was completely occupied by argon gas and contained no atmospheric gases. The ball milling speed maintained throughout the mechanical alloying process was 200 rpm. The jars and metal powder were handled inside the glove box shown in Fig. 2.7. The glove box environment was alternately changed between evacuated mode and argon gas mode for handling the milling media and metal powders and also for storing MA powder.

In addition, mixture of elemental powders of Al and Fe (Fe_{50}-Al_{50} system only) were also ball milled (Retsch PM-100) in a **toluene** atmosphere to prevent atmospheric contamination. The milling media used in this instance was **tungsten carbide** jar and balls. The composition of tungsten carbide jar and balls was 94 % WC, 6.0 % Co, hardness value (H_V) was 1150 kg/mm^2 (11.2 GPa) while the density was 14400 kg/m^3. The volume of tungsten carbide jar was 250 ml, the effective volume of material along with balls was between 25 to 150 ml and 50 balls of 10 mm diameter were used. Initial particle size and purity of elemental powders was around 60µm and 99.5% respectively. The ball to powder weight ratio was 10:1 and the milling speed was 200 rpm. Jar and balls were cleaned to remove the coating from previous milling operations, the cleaning involved rotating the jar filled with balls and toluene, running the ball mill with toluene solution cleans the balls and the jar from impurities and elements present from the previous milling operations.

The ball milling was continued uninterrupted for longer duration of 400 hours while the milling was stopped at 100 hour, 150 hours and so on for characterisation and for consolidation purposes.

3.2.2 Powder consolidation

Mechanically alloyed powders (of both the material systems as described in section 3.2.1) as a function of different ball milling durations were consolidated to bulk-solid form by two techniques. The consolidation techniques utilized to consolidate the mechanically alloyed powder are known as Equal Channel Angular Pressing with Back Pressure (ECAP-BP) and cold compaction followed by pressureless sintering process. This section describes the experimental techniques involved in both the consolidation processes.

3.2.2.1 ECAP-BP operation

The equal channel angular pressing with back pressure (ECAP-BP) die consisted of two halves (Fig. 3.2 'a') and when assembled together, the die cavity (channel) formed a circular geometry of 10 mm diameter channel. The assembled die block is inserted into the cylindrical metal jacket as shown in the Fig 3.2 (b). There are four holes in the cylindrical jacket for providing electrical heating of the die to permit isothermal processing within the temperature range of 20^0 – 600^0 C. further, the cylindrical metal jacket with the die is placed in a 1000kN press to exercise the forward pressure of pressing. The press has two plungers; one for exerting the forward pressure during the vertical downward motion while the other is horizontally positioned for exerting a preset back pressure. The vertical entry channel of the ECAP die is 75 mm in length as shown schematically in Fig. 2.36 and makes a 90^0 angle (Φ) with the horizontal channel. The diameter of the channels is 10 mm. The mechanically alloyed powder was poured directly into the vertical entry channel of the cold die, while pouring the back pressure punch was positioned deep within the horizontal channel to contain the powder within the vertical channel. The system was then heated to a temperature of 450^0 C within 10 minutes and ECAP process started with the forward punch moving with a velocity of 2 mm/sec. As the forward pressure gradually increased, a large hydrostatic pressure was created in the vertical channel of the die, pre-compacting the mechanically alloyed powder at the elevated temperature. Once the forward pressure exceeded the preset back pressure (could be varied from 20 to 500 MPa), shear plastic deformation of the pre-compacts began with the flow into the horizontal channel against the back pressure punch.

This die is equipped with four electric resistance heaters surrounding the entry channel and the corner between the channels. The heating system is controlled by a thermocouple located in the die close to the corner and allows maintaining stable testing temperatures up to a maximum of 600°C. The velocity of the forward pressure is controlled by computer. The ECAP machine has a capacity of 50 tonnes forward force and 25 tonnes of back force. Independently controlled back pressure ECAP equipment which was used for this research was designed and fabricated in the Materials Department at the Monash University (Clayton), Melbourne, Australia. The unique equipment provides computer controlled ECAP with back pressure kept at a constant preset level.

Temperature is controlled to ±1 ^{0}C through a thermocouple in contact with the die near the intersection of the channels.

Figure 3.2 a) ECAP-BP die halves with the consolidated pellet located within the channels. b) ECAP-BP rig located at Monash University, Clayton, Melbourne shows the cylindrical metal jacket with heating facility.

3.2.2.2 Cold compaction, sintering and annealing process

Mechanically alloyed (ball milled in SS-MM) powder is mixed with ethylene bis stearamide (0.5 wt %) in a ball mill at a low speed of 100 rpm using steel balls for 20 minutes. Ethylene bis stearamide (EBS) is derived from stearic acid and ethylenediamine, it is a waxy white solid and is also found as powder or beads and it promotes flowability, binding and reduces viscosity. Metal powder mixed with the lubricant/binder is transferred to a cylindrical steel die of 20 mm internal diameter, the powders were uniaxially cold pressed to cylindrical shape with a diameter of 20 mm and a thickness of 4 mm (approximately) with a compressive pressure of 1.2 GPa using the 50 ton hydraulic press shown in Figure 3.3. The facility shown in Figure 3.3 is located at the metal powders laboratory at the institute of frontier materials in Deakin University Waurn ponds Victoria Australia was utilized for this research work. Zinc stearate was used as a die wall lubricant.

Cold compacts (green compacts) produced by the above mentioned process were **sintered** in the Gero furnace (Fig 3.4).

Figure 3.3 Hydraulic press (50 ton capacity) located at the metal powders laboratory at ITRI, Deakin University, Waurn Ponds, Geelong, Victoria, Australia.

The sintering process consisted of mounting the green compacts on alumina crucibles, the crucibles along with the compacts are initially placed in the preheat zone section of the furnace, the lubricant and binder added to facilitate the compaction are removed in this section of the furnace. Compacts then enter the high heat section of the furnace and are exposed to the sintering temperature of 1250 ^{0}C (Fe_{50}-Al_{50} system) and 900 ^{0}C (Al_{90}-Fe_{10} system) for 30 minutes, the heating rate involved was 50 ^{0}C/min. The entire sintering process was carried out in an atmosphere of nitrogen gas. Initially after placing the samples in the preheat zone, the furnace is evacuated and then filled with nitrogen gas before heating begins. Finally the sintered bulk components are cooled to room temperature below which no atmospheric contamination occurs. **Sintering** of the green compacts (obtained by consolidating mechanically alloyed powder) were carried out in the Gero vacuum horizontal tube furnace at the ITRI, Deakin University, Australia. The furnace can either work in an evacuated atmosphere or in an inert gas (nitrogen) atmosphere. The high grade insulation materials (ceramic fibre module Fig 3.4 left) guarantee low energy consumption and high heating rates, due to their low thermal conductivity. The insulation and the SiC heating elements are installed in a rectangular housing. For application under vacuum or process gas, a comprehensive range of accessories is available. Tight, high purity Al_2O_3 and Al_2O_3/SiO_2 tube materials, water cooled stainless steel flanges and gas supply equipment allow for thermal treatment under specified atmospheres. In such treatment processes, the gas flow can be controlled either manually by means of a flow meter, or automatically by means of a mass flow controller. For operating in a vacuum atmosphere, complete vacuum pump systems (rotary vane pumps, turbo pumps), data recording systems and visualizing software complete the different accessories (Fig 3.4 right) used.

In another set of consolidation experiment, Fe_{50}-Al_{50} system alloy powders synthesized by mechanical alloying (ball milling duration of 185 hours in toluene atmosphere) in tungsten carbide MM were cold compacted in cylindrical die using a uniaxial pressure of 1.0 GPa for 2 min. Cold compacts were sintered at 1000 ^{0}C for 30 min in a Gero furnace (Fig. 3.4) in vacuum mode. The heating and cooling rates were adjusted to be 5 ^{0}C/ min to provide uniform sintering environment; while, the vacuum was maintained at 10^{-4} Pa. Subsequently, cylindrical shaped specimens with a diameter and length of 10 mm were cut and polished to mirror finish with parallel end faces. Furthermore these specimens were **annealed** in Gero furnace at 600 ^{0}C for 60 min to remove the disorder induced during mechanical alloying, cutting and polishing operations.

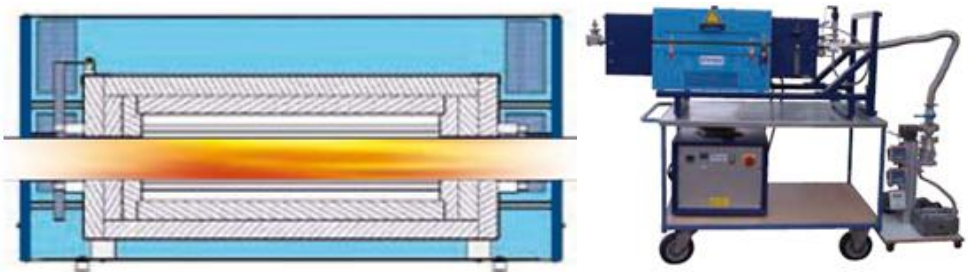

Figure 3.4 left) cross sectional view of Gero horizontal tube furnace show various layers of insulating material. Right) Gero furnace with various accessories

3.2.2.2.1 Deformation by compression

Annealed (refer section 3.2.2.2) bulk samples with a diameter and length of 10 mm were subjected to plastic deformation by compression process performed uniaxially at room temperature using MTS 858 tensile tester shown in Figure 3.5. Uniaxial compression under different strain rate can be achieved using the electro hydraulic loading system of MTS equipment. Different compression loads were applied to obtain a range of stresses from 0.5 GPa to 8 GPa at a loading rate of 1kN/s and a enduring time of 100 sec. The detailed specification of the MTS 858 tensile tester which was used for exerting compression load on the bulk samples is given below. This facility is available at the ITRI, Deakin University, Geelong, Victoria, Australia and it was used for this research work.

Figure 3.5 MTS 858 tensile and fatigue tester

The 858 material testing system is a cost-effective choice for low force static and dynamic testing applications. Designed to preserve valuable floor space, the 858 load unit can fit conveniently on an existing laboratory bench, or sit on its own portable, custom cart. While extremely compact, the 858 system provides a broad range of test enhancing features, including:

I. Force ranges from 5 kN to 25 kN
II. The ability to test lower strength materials ranging from plastics to aluminum

III. Accommodation of subsized to standard specimens
IV. The capability to perform tension, compression, bend and fatigue tests; specialized tests for biomedical and biomechanical testing; and durability testing on small components
V. Wide column spacing to accommodate larger fixtures, environmental chambers and furnaces

Also includes the following specifications:

I. 25kN Servo Hydraulic
II. Hydraulic wedge grips
III. Work opening 466x789mm
IV. Stroke ±50mm
V. Frequency30 Hz

3.3 Characterization

This section describes the experimental techniques: Performed for structural, phase transformational, morphological and metallographical characterization of unmilled and ball milled powders and also consolidated materials. Specification and operating principles of various equipments used in the characterization by XRD, DSC, SEM and TEM are mentioned and explained. Sample preparations for TEM, SEM operation and metallography are elaborately reported.

3.3.1 XRD operation

X'Pert PRO MRD XL shown in Figure 3.6 is an enlarged and improved version of Panalytical's proven X'Pert PRO MRD system and is equipped with texture and stress optics for measurement of residual stress and pole figure of metallic samples. X'Pert PRO MRD XL x-ray diffractometer with a copper anode (K_α = 0.154060) material was utilised to examine and investigate the structural parameters of mechanically alloyed powder and consolidated bulk samples at various stages of ball milling and consolidation process. The experiments have been carried out at the Institute for Technology Research and Innovation, Centre for Material and Fibre Innovation, Deakin University, Geelong, Australia. All diffraction patterns have been recorded using a continuous mode. This means that the sample and/or the detector rotate in a continuous way. The generator settings (at room temperature) of 30 mA and 40 kV have been selected and a step size of 0.05 is selected in order to have well-defined x-ray diffraction (XRD) peaks with a sufficient signal-to-noise ratio to properly fit the patterns. All the XRD patterns/profiles obtained during this investigation have been characterised by Xpert high score plus software, the software has been utilised in matching the XRD pattern to obtain phase identification and all the relevant structural parameters including quantitative analysis.

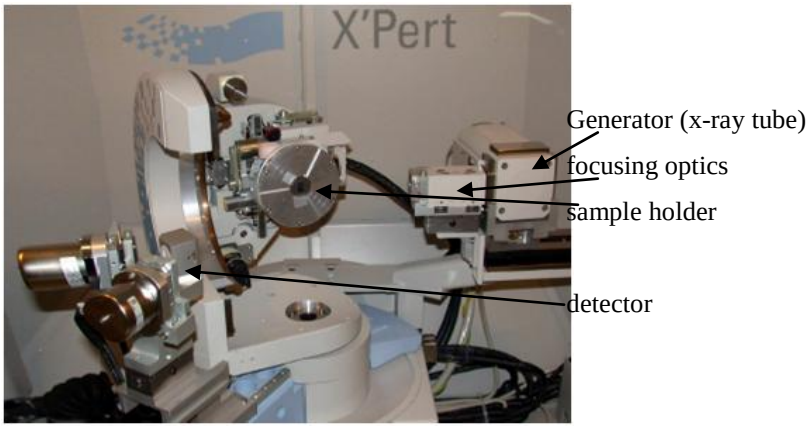

Figure 3.6 X'Pert PRO MRD XL X-Ray diffraction equipment

The effective grain size, d, and lattice strain, ε, were calculated by applying the Hall-Williamson formula to several diffracted X-ray peaks and also by scherrer equation. The lattice parameters were determined using at least three higher angle 2θ peaks. The long range order (LRO) parameter, 'S', was determined by a comparison of the relative integrated intensities of superlattice (h+k+l=odd) and fundamental (h+k+l=even) peaks of disordered/partially ordered sample with respect to the well-annealed reference material (Qi Zeng., Ian Baker. 2007) as shown in equation 3.1.

$$S = \{(I_S/I_F)_{DIS}/(I_S/I_F)_{ORD}\}^{1/2} \quad \text{Eqn 3.1}$$

where (I_S/I_F)dis and (I_S/I_F)ord are the intensities of the superlattice reflection relative to the fundamental line for disordered (dis) and fully ordered annealed reference (ord) powders, respectively. Fundamental reflection (220/110) was chosen for determination of 'S' in order to minimize texture effects.

Samples for **texture** measurement were cut from the centre of the planes of each billet and polished to a metallographic finish. To begin the texture measurements, the first step in the measurement of pole figures was to determine and index the Bragg angles for the sample and thus determine the diffraction planes of interest. The crystal planes are chosen from the absolute scan (θ-2θ pattern); we need strongly diffracting peaks (high intensity in θ-2θ pattern) for complete texture analysis. Discrete peaks are preferably chosen at 2θ values between 20^0 and 50^0 for optimum results. It is necessary to perform background corrections and defocusing measurements. By removing the background and correcting for the beam defocusing that occurs as the ψ (psi) angle increases, more accurate pole figures are produced. To run a pole figure measurement, set the correct 2θ position for the selected crystal plane (ex, 110 AlFe), the scan mode is set to continous and the measurement details are shown in Table 3.1 and Figure 3.7 for a sufficient

detailed texture analysis. Figure 3.7 and table 3.1 gives the sample rotation along 'Φ' and 'ψ' angles and also the steps involved in the operation of texture measurements.

Table 3.1 Texture operation specifications

	psi	phi
Start angle (deg)	0.00	0.00
End angle (deg)	80	360
Step size (deg)	2.00	5.00

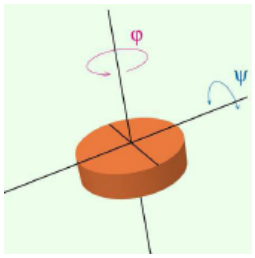

Figure 3.7 Texture sample rotation.

3.3.1.1 Silicon standard

A well crystallized Si standard (i.e., a crystal with sufficiently large crystallites and very low defects concentration leading to near zero microstrains, thus assumed to have no size and strain broadening) has been used as the reference sample (Fig 3.8) to correct the instrumental broadening. The X-ray diffraction peaks are broadened due to many reasons; crystallite size refinement and microstrain in addition to the instrumental effects are some of the possible reasons. Thus, we need to deduct the broadness of XRD peaks caused by the instrument effect. X- ray diffractogram obtained from such a well crystallized-silicon sample is shown (Fig 3.9) and will be utilized to calculate the instrumental broadening effects. The silicon standard XRD profile obtained has been indexed by Xpert High Score Plus software with the relevant matching pattern shown in Fig 7.1 in appendix. The peak list with structural parameters obtained from the matching pattern of silicon standard is shown in the Table 3.2. The full width at half maxima (FWHM) for the most intense 111 peak is 0.2936 at 2θ=28.4667. Thus, $\beta_{standard} / \beta_{INST}$ (0.2936^0) is substituted in the following equation (3.2) to obtain the β / β_{SAMPLE} (FWHM) which is then substituted in the scherrer equation.

$$\beta = \beta_{observed} - \beta_{standard} \quad \text{Eqn 3.2}$$

Thus β is employed in the scherrer equation 3.3 as shown:

$$D = K \lambda / \beta \cos\theta \quad \text{Eqn 3.3}$$

where 'β' is the FWHM, 'K' the scherrer constant, 'D' the crystallite size and 'θ' the Bragg angle.

Figure 3.8 Crystallized Si standard.

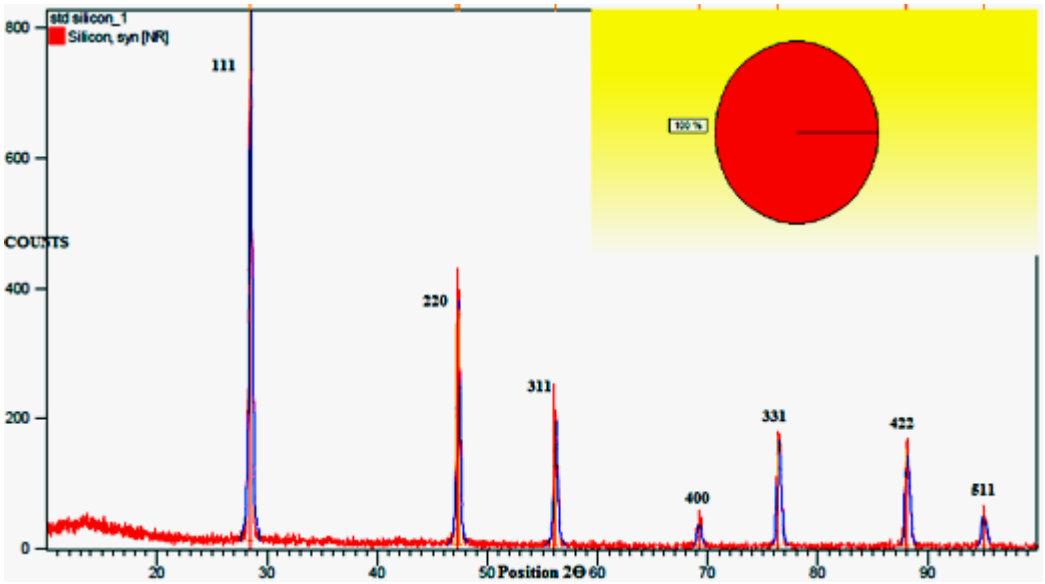

Figure 3.9 XRD pattern of standard silicon sample

Table 3.2 Standard **Si** sample peak list with structural parameters

Peaks	2θ	hkl	d(Å)	FWHM	Rel Int. (%)	Matched
1	28.4667	111	3.13293	0.2936	100.00	00-026-1481
2	47.3120	220	1.91978	0.3037	48.02	-do-
3	56.1398	311	1.63702	0.3191	23.85	-do-
4	69.1604	400	1.35721	0.3105	4.51	-do-
5	76.4021	331	1.24559	0.2947	21.03	-do-
6	88.0575	422	1.10831	0.3090	18.48	-do-
7	94.9893	511	1.04488	0.3185	6.25	-do-

Phase transformation during Mechanical alloying as a result of high energy rate ball milling is analysed by XRD. The effective grain size, d, and lattice strain were calculated by applying the Hall-Williamson formula to several diffracted X-ray peaks (Basavaraju S., Baker I. A. 2004) and also scherrer equation was utilized as follows:

$$\beta_{sample} \cos\theta = k\lambda / d + 2\varepsilon \sin\theta \qquad \text{Eqn 3.4}$$

where k is the Scherrer constant; λ is the wavelength and θ is the Bragg angle. β_{sample} was obtained from equation 3.5

$$\beta^2_{SAMPLE} = \beta^2_{EXP} - \beta^2_{INST} \qquad \text{Eqn 3.5}$$

where β_{EXP} is the full width at half maximum (FWHM) of the samples, and β_{INST} was the FWHM of a fully-ordered large-grained sample.

3.3.1.2 X-ray penetration depth in FeAl alloys

The X-ray penetration depth, P_d, can be roughly estimated by means of X-ray absorption from a homogeneous substance. The mass absorption coefficient of Fe and Al are 308 cm^2/g and 48.7 cm^2/g respectively (for Cu K_α radiation) and their atomic masses are 55.85 amu and 26.98 amu respectively.

In $\mathbf{Fe_{50}Al_{50}}$ (atomic %) alloy, the mass absorption coefficient is calculated as 222.43 cm^2/g and its density is estimated to be around 4.85 g/cm^3. X-ray penetration depends on the mass absorption coefficient and density of the alloy diffracting the incident beam as well as on the Bragg angle (2θ). Therefore, the x-ray penetration depth (P_d) has been determined for Bragg angles of 15^O, 65^O, and 120^O. These angles correspond to minimum, middle and maximum 2θ scan (15^O to 120^O) employed during the diffraction process of the MA powder samples as well as powder consolidated samples:

$P_d = 5.5$ μm at $2\theta=15^O$ Eqn 3.6

$P_d = 19$ μm at $2\theta=65^O$ Eqn 3.7

$P_d = 18$ μm at $2\theta=120^O$ Eqn 3.8

Similarly for $\mathbf{Fe_{10}Al_{90}}$ (atomic %) alloy, the mass absorption coefficient and density are 100.56 cm^2/g and 3.1 g/cm^3 respectively and the x-ray penetration depth estimated during the XRD characterization of the MA powder and consolidated samples are as follows:

$P_d = 19$ μm at $2\theta=15^O$ Eqn 3.9

$P_d = 67$ μm at $2\theta=65^O$ Eqn 3.10

$P_d = 64$ μm at $2\theta=120^O$ Eqn 3.11

3.3.2 DSC operation

Application of Differential scanning calorimeter (DSC) to severe plastically deformed (SPD) materials (ECAPed material) has increased recently; however, there is little systematic study of the thermal stability of ultra fine grained (UFG) materials processed by ECAP. However, an investigation of the thermal stability of ECAP-processed materials is important because these materials not only have very small grain sizes but they may have high dislocation densities, vacancy concentrations and internal stresses. As a result, the ultrafine microstructures are often inherently thermally unstable. Since the energy released in DSC analysis is directly related to microstructural changes, such as changes in the dislocation densities and the occurrence of grain growth, DSC analysis is an especially effective tool for studying the thermal stability of UFG materials.

The experiments were carried out using the heat flux (Netzsch Fig. 3.10) DSC facility available in the thermal laboratory of CMFI group at the Institute for Technology Research and Innovation, Deakin University, Victoria, Australia. The equipment consists of a sliding (hoisting) furnace which encloses both the crucibles (reference and sample) is shown in the Figure 3.10 left, alumina or zirconia or yttria crucibles are used. Both are connected to each other and to the furnace through a high conductivity heat flux plate (shown in figure Fig 3.10 right) usually made up of metals, quartz or ceramics. The temperature sensors (thermocouple) are attached to this plate, difference between the sample and the reference temperature during controlled heating/cooling is recorded and correlated with the enthalpy change in the sample as mentioned in the literature. The temperature difference ($\Delta T = T_S - T_R$) is recorded interms of voltage signal (millivolts divided by the sample mass). Sample weight taken is in the range of 5 to 20 mg and a heating rate of 10 ^{O}C/ min is chosen. Both the crucibles are closed with a lid in order to prevent sample radiation loss, contamination of different sensitive parts of the instrument, and help maintain an isothermal sample. Alumina powder obtained from the instrument maker was used as a reference material during the DSC analysis of all the samples (Powder, ECAP and Sintered). High purity inert gas (argon) atmosphere is used inside the furnace to avoid atmosphere contamination and to increase the thermal conductivity of the furnace atmosphere. Care was taken to completely evacuate the instrument before purging with argon.

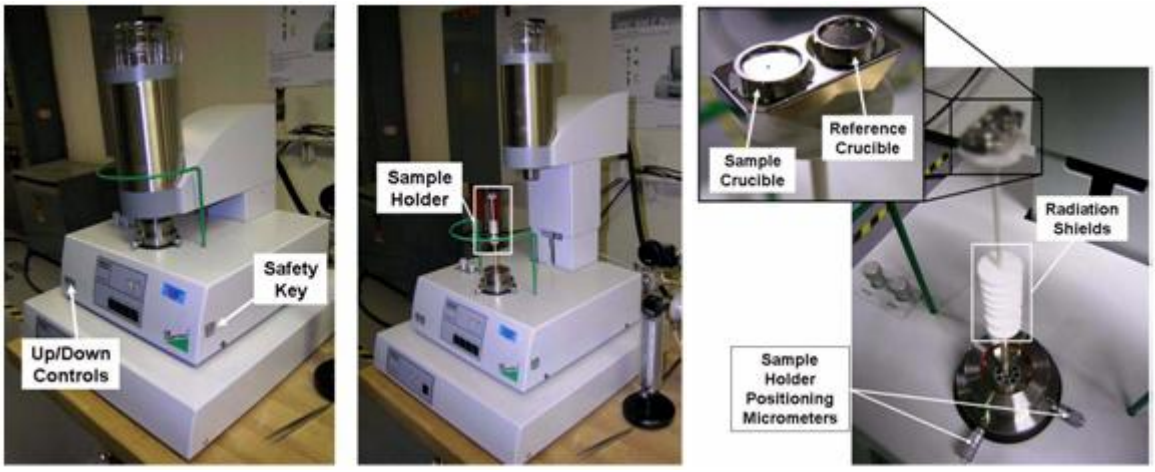

Figure 3.10 left shows the DSC equipment with control and safety knobs to move the furnace either vertically up or down. Middle) Furnace lifted up exposing the sample holder. Right) Two crucibles and radiation shield are seen.

3.3.3 Metallographic preparations

Metallography studies involved precise cutting of the consolidated (ECAP-BP and sintered) bulk samples. Precision wafer cutting is used for sectioning very delicate samples of height 10 mm. Precision wafering wheels of alumina or silicon carbide typically have micrometer-length movement along horizontal axis for precise alignment and positioning of the sample and have

variable loading and cutting speed control. Step motor controls the movement of the sample in both X- and Y-directions enabling very precise positioning. The high resolution of the step motor makes it possible to position the sample with an extraordinary precision of 5 μm. The total movement of the sample in the X-direction is 60 mm. Sample rotation or oscillation reduces the contact area between cut-off wheel and sample to a minimum. This results in a decrease in frictional heat and allows fast cutting of extremely hard materials. Abrasive cutting of the sample is done using an ideal cutting fluid that removes the cutting swarf and degraded abrasive blade material. It should have a relatively high flash point because of the sparks produced during abrasive sectioning. Precision table top cut-off machine (Fig. 3.11) for precise and deformation free cutting of the sample was used and the detail specifications are given below.

Figure 3.11 Portable table top precision cut-off machine. Courtesy: www.struers.com

Make: Struers Acutom 50

i. Sample rotation or oscilliation
ii. Cutting speeds: upto 3000 rpm
iii. Pre-set, constant cutting feed speed 0.005 - 3.00 mm/sec
iv. Multi programmable methods
v. Positioning accuracy of 5 μm
vi. Built in recirculation cooling unit
vii. Enclosed cutting chamber with safety switch
viii. Adjustable force limit

For hot mounting of the cut sample, the sample is placed in the mounting press (Fig. 3.12), the resin (polyfast) is added, and the sample is processed under heat (180 ^{0}C) and high pressure. Two types of hot mounting resins are available; thermosetting resins cured at elevated temperatures. They are also called duroplastics. Thermoplastic resins soften or melt at elevated temperatures and harden during cooling. Although thermosetting resins could be ejected at high temperatures, it is advisable to cool the mounts under pressure. This will result in the least shrinkage and maintain good adhesion between resin and sample. All Struers mounting presses use water cooling to allow the shortest possible mounting time. Polyfast resin powder of required quantity is poured into the

two cylinders and over the sample placed inside. Polyfast resin is used for conductive mounts (Fig. 2.37) used in SEM to prevent the specimen from building up a charge. Semi-automatic mounting press was used for the hot mounting of all the consolidated samples and the specification of the equipment is given below: Method parameters (temperature, pressure, heating time, and cooling time) can be controlled individually, ensuring full flexibility in mounting. Specifications of the equipment are given below:

Figure 3.12 Hot compression mounting equipment along with resin mounted samples.

Make: Struers Labopress 1

i. Low energy consuming heating / cooling unit
ii. Two heating levels
iii. Extended temperature range: 80-180 °C
iv. Individually controlled parameters: temperature, force/pressure, heating time, cooling time
v. Powerful heating unit (1000 W)

Abrasive grinding was performed on the mounted samples to remove the damage caused during cutting and sawing operations and to restore the microstructural integrity of the specimen for accurate analysis. For this purpose SiC abrasive papers of different grit sizes were used, grit sizes varied from 240, 600, 1200 and 2400 and these abrasive papers were used successively one after the other with water as the lubricant. Struers Rotopol 1 (Fig. 3.13 left) make grinding equipment was used for this purpose which had the option of different rotational speed (RPM 150 and 300). Final polishing is done on a MD-Chem polishing pad with OP-S (oxide polishing) suspension in which colloidal silica (SiO_2) is used as the abrasive as shown in Figure 3.13 (right). The equipment used for this purpose was Struers-Tegrapol 21 capable of polishing 6 samples at a time and is programmable for different speeds, pressure and duration of polishing. Polished samples are subjected to etching by an etchant whose composition consists of 2.5 ml HNO_3, 1.5 ml HCl, 1.0 ml HF and 95 ml DI water.

Further, Olympus high resolution (DP70) Optical Microscope and camera was used for the examination and capture of images of metallographic specimens.

Figure 3.13 Left) Grinding equipment. Right) Fine polishing and etching equipment.

3.3.4 SEM operating specifications

The LEO 1530 high resolution field emission scanning electron microscope (SEM), together with an energy dispersive x-ray spectroscopy detector (EDS system from Gresham) was used to visualise and to analyse surface features of material as small as 0.1 micron in diameter. This makes SEM / EDS a suitable system for the analysis of powder as well as consolidated bulk samples for the analysis of morphology, phase identification, various elements present and grain boundaries. The SEM facility available at the Institute of Frontiers Materials in Deakin University, Australia was utilised for this research work and the detailed specifications of the equipment are given below:

i. Resolution: 1 kV / 3 nm, 20 kV / 1 nm
ii. Magnification: 20X to 900,000X
iii. Accelerating Voltage: 200 V to 30 kV
iv. Probe Current: up to 10nA
v. Electron Gun: Thermal field emission type
vi. Specimen Stage: x=75 mm, y=75 mm, z=25 mm (all motorized), Working distance 2mm - 45mm
vii. Detectors: In-Lens annular (SE1)
viii. Secondary Electron (SE2)
ix. Backscattered electron diffraction (BSD)
x. Electron Backscatter Diffraction (EBSD)
xi. Energy dispersive x-ray detector (EDX/EDS)

Image Processing, Pixel averaging: Frame/line averaging & integration, Continuous averaging:

i. Image Store Resolution 512 x 384 3072 x 2304 pixel
ii. Thermal tension-compression stage 800 C + 5kN & 1kN load cells
iii. EBSD capable

In addition to the above, SEM images were also obtained by Zeiss Supra 55VP FEG SEM. The SEM had features like EBSD (Nordlys F), EDX (INCA X-Max 20 SDD), Zeiss angle selective

back scattered (AsB) electron detector, Inlens SE, Insitu straining/heating compatible with EBSD and AsB detectors. Further, some of the SEM images were obtained by Jeol thermionic (tungsten filament).

3.3.5 TEM operations

Phillips CM 200 transmission electron microscope (TEM) with an operating voltage range of 20-200 KV and a resolution of 2.4Å was utilised in investigating the structural property and to determine particle size of mechanically alloyed sample.

3.3.5.1 Powder sample preparation

The powder sample (nanoparticles) is dispersed in a solution using ultrasonication for five minutes. The solution used

(a) Should be chemically inert,
(b) Should not result in agglomeration of the nanoparticles,
(c) Should not leave carbon residues, and
(d) Should evaporate in a reasonable time frame (let us say 10-20 minutes) at room temperature.

A simple method of examining whether the solution leaves carbon residues or not is to keep a couple of drops on a clean glass slide and observe after evaporation; if the glass slide is not clear, then the solution is not useful. Hexane is a suitable medium; methanol and ethanol can be tried. The suspended particles are lifted on a carbon-coated copper grid (of 200 or 300 mesh) with the help of forceps, by dipping the grid in the beaker gently and withdrawing horizontally. The grid is dried on a filter paper under an infrared lamp, followed by inspection in the TEM. The exercise is repeated until a satisfactory collection is obtained.

3.3.5.2 Bulk sample preparation

Sample preparation is very critical in TEM characterization, the specimen you want to look at must be of such a low density that it allows electrons to travel through the solid metal/alloy. There are different ways to prepare the material for observing under TEM, the following sample preparation methods were followed.

3.3.5.2.1 Sectioning the sample

The bulk samples were sectioned into thin wafers, approximately < 0.5 mm in thickness. The sectioning was done using the Struers Accutom high speed wafering saw. Selection of proper wafer blade and saw are very important during this step. This step will determine the orientation of the sample in the microscope, since crystallographic orientation is important, the material is

positioned carefully in the saw mount. The saw cuts were perpendicular to the axis of the electron beam in the final sample.

3.3.5.2.2 Cutting 3 mm Disc

The next step is to cut 3 mm discs from the thin wafer. Affix the sample material to the aluminum mounting slide. Alternately, affix a clear glass cover-slip on top. This step ensures that the surface of interest is undamaged during cutting. Affix with low-temperature melting point wax, place the slide on the hot plate set approximately to 70 ^{0}C. Apply a small amount of the "crystal bond" wax and allow to melt. Remove the slide from the hot plate and immediately place the sample onto the melted wax. Position the sample/Al slide onto the magnetic base of the ultrasonic cutting tool. Align the area of interest of the sample under the cutting tool. Place a small amount of cutting medium onto the sample. Lower the cutting tool to the sample surface. Begin the cutting. Remove the Al slide from the magnetic base and release the sample disc.

3.3.5.2.3 Dimpling

Bulk samples should be dimpled from both sides. Measure the initial thickness of the sample and plan the next steps before beginning to dimple. Affix the 3mm disc onto the center of the dimpling stub with melted wax or cyanoacrylate glue. Position the stub into the positioning ring on the Gatan dimple grinder. Turn on the table rotation and observe the rotation of the sample with the small optical microscope. The cross-hairs indicate where the dimple centre will be located. Move the positioning ring so that the region of interest is at the cross-hair intersection. Remove material from first side until the dimple bottom is approximately in the center of the original disc. Turn over, and remove material from second side until final thickness is achieved. The brass dimpling wheel is started. The abrasive paste is mixed with a small amount of water or diamond paste extender. Progressively smaller paste is used to remove calculated thicknesses of material. Calculate the total thickness we wish to remove before starting, and adjust the removal amount accordingly. Best results are obtained when a depth equal to three times the paste grit size is removed by the next smaller paste.

The final stages of dimpling are critical in producing a successful sample. Working slowly and carefully, it is essential that the last polishing step, which produces a scratch-free, mirror finish, would be completed when the sample is at the desired final thickness. The felt-covered wheel and 3 μm paste are used, followed by 1 μm paste, to remove the last 10 μm of material (i.e. when the total thickness remaining at dimple bottom is approximately 20 μm). All the steps involved in thinning the sample are followed, using progressively smaller diamond paste. Not a single paste size is skiped. This is essential in order to remove the scratches of the previous paste size. Be sure to leave enough material so that we can finish with the felt-covered wheel. A scratch-free, mirror-

like surface is necessary. The finished disc with highly polished dimpled surfaces on both sides is approximately 300 μm in thickness at the edge, and less than 10 μm thickness in the centre as shown in Figure 3.14. When the dimple operation is completed, the sample is removed from the stub by soaking in acetone (in a covered container). The possibility of damaging the sample is too great. The sample is soaked in clean acetone after removal to thoroughly remove the wax or glue. The dimpled sample is handled very carefully as it can easily be damaged.

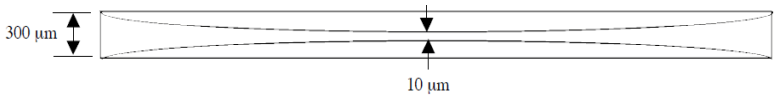

Figure 3.14 Shows the finished disc obtained from dimpling process.

3.3.5.2.4 Ion milling

The final step in TEM sample preparation is ion-beam milling done using the Gatan PIPS (Precision Ion Polishing System). It is equipped with a LN_2 cooling stage to prevent sample damage from heating. The PIPS uses higher flux and lower angles, and is designed for short-term milling. The milling progress is monitored periodically, the mounted camera is used to observe milling progress. This is done while milling by retracting the milling chamber shutter. Transmitted light is used to determine when a hole has been formed in opaque samples. The sample was examined with reflected light to monitor the surface roughness, and to observe "Newton's Rings." Reflected light on a highly polished, curved surface will often produce "Newton Rings" if the material is thin enough. These are colored concentric rings that arise from interference of reflected and transmitted waves. In ideal situations, these rings can give accurate indication of sample thickness. They usually appear only when the sample is <5 μm in thickness. A very deep violet almost black color indicates the sample region is good for TEM.

3.4 Assessment of Properties

In this section experimental techniques to determine various properties of MA (ball milled) powder as well as consolidated samples are described. Procedure to determine magnetic and mechanical properties as well as to apply compression stresses are explained with the specification of the various equipment used for the purposes.

3.4.1 VSM operation

During this research work, Lakeshore vibrating sample magnetometer (VSM) was utilized for investigating magnetic behaviours of powder as well as powder consolidated bulk samples. The maximum magnetic field applied in this research is 20 KOe, while the measurement temperature varied from room temperature to 850 ^{0}C for thermo magnetic analysis. All samples were ground

into powder form and pressed into pellets of 5mm in diameter before being fixed onto a sample holder for each measurement.

The Curie temperature T_C was determined from the variation of magnetic moment (M) with temperature (T) in a constant applied field of 100 Oe. For thermo magnetic measurements, powders were blended with a high-temperature cement binder, and the magnetization was measured (using VSM) with an applied field of 100 Oe at a heating rate of 60 ^{0}C/min in the temperature range of 0–800 ^{0}C. For room-temperature magnetic hysteresis measurements, 10–15 mg of powder was mixed with molten wax in a Teflon sample holder to form a cylinder 1.5 mm in diameter and 4.5 mm in length. Saturation magnetization (M_S), coercivity (H_C) and remanence (M_R) measurements were carried out at room temperature using the VSM under an external magnetic induction field of 20 kOe. M_S was defined by the classical law of approach to saturation,

$$M = M_S (1 - a/H - b/H2) - \chi H \qquad \text{Eqn 3.12}$$

where H is the applied field, M_S the saturation magnetization, χ is the field-independent susceptibility and ‘a’ and ‘b’ are coefficients which depend on the magnetic and structural properties of the sample. Parameter ‘b’ is related to the anisotropy and magnetostriction of the sample. Parameter ‘a’ is usually assumed to arise from inhomogeneities in the sample.

3.4.2 Nano-indentation technique

This technique is widely used in the characterization of mechanical properties like elastic modulus and nanohardness of bulk samples obtained by consolidating metal/alloy powders by SPD process. Due to the very small residual impression left behind by the nano indenter on the surface of the material being characterized, the technique is best known as non destructive one. Mechanical properties are directly determined from the nanoindentation load-displacement curve without measuring the area of the indentation. During nanoindentation, an indenter with a known geometry and properties (e.g., elastic modulus, Poisson’s ratio) is forced into the flat polished (metallographically prepared) surface of a material with unkown properties followed by unloading. Load (force) and indentation depth (displacement) are continuously recorded during the loading and unloading segment of the test, thus both nanohardness as well as elastic modulus are simultaneously determined.

Nano-indenter is operated in the load control mode using a Berkovich-type, pyramidal-shaped diamond indenter. The indentation function consisted of a loading segment of 30 s, applying a maximum force of 20 mN, a load-holding segment of 10 s, and an unloading segment of 15 s. Thus, allows the indenter load and penetration depth to be monitored continuously during loading and unloading. The CSIRO (Commonwealth Scientific and Industrial Research Organisation) -

Ultra Micro Indentation System (informally a Nano Hardness Tester shown in Fig. 3.15) available at the Institute of Frontiers Materials in Deakin University, Geelong, Victoria, Australia was used to determine elastic modulus, pile up effect, load vs displacement and hardness in the ECAP-BP consolidated bulk and sintered bulk samples. We often use the nano hardness in conjunction with the attached atomic force microscope to examine indents for changes in profile, hardness or phase.

Figure 3.15 ultra micro indentation system (Nano hardness).

Make and specification of the CSIRO-UMIS nano hardness system are given below

Make: CSIRO. Specifications:

I. Depth Range: 2 to 20 micron
II. Depth Resolution: 0.003nm
III. Load Range: 50mN - 500mN
IV. Minimum Load: 2mN
V. Load Resolution: 0.002mN
VI. Positioning Stages: 0.1mm step size

CHAPTER 4: BALL MILLING AND CONSOLIDATION (Al_{50}-Fe_{50} SYSTEM)

Elemental powders of Al and Fe taken in the proportion of 50 atomic % each (Al_{50}-Fe_{50} system) have been subjected to mechanical alloying using high energetic ball mill. Mechanical alloying was carried out in toluene liquid medium with tungsten carbide (WC) as milling media (MM), ie, material of grinding balls and milling jars (vials). The milling process is interrupted at predetermined intervals and small quantity of the milled powder is taken out from the jar for characterization purpose. Further, nanocrystalline powders were consolidated by cold compacting and sintering at different times of soaking. Resulting annealed compacts were compressed to a stress values ranging from 0.5 GPa to 8 GPa. These deformed compacts which are the products of nanocrystalline materials were experimentally analysed for structural characterization, magnetic, and mechanical properties in this chapter.

In another set of experiments, elemental powders of Al and Fe taken in the proportion of 50 atomic % each (Al_{50}-Fe_{50} system) have been subjected to mechanical alloying by ball milling carried out in argon atmosphere with stainless steel MM, ie, material of grinding balls and milling jars. Further, nanocrystalline powders obtained by mechanical alloying are consolidated in two different routes: (i) consolidation by cold compaction and sintering and (ii) consolidation by equal channel angular pressing with back pressure (ECAP-BP). Materials were analysed for physical characterization at every step of the process. The final resulting ECAP-BP pellets and sintered compacts were tested for magnetic and mechanical properties. The events of phase transformation over the processes are captured using XRD, DSC and metallography. In addition, texture analyses of the consolidated pellets as well as that of sintered compacts are done by XRD texture measurement. The results of these experiments are presented and discussed in the present chapter.

4.1 Pure Al and Fe Powders

Mixture of elemental powder of Al and Fe with an atomic composition of 50 % each and not subjected to any processing is characterized by XRD to determine the structural parameters. Further, the unmilled powders are also characterized by SEM.

4.1.1 XRD of elemental powders

Tables 4.1 and 4.2 present XRD results of pure Al and Fe powders. From the values presented in tables it can be inferred that lattice parameter (a) of pure Al is 0.4044 nm and that of pure Fe is 0.2862 nm.

4.2 Ball Milling in WC Milling Media (MM)

Elemental powders of Al and Fe in an atomic composition of 50 % each were ball milled upto 185 hours in toluene atmosphere using **tungsten carbide (WC) milling media** (**MM**-vial and balls). Small quantities were taken out of the milling jar at a suitable interval of milling duration for characterisation purpose. Accordingly, the milled powders were analysed by XRD, DSC, VSM, SEM and TEM.

4.2.1 XRD results of ball milled powder (WC-MM)

Results of XRD analysis for mechanically alloyed Al and Fe powder by ball milling for different duration of time are presented in table 4.3 to 4.10. XRD profiles from which analysis was carried out are given in appendix from Fig. 7.2 to Fig. 7.14. Structural characteristics like lattice parameter 'a' and crystallite size 'D' are calculated for different durations of time and listed in table 4.11. Following inferences could be drawn from the values presented in Table 4.11:

(i) Microalloying (though the crystallite size attained is sub micron size, it is still called as microalloying) by ball milling has caused drastic reduction in the size of the crystallites. It decreased for pure Fe from 60 μm to 86 nm when milled for one hour. That is indicated by the peak broadening and calculated using Scherrer equation utilising changed full width at half maximum (FWHM) values as registered by the XRD profiles. Further, it could be noted that the size decreases as the time of milling is increased attaining 12 nm at the end of 65 hours.

(ii) Micro alloying by ball milling has caused increase in lattice parameter 'a' from 0.2862 nm for pure Fe to a maximum value of 0.2880 nm at the end of 20 hours of ball milling time. This is indicated in XRD pattern by peak shift. This is due to entry of Al atoms into Fe lattice, substituting iron atoms in the lattice randomly, giving rise to disordered solid solution-Fe (Al). This inference is supported by the fact that intensity of elemental peaks for Al decreases from 375 counts (Fig. 7.2 appendix I) at one hour milling time to lower values of counts at higher milling time. Absence of superlattice peaks in any one of the XRD profiles proves that the structure is disordered. These results suggest that formation of an ordered phase is not possible by micro alloying in ball mill as revealed by this investigation.

(iii) While the solid solution formed possesses the same crystal structure as that of pure Fe (bcc) but is characterised by a larger lattice parameter (0.29316 nm) formed at the end of 185 hours of ball milling time.

(iv) XRD profiles revealed the presence of pure Al even after milling for a long time. This suggests that disordered solid solution Fe (Al) co-exists with elemental phase.

(v) However, the formation of clusters of short range ordered phase cannot be ruled out albeit, to a very small extent. The XRD pattern for 50 and 65 hours ball milled sample shows low intensity superlattice peaks (100, 111 and 210) indicating certain type of ordered region within the disordered structure. Such results were reported by Fan R. et.al. (2005), who have worked on Fe-28Al system. The short range order (SRO) formation could be caused by the increased temperature attained during milling; local heating during mechanical alloying of elemental powders may increase upto several hundred degrees (Xi S. Q et al 2007).

(vi) Contrary to expectation the lattice expansion which has been progressing during milling upto 30 hours is absent when powder is milled for 40 hours. The lattice parameter of powder milled for 40 hours is 0.2863 nm compared to 0.2862 nm for pure iron. It could be due to higher enthalpy required for vacancy migration which resists the entry of substitutional Al atoms into Fe lattice. Such a mechanism is proposed by Zhang B. Q. et.al (2003). However, lattice expansion is seen to be progressing further, when milling is carried out beyond 40 hours. It could be conceived that the lattice expansion is characterised by disordered structure while lattice contraction accompanies an ordered (SRO) phase. It is because the ordered structure is thermodynamically more stable and offers greater resistance to crystallite refinement while disordered state is a metastable one.

(vii) When milling is carried out for longer duration, beyond 65 hours, only fundamental peaks corresponding to BCC Fe (Al) solid solution phase are visible with greater intensity while elemental peaks of Al (111 and 311) have almost disappeared. This indicates that the separate Fe and Al elemental phases are being replaced by BCC Fe (Al) solid solution phase.

(viii) The XRD pattern for the powder milled for 185 hours as presented in Fig 7.14 in appendix shows a significant difference. A broad asymmetric diffraction profile is seen to replace well defined sharp diffraction lines. This kind of pattern indicates the presence of an amorphous phase and high level of grain refinement. Further, high density crystal defects are known to generate in such type of XRD profile (Mhadhbi M. et al. 2010).

Table 4.1 Pure **Al** XRD peaks, indexing and structural parameters

peaks	2θ	$\sin^2\theta$	$\sin^2\theta/\sin^2\theta_{min}$	$h^2+k^2+l^2$	hkl	Lattice parameter 'a' in nm
1	38.52	0.1088	1 × 3	3	111	**0.4044**
2	44.76	0.1450	1.33 × 3	4	200	0.4045
3	65.14	0.2898	2.66 × 3	8	220	0.4047
4	78.26	0.3983	3.66 × 3	11	311	0.4048
5	82.47	0.4345	3.99 × 3	12	222	0.4048
6	99.11	0.5792	5.32 × 3	16	400	0.4048
7	112.03	0.6876	6.32 × 3	19	331	0.4049

Table 4.2 Pure **Fe** XRD peaks, indexing and structural parameters

Peaks	2θ/θ	$\sin^2\theta$	$\sin^2\theta/\sin^2\theta_{min}$	$h^2+k^2+l^2$	hkl	d_{space} in nm	'a' in nm
1	44.73/22.365	0.1447	1× 2	2	**110**	0.2024	**0.2862**
2	65.07/32.535	0.2892	1.99× 2	4	200	0.1432	0.2864
3	82.4/41.2	0.4338	2.99× 2	6	211	0.1169	0.2863
4	99.0/49.5	0.5782	3.99× 2	8	220	0.1012	0.2862
5	116.45/58.225	0.7227	4.99× 2	10	310	0.0906	0.2865
6	137.24/68.62	0.8671	5.99× 2	12	222	0.0827	0.2864

Table 4.3 XRD peaks and structural parameters of powder ball milled for **one hour**

Peaks at 2θ	hkl	fcc/bcc	Fe/Al	d_{space} in nm	FWHM	Lattice strain %	'a'lattice parameter in nm	'D' crystallite size in nm
38.32	111	fcc	Al	0.2343			0.4058	35.2
44.56*	**110/200**	bcc/fcc	Fe/Al	0.2033	**0.4000**	**0.282**	**0.2875**/0.4066	85.9
64.9	200/220	bcc/fcc	Fe/Al	0.1434			0.2868/0.4055	
78.04	311	fcc	Al	0.1223			0.4056	
82.108	211/222	bcc/fcc	Fe/Al	0.1170			0.2865/0.4052	
98.464	220/400	bcc/fcc	Fe/Al	0.1012			0.2862/0.4048	
110.92	331	fcc	Al	0.0929			0.4049	
115.924	310/420	bcc/fcc	Fe/Al	0.0905			0.2861/0.4047	

*Fundamental peak = h+k+l = even. FWHM-full width at half maximum. 2θ-Bragg angle

Table 4.4 XRD peaks and structural parameters of powder ball milled for 10 hours

Peaks at 2θ/θ	hkl	fcc/bcc	Fe/Al	d_{space} in nm	'a' lattice parameter in nm	FWHM	'D' crystallite size in nm
38.296/19.148	111	fcc	Al	0.2347	0.4065		29.34
44.512/22.256	**110/200**	bcc(fcc)	Fe/Al	0.2032	**0.2874**/0.4064	0.44^0	20.4(61.3)
64.732/32.366	200/220	bcc(fcc)	Fe/Al	0.1434	0.2868/0.4055		
77.68/38.84	311	fcc	Al	0.1221	0.4049		
81.868/40.934	211/222	bcc/(fcc)	Fe/Al	0.1169	0.2863/0.4049		
98.512/49.256	220/400	bcc/(fcc)	Fe/Al	0.1012	0.2862/0.4048		
111.376/55.688	331	fcc	Al	0.0929	0.4049		
115.78/57.89	310/420	bcc(fcc)	Fe/Al	0.0906	0.2865/0.4051		

Table 4.5 XRD peaks and structural parameters of powder ball milled for 20 hours

Peaks /2θ/θ	hkl	bcc/fcc	Fe(Al) phases	d_{space} nm	'a'lattice parameter nm	'D' crystallite size nm	FWHM
38.212/19.106	111	fcc	Al	0.2346	0.4063	21.98	
44.428/22.214	**110/200**	bcc/fcc	Fe/Al, (Fe(Al)	0.2037	**0.2880**/0.4074	(35.8)	0.54^0
64.468/32.234	200/220	bcc/fcc	Fe/Al, (Fe(Al)	0.1431	0.2862/0.4047		
77.86/38.93	311	fcc	Al	0.1218	0.4039		
81.916/40.958	211/222	bcc/fcc	Fe/Al, (Fe(Al)	0.1169	0.2863/0.4049		
98.212/49.106	220/400	bcc/fcc	Fe/Al, (Fe(Al)	0.0894	0.2528/0.3576		
112.468/56.234	331	fcc	Al	0.0922	0.4018		
115.588/57.794	310/420	bcc/fcc	Fe/Al, (Fe(Al)	0.0905	0.2861/0.4047		

Table 4.6 XRD Peaks and structural parameters of powder ball milled for **30 hours**

Peaks at 2θ/θ	hkl	Bcc /fcc	Phases	'd'$_{space}$ in nm	'a' lattice parameter nm	FWHM 2θ	'D' crystallite size nm
38.26/19.13	111	fcc	Al	0.2336	0.4046		14.66
44.476/22.238	**110/200**	bcc	FeAl, Fe/Al	0.2031	**0.2872**/0.4062	0.55^0	34.3
64.708/32.354	200/220	bcc	FeAl, Fe/Al	0.1430	0.2860/0.4044		
72.4/36.2	**210 S***	bcc	FeAl, Fe/Al				
78.1/39.05	311	fcc	Al	0.1217	0.4036		
81.916/40.958	211/222	bcc	FeAl, Fe/Al	0.1171	0.2868/0.4056		
98.356/49.178	220/400	bcc	FeAl, Fe/Al	0.1013	0.2865/0.4052		
Absent	331			**Absent**			
115.924/57.962	310/420	bcc	FeAl, Fe/Al	0.0907	0.2868/0.4056		

*S-superlattice peak (h+k+l=odd).

Table 4.7 Indexing and structural parameters of powder ball milled for 40 hours

Peaks at 2θ	θ	$Sin^2θ$	$Sin^2θ/sin^2θ_{min}$	$h^2+k^2+l^2$	hkl	fcc	bcc	FWHM	'a' nm	'D' nm
37.926	18.963	0.1055	1 x 3	3	111	√			0.4049	21.9
44.624	22.312	0.1441	1.36 x 3	4/2	110		√	0.6	**0.2863**	28.6
64.837	32.418	0.2874	2.73 x 3	8/4	200		√			
71.15	35.575	0.3385	3.21 x 3	10/5	210		**S** √			
77.945	38.972	0.3955	3.75 x 3	11	311	√				
82.058	41.03	0.4309	4.08 x 3	12/6	211		√			
98.548	49.274	0.5743	5.44 x 3	16/8	220		√			
116.194	58.09	0.7205	6.83 x 3	20/10	310		√			

*FWHM-full width at half maximum, a-lattice parameter, D-crystallite size, S-superlattice peak

Table 4.8 Indexing and structural parameters of powder ball milled for 45 hours

Peak at 2θ	θ	$Sin^2θ$	$Sin^2θ/sin^2θ_m$	$h^2+k^2+l^2$	hkl	fcc	bcc	FWHM	'a' nm	'D' nm
38.368	19.184	0.1079	1 x 3	3	111	√			0.4057	
44.556	22.278	0.1437	1.33 x 3	4/2	**110**		√	0.7^0	**0.2868**	21.5
64.82	32.41	0.2873	2.66 x 3	8/4	200		√			
78.00	39.00	0.3960	3.67 x 3	11	311	√				
81.888	40.944	0.4294	3.98 x 3	12/6	211		√			
98.701	49.35	0.5756	5.35 x 3	16/8	220		√			
116.075	58.04	0.7198	6.67 x 3	20/10	310		√			

Table 4.9 Indexing and structural parameters of powder ball milled for 50 hours

Peaks at 2θ	θ	$Sin^2\theta$	$Sin^2\theta/sin^2\theta_m$	$h^2+k^2+l^2$	hkl	fcc	bcc	FWHM	'a' nm	'D' nm
30.64	15.32	0.0698	1 x 2	2/1	100		**S** √			
38.14	19.07	0.1067	1.53 x 2	3	111	√				
44.42	22.21	0.1428	2.05 x 2	4/2	**110**		√	0.8^0	**0.2875**	17.2
53.8	26.9	0.2046	2.93 x 2	6/3	111		**S** √			
64.68	32.34	0.2861	4.09 x 2	8/4	200		√			
71.42	35.71	0.3406	4.88 x 2	10/5	210		**S** √			
78.3	39.15	0.3986	5.7 x 2	11	311	√				
81.78	40.89	0.4285	6.14 x 2	12/6	211		√			
98.02	49.01	0.5697	8.16 x 2	16/8	220		√			
116.2	58.1	0.7207	10.19 x 2	20/10	310		√			

Table 4.10 Indexed and structural parameters of powder ball milled for 65 hr

Peaks at 2θ	$Sin^2\theta$	$Sin^2\theta/sin^2_m$	$h^2+k^2+l^2$	hkl	fcc	Bcc (F*/S*)	FWHM	Lattice strain %	'a' nm	'D' nm
30.58	0.0695	1 x 2	2/1	100		**S***-FeAl				
37.62	0.1039	1.5 x 2	3	111	√	Al				
44.34	0.1419	2.0 x 2	4/2	110		F*-FeAl	1^0	**1.021**	**0.2876**	12.3
54.5	0.2096	3.0 x 2	6/3	111		**S*** FeAl				
63.46	0.2765	4.0 x 2	8/4	200		F*-FeAl				
81.2	0.4235	6.0 x 2	12/6	211		F*-FeAl				
98.06	0.5701	8.0 x 2	16/8	220		F*-FeAl				
108.6	0.6594	9.5x 2	19	331	√	Al				
115.6	0.7165	10 x 2	20/10	310		F*-FeAl				

S-Super lattice peak and F-Fundamental peak

Table 4.11 Structural parameters relevant with milling time.

Milling time in hr	Peaks at 2θ	hkl/phase	Lattice parameter 'a', Fe(Al) in nm	FWHM degrees	Crystallite size in nm 'D'	Peak height (intensity)	Lattice strain %
0	44.73	110/Fe	0.2862		60microns		
		111Al					
1	44.56	110/200 Fe/Al	0.2875/0.4066	0.40	85.9	320	0.282
		111Al				**335**	
10	44.512	110/200 Fe/Al	0.2874/0.4064	0.44	61.3	540	0.343
		111Al				**205**	
20	44.428	110/200 Fe/Al	**0.2880**/0.4074	0.54	35.8	390	0.480
		111Al				**165**	
30	44.476	110/200 Fe/Al	0.2872/0.4062	0.55	34.3	435	0.492
		111Al				**155**	
40	44.624	110/200 Fe/Al	0.2863/0.4049	0.6	28.6	86	0.552
		111Al				**10**	
45	44.556	110/200 Fe/Al	0.2868/0.4057	0.7	21.5	104	0.674
		111Al				**6**	
50	44.42	110/200 Fe/Al	0.2875/0.4066	0.8	17.2	585	0.793
		111Al				**4**	
65	44.34	110/200 Fe/Al	0.2876/0.4068	1.0	12.3	500	1.021
		111Al				**2**	
185	43.86	110 Fe(Al)	0.29316	5.0		60	

4.2.2. DSC analysis of ball milled powder (WC-MM)

This was to investigate transformative behaviour of ball milled product in two different modes, in argon atmosphere using stainless steel (SS) milling media (MM) and in the presence of toluene using tungsten carbide (WC) milling media (MM).

The ball milled powder (tungsten carbide MM using toluene) samples were analysed using differential scanning calorimeter. These DSC profiles are presented in Fig 4.1 to 4.4. Having studied the peak of the profile and referring the appropriate literature (Morris-Munoz M. A. et al. 1999) following inferences are drawn:

1) In general powder samples examined exhibit four exothermic peaks; they are in the temperature range of:
    a) 275^0-350^0 C
    b) 390^0-400^0 C
    c) 440^0 C
    d) 530^0 C
2) Peaks in the temperature range of 275^0-350^0 C corresponds to transformation to ordering from near ideal Fe-Al solid solution, such change occurs by the mechanism of atomic exchange of positions, vacancy diffusion or movement of dislocation creating antiphase boundary. Total enthalpy which is proportional to the peak height corresponds essentially to volume fraction of solid solution generated during milling.
3) The peak at 390 – 440^0 C corresponds to formation of fine layers of Fe-Al from the pure elements. As milling progresses for longer time the layer becomes finer which is revealed in peak occurring at lower temperature, going down to 390^0 C for 50 hours of milling compared to 440^0 C for 10 hours of milling (Fig 4.1 to 4.3). Peaks at higher temperature (point 3 & 4 in Fig 4.2 & 4.3) are associated with disappearance of various defects, and events like recrystallisation and grain growth of intermetallics.
4) Metallurgical events started showing up only when milling was carried out for 10 hours. At the end of 10 hours of milling the dominant event is the process of alloying. Samples ball milled for 20 hours exhibit peak (1) corresponding to short range ordering (SRO) or vacancy migration apart from forming disordered alloy (Mhadhbi M. et al. 2010). The tendency for short range ordering increases with time of milling.
5) Peaks related to alloying of elemental phases are high in intensity in the sample ball milled for 30 hours. As the time of milling progresses, high temperature peaks dominate indicating that recrystallisation and grain growth are very much in action.

6) Similar tendency continues further upto 50 hours and 65 hours of ball milling. At the end of 65 hours of milling, the intensity of mid temperature peak has been reduced to a minimum suggesting that presence of elemental phases is negligible.
7) Variation of enthalpy with respect to the time of milling is shown in the graph presented in Fig 4.4. Like XRD results, this also suggests the formation of disordered solid solution of Fe and Al, which would later transform to short range ordered structure mostly associated with vacancy migration.
8) DSC curves in Figure 4.4 illustrate crystallisation of amorphous phase in 165 and 185 hours of ball milled powder.

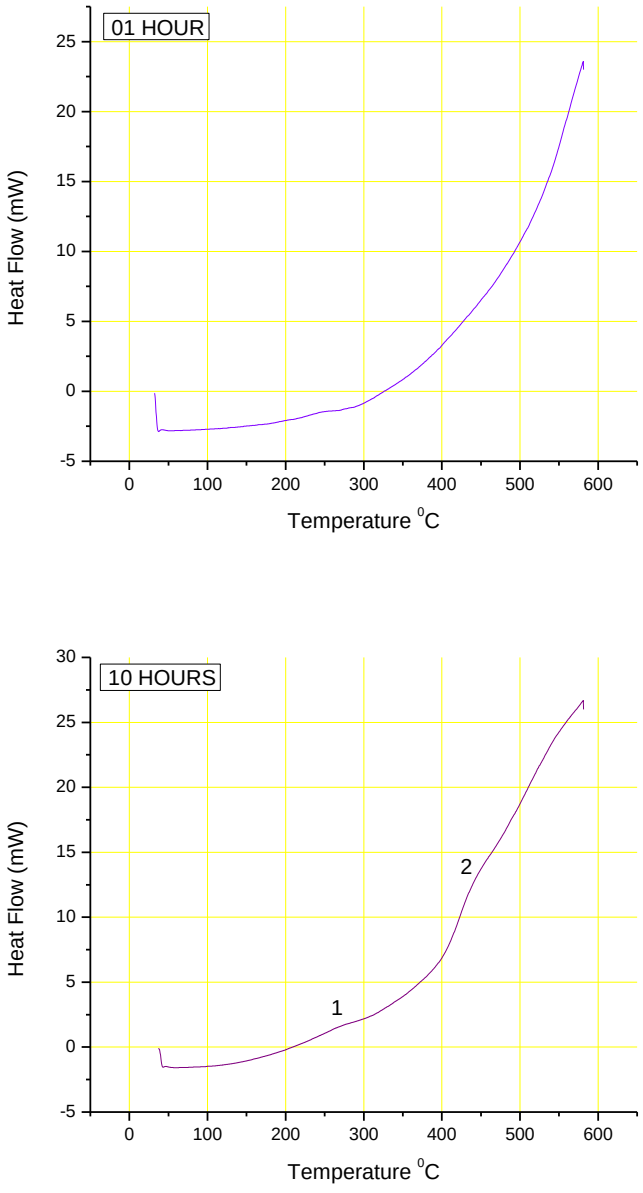

Figure 4.1 DSC curves of powder ball milled for 01 and 10 hours.

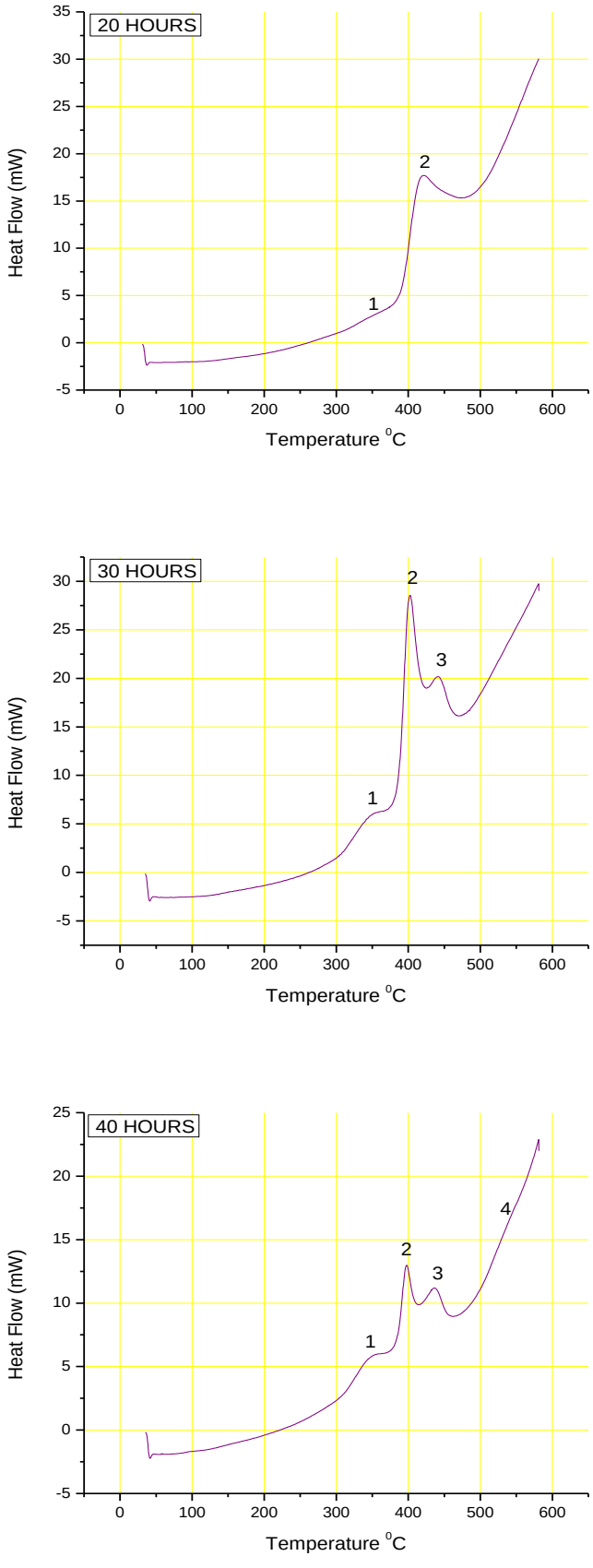

Figure 4.2 DSC curves of powder ball milled for 20, 30, and 40 hours.

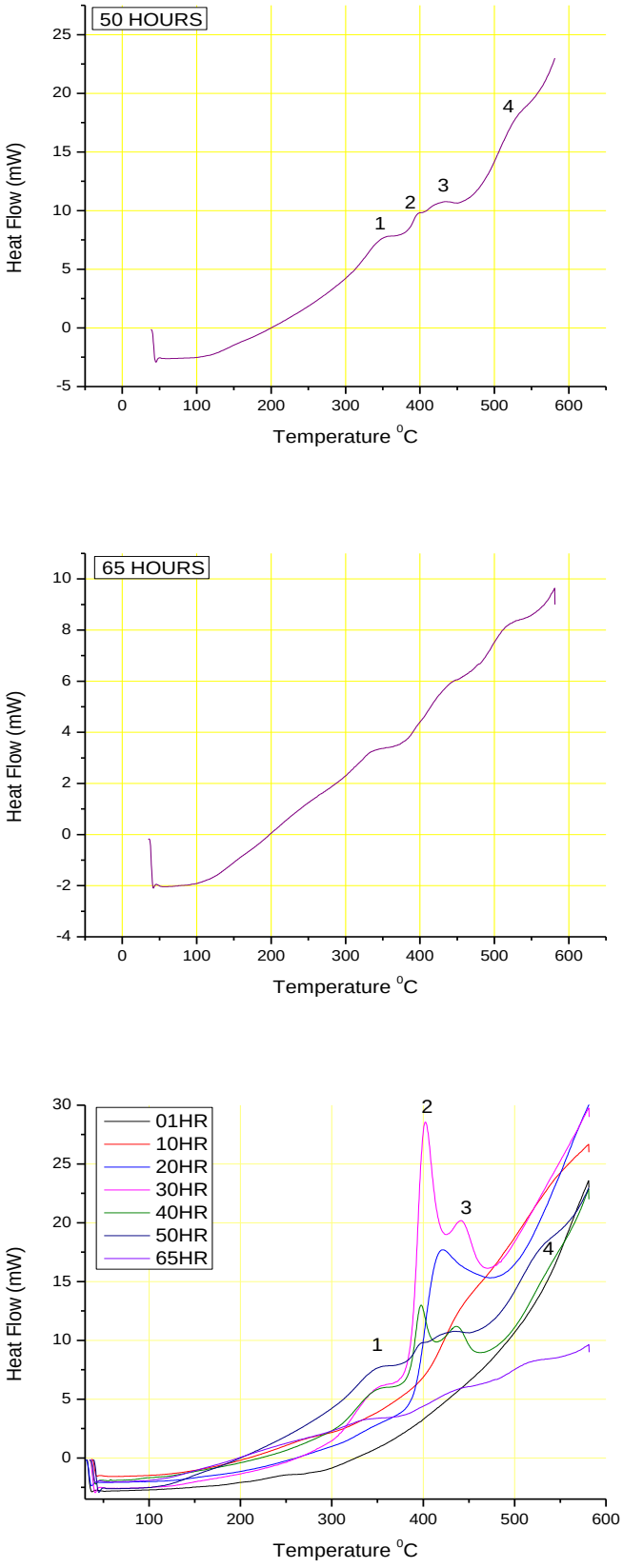

Figure 4.3 DSC curves of powder milled for 50 and 65 hours and superimposition of curves for powders milled from 01 hour to 65 hours

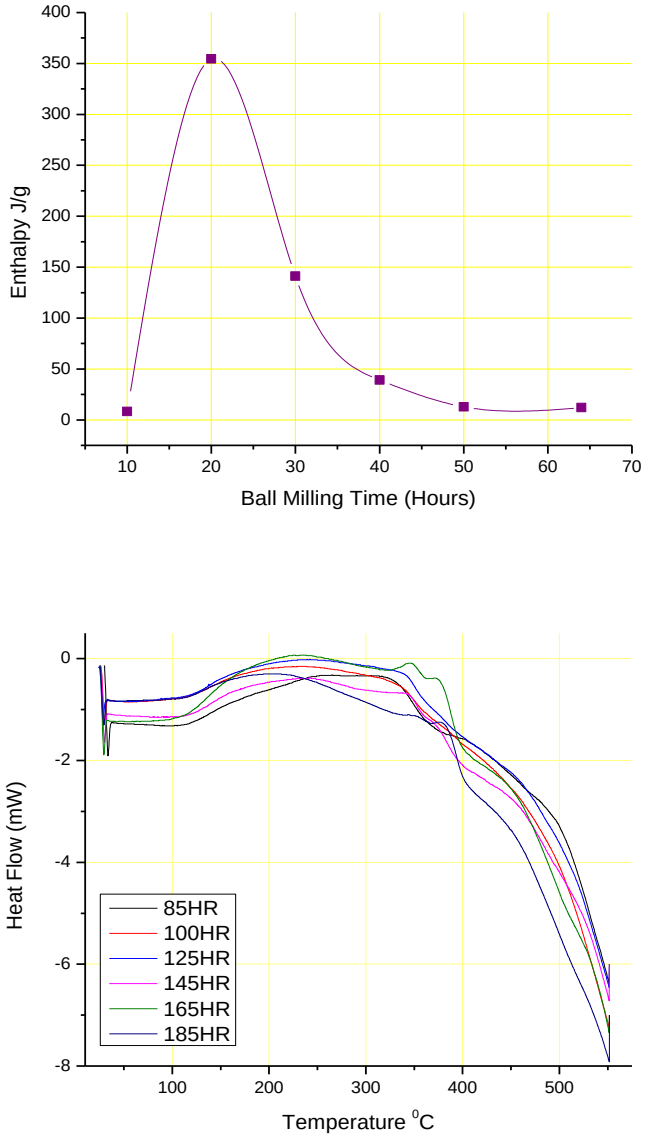

Figure 4.4 Enthalpy as a function of milling time. DSC curves of powder samples milled from 85 to 185 hours.

4.2.3 Magnetic features of ball milled powder (WC-MM)

Room temperature magnetisation (M) – applied field (H) curves (hysteresis loops) and magnetic parameters of mechanically alloyed powder as a function of ball milling time are shown in Fig. 4.5, and listed in Table 4.12 respectively. Following inferences could be drawn from the M-H curves and the values presented in the table:

1) Typical ferromagnetic loops are obtained for all the mechanically alloyed powder, showing unambiguously that the powders are ferromagnetic at room temperature.
2) Saturation magnetisation (M_S) decreases from 122 emu/gm to 76.5 emu/gm with increase in ball milling duration from one hour to 65 hours.

3) The decrease in M_S is mainly due to the progressive alloying of Al in Fe. Al diffusion into Fe decreases the magnetic moment of individual Fe sites due to a decrease in the direct ferromagnetic interaction between Fe–Fe sites, inducing an anti-ferromagnetic super-exchange interaction between Fe sites interfered by Al atoms (Plascak J. et al. 2000).
4) The process of MA as a function of high energy rate ball milling in a toluene liquid environment eliminates the milling media and atmospheric contamination. Zeng Q. and Baker I. (2006) have mentioned an increase in M_S with increasing milling time could be attributed to Fe contamination from the milling media and oxidation of Al, such variations in M_S have not occurred during the present investigations.
5) Compared to a narrower hysteresis loop at lower milling duration, a wider hysteresis loop (higher milling duration > 30 hours) exhibits hard (H_C > 125 Oe) magnetic properties like lower permeability, higher retentivity, higher coercivity, higher reluctance, and higher residual magnetism. Thus M_R and H_C increase with increased duration (> 30 hours) of ball milling.

From Figure 4.6 the following inferences could be drawn:

1) Decrease in coercivity (H_C) and remanent (M_R) is observed at longer milling duration (>50 hours).
2) M_S decreases steeply beyond 50 hours of ball milling duration. Such changes observed are due to the cluster of SRO (presence of low intensity superlattice peaks) prevailing in the MA powder sample beyond 50 hours of ball milling duration.
3) M_R decreases between 30 to 40 hours of milling duration in addition to the decrease beyond 50 hours of milling while, H_C increases continuously only to fall between 50 to 65 hours of milling duration.
4) In fully ordered Fe–50 at% Al, a Fe atom has an average of 2 Fe atoms as nearest neighbors (out of a maximum possible eight in the bcc structure). With complete disorder, a Fe atom has an average of 6 Fe atoms as nearest neighbours (Raviprasad K., Chattopadhyay K. 1992). Thus lower magnetic parameters are observed during ordering (SRO is observed beyond 50 hours of milling time) than during disorder phenomenon.
5) The correlation between the lattice parameter and the saturation magnetization in **Figure 4.7** hints at another possible factor influencing the magnetic transition in ball milled Fe-Al system as mentioned below:
6) The lattice parameter decrease means that the distance between (110) planes and, thus, the Fe–Fe interatomic distance, decreases ultimately leading to a decrease in the magnetic moment.
7) Lattice contraction occurs between one to 10 hours and 20 to 40 hours of milling time, some of the possible causes for such a volume change are formation of short cluster of

ordered boundary within the disordered structure, higher enthalpy required for vacancy migration which resists the substitution of Fe atoms with Al in the Fe lattice structure or oxidation during milling, which decreases Al content.

8) Both the order (SRO) and the lattice contraction cause a decrease in magnetism for mechanically alloyed Fe (Al) solid solution. However, the contribution of the volume change is greater than the effect of short range order to the total reduction of magnetic moment during MA of Fe-Al as reported by Zeng.Q. and Baker.I. (2006).

9) From the above discussions it is quite transparent that magnetic parameters decrease initially (0 to 30 hours of milling time) due to diffusion of Al in Fe while at longer milling time (> 30 hours), the decrease is due to combined efforts of Al diffusion coupled with lattice contraction and SRO. Due to combined influence of these factors, the effect of lattice expansion which occurs has no influence on the magnetic properties at this stage of milling time.

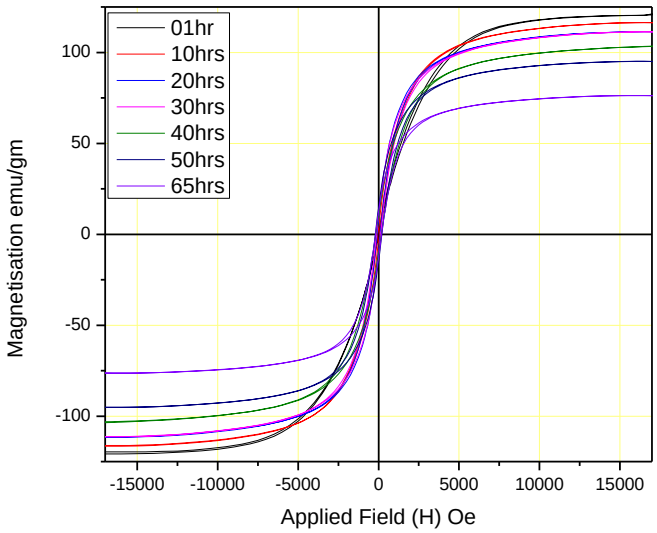

Figure 4.5 M-H (hysteresis loops) curves of powder ball milled from one hour to 65 hours

Table 4.12 Room temperature magnetic parameters of ball milled powders (01h to 65h)

Sample Type (milling Hours)	Saturation Magnetization (emu/gms) (Ms)	Remanent Magnetization (emu/gms) (Mr)	Coercivity (Hc) Oe	Squareness (Mr/Ms)
01	122	0.989	20.5	8.1065×10^{-3}
10	116.5	3.77	48.0	0.0323
20	111.5	8.258	90.5	0.0740
30	111	10.6	128.5	0.0954
40	103.7	10.0	170.5	0.0964
50	95.13	14.78	203	0.1553
65	76.5	12.78	191	0.1670

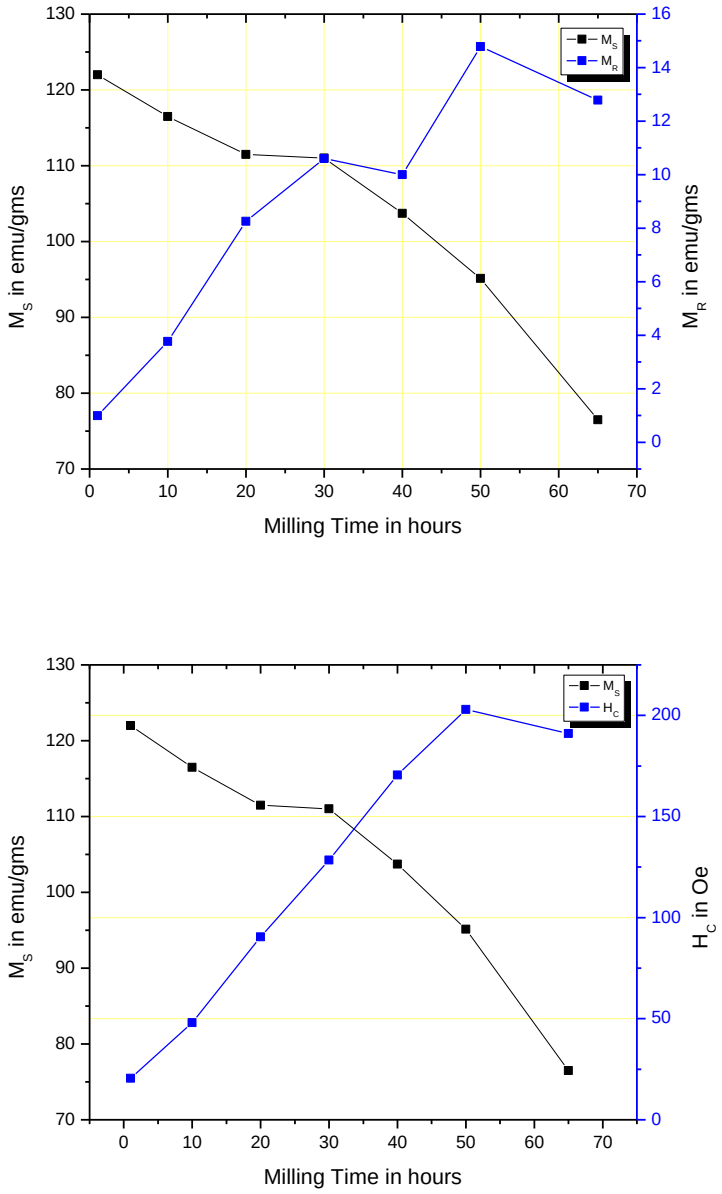

Fig 4.6 M_S, M_R and H_C as a function of ball milling time.

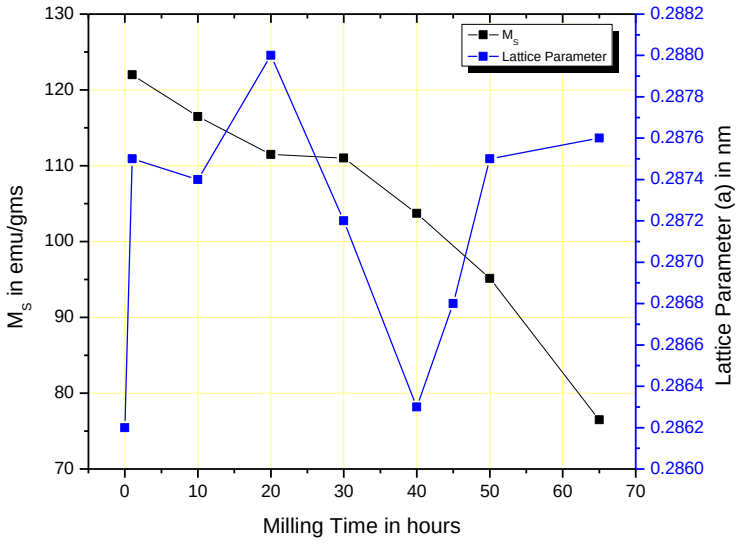

Figure 4.7 M_S & lattice parameter as a function of ball milling time.

4.2.4 Thermo-magnetic analysis of ball milled powder (WC-MM)

Magnetic properties of mechanically alloyed powder as a function of ball milling duration depends on the changes in temperature as shown in Figure 4.8. Accordingly, the following inferences could be drawn:

1) At room temperature all the mechanically alloyed powder samples show ferromagnetic phase, such a phase decreases notably with increase in milling duration and temperature. It is expected that the dissolution of nonmagnetic (Al) element in the ferromagnetic metal (α-Fe) with increasing temperature reduces magnetisation during the mechanical alloying. In addition, powders which are totally alloyed by ball milling and which do not contain any traces of elemental phases are normally disordered with a ferromagnetic phase except for SRO. Such mechanically alloyed powder transforms into ordered intermetallic paramagnetic phase upon heating. However, intermetallic $AlFe_3$ structure is ferromagnetic mainly because of its atomic structure.
2) Powder sample mechanically alloyed for **one** hour duration shows a marginal decrease in magnetisation in the temperature range of 20 ^{0} to 380 ^{0}C, thereafter, a slight increase in magnetisation in the temperature range of 380 ^{0} to 520 ^{0}C is observed which may correspond to some phase transformation. The magnetisation decrease is steep beyond 700 ^{0}C reaching a minimum value of 5.0 emu/gms at 800 ^{0}C, decrease is due to progressive alloying of elemental phases and large quantity of elemental unalloyed Fe could be the possible cause for ferromagnetic (5.0 emu/gm) behaviour.

3) Powder sample mechanically alloyed for **10** hours of milling duration has a marginal decrease in magnetisation at low temperature while the decrease is steep in the temperature range of 340 ^{0} to 440 ^{0}C. DSC investigation of powder sample ball milled between 10 to 20 hours of duration showed exothermic peak in the temperature range of 350 ^{0} to 420 ^{0}C pertaining to alloying of elemental phases. Magnetisation (9.14 emu/gms) at 600 ^{0}C and at room temperature for 10 hour ball milled powder is quite high compared to other ball milled powders; such behaviour is due to the presence of large amount of unalloyed Fe and disordered ferromagnetic clusters. XRD results too have shown such phases and disordered structure in the powder sample.
4) Powder sample ball milled for 30 hours exhibits a large decrease (steep) in magnetisation in the temperature range of 360 ^{0} to 620 ^{0}C. The DSC investigation of the sample revealed exothermic peaks related to SRO / alloying of elemental phases in the temperature range of 340 ^{0} to 440 ^{0}C. The powder sample never attains paramagnetic phase even after heating beyond 600 ^{0}C, possesses a minimum of 2.5 emu/gm at 680 ^{0}C. Such a magnetic behaviour is related to the presence of unalloyed elemental Fe and disordered ferro magnetic clusters in the alloyed powder.
5) The Curie temperature T_C, at which ferromagnetic to paramagnetic (<2 emu/gms) transition occurs are 580 ^{0}C, 520 ^{0}C and 600 ^{0}C for 40 h, 50 h and 65 h milled samples respectively as observed from Figure 4.8. The ferromagnetic to paramagnetic transitions are irreversible since the prolonged heating leads to the formation of stable FeAl intermetallic phases. The magnetization values are 0.8, 0.5 and 1.5 emu/gm for 40h, 50h and 65h ball milled powder samples respectively at around 680 ^{0}C.

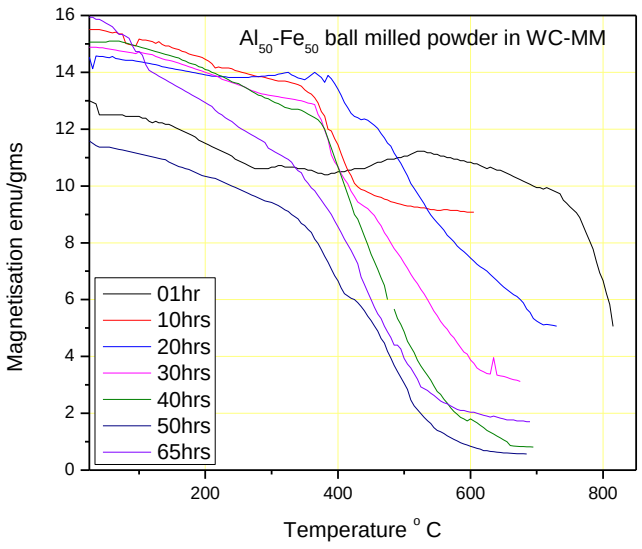

Figure 4.8 Thermo magnetic curves of powder ball milled from 01 h to 65 h.

4.2.5 SEM analysis of unmilled and ball milled powder (WC-MM)

Secondary electron photomicrographs of powdered samples mechanically alloyed for different time duration from one hour to 65 hours are presented in **Fig. 4.9**. It can be seen that there is a progressive communition of powder leading to drastic reduction in size with continued milling. The process of globular clustering of many fine particles is discernible in the exhibited images. The elements of fracturing, shear deformation, coagulation of particles and spherical formation can be noted in these images. Such events are very much visible when mechanically alloyed samples are viewed at higher magnification as presented in **Fig. 4.10**.

EDS analysis of these mechanically alloyed powders is carried out and results of it is presented in Table 4.13. Typical EDS analysis with graphical details along with SEM image for 65 hours ball milled powder are presented in **Fig. 4.11**. Similar analysis for other samples is available in appendix (Fig 7.15 to 7.19). Following inferences can be drawn from the results presented in **Table 4.13**:

(i) Al particle is almost in pure form for one hour mechanically alloyed powder indicating that the process of alloying by the entry of one kind of atom into the lattice of other is yet to begin.

(ii) As the duration of milling increases the process of alloying progresses by the entry of one kind of atom into the lattice of the other, triggering a host of metallurgical events.

(iii) The process of alloying continues upto 50 hours of milling and stops. At the end of 65 hours of milling there is no visible change in composition of powder indicating that further change in energy of milling would be utilised for various metallurgical events to happen inside individually alloyed finely communited powder particles.

4.2.6 Particle size measurement by SEM and TEM

SEM and TEM are used to measure the particle size of milled powder, albeit, on a limited number of powder samples. The SEM photomicrograph of the particles milled for 15 hours as presented in Fig 4.12 (a), indicates that most of the particles are less than 673 nm in size. Further, the TEM photomicrograph of the particles milled for 40 hours as presented in Fig 4.12 (b) shows that the particle size could be as small as 100 nm which would further get reduced to approximately 70 nm when milled for 50 and 65 hours (Fig 4.12 (c & d)). It is evident that ball milling causes reduction in size of the particles to nano range. Particles which look coarser in size in some of the regions on the photomicrographs are due to agglomeration of the fine powder.

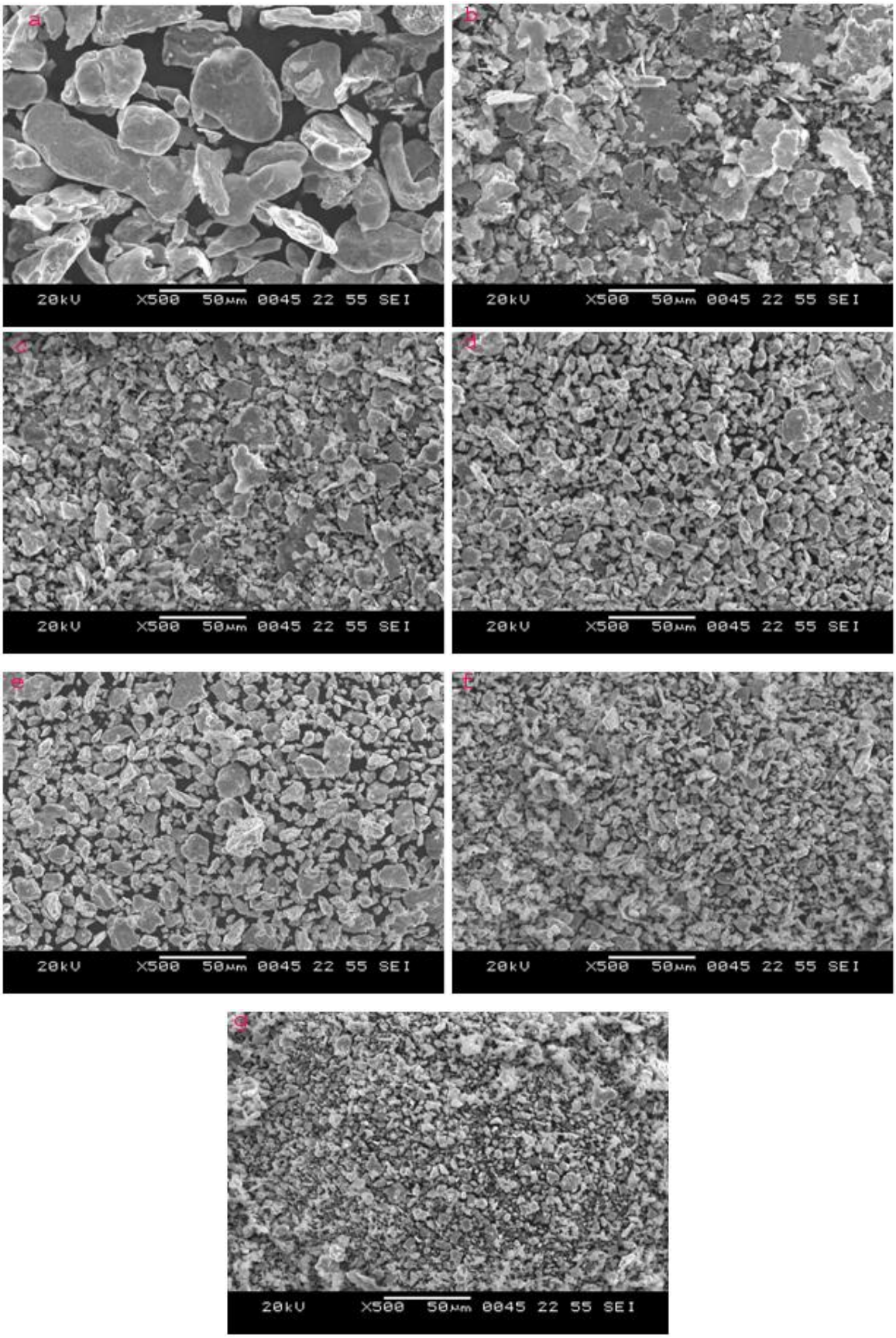

Figure 4.9 SEM micrograph shows morphology of powder particles ball milled for different time a) 1 h. b) 10 h. c) 20 h. d) 30 h. e) 40 h. f) 50 h. g) 65 h.

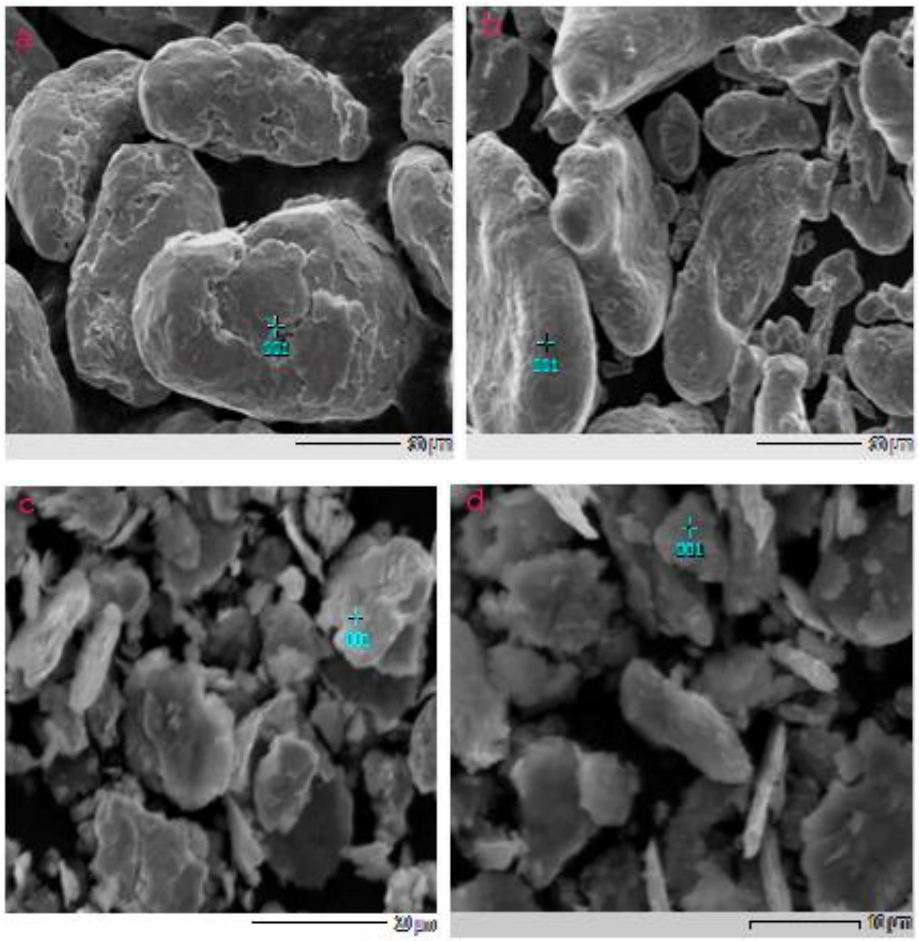

Figure 4.10 SEM micrographs of powder a) unmilled Fe, b) unmilled Al, c) milled for 10 h, d) milled for 20 h

Table 4.13 EDS compositional analysis

Ball milling duration-hr	Elements	KeV	Mass %	Counts	Atomic % compound
01 h	**Al**	1.486	99.44	52701.72	99.73
	Fe	6.398	0.56	94.71	0.27
10 h	**Al**	1.486	3.01	1036.91	6.04
	Fe	6.398	96.99	10732.94	93.96
20 h	**Al**	1.486	12.15	4424.38	22
	Fe	6.398	87.85	10276.73	78
40 h	**Al**	1.486	16.99	3327.80	30
	Fe	6.398	83.01	5222.59	70
50 h	**Al**	1.486	31.57	9116.85	49
	Fe	6.398	68.43	6348.30	51
65 h	**Al**	1.486	33.08	7595.85	**51**
	Fe	6.398	66.92	4937.26	**49**

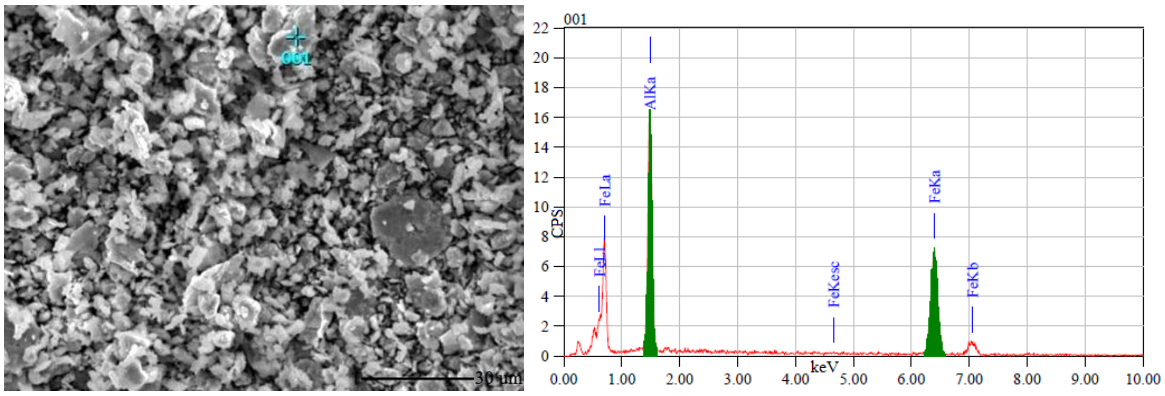

Fig 4.11 Spot SEM-EDS image and spectra of powder ball milled for 65 h

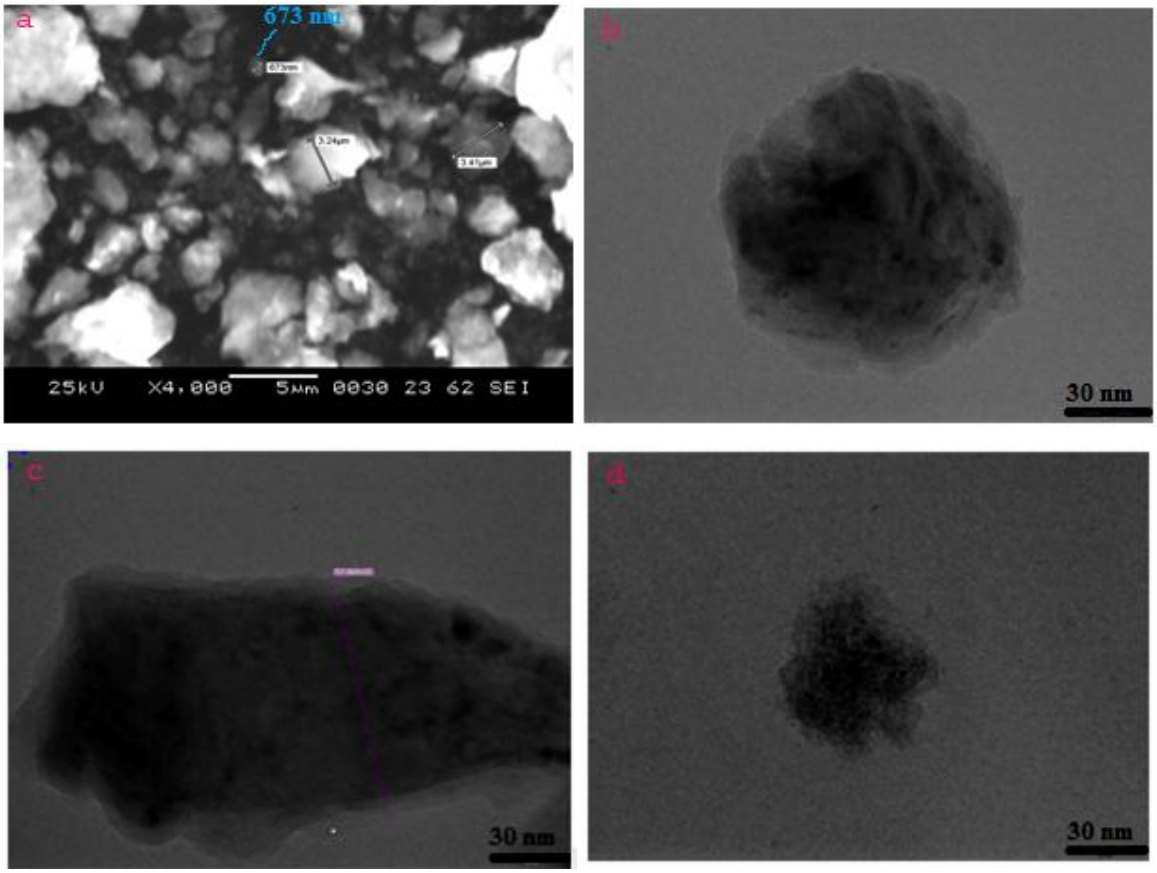

Figure 4.12 a) SEM/TEM micrographs of powder a) milled for 24 h. b) milled at 40 h. c) milled at 50 h. d) milled at 65 h.

4.2.7 Consolidation and deformation of annealed compacts

Elemental powders of Al and Fe with an initial composition of 50 atomic % each which was mechanically alloyed by ball milling time of 185 hours in a tungsten carbide (WC) milling media (MM) as reported in section 4.2. Such a mechanically alloyed powder possesses amorphous structure as characterised by XRD in section 4.2.1. Further, the mechanically alloyed amorphous

powder is cold compacted in a cylindrical die using uniaxial pressure as reported in section 3.2.2.2. The cylindrical compacts are further sintered and annealed in an evacuated furnace; annealed compacts are then deformed by a series of compressive stresses as reported in experimental section 3.2.2.2.1.

4.2.7.1 XRD analysis of annealed and deformed compacts

XRD profile of annealed compact and also profiles of annealed compacts plastically deformed (compressed) upto 0.5, 3, and 8 GPa are shown in Fig. 4.13 and 4.14. The annealed compact exhibits an XRD spectrum consisting of ordered BCC FeAl structure, observe the bcc fundamental (200, 211, 220 and 310) and superlattice peaks (100, 111, 210 and 300). Observe the diminishing of superlattice peaks in the XRD patterns for annealed compact deformed in the stress range of 0.5 GPa to 3 GPa and finally vanishing of these peaks for compacts deformed beyond 4 GPa (Refer Fig. 4.13, 4.14, & Table. 4.14). Vanishing of superlattice peaks (h+k+l = odd) indicate a transition to disorder from an ordered structure. For annealed compacts subjected to mild plastic deformation (0.5 to 3 GPa), traces of super lattice peaks (100) are still visible, indicating that a less intense disordering process occurred. Transition metals and alloys that exhibit order to disorder transformation could exist in an intermediate state. Thus the degree of ordering becomes an essential requirement for characterizing such a system, the long range order (LRO) parameter 'S' is determined as explained in section 3.3.1.

Annealed solid compact exhibits a LRO parameter 'S' of 0.70 as indicated in Table. 4.14, the result indicates a highly ordered structure. Whereas, a nearly fully disordered structure is obtained in annealed compact plastically deformed at stresses $\geq$ 4 GPa (LRO = 0.20). However, intermediate states are obtained for annealed compacts plastically deformed at 0.5, 2, and 3 GPa with a LRO parameter of 0.50, 0.40, and 0.30 respectively. Thus, the degree of ordering increases with a decrease in deformation stresses (Morris D. G. et al. 2002).

Broadening of XRD peaks (Fig. 4.13 & 4.14) is observed with increase in compression stress, this is due to crystallite size refinement and an increase in microstrain as indicated in Table 4.14, although the microstrain does not increase appreciably for annealed compacts deformed beyond 3 GPa. Figure 4.14 (8 GPa) shows the X-ray diffraction profile of annealed compact plastically deformed at 8 GPa. The X-ray diffraction profile clearly shows that the deformed compact is amorphous, while traces of crystalline phase existing in the deformed compact is indicated by the presence of only one low intensity broader peak (AlFe, 110).

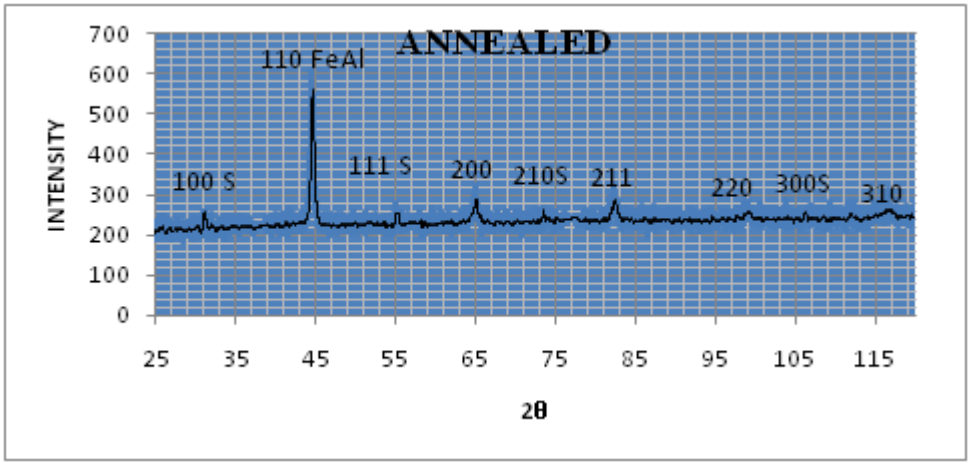

*S-Superlattice reflections are – 100, 111, 210 and 300

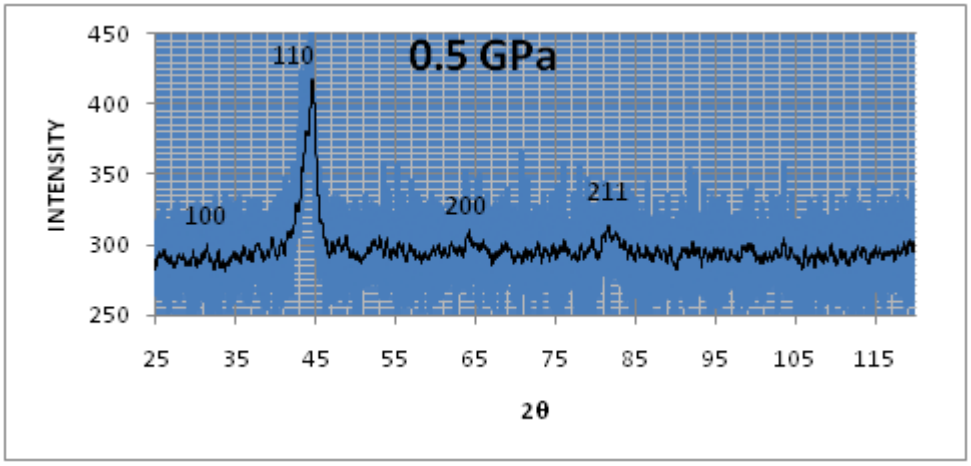

*S-Superlattice reflection is 100

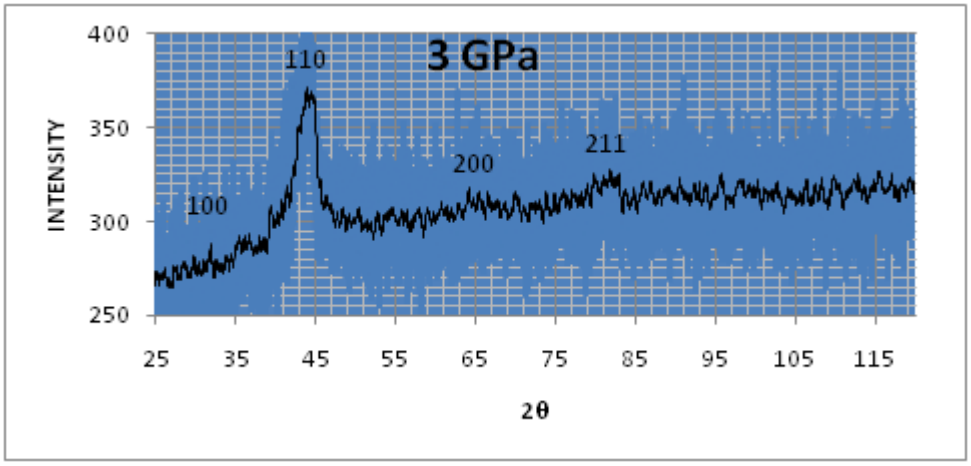

Fig 4.13 XRD profiles of bulk compact a) sintered and annealed, b) compressed at 0.5 GPa, c) compressed at 3 GPa.

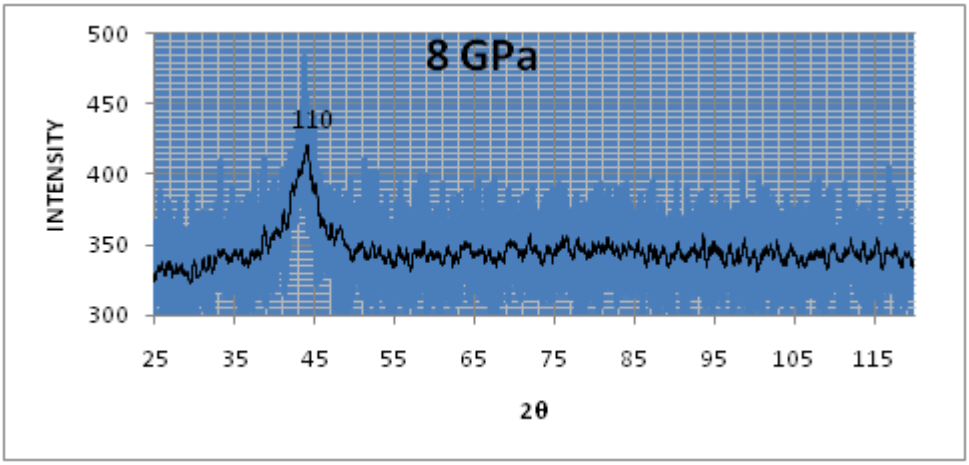

Figure 4.14 XRD profile of annealed bulk compact compressed at 8GPa

The amount of plastic deformation in the annealed compact increases with an increase in compression stress, leading to a decrease in crystallite size and a large increase in microstrain, both tend to stabilise for loads greater than 4 GPa as shown in Table 4.14. Increase in compression stress leads to greater deformation causing the lattice parameter to expand. This phenomenon is clearly evident by the XRD peak shift to lower Bragg angles as the deformation increases. In contrast, the LRO parameter decreases continuously during the low stress region and remains rather constant for higher stress regions (≥ 4 GPa), while the lattice parameter exhibits a continuous increase as shown in Fig. 4.15. However, the crystallite size decreases upto 4 GPa load, beyond which it tends to a marginal decrease, while the lattice parameter increases continuously as shown in Fig. 4.16.

Table.4.14. Structural and magnetic parameters and micro hardness of annealed/deformed compacts

Compression stress (GPa)	Superlattice Peaks	Bragg Angle (2θ) 110 peak	Lattice parameter 'a' nm	LRO 'S'	Crystallite size 'D' nm	Micro strain %	M_S emu/g	H (GPa)
0 (Annealed)	100, 111,210 and 300	44.452	0.28924	0.70	>225	0.2	1.5	2.5
0.5	100	43.22	0.28928	0.50	175	0.8	1.85	2.8
2	100		0.29099	0.40	130	1.3	13.00	4.6
3	100	42.08	0.29176	0.30	110	1.8	24.42	6
4	Nil		0.29231	0.20	98	1.82	66.23	6.9
6	Nil		0.29306	0.22	88	1.8	95.06	7.2
8	Nil	42.8	0.29311	0.21	84	1.86	116.4	7.1

*LRO-long range order parameter 'S', saturation magnetisation-M_S, nano hardness-H

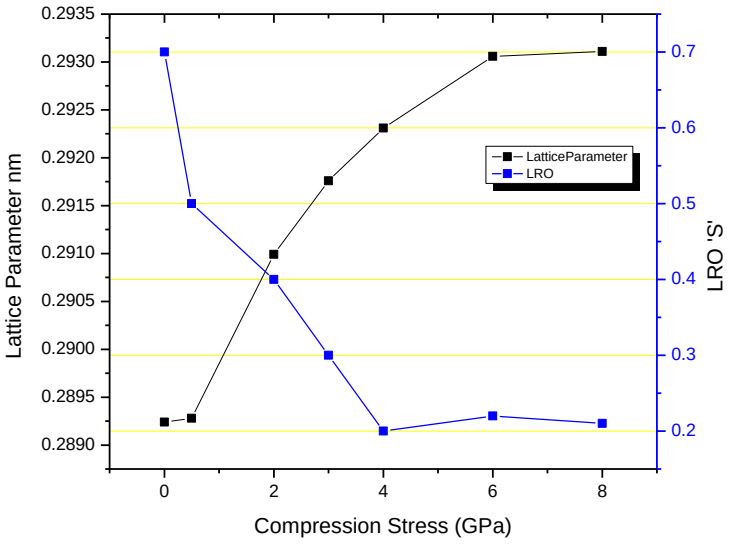

Fig 4.15. Lattice parameter increases continuously with increase in stress while LRO stabilises at stresses ≥ 4 GPa

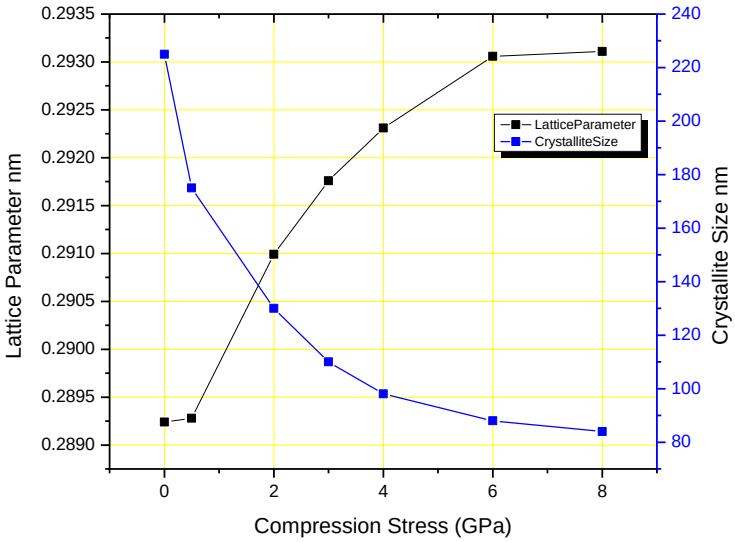

Fig 4.16 Steady decrease of crystallite size up to 4 GPa stress, thereafter it saturates with further increase in stress.

4.2.7.2 Magnetic features of annealed and deformed compacts

Ordered B_2 phase $Fe_{50}Al_{50}$ shows virtually no magnetization at room temperature as reported earlier (Zeng Q and Baker I 2006), such a paramagnetic behaviour (< 2 emu/g) is observed for the annealed sample as indicated in Table. 4.14. Annealed compacts subjected to plastic deformation

through compression stress (2, 4, 6 and 8 GPa) exhibits magnetic hysteresis behaviour as shown in Fig. 4.17. The compact compressed at 0.5 GPa shows no ferromagnetic behaviour (< 2 emu/g), the saturation magnetization (M_S) increases with an increase in compression stress as shown in Fig. 4.18. The increase in M_S during plastic deformation is attributed to the simultaneous increase of both antisite atoms (atoms occupying the wrong atomic site) and lattice expansion (Apinaniz E. et al. 2004). The M_S increase is low during initial stress range (0 to 3 GPa) predominantly because the deformed compact possess varying degree of ordering (LRO of $\geq$ 0.3), while the increase is steep for compact stressed between 3 GPa to 4 GPa, because of transition to complete disorder (LRO $\leq$ 0.2). Anti site atoms are directly related to the long range order (LRO) parameter, no anti site atoms are present for an ordered structure (LRO > 0.7), while the disordered structure (LRO < 0.2) possesses several anti site atoms. During plastic deformation of bulk compacts, LRO parameter decreases to 0.2 at 4 GPa stress, with further increase in stress there is no appreciable change in LRO as shown in Fig. 4.18. Interestingly, the M_S increase and lattice expansion is continuous with increase in deformation stress as shown in Fig. 4.19. Consequently these results demonstrate the increase in M_S during the plastic deformation to factors like applied stress, LRO parameter and lattice expansion. Thus, during the low stress (< 4 GPa) range, LRO parameter and lattice expansion cause an increase in M_S while during the high stress (> 4 GPa) range, lattice expansion alone has a profound influence on M_S increase. Earlier articles have reported influence of lattice expansion on magnetism for ball milled FeAl alloy system (Nogues J. et al 2006).

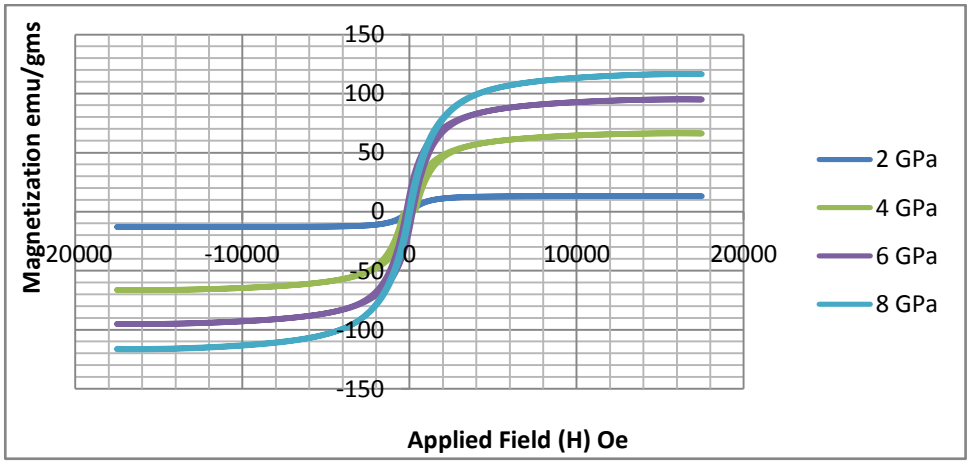

Fig 4.17 Magnetization increases with an increase in deformation, 0.5 GPa deformed (not in pic) compact shows no magnetic behaviour.

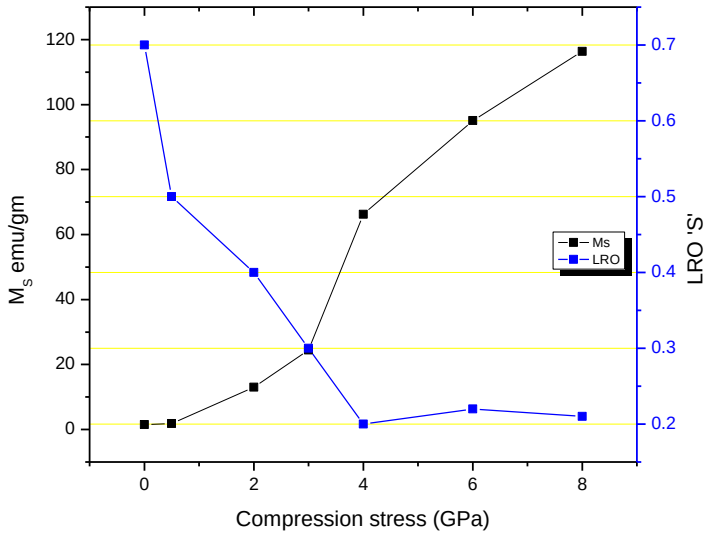

Fig 4.18 M_S increase is low during initial stresses and steep during 3 to 4 GPa and shows a continuous increase.

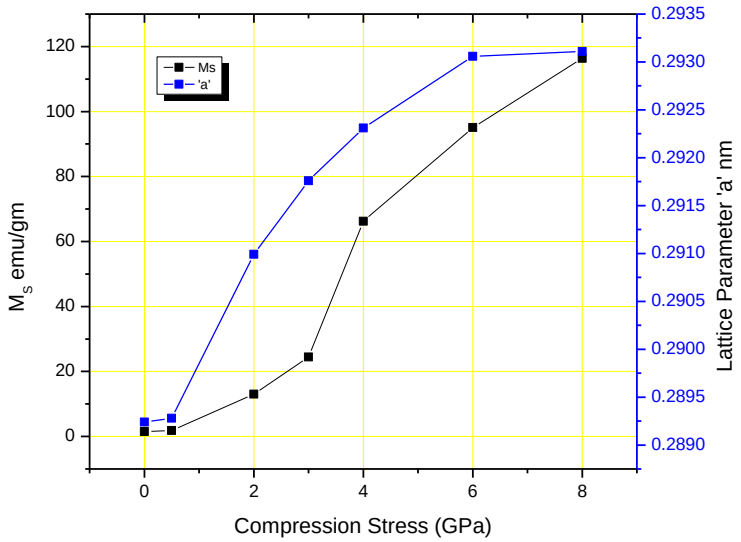

Fig 4.19 variation of M_S and lattice parameter as a function of stress.

4.2.7.3 Nanoindentation analysis of annealed and deformed compacts

Plastic deformation causes simultaneously both a transition to magnetic behaviour (M_S increases continuously as indicated in Fig. 4.20) as well as hardening process, the hardness increases from 2.5 GPa for annealed compact to 7.1 GPa for compact compressed at 8 GPa. Nano hardness increase during plastic deformation is profound during low stress range (< 4 GPa) followed by a

uniform like behaviour as shown in Fig 4.21. Ball milled amorphous Fe ribbons were consolidated by high pressure torsion showed soft magnetic behavior, higher Curie temperature and enhanced nano hardness (Sort J. et al. 2004). Interestingly, a similar behaviour is observed in the variations of LRO parameter and crystallite size during the course of plastic deformation as shown in Figures 4.21 and 4.16. Order to disorder transition during low stress range caused by the increase in the occupancy of atoms in the wrong atomic sites influences the hardening phenomena. Crystallite size refinement leads to an increase in grain boundary area, grain boundaries act as barriers of metal flow during hardness indentation, thus, leading to increased hardness values. Several factors are responsible for nano hardening behaviour in addition to anti sites in the ordered matrix and crystallite size refinement; factors like dislocation and vacancy contribute to a certain extent on the hardening phenomena (Meyers M. A. et al. 2006).

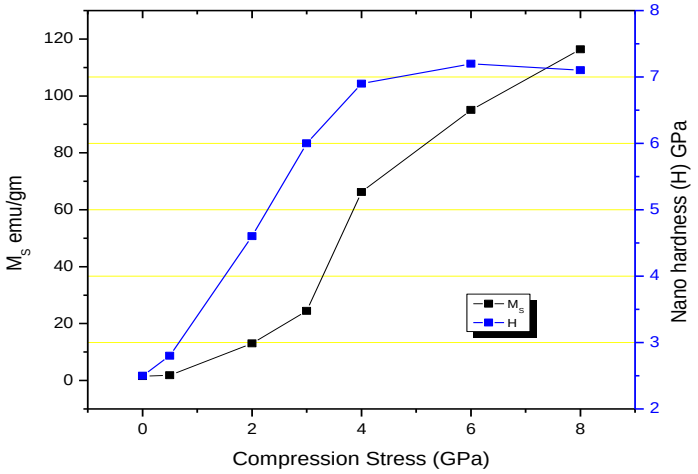

Fig 4.20 Nano hardness and M_S variations as a function of stress.

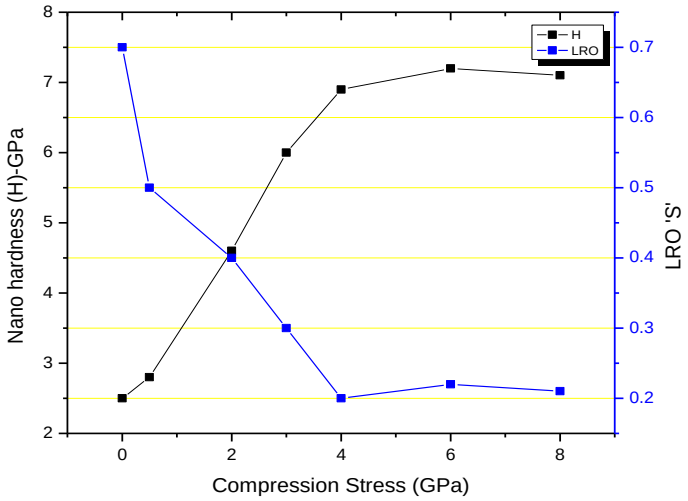

Fig 4.21 Nano hardness and LRO as a function of compression stresses

4.3 XRD of Unmilled Elemental Powders

X-ray diffraction profiles of elemental unmilled powder mixture with an atomic composition of 50 each is shown in Fig 7.20 (appendix) and its structural parameters are listed in Table 4.15. A few peaks of elemental Al and Fe overlap (Fe/Al, 110/200, 200/220, 211/222, 220/400 and 310/420) with each other at identical Bragg angles, it is quite evident from the profile that Al (111) peak has the highest intensity (counts of 1533.32 with an integrated intensity of 161332.4) among all the peaks in the diffractogram. The lattice parameter of unmilled elemental Al and Fe are 0.4048 and 0.2863 nm obtained from 200 and 110 Bragg peaks respectively, while high relative intensity (100%) for 111 Al peak is also observed. All the peaks in the diffractogram are symmetrical and narrow (FWHM=0.3147^0) in shape, the crystallite size obtained from the elemental peak (200/110 (Al/Fe)) at a Bragg angle of 44.7351^0 is 415 nm.

All the peaks in the XRD profile have been precisely matched by the two patterns (No: 03-065-2869 or 03-065-4899) obtained from xpert high score data as shown in Fig 7.21 in appendix. Structural parameters (Table 7.1 in appendix) obtained from these matching patterns are identical with that listed in Table 4.15 for unmilled powder mixture, thus precise indexing and phase identification of the XRD profile for unmilled powder mixture is complete.

From the results and discussions given in this section it is evident that the phases present in the unmilled mixture of powder at pre-mechanical alloying stage are elemental Al and Fe, no strain is induced in the powder and neither any solid solution phase is present.

Table 4.15 XRD Peaks and structural parameters of unmilled (0-hr) mixture of powder

Peak Pos. 2θ	hkl Al/Fe	Height [cts]	FWHM 2θ	d-spacing [Å]	'a' nm Al/Fe	D-nm	Integrated Intensity (II)	Rel. Int (%)	Matched by Ref. Pattern No
38.4883	111 Al	1533.32	0.2914	2.33711	0.4048		161332.4	100.0	03-065-2869
44.7351	200/ **110** Al/**Fe**	799.22	**0.3147**	2.02419	**0.4048/ 0.2863**	**415**	184157.88	52.12	03-065-2869; 03-065-4899
65.1131	220/ 200	374.66	0.3180	1.43143	**0.4050/ 0.2864**			24.43	03-065-2869; 03-065-4899
78.2460	311	360.79	0.3065	1.22078	0.4049			23.53	03-065-2869
82.4377	222/ 211	131.17	0.3289	1.16900	0.4049/ 0.2864			8.55	03-065-2869; 03-065-4899
99.0718	400/ 220	53.15	0.3528	1.01247	0.4052/ 0.2865			3.47	03-065-2869; 03-065-4899
112.0545	331	137.62	0.3730	0.92885	0.4045			8.98	03-065-2869
116.5799	420/ 310	126.11	0.4001	0.90547	0.4047/ 0.2862			8.22	03-065-2869; 03-065-4899

4.4 Ball Milling In Stainless Steel (SS) MM

Milling media material plays an important role in fracture process of individual powder particles and communition and mechanical alloying of pure elemental powder. Elemental powders of Al and Fe with an initial atomic composition of 50 % each is mechanically alloyed by ball milling process using planetary ball mill, the ball milling duration extended upto 400 hours of time. The milling media used was stainless steel balls and jars, while the milling process was performed in an inert gas (argon) envelope as reported in section 3.2.1.1.1. Small quantity of milled powder was taken out of the vial at regular intervals of milling duration for characterization purpose. The following section describes the results of various characterization process followed by analysis and discussions of magnetic properties.

4.4.1 XRD analysis of ball milled powder (SS-MM)

Results of XRD analysis for mechanically alloyed Al and Fe powder by ball milling for different durations of time in stainless steel jar and balls as milling media with argon atmosphere are presented in Tables 4.16 to 4.22. XRD profiles from which analysis was carried out are shown in Fig 7.22 to 7.28 in appendix. Structural characteristics like lattice parameter 'a', crystallite size 'D', full width at half maximum (FWHM) of Bragg peaks, integrated intensity (II), planar spacing 'd', peak height (counts) and identified phases for different duration of ball milling time are listed in the consolidated Table 4.23. Combined XRD profile of unmilled and ball milled powders at different duration of time is shown in Fig. 4.22. Following inferences could be drawn from the values presented in Table 4.23, combined XRD profile in Fig. 4.22 and also from all the figures and tables mentioned in this paragraph.

(i) Compared to XRD profile of unmilled powder, 30 hours ball milled powder profile exhibits broadened overlapped peaks of Al/Fe which shift to lower Bragg angles (44.6528^0 of 200/110 Al/Fe peak) coupled with lattice expansion (0.28676 nm) and increased integrated intensity (185708.72). In addition, intensity (26.49 counts of Al 111 peak) of elemental Al peaks decreases, such changes in structural parameters as a function of ball milling duration is due to the process of alloying by Al diffusion into Fe lattice. Size of the crystallite decreased to 76 nm from over 415 nm; when milled for 30 hours. Thus, peak broadening (FWHM=0.4074^0) is associated with crystallite size refinement coupled with increase in lattice strain to the tune of 0.3 %.

(ii) Increasing the milling duration to 60 hours has yielded following changes:

a) Asymmetry in the shape of overlapped peaks occur which is ascribed to the formation of a new alloy; such a phase is indicated by the emergence of new peaks ($2\theta = 43.7056^0$, 63.5969^0 and 80.3920^0) to the left of overlapped ones ($2\theta = 44.6442^0$, 64.9777^0 and 82.3046^0).

b) These new peaks ($2\theta = 43.7056^0$, 63.5969^0 and 80.3920^0) have been indexed as Al-Fe solid solution peaks and precise Miller indices assigned to each of these peak as 110, 200 and 211 as indicated in Table 4.17. The Bravais lattice of the solid solution has been identified as Bcc consisting of fundamental (h+k+l=even) reflections of mixed/unmixed type. The solid solution has a lattice parameter (0.29266 nm) larger than that of unmilled and ball milled Fe.

c) As in the previous (30 hours) case, lattice expansion of Fe ('a' upto 0.28682 nm) and peak broadening (FWHM=0.5872^0) which is associated with crystallite refinement and increased lattice strain continues to happen during further milling operation.

d) Profile of ball milled powder indicates the presence of elemental Al and Fe in addition to solid solution.

(iii) Increasing the milling duration to 100 hours shows that the solid solution has formed to a large extent with high solute concentration in the solid solution as indicated by the following structural changes analysed from the profile:

a) The Al-Fe solid solution peaks (110) have gained in intensity (228 counts).

b) While shifting of overlapped peaks of Al/Fe (200/110) to lower Bragg angles (44.6248^0) compared to 60 hours milled profile, lattice expansion ('a' upto 0.2869 nm) and peak broadening (FWHM=0.6499^0) continues further. Peak shifting is associated with the process of alloying while; crystallite size further reduces to 24 nm.

c) Lattice expansion of solid solution (0.2927 nm) relates to the production of antisite defects.

(iv) Increasing the milling duration to 150 hours does not bring any change in the metallurgical events, qualitatively. It should be noted that process of formation of solid solution continues at the expense of Al (decrease in height of Al 111, height=9.66 cts) and Fe powders, XRD profile of which shows reduced integrated intensity value of 185873.36. Al (311 and 331) peaks are almost invisible. There is an increase in lattice strain to the tune of 1.5 % but simultaneously accompanying an increase in the crystallite size upto 32 nm in Al-Fe solid solution, whose lattice parameter has marginally decreased to 0.2923 nm. The increase in crystallite size associated with lattice contraction is attributed to co-agulation and grain growth which is the result of high temperature in the milling vial caused by frictional losses. Contrary to expectation, solid solution formed in the milling vial is in non equilibrium condition due to severe plastic deformation of milled materials. Other investigators (Krasnowski M. et al. 2006) have shown that solid solution forms not by

gradual entry of individual atoms of Al in Fe lattice; instead it occurs by rapid formation of small zones of supersaturated Al-Fe solid solution, finally approaching equilibrium level in due course; the ballistic diffusion giving rise to normal diffusion.

(v) Increasing the milling duration to 200 hours has resulted in complete consumption of pure Al and Fe powders giving rise to 100 percent solid solution. Such resulting change in phase is proved by the 110 Al-Fe solid solution peak gaining substantial height (756.82 counts). While, peaks (111, 311 and 331 etc) related to elemental phases are not visible. Solid solution phase is disordered one which could be inferred by the absence of super lattice reflection.

(vi) Increasing the milling duration to 300 hours has brought some unexpected results. Solid solution peak (110) has narrowed (FWHM=1.1594^0) with increased integrated intensity (106517.23) and reduced lattice strain (1.2 %). However, the lattice ('a' upto 0.2933 nm) is noted to be expanded due to disorder while the height has drastically reduced to 204 counts. In addition, very low intensity super lattice peaks have emerged indicating the development of short range order (SRO) in the milled materials; due to migration of vacancies as a result of diffusion of Al in Fe lattice (Zeng Q. and Baker I. 2006 and Mhadhbi M. 2010).

(vii) The grains which have managed to survive the onslaught of mechanical energy for 300 hours have been refined to the level of just 5 nm when milled for 400 hours. Lattice strain in such crystallites is quite high, reaching upto 2.215 %. An expanded lattice ('a' upto 0.2934 nm), with an increase in the area (106785.99) under the peak associated with peak broadening (FWHM = 2.0498^0) coupled with peak shift to lower Bragg angle (43.5762^0) and reduced height (192 counts) are clear indication of early trend towards amorphisation (Xiaoyin Cheng et al. 2006) of mechanically alloyed powder.

(viii) In addition to Scherrer equation, Hall-Williamson plot (Fig 7.29 in appendix) was constructed to precisely determine crystallite size and lattice strain. All the XRD profiles (Fig. 7.22 to 7.28) of ball milled powders are precisely matched with patterns (reference patterns in Fig. 7.30 to 7.33) obtained from Xpert High Score Plus Software[1] for the purpose of indexing (phase identification and quantification). In addition, structural parameters (Tables 7.2 to 7.7) obtained from the reference patterns are almost identical with those obtained by analyzing XRD profiles of ball milled powder.

[1] Xpert High score plus is a software installed in the Panalytical X-Ray Diffraction equipment, used in the analysis of scanned Profiles. Some of the features the software incorporates are peak profile fitting, background correction, rietveld analysis, pattern matching, Scherrer calculator and to draw hall Williamson plot. In addition, quantification of phases along with crystal structure can be obtained.

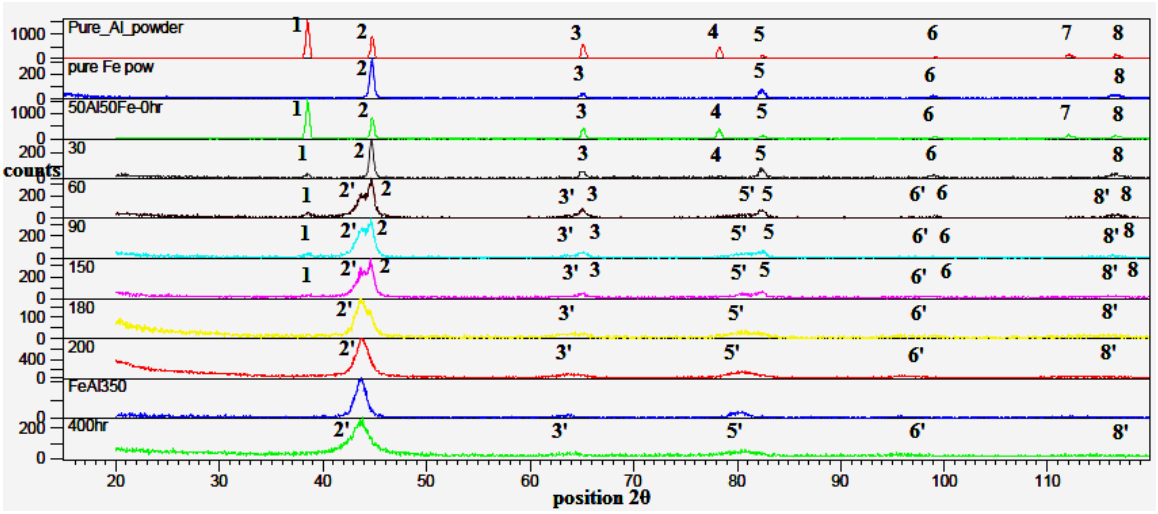

Figure 4.22 XRD profile of unmilled and ball milled powders: **Pure Al**, peak **1** (111 Al), **2** (200), **3** (220), **4** (311), **5** (222), **6** (400) and **7** (331) and **8** (420). **Pure Fe** peak **2** (110), **3** (200), **5** (211), **6** (220), **8** (310). **50Al50Fe-0hr** peak **1** (111 Al), **2** (110/200 Fe/Al), **3** (200/220 Fe/Al), **4** (311 Al), **5** (211/222 Fe/Al), **6** (220/400Fe/Al), **7** (331Al) and **8** (310/420 Fe/Al). **60** Peak **1** (111 Al), **2'** (110 FeAl), **3'** (200 FeAl), **5'** (211 FeAl), **6' (220FeAl)** and **8' (310FeAl)**

Table 4.16 XRD Peaks of powder ball milled for 30 hours (SS-MM)

Peak Pos. 2θ	hkl	Height [cts]	FWHM 2θ	d-spacing [Å]	'a' nm	'D' nm	II	Rel. Int. [%]	Matching No. Ref. Pattern
38.4569	111Al	26.49	0.4061	2.33895	0.40512		162674.27	9.17	03-065-2869
44.6528	200/**11 0**Al/**Fe**	289.00	**0.4074**	2.02773	**0.40555 / 0.28676**	**75.7**	185708.72	100.0	03-065-4899; 03-065-2869
65.0262	220/20 0Al/Fe	49.87	0.5418	1.43313	**0.40535 / 0.28663**			17.26	03-065-4899; 03-065-2869
78.2683	311Al	9.33	0.6728	1.22049				3.23	03-065-2869
82.3450	222/21 1Al/Fe	59.06	0.5925	1.17008				20.44	03-065-4899; 03-065-2869
98.9211	400/22 0Al/Fe	18.07	0.7735	1.01361				6.25	03-065-4899; 03-065-2869
112.015	331Al			0.92906					
116.398 4	420/31 0Al/Fe	25.71	1.0451	0.90636				8.89	03-065-4899; 03-065-2869

*SS-MM-stainless steel-milling media, II-integrated intensity, a-lattice parameter, D-crystallite size

Table 4.17 XRD Peaks and structural parameters of powder ball milled for 60 hours (SS-MM)

Peak Pos. 2θ	hkl	Height [cts]	FWHM 2θ	d-spacing [Å]	a nm	'D' nm	II	Rel. Int. [%]	Matched by Ref. pattern
38.5105	111 Al	**26.54**	0.5255	2.33582			162158.17	8.38	00-004-0787
43.7056	**110 FeAl**	**180.36**	**1.1648**	2.06945	**0.29266**		105735.71	56.91	03-065-0985
44.6442	200/ 110 Al/Fe	316.90	**0.5872**	2.02810	0.40562/ **0.28682**	**29.3**	185807.5	100.0	03-065-0985; 00-004-0787; 03-065-4899
63.5969	**200 FeAl**	13.13	0.5186	1.46185				4.14	03-065-0985
64.9777	220/200 Al/Fe	55.65	1.0845	1.43409				17.56	00-004-0787; 03-065-4899
80.3920	**211 FeAl**	18.51	2.5471	1.19351				5.84	03-065-0985
82.3046	222/ 211Al /Fe	56.97	0.8397	1.17056				17.98	00-004-0787; 03-065-4899
99.0088	400/ 220Al /Fe	11.40	0.7491	1.01294				3.60	00-004-0787; 03-065-4899
112.1876	331Al	2.25	3.6445	0.92812				0.71	00-004-0787
116.4405	420/ 310Al /Fe	19.35	1.1534	0.90615				6.11	00-004-0787; 03-065-4899

Table 4.18 Peak list and structural parameters of powder ball milled for 100 hours (SS-MM)

Peak Pos. 2θ	hkl	Height (cts)	FWHM 2θ	d-spacing (Å)	'a' nm	'D' nm	Inegrated Intensity (II)	Lattice strain %	Rel. Int. (%)
38.5579	111Al	19.89	0.8837	2.33305	0.4041		161642.07		6.68
43.7028	110AlFe	**228.05**	**1.3168**	2.06958	**0.2927**	**8.4**	105735.71	1.397	76.57
44.6248	200/**110** Al/**Fe**	297.82	**0.6499**	2.02894	0.4058/ **0.2869**	**24**	186037.99		100.0
63.6503	200AlFe	12.97	3.3142	1.46076					4.36
65.0093	220/200 Al/Fe	37.56	0.9547	1.43347					12.61
78.227	311Al			1.22103					
80.5642	211AlFe	26.53	2.5633	1.19140					8.91
82.3039	222/211 Al/Fe	47.93	0.8674	1.17056					16.09
97.0235	220AlFe	14.46	0.3782	1.02831					4.85
98.9834	400/220 Al/Fe	9.55	1.2517	1.01314					3.21
112.6598	331Al	2.54	4.0000	0.92557					0.85
116.2421	420/310 Al/Fe	11.87	2.2841	0.90712					3.99

Table 4.19 Peak list and structural parameters of powder ball milled for 150 hours (SS-MM)

Peak Pos. 2θ	hkl	Height (cts)	FWHM 2θ	d-spacing (Å)	'a' nm	'D' nm	II	Lattice strain %	Matched by
38.4612	111Al	9.66	4.0000	2.33869	0.4049		162571.05		00-004-0787
43.7580	110FeAl	215.31	**1.4179**	2.06710	**0.2923**	**7.6**	**105378.49**	**1.507**	00-004-0787; 03-065-4899; 03-065-6132
44.6258	200/**110** Al/**Fe**	300.70	**0.5600**	2.02889	0.4056/ **0.2868**	**32.3**	185873.36		00-004-0787; 03-065-4899; 03-065-6132
63.991	200FeAl			1.454	0.2908				03-065-6132
64.7911	220/200 Al/Fe	24.23	2.2532	1.43777	0.4064/ 0.2874				00-004-0787; 03-065-4899; 03-065-6132
80.6992	211FeAl	25.20	3.3270	1.18974					00-004-0787; 03-065-4899; 03-065-6132
82.3451	222/211 Al/Fe	52.08	0.5205	1.17008					00-004-0787; 03-065-4899; 03-065-6132
96.9917	220AlFe	5.95	1.3677	1.02856					00-004-0787; 03-065-4899; 03-065-6132
98.9825	400/220	10.68	0.8538	1.01314					00-004-0787; 03-065-4899; 03-065-6132
116.2761	420/310	8.86	2.0987	0.90696					00-004-0787; 03-065-4899; 03-065-6132

Table 4.20 Peak list and structural parameters of powder ball milled for 200 hours (SS-MM)

Peak Pos. 2θ	hkl AlFe	Height (cts)	FWHM 2θ	d-spacing (Å)	'a' nm	'D' nm	II	Micro strain %	Rel. Int. (%)	Matched by Ref Patterns
43.7583	110	756.82	**1.3707**	2.06709	**0.2923**	**8.1**	1053 78.49	1.455	100	03-065-0985
63.8388	200	39.22	3.1648	1.45690	0.2914				5.18	03-065-0985
80.4512	211	98.89	2.1958	1.19278	0.2922				13.0	03-065-0985
96.2578	220	21.36	2.8381	1.03445	0.2925				2.82	03-065-0985
113.153 2	310	11.54	4.0000	0.92293	0.2918				1.52	03-065-0985

Table 4.21 Peak list and structural parameters of powder ball milled for 300 hours (SS-MM)

Peak Pos. 2θ	hkl AlFe	Height (cts)	FWHM 2θ	d-spacing (Å)	'a' nm	'D' nm	II	Lattice strain %	Rel. Int. (%)	Matched by Ref Patterns
43.6096	110	**203.95**	**1.1594**	2.07379	**0.2933**	**10**	106517. 3	1.223	100	03-065-0985
63.5033	200	10.74	2.2079	1.46378	0.2928				5.27	03-065-0985
80.1727	211	24.69	1.8279	1.19623	0.2929				12.1	03-065-0985
95.8961	220	5.88	2.5619	1.03739	0.2933				2.88	03-065-0985
112.706	310	3.22	4.0000	0.92532	0.2925				1.58	03-065-0985

Table 4.22 Peak list and structural parameters of powder ball milled for 400 hours (SS-MM)

Peak Pos. 2θ	hkl AlFe	Height (cts)	FWHM 2θ	d-spacing (Å)	'a'nm	'D' nm	II	Micro strain %	Rel. Int. (%)	Matched by Ref Patterns
43.5762	110	**192.07**	**2.0498**	2.07530	**0.2934**	**4.9**	106785.9	2.215	100	03-065-6132
63.5572	200	9.10	3.2079	1.46267	0.2926				4.74	03-065-6132
80.5095	211	20.51	2.6955	1.19207	0.2919				10.7	03-065-6132
95.4127	220	4.77	0.0478	1.04136					2.48	03-065-6132

Table 4.23 Peak list and structural parameters of powder unmilled and ball milled (SS-MM)

Milling time (Hr)	Peak Position (2θ)	hkl	Ht cts	FWHM (2θ)			'd' spacing (nm)	'a' (nm)	'D' (nm)	Lattice strain %
				PB	IB	β				
0	44.7351	200/110 Al/Fe	799	0.3147	0.294	0.021	0.202479	0.4048/ **0.2863**	> 415	0.12
30	44.6528	200/110 Al/Fe	289	0.4074	0.294	0.113	0.202773	0.4055/ **0.28676**	**76**	0.299
60	**43.7056** 44.6442	**110AlFe** 200/110 Al/Fe	180 316	1.1648 0.5872	0.294	0.871 0.293	0.206945 0.202810	**0.29266** /0.0.405 62/0.**28 682**	9.8 **29.3**	1.226 0.540
100	**43.7028** 44.6248	**110AlFe** 200/110 Al/**Fe**	**228** 297	1.3168 0.6499	0.294	1.023 0.356	0.206958 0.202894	**0.2927/** 0.4058/ **0.2869**	8.4 **24.1**	1.397 0.616
150	**43.7580** 44.6258	**110AlFe** 200/110 Al/Fe	215 300	1.4179 0.5600	0.294	1.124 0.266	0.20671 0.202889	**0.2923/** 0.4056/ 0.2868	7.6 **32.3**	1.507 0.507
200	**43.7583**	110AlFe	756	1.3707	0.294	1.077	0.206709	**0.2923**	8.1	1.455
300	**43.6096**	110AlFe	203	1.1594	0.294	0.865	0.207379	**0.2933**	10.1	1.223
400	**43.5762**	110AlFe	192	2.0498	0.294	1.756	207530	**0.2934**	4.9	2.215

Ht-height, PB-peak broadening, IB-instrument broadening. β=PB-IB=FWHM-full width half maxima

4.4.2 DSC analysis of ball milled powder (SS-MM)

Thermal effects on the powder which are mechanically alloyed (by ball milling) in Ar atmosphere utilizing stainless steel milling vials and balls (MM) is investigated using DSC. The profiles of DSC experiments are presented in Fig.4.23 and also in appendix (Fig 7.34 to 7.37). Following inferences can be drawn from the profiles:

(i) Powder which is ball milled for less than 100 hours of time has shown exothermic peak around the temperature of 380^0 C. This peak could be attributed to the alloying process by the mechanism of diffusion. As cited in the literature (Morris-Munoz M. A. et al. 1999), the temperature range of $380^0 – 450^0$ C is conducive for diffusion of fine layers of Al into Fe.

(ii) Powders which are ball milled for 200 to 400 hours of time have shown exothermic humps in the temperature range of 500 to 700^0 C. It is most probably due to crystallization of amorphous phase which suggests that slight amorphisation had occurred during ball milling. The presence of such amorphous phase in the milled material has been proved by

XRD results (section 4.5.1). Many equilibrium phases would be precipitated when metastable amorphous phases are thermally activated at 500^0 – 700^0 C. They are deciphered to be AlFe and $AlFe_3$ intermetallics. It can be argued that the short range order observed for powder samples milled for 400 hours is in a metastable one and it transforms to stable 'long range order' when heated to 300^0 C. This transition is indicated by an arrow on the DSC profile.

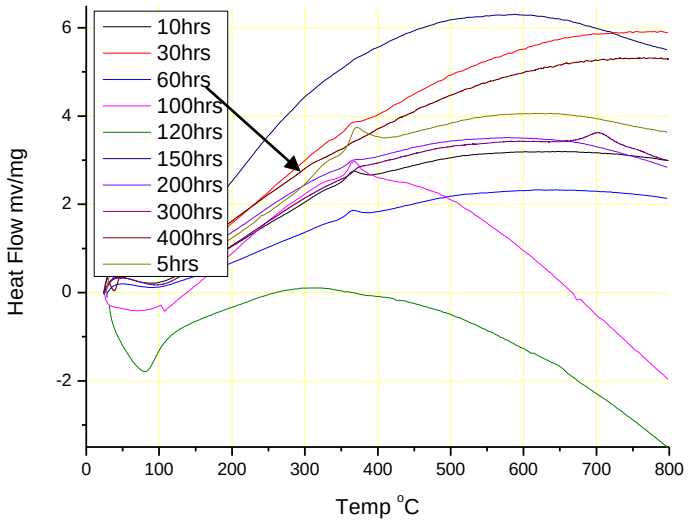

Figure 4.23 DSC curves of elemental powder ball milled for different durations (SS-MM).

4.4.3 Magnetic features of ball milled powder (SS-MM)

The magnetic properties (saturation magnetization Ms, remanent magnetization M_R and coercivity Hc) have been reported for Al_{50}-Fe_{50} system for different milling durations performed at 200 rpm in an argon atmosphere in Fig. 4.24, Table 4.24 and also Fig 7.38 to 7.41 in appendix. Accordingly, the following inferences could be drawn:

1) The M_S is the magnetization required to align all the magnetic domains in a particular direction. It is to be noted that nanosized (D=24 nm in 100-h MAed sample) Fe particulates makes it a lot more difficult to align these domains to obtain high magnetic parameters. Powder sample ball milled for 100 hours shows highest M_S (72.65 emu/g) among all the MA powder samples. This reveals the presence of unalloyed elemental Fe which is consistent with the XRD and DSC results for the MA powder.
2) The magnetization (M) vs applied field (H) curves show typical soft magnetic properties, upto a milling duration of 200 hours, the magnetization decreases with increase in milling duration. Such a magnetic behavior in ball milled powder is similar to the results obtained for Al_{50}-Fe_{50} system ball milled in tungsten carbide and toluene media.

3) The magnetisation increases from 37.91emu/gm for 200 hours milled powder to 67.38 emu/gm at 300 hours of milled powder. Such change in M_S is attributed to larger lattice parameter (0.2933nm) in the 300 hour ball milled powder compared to 200 hour milled powder (lattice parameter is 0.2923 nm). Lattice expansion induced disordering due to ball milling causes ferromagnetism (Hernando A. et al. 1998). The lattice expansion of AlFe leads to the narrowing of its electronic band structure increasing the magnetic moment. An alternative explaination is based on the formation of either antiphase boundaries (APBs) (Wu D. et al. 2004) leading to the formation of Fe–Fe chains which, in turn, create ferromagnetic clusters. Increase in M_S observed in 300 hours milled powder is also due to anti site defects introduced by atomic intermixing. XRD results in section 4.4.1 have confirmed such a disordered Fe (Al) solid solution phase with lattice expansion in the 300 hour ball milled powder.
4) Based on the present results, it is obvious that the magnetization can be modified by crystallite size and lattice parameter. Thus, ball milling introduces vacancies, partial order within the disordered domain (antisite defects) and lattice expansion which contribute significantly to magnetic properties. Past literature has shown that during ball milling, initial deformation induces high dislocation density and APB (Amils X. et al 2000) in Fe-40 Al powders.
5) Powder sample ball milled for 300 hour duration possesses highest H_C (151.64 Oe) among the various powders while the 400 hour milled powder has the least H_C (26.88 Oe). Low value of H_C can be due to low magnetic anisotropy prevailing in the longer duration (400 hour) of milled powder. Although, some effects due to contamination from the milling media and oxidation of Al could be the possible reason for H_C increase (300-h).
6) Almost complete alloying of elemental phases coupled with the formation of SRO could be the possible reasons for low M_S (21.37 emu/gm) in the 400 hour ball milled powder, such magnetic results were obtained and reported in section 4.2.3. XRD result for the sample shows a weak super lattice (100) peak confirming the SRO without much change in the lattice parameter (0.2934 nm) compared to 300 hours of milling duration.

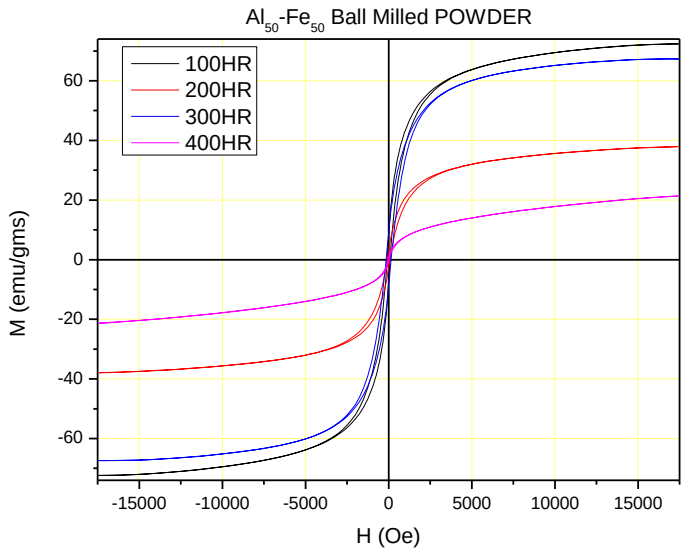

Figure 4.24 Hysteresis loops of elemental powder ball milled (MA) for different hours (SS-MM).

Table 4.24 Room temperature magnetic parameters of MA powders obtained by different ball milling durations (SS-MM)

SAMPLE TYPE	M_S (emu/gm)	M_R (emu/gm)	H_C (Oe)	Weight in gms
50Al 100hrs Powder	72.65	7.813	88.93	0.0634
50Al200hrs Powder	37.91	2.843	77.11	0.0954
50Al300hrs Powder	67.38	9.066	151.64	0.0982
50Al400hrs Powder	21.37	0.9173	26.88	0.0531

M_S-saturation magnetisation, M_R-remanent magnetisation, H_C-coercivity

4.4.4 Thermo magnetic analysis of ball milled powder (SS-MM)

Temperature dependent magnetization curves are shown in Fig. 4.25, following inferences could be drawn from these curves:

1) All the MA powder samples show ferromagnetic properties at room temperature, the amount of this phase decreases notably with increasing temperature. Such results are similar to powder samples ball milled in tungsten carbide and toluene milling media.
2) 100-h mechanically alloyed powder sample shows pronounced ferromagnetic behavior followed by 300-h, 200-h and 400-h MA samples. Magnetization of the MA powder (100-h) decreases at a fairly high rate throughout the temperature range (upto 700 ^{0}C) studied, though; the slope of the curve is steep beyond 380 ^{0}C reaching a paramagnetic phase (< 2 emu/g) at around 675 ^{0}C. Such a steep decrease in ferromagnetism at temperature of 380 ^{0}C and beyond is attributed to the progressive alloying of the elemental phases, DSC

analysis too revealed an exothermic peak at 380 ^{0}C related to the alloying of elemental phases while, the peak at 650 ^{0}C relates to the ordering in the 100-h sample. XRD results have consistently given evidences of phase changes from elemental to solid solution as a function of ball milling time.

3) The decrease in ferromagnetism (200-h and 300-h) with increase in temperature is not as steep as the 100-h milled powder, these samples possess disordered Fe (Al) solid solution phase at room temperature. The decrease in these two samples is mainly caused by the transition to an ordered phase with an increase in temperature. DSC exothermic hump at 600 ^{0}C and peak at 700 ^{0}C for 200-h and 300-h powder samples respectively are due to complete ordering (paramagnetic phase).
4) The proportion of disordered clusters determining the ferromagnetic properties of the solid solution decreased at a milling duration of 400-hours due to the formation of SRO as discussed in the previous section. Thus, 400 hour ball milled powder shows the least magnetization at room temperature. The paramagnetic (<2 emu/g) phase observed at a temperature range of 250 ^{0} to 300 ^{0}C in the 400-h sample is attributed to the transformation to ordered phase from SRO that existed at room temperature.
5) Lattice expansion leads to disorder resulting in the samples exhibiting higher magnetic properties. The ordering of various ball milled powders at elevated temperature is shown by DSC results while, lattice expansion, transition from disorder to SRO are observed in the XRD results. Thus, VSM, DSC, XRD, SEM and TEM results concur with each other.

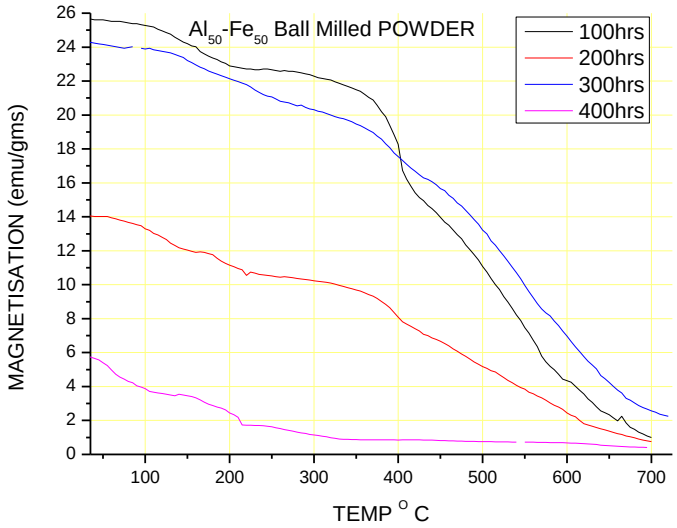

Figure 4.25 variation of magnetisation with temperature of ball milled powders (SS-MM)

4.4.5 TEM analysis of ball milled powder (SS-MM)

TEM images of powder particles ball milled for 400 hours are presented in Figs 4.26 and 4.27. The perspective obtained by the features of these images corroborate the inferences arrived at by other characterization techniques. Following features are clearly visible in TEM images:

(i) Fragments of mechanically alloyed powders due to repeated fracturing and welding during ball milling (Fig. 4.26 (a)): Some of the agglomerated ball milled powder fragments are greater than one μm, while, one of the agglomerated milled powder lump is a collection of nano sized (20 nm) crystalline particles of Fe and Al (Fig 4.26 (b)).

(ii) Amorphisation to certain extent of mechanically alloyed powders: This is evidenced by the featureless contrast in the major portion of TEM image (Fig. 4.26 (b)). The existence of halo continuous rings in the corresponding selected area diffraction pattern (SADP in Fig.4.27 (a)) confirms the same structure. Nevertheless, the presence of minute spots in the rings beside the amorphous halo is attributed to polycrystalline Al-Fe solid solution which possesses a BCC crystal structure. The Bragg peaks (XRD) of solid solution were indexed to have appeared from similar crystallographic planes as that of SADP rings which proves the TEM results.

(iii) The typical morphology (Fig 4.27 b) of the structure observed within an as-milled powder particle in which the size of the nanocrystalline domains appear to be less than 20 nm. The crystallite size obtained by XRD for the same powder sample too showed less than 20 nm as shown in section 4.4.1.

(iv) The presence of separate Al and O peaks in the EDS spectra indicates the composition (AlO) of amorphous region. However, the crystalline region showed the composition of Al-Fe solid solution in the spectra (Al and Fe peaks) presented in Fig 4.27 (c).

(v) Severe plastic deformation of mechanically alloyed powders: the TEM micrograph presented in Fig 4.28 illustrates a number of features associated with severe plastic deformation of particles. Destruction of grain boundaries and ill defined grains is one of the features. Increase in dislocation density, formation of dislocation cells leading to generation of subgrains. It is known that formation of such a low angle grain boundary causes the reduction in lattice strain (observed in powder milled for 300 hours). It is shown that increasing the milling time further (400 hours), will transform the low angle grain boundaries to high angle one by grain rotation, giving rise to nanostructured material (Amils X. et al. 2000).

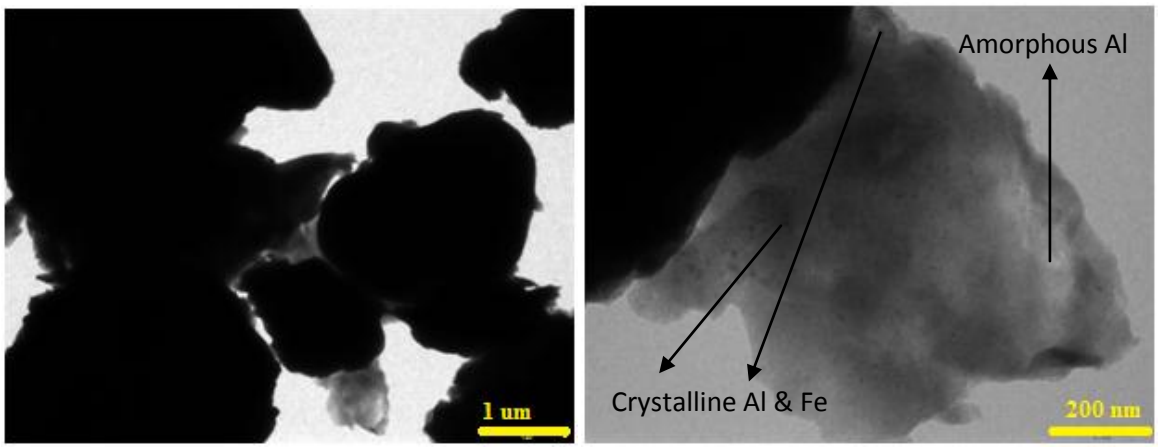

Figure 4.26 TEM images. a) Agglomerated mechanically alloyed powder. b) Partial amorphous phase and nano sized Fe particles are observed.

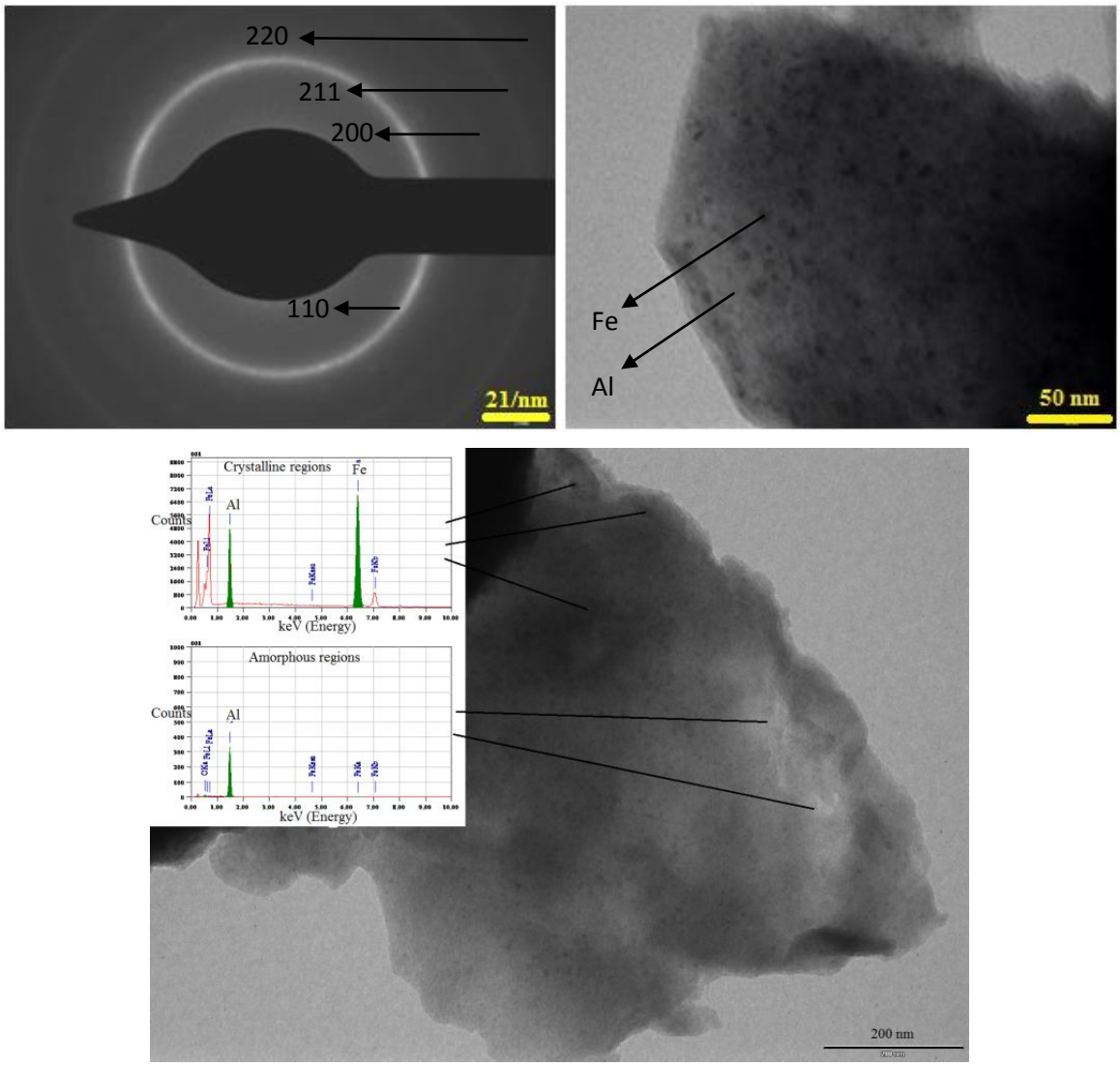

Figure 4.27 a) Morphology of ball milled powder particle. b) Selected area diffraction pattern. c) EDS spectrum of different regions within the ball milled powder sample.

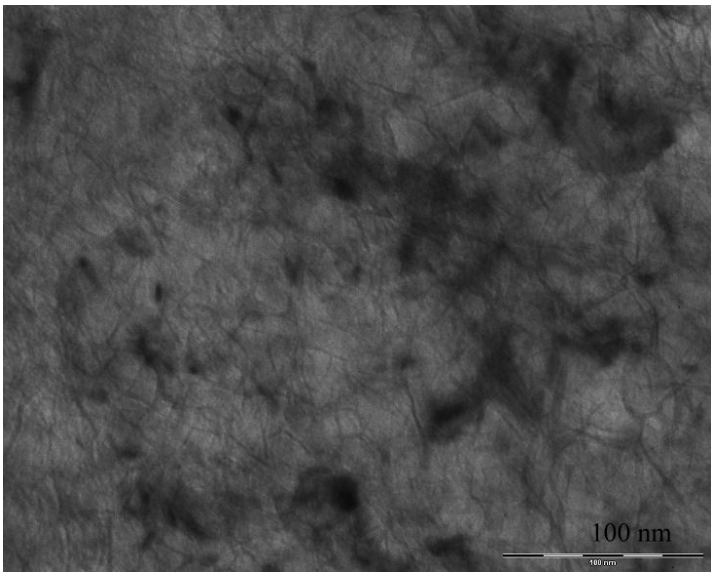

Figure 4.28 TEM image of powder ball milled for 300 hours.

4.4.6 Consolidation by ECAP-BP

Consolidation of mechanically alloyed (ball milled in stainless steel MM) powders (Al_{50}-Fe_{50} system) into bulk, full density pellets preserving nanometric grain size is crucial for possible practical applications of nanophase materials. ECAP-BP processing is a consolidation method which has demonstrated the capability of retaining the ultra fine-grained size synthesized by ball milling of elemental powders. The consolidation process does not result in extensive grain growth, experimental details of the consolidation process has already been reported in section 3.2.2.1. Pellets (Fig. 4.29 'a') synthesized by consolidation of ball milled powder (at different milling duration) are characterized by XRD, DSC, SEM and TEM to investigate phase transformation, structural properties, grain size and morphology. Certain portions of the pellets are hot mounted using polyfast (Fig. 4.29 'b') for metallography and nanoindentation analysis. In addition, texture and magnetic properties of the pellets are investigated by XRD and VSM. Accordingly, the following sections presents the **results** and **discussions** of various investigations performed.

Figure 4.29 ECAP-BP consolidated pellets a) From left to right: pellets synthesised by consolidating powders milled for 400, 300, 200, 180 and 150 hours. b) Portion of the ECAP-BP pellet on a conductive (polyfast) mount.

4.4.6.1 XRD analysis of the pellets

XRD profiles of pellets synthesized by consolidation of mechanically alloyed powders as a function of milling time are shown in Fig. 7.42 to 7.48 in appendix. Structural parameters obtained from these profiles are listed in tables 7.8 to 7.13 in appendix. Using these profiles, a merged XRD profile is generated and presented in Fig 4.30. Table 4.25 to 4.27 presents various structural parameters of ECAPed pellet materials. Thus, important inferences can be drawn from the values presented in the above tables.

Elemental powders ball milled for 100 hours has been consolidated by ECAP-BP process at 150 ^{0}C and shows following features in a pronounced way:

(i) Reflection narrowing: FWHM has gone down to 0.9850 ^{0} compared to 1.3168 ^{0} of unconsolidated milled powder. Peak narrowing is obviously due to increased crystallite size, found to be 12.4 nm which is an increase from 8.4 nm for unconsolidated milled powder. Further, peak narrowing ie, coarsening of crystallite is associated with reduction in lattice strain which measures upto 1.015 % compared to 1.4 % in unconsolidated powder. As a consequence of peak narrowing, the integrated intensity (103810.24) of the pellet was far less than that of unconsolidated milled powder which measures upto 105735.71.

(ii) Lattice contraction: It is revealed by the diffraction peak (110 AlFe) shift to higher (44.0115 ^{0}) Bragg angle with the lattice parameter (a) getting reduced to 0.29073 nm for the pellet material. In contrast, the unconsolidated milled powder whose lattice parameter 'a' was 0.2927 nm (section 4.4.1) for the same diffraction peak emerged at a lower Bragg angle (43.7028 ^{0}).

(iii) Such changes in structural parameters during consolidation initiates transformation of the solid solution into a disordered transition alloy (LRO=0.3 from table 4.26).

Increasing the consolidation temperature from 150 ^{0}C to 300 ^{0}C brings following changes:

(i) Further lattice contraction is observed from a=0.29073 nm to 0.29048 nm.
(ii) Further increasing the level of ordering (LRO being increased to 0.36), transforming the solid solution to disordered transition alloy and
(iii) Appearance of a new phase (AlH_3) as a result of hydrogen contamination is identified. The source of hydrogen could be atmosphere or trace of that gas dissolved in the matrix of Al. Al usually contains a trace of hydrogen, irrespective of its origin of production.

Increasing the consolidation temperature to 450 ^{0}C brings about events like coarsening of crystallite and ordering of solid solution to a certain extent if not fully. Apart from this, the following changes are worth noting:

(i) The crystallite growth is restricted to 13.4 nm, the reason for this is obvious. The consolidation of powders by ECAP-BP is carried out by the application of forward pressure against a preset back pressure of 350 MPa. Such a high compression pressure along with quick heating and cooling (with high rates) is capable of restricting the growth of the crystallites.
(ii) Disorder to partially ordered state; as indicated by the LRO parameter 'S' of 0.45. This suggests that increasing the processing temperature causes transition of fully disordered structure into partially ordered one during consolidation. This proves that the AlFe alloy belongs to the category of transitional alloys.

Increasing the consolidation temperature to 500 ^{0}C yields specific intermetallic phases like AlFe and $AlFe_3$. This fact is supported by the XRD results and LRO parameter 'S' value of 0.68 in this case. Lattice strain and integrated intensity of 110 peak (AlFe phase) of the pellet decreased to 0.952 % and 102613.67 respectively compared to unconsolidated ball milled powder.
Further increase in temperature to 600 ^{0}C, allows to obtain a fully ordered (LRO 'S' of 0.85) AlFe alloy of intermetallic phase.
Further, elemental powders mechanically alloyed by a ball milling duration of 150-h, 180-h, 200-h, 300-h and 400-h have been consolidated by ECAP-BP, with the processing temperature varying from 300 ^{0}C to 500 ^{0}C. These pellets exhibit similar trends as explained above; qualitatively they are same; only the changes would take place at different temperatures of consolidation for specific

duration of ball milling as shown in the table 4.27. However, certain unique structural parameters which are noteworthy of mentioning are as follows:

(i) Pellet obtained by consolidating 400 hour ball milled powder at 500 ^{0}C exhibits an intermetallic phase (AlFe/$AlFe_3$).

(ii) LRO 'S' and lattice parameter are 0.75 and 0.2911/0.58 nm respectively obtained from 110/220 (AlFe/$AlFe_3$) peak. Further, crystallite size at 8.7 nm is the least among the pellets.

(iii) The integrated intensities of the superlattice peak (100=19968.33) and 110 fundamental (104255.78) are highest among the consolidated pellets.

(iv) It is noted that the lattice parameter (0.28995 nm) of the AlFe nanoparticle (300-h pellet) obtained in the present investigation is in good agreement with that of bulk AlFe phase (0.28954 nm) as published in the literature (Pithawalla Y. B. et al. 2001).

(v) Further, it is revealed by XRD analysis that $AlFe_3$ phase possesses DO_3 structure which is ferromagnetic (Zeng Q. and Baker I. 2006).

(vi) Since grain growth is a diffusional process during elevated temperature consolidation, back pressure assisted ECAP decreases the diffusional coefficient thereby restricting the grain boundary mobility (Krasnowski M. Kulik T. J. 2007).

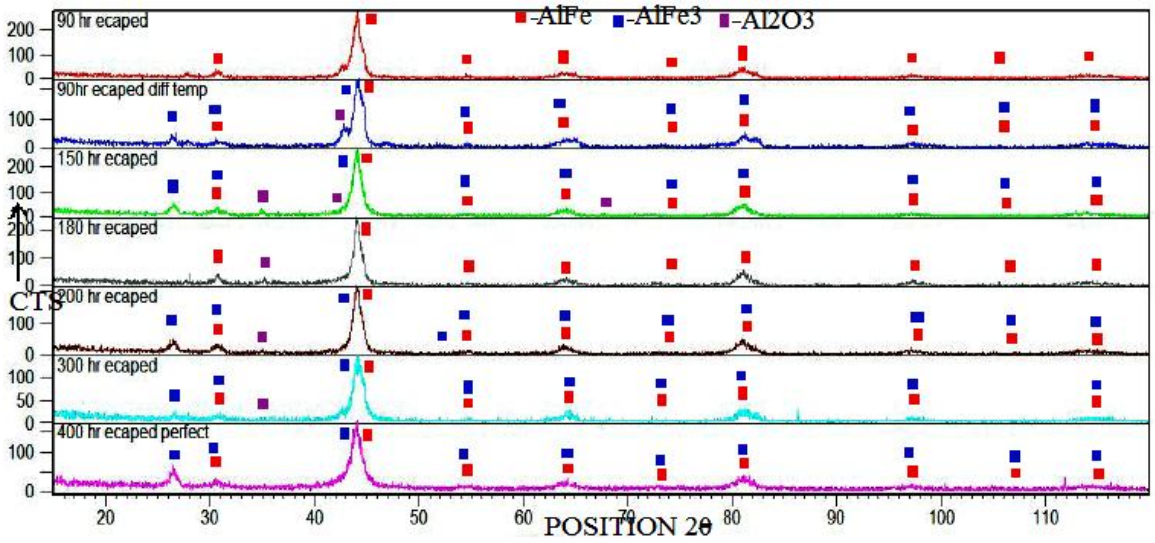

Figure 4.30 combined XRD profiles of ECAP-BP pellets obtained by consolidating mechanically alloyed powders processed at different ball milling durations.

Table 4.25 Structural parameters of ECAP-BP pellet (100-h) processed at 150 ^{0}C

Peak Pos. 2θ	Height (cts)	phase	FWHM 2θ	d-spacing (Å)	'a' nm,	'D' nm	II	Lattice strain%	Matched by Ref. pattern
27.8023	10.38	AlH3	0.4341	3.20627					01-071-2421
30.6953	18.64	AlFe (100)	0.9286	2.91036					03-065-6132
42.5918	41.07	Al_2O_3	0.5140	2.12096					
44.0115	**236.13**	**AlFe (110)**	**0.9850**	**2.05578**	**0.29073**	**12.4**	**103810.24**	**1.015**	03-065-6132
56.9100	1.00	AlFe	0.0900	1.61668					01-071-2421
64.0073	16.10	AlFe	1.9268	1.45347					03-065-6132; 01-071-2421
81.0557	31.24	AlFe	1.7517	1.18541					03-065-6132
97.2441	6.72	AlFe	2.1452	1.02657					03-065-6132
114.4561	6.61	AlFe	3.7597	0.91612					03-065-6132

Table 4.26 LRO and lattice parameter of ECAP-BP pellet (100-h) processed at various temperatures

TEMPERATURE ^{O}C	LRO 'S'	LATTICE PARAMETER 'a' nm (AlFe/**$AlFe_3$**)
150	0.3	0.29073
200	0.32	0.29066
300	0.36	0.29048
400	0.4	0.29022
450	0.45	0.28987
500	0.68	0.2891/ **0.57975**
550	0.79	0.28852
600	0.85	0.2882

Table 4.27 structural parameters of ECAP-BP consolidated pellets

ECAP-BP SAMPLES	Peak Pos.(2θ)	hkl of **S**/F	Phase	'a' nm	'D' nm	Micro strain %	FWHM 'β' (2θ	II of 100S/ **110F**	LRO 'S'
100-h-150^0 C	44.0115	110	AlFe	0.29073	12.4	1.015	0.9850	----	0.3
100-h-450^0 C	44.1482	110/220	AlFe	0.28987	13.4	0.954	0.9340	19702.12	0.45
150-h-500^0 C	30.6583**S** /44.0110	**100**/110/ 220	AlFe/ $AlFe_3$	0.29074/ 0.5815	12	1.041	1.0076	19922.03 /**103845**	0.7
180-h-450^0 C	44.0402	110	AlFe	0.29055	12.7	0.995	0.9684	19825.3	O.5
200-h-500^0 C	30.6622S /44.0416	**100**/110/ 220	AlFe/ $AlFe_3$	0.29054/ 0.5811	12.9	0.985	0.9588	19914.32 /**103721**	0.65
300-h-300^0 C	30.8129S /44.1356	**100**/110/ 220	AlFe	0.28995	9	1.281	1.2257	19601.86 /**102702**	0.4
400-h-500^0 C	30.6177/ 43.9566	**100**/110/ 220	AlFe/ $AlFe_3$	0.2911/ 0.58	8.7	1.351	1.2836	19968.33 /**104255**	0.75

LRO-long range order, II-integrated intensity, D-crystallite size, a-lattice parameter, FWHM-full width half maxima. S-superlattice reflection (100). F-fundamental reflection (110)

4.4.6.2 Optical micrographs (OM) of pellets

Optical photomicrographs of the pellets synthesized by ECAP-BP consolidation process are presented in Figures 4.31 to 4.34. From these photomicrographs following features can be noted:

(i) Significant refinement of compacted particles at the intersection of the two channels during consolidation is evidenced. Elongated particles are visible at the intersection of the two channels whereas equiaxed particles are visible at the entrance of the horizontal channel (Fig 4.31 a).

(ii) Fine particles are present along with comparatively coarse particle. Mechanical alloying by ball milling has resulted in reduction in particle size which are distributed in bimodal form (Fig 4.32 a & b).

(iii) Pores were present and uniformly distributed throughout (Fig 4.33 a). In addition, pores are also visible in the photomicrographs shown in Fig 4.32 (a & b).

(iv) Elongated particles are visible in the longitudinal section of the sample (Fig 4.33 a and b). Mechanical interlocking of the particles are also evidenced in the photomicrographs.

(v) Localized fragmentation and mechanical interlocking of realigned particles cause densification (Fig 4.33 b). There is evidence of alignment of particles with respect to the direction of plastic deformation. Alignment of ductile phase particles, namely Al can be seen. These ductile Al particles help in increasing the density by local accommodation.

(vi) Relative particle motion contributes significantly to early stage packing. The mechanisms for densification involve compression in the vertical channel and subsequently shear deformation in the horizontal channel.

(vii) Further it could be inferred that pellets consolidated at higher temperature (450^0 C) with higher back pressure (480 MPa) possess better density (with almost nil porosity, Fig. 4.34 a) compared to those consolidated at lower temperature (300^0 C) with lower back pressure of 200 MPa (Fig 4.34 b).

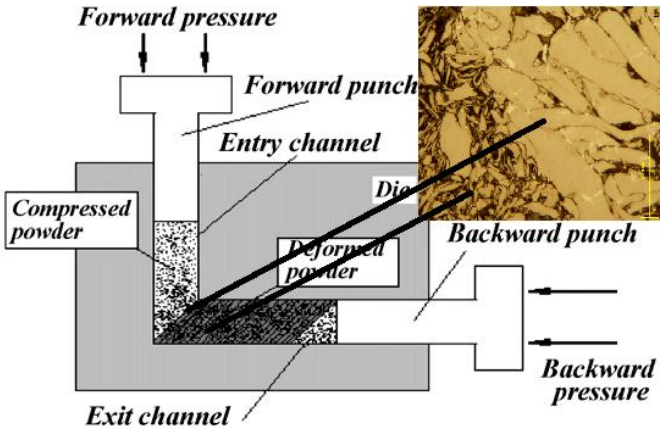

Figure 4.31 particle refinement and densification in the ECAP-BP die

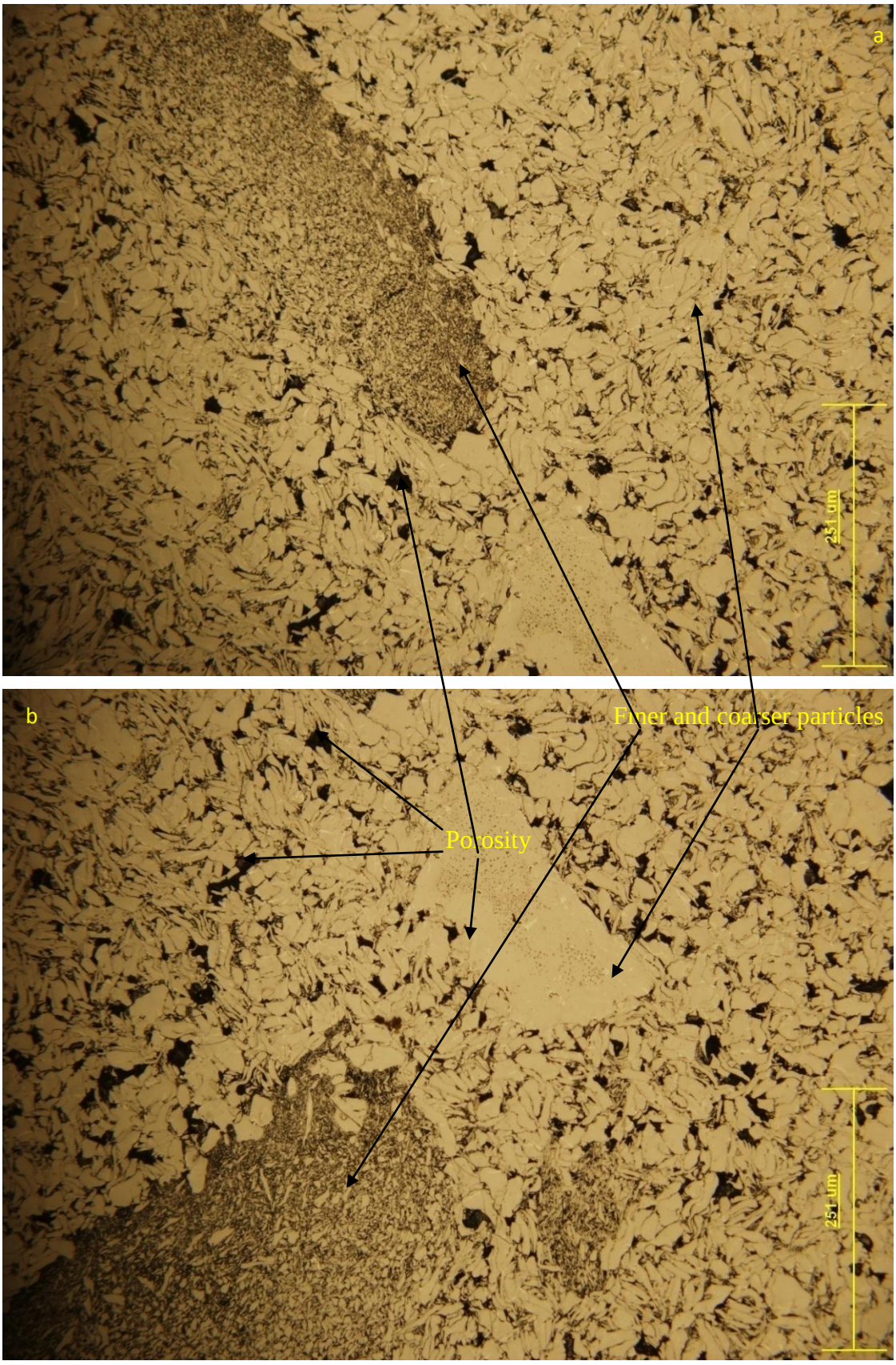

Figure 4.32 a & b) bimodal particle size and porosity distribution in the pellets

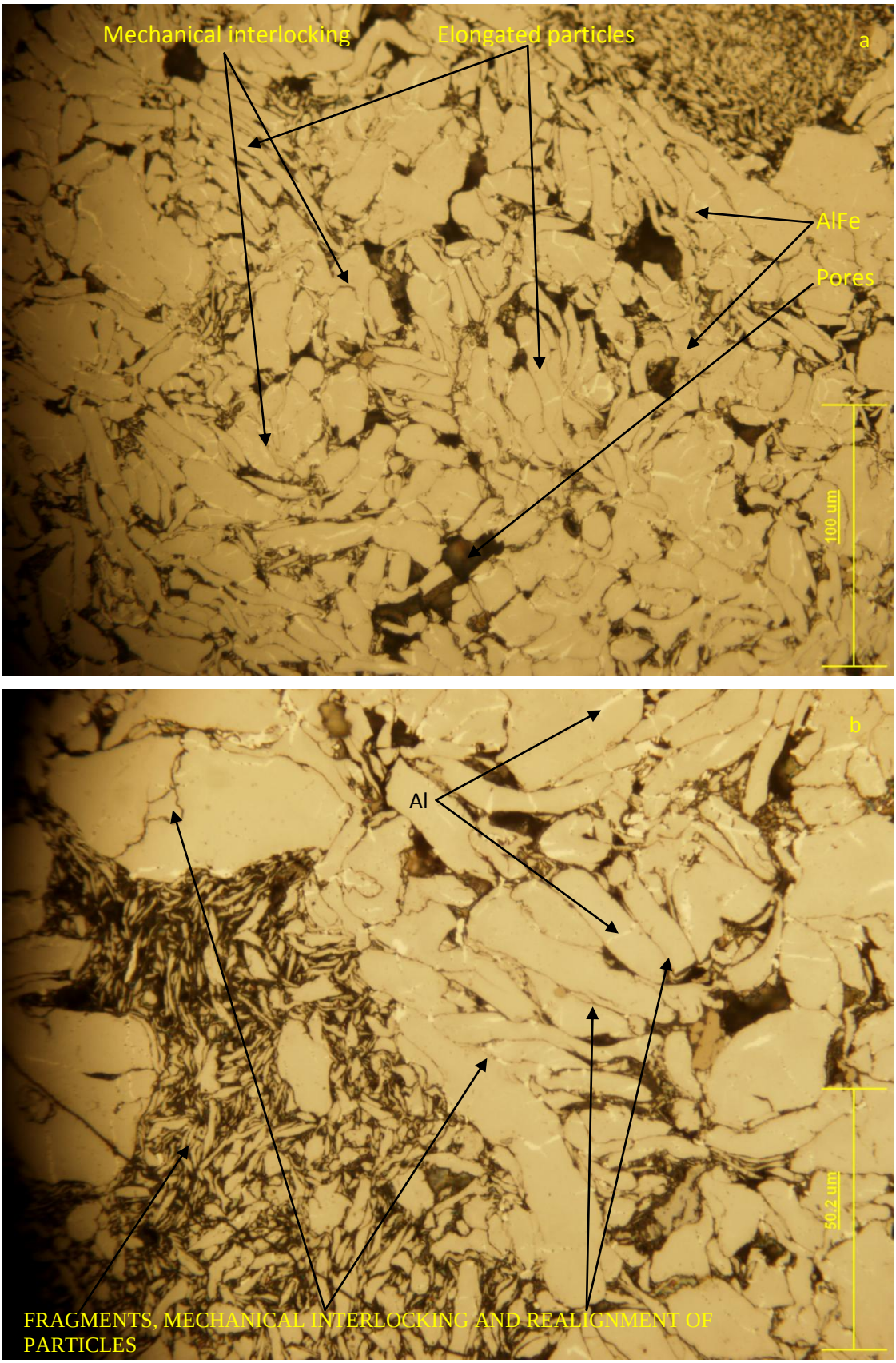

Figure 4.33 a and b) particle elongation, fragmentation, realignment and mechanical interlocking

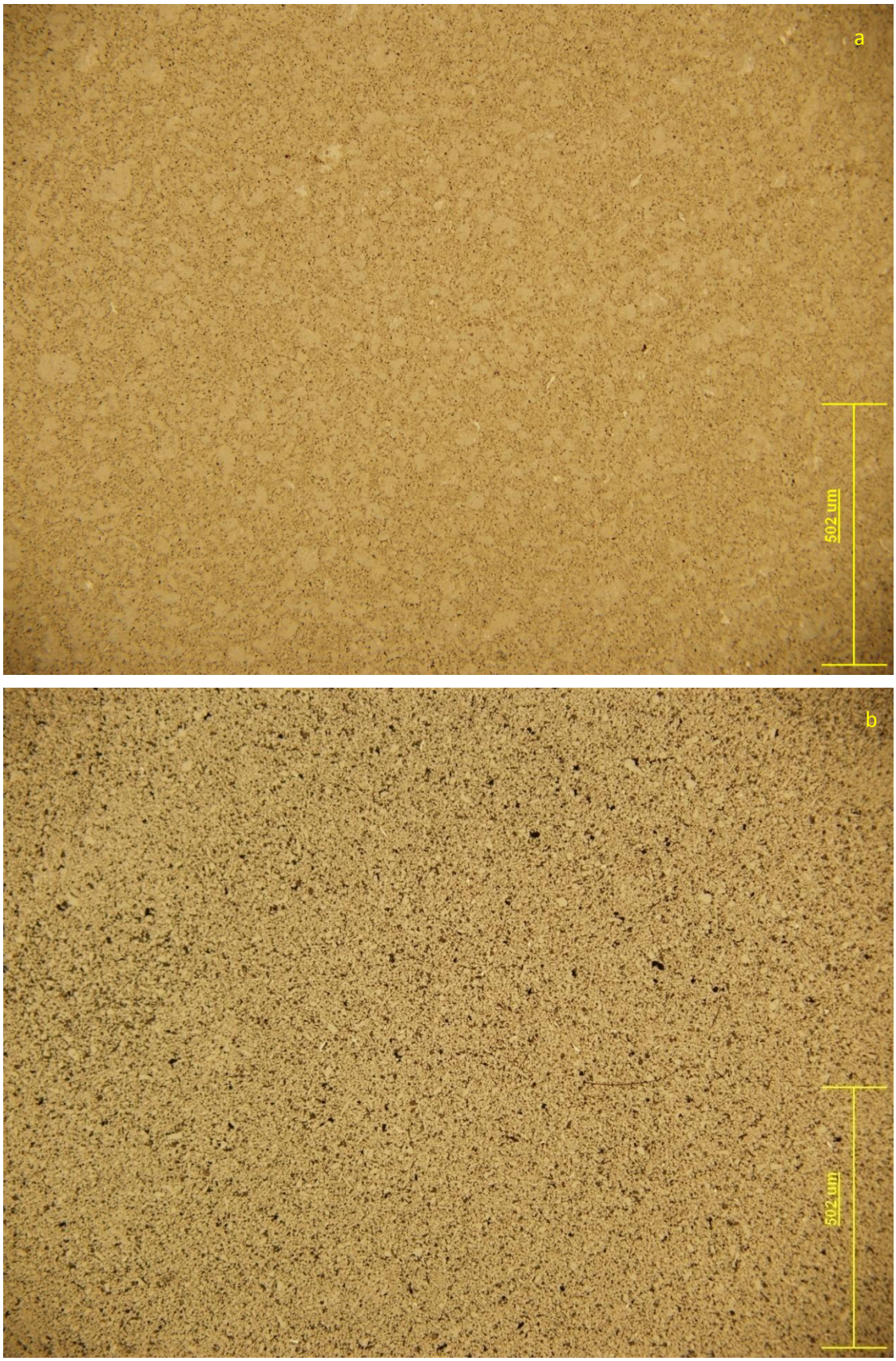

Figure 4.34 OM images of pellets consolidated at a) higher processing temperature and pressure and b) lower processing temperature and pressure

4.4.6.3 FEG-SEM analysis of the pellets

Al-Fe powders which are mechanically alloyed for 200 hours, 300 hours and 400 hours are consolidated into pellets by ECAP-BP process under various conditions are analysed by field emission gun (FEG) SEM and photomicrographs are presented in the figures 4.35 to 4.38. Figure 4.35 shows the micrographs of pellets (200 hours) consolidated at temperature less than 300 ^{0}C and with the back pressure less than 200 MPa. Following features can be noted in the photomicrographs:

(i) The pellet contains intermetallic phases (AlFe/$AlFe_3$). They are plastically deformed along the direction of shear force. It is possible that high amount of deformation can increase the rate of diffusion of atoms quickening the formation of intermetallic phases (Fig 4.35 a).

(ii) Bonding of phases accompanied by annihilation of voids is observed.

(iii) The pellet contains cracks and porosities.

(iv) Typical honeycomb structure is observed in figure (4.35 b and 4.36 a). Reference to such a structure is not found in the literature. It is conceived to be due to the flow of ductile material like Al around hard particles like intermetallics under the hydrodynamic condition of pressure. Second phase particles could have decohesed with surrounding Al matrix when the load was released might have fallen out or etched out giving rise to the appearance of the honeycomb structures.

(v) Typical surface appearance at the centre of a porous pellet is shown in Fig. 4.36 b, nano sized (<100 nm) particles are loosely bonded to each other. Such morphology is due to the insufficient plastic deformation and low densification caused by low compression and temperature.

(vi) Fig. 4.37 a shows the SEM photomicrograph of the pellet (400-h) consolidated with a back pressure of 480 MPa and at 450 ^{0}C temperature. It reveals that quality of the product improves with increasing pressure and temperature of consolidation. Metallurgical events like grain refinement and nucleation of nanopores are noted.

(vii) Fig. 4.37 b shows the photomicrograph of pellet consolidated with a back pressure of 300 MPa and at temperature of 300 ^{0}C using the powder which was mechanically alloyed for 300 hours of ball milling duration. Oxygen contamination triggered by the formation of metallic oxides (Al_2O_3 or Fe_30_4) is seen.

(viii) Metallurgical features like honeycomb structure, nucleation of nanopores, precipitation of second phase particles, plastic deformation and undeformed zones are also observed in photomicrographs (Fig. 4.38 a and b) obtained from pellets (consolidated from powder milled for 300 hours) processed at higher temperature (350 ^{0}C) and back pressure (350 MPa).

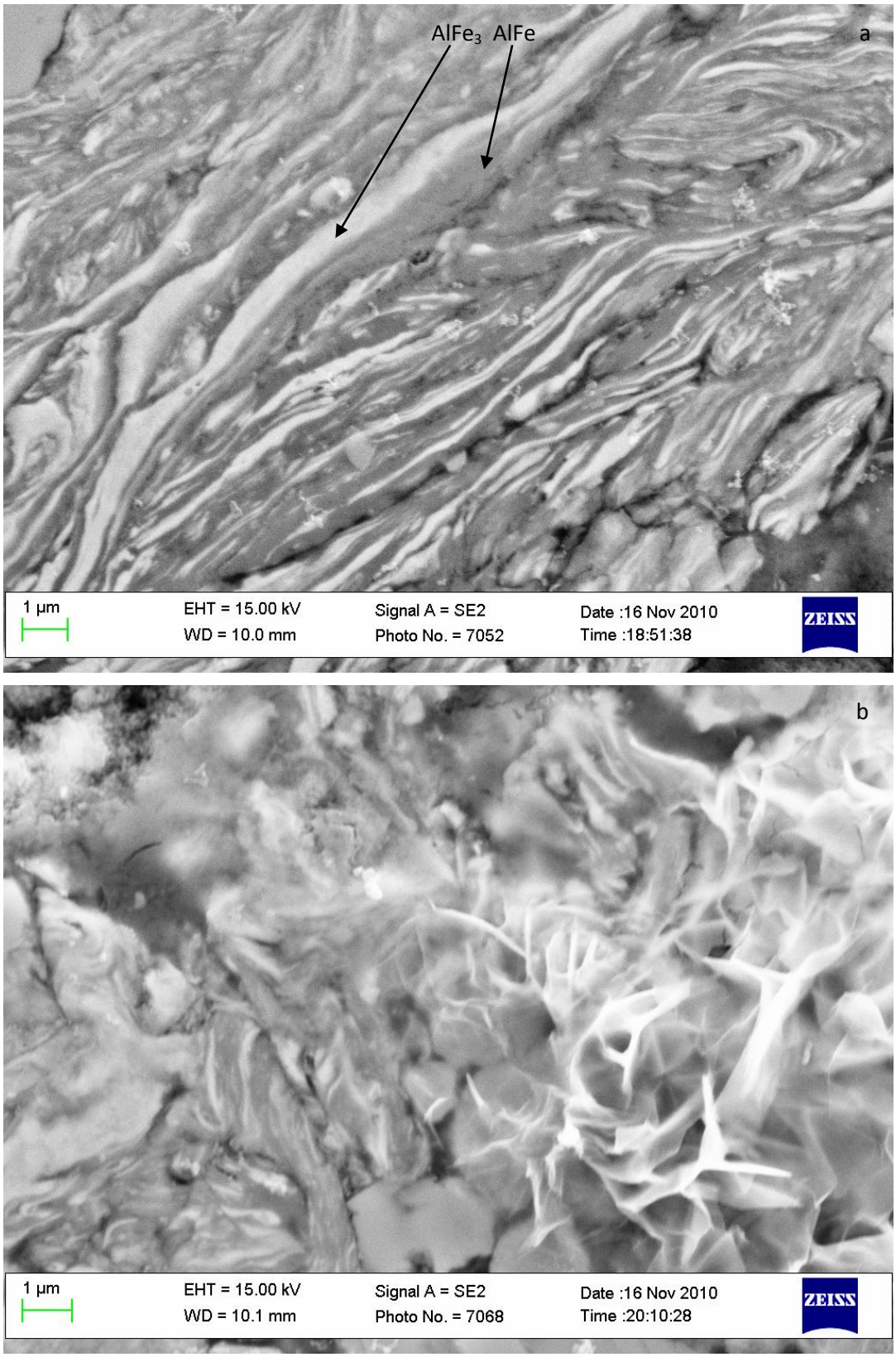

Figure 4.35 a) plastic flow of metal along the deformation direction, 200-h pellet b) cracks and porosity visible

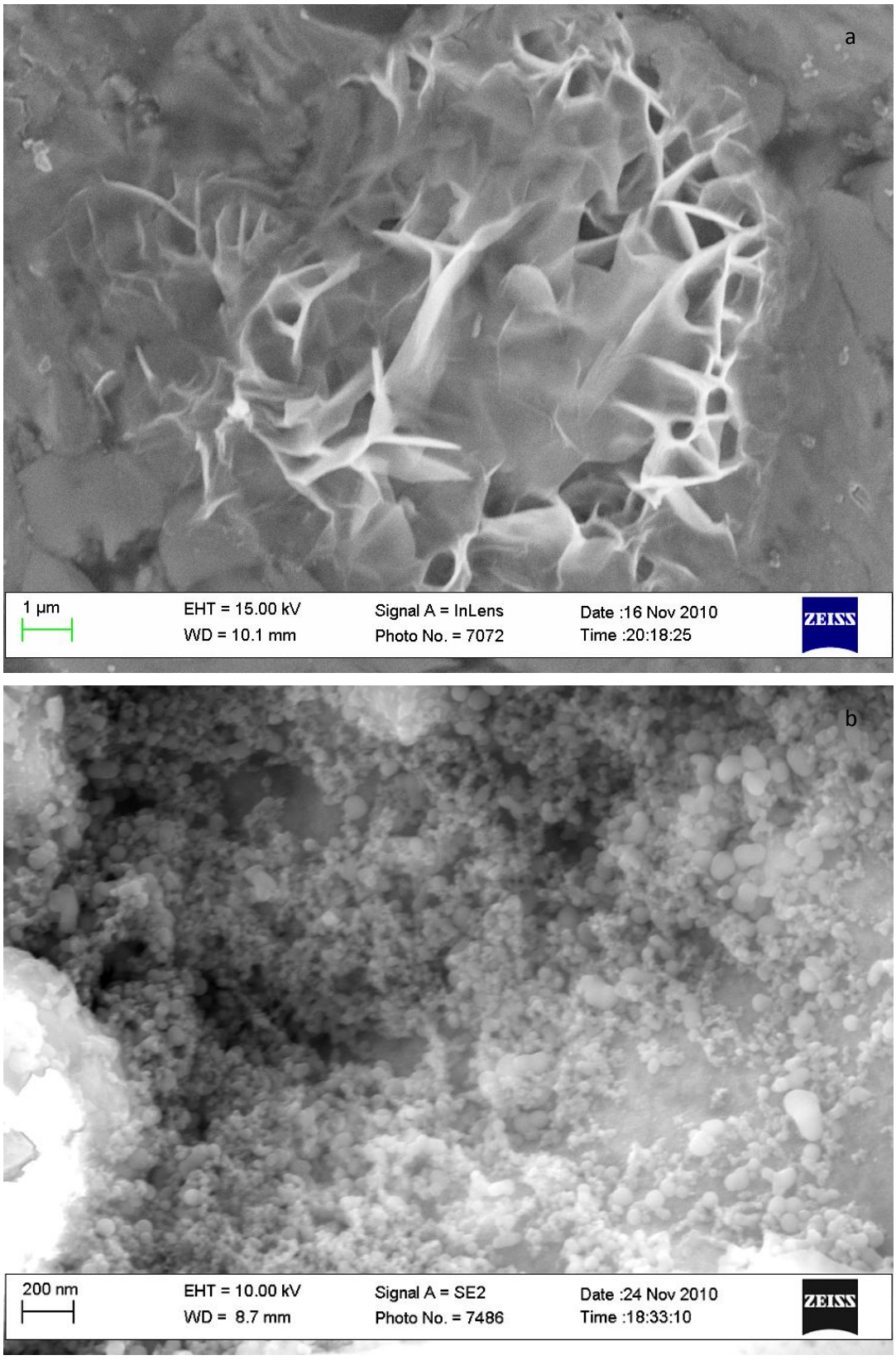

Figure 4.36 a) Interparticle welding into continuous axial wires or fibrous type structures due to plastic metal flow, b) Typical surface appearance of a porous Al-Fe compact

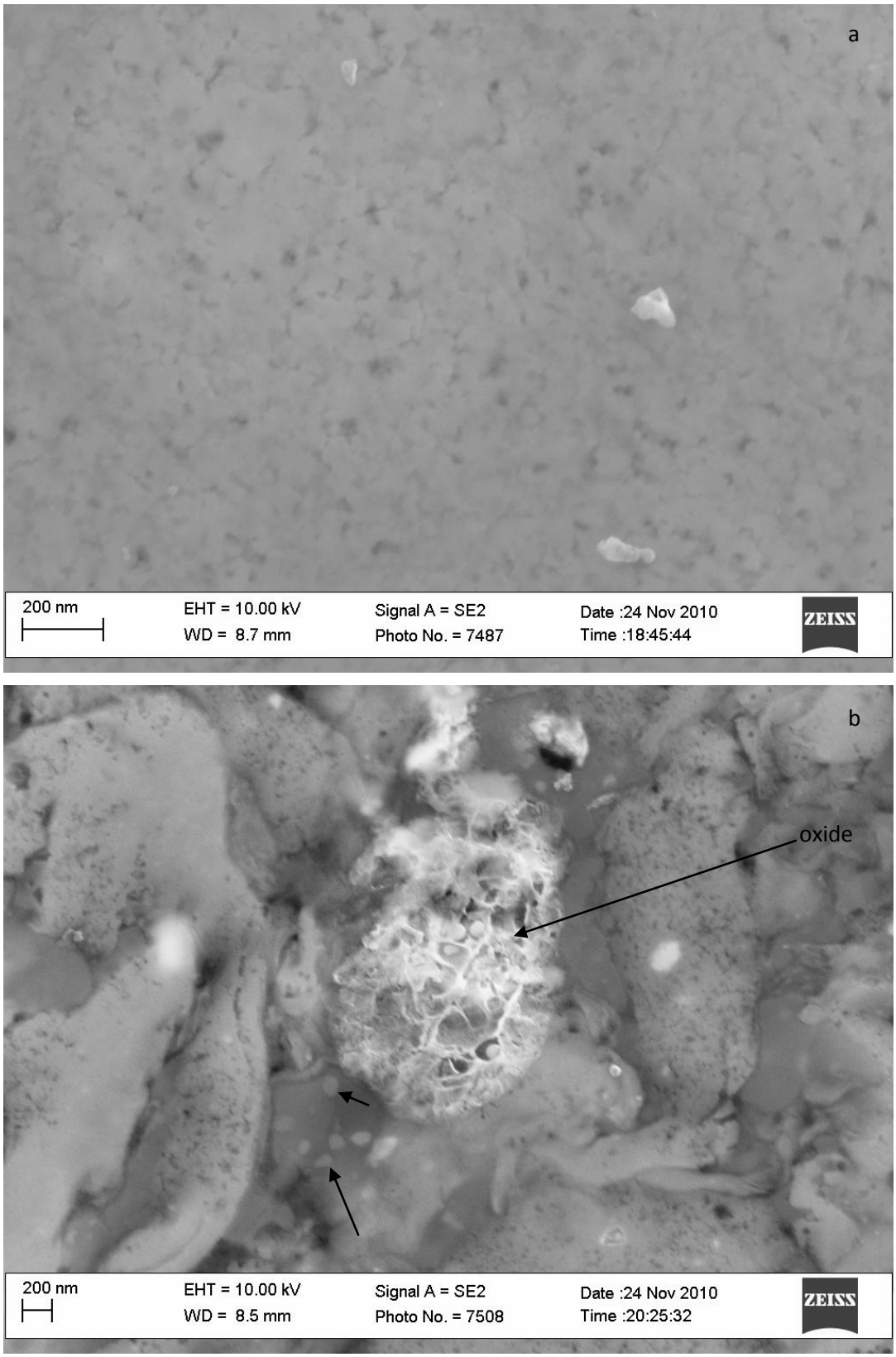

Figure 4.37 a) Nanopores and ultrafine grains are visible, b) Evolution of low angle grain boundaries (indicated by arrows) in addition to nanopores and O_2 contamination are visible

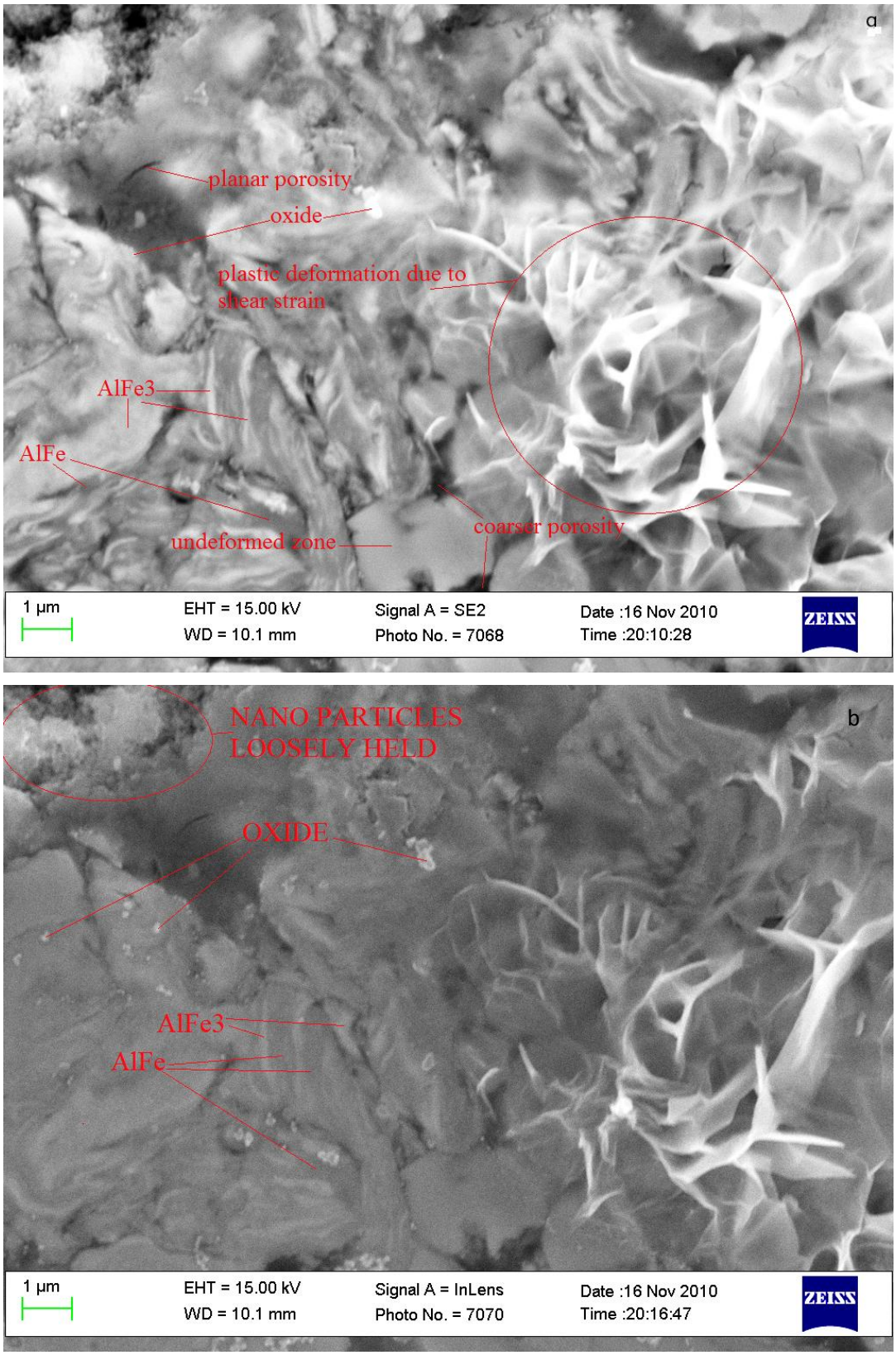

Figure 4.38 a) Fine planar porosities and dispersed coarse porosities are observed in addition to intermetallic phases, undeformed and oxide regions, b) Loosely bonded nano particles are observed.

4.4.6.4 Nanoindentation of the pellets

Using the techniques of nanoindentation mechanical properties of various pellets synthesized by ECAP-BP process using mechanically alloyed powder are analysed. The indentation depth limit is 500 nm with a maximum applied load of 20 mN. Load displacement curves obtained by nano-indentation tests are shown in Fig 4.39 & 4.40. Data obtained by these curves are used to determine two important mechanical properties of the material viz: (i) hardness and (ii) elastic modulus. The variation of these properties with depth of indentation is depicted in Fig 4.41 to 4.43. Analysis of these profiles brings out the following important inferences:

(i) Consolidated pellets synthesized from powder which has been mechanically alloyed for a longer duration of ball milling time possess higher hardness compared to those carried out for shorter duration of time. As the milling time increases the grains becomes finer resulting in the pellets of higher hardness. The presence of intermetallic phase is the reason for difference in the hardness. The higher hardness is mainly attributed to higher level of AlFe/$AlFe_3$ phases which are expected to possess covalent bond to a substantial portion. Hardness of consolidated material (100-h pellet) varies from 3.5 to 9.8 GPa depending on the content of intermetallic phase in the pellet.

(ii) The values of elastic modulus also follow similar trend as hardness. Consolidated powders mechanically alloyed for longer duration registers higher elastic modulus compared to those carried out for lower duration. Elastic modulus of the consolidated products change from 40 to 64 GPa depending on the AlFe/$AlFe_3$ contents, which in turn depends on the duration of mechanical alloying. As in the case of hardness, the nature of bond between the atoms is responsible for change in elastic modulus. Transitional alloy (having LRO $\leq$ 0.3) which consists of metallic bond records lower elastic modulus compared to AlFe/$AlFe_3$ intermetallic phases which consists of predominantly covalent bond apart from metallic bonds.

(iii) Pop in behaviour is observed in the load-displacement curve for one of the pellets; it is presented in Fig 4.40. This behavior is associated with large scale dislocation motion with the onset of plastic deformation. Another reason for such a behavior is the presence of a pore or collapsed vacancies below the advancing indenter.

(iv) Wider (scattered) distribution of nano-indentation profiles (Fig 4.41, 4.42 & 4.43) is due to the fact that the load induced deformation is dominated by the local phase composition rather than the bulk mechanical properties. While, the absence of such a scatter indicate the homogeneous nature of a material.

(v) Hardness and elastic modulus range (2 to 13 GPa and 128 to 248 GPa respectively) are much higher in the 200-h pellet compared to 100-h pellet.

(vi) However, pellets consolidated from powder milled for 400 hours has slightly better range of mechanical properties than 200-h pellet. The range varies from 6 to 20 GPa (hardness) and 130 to 240 GPa (elastic modulus).

(vii) Pellet (100-h) possessing long range disorder (LRO ≤ 0.45) show lower elastic modulus as a result of larger interatomic distance prevailing compared to a crystalline one. Thus, mixture of metallic and covalent bond is responsible for higher elastic modulus in those pellets which possess intermetallic phase (Zhang M. X. et al. 2010).

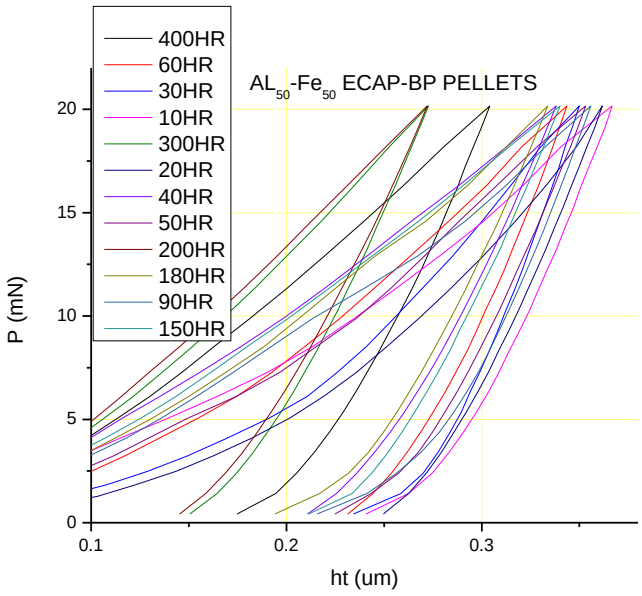

Figure 4.39 Load as a function of penetration depth of various ECAP-BP consolidated pellets

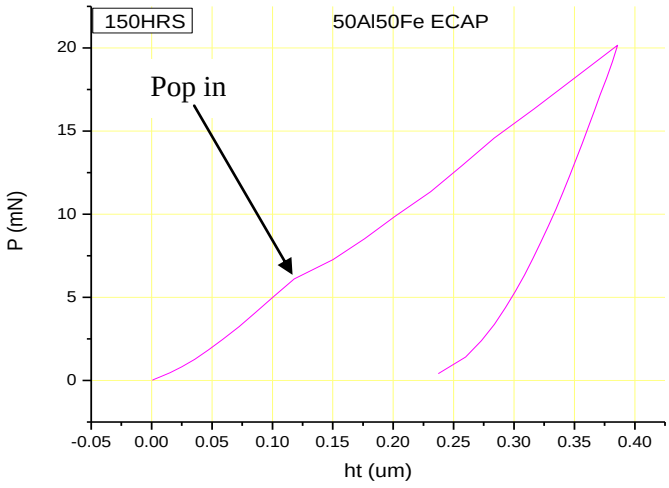

Figure 4.40 Nanoindentation; load vs displacement curve of ECAP-BP consolidated pellet.

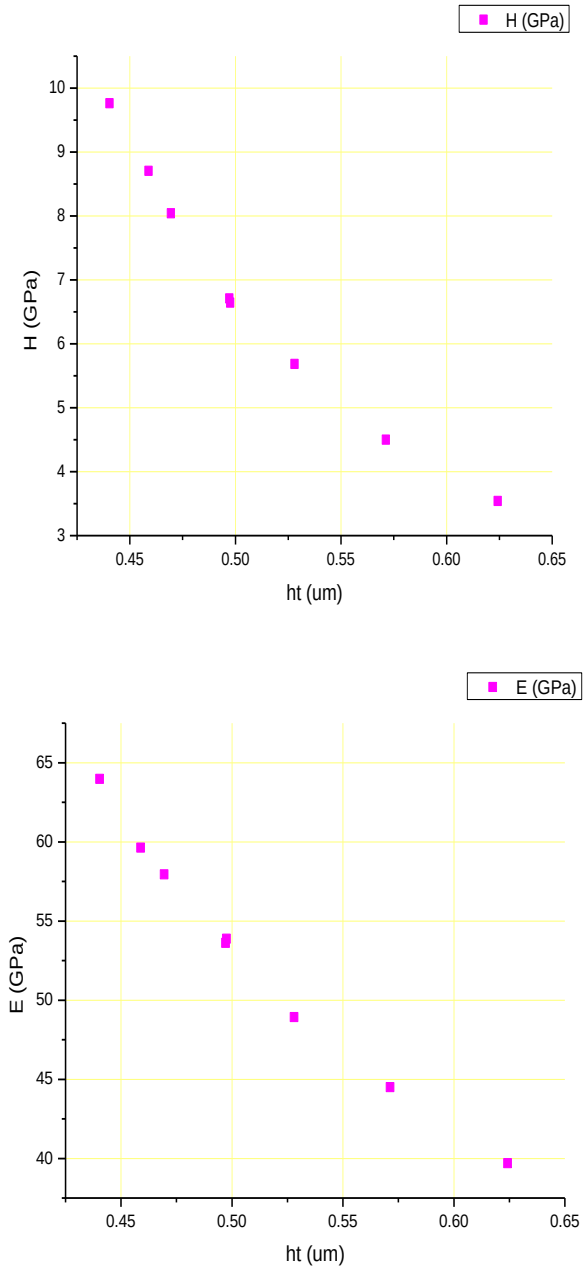

Figure 4.41 Nano hardness and elastic modulus of 100-h ECAP-BP consolidated pellet.

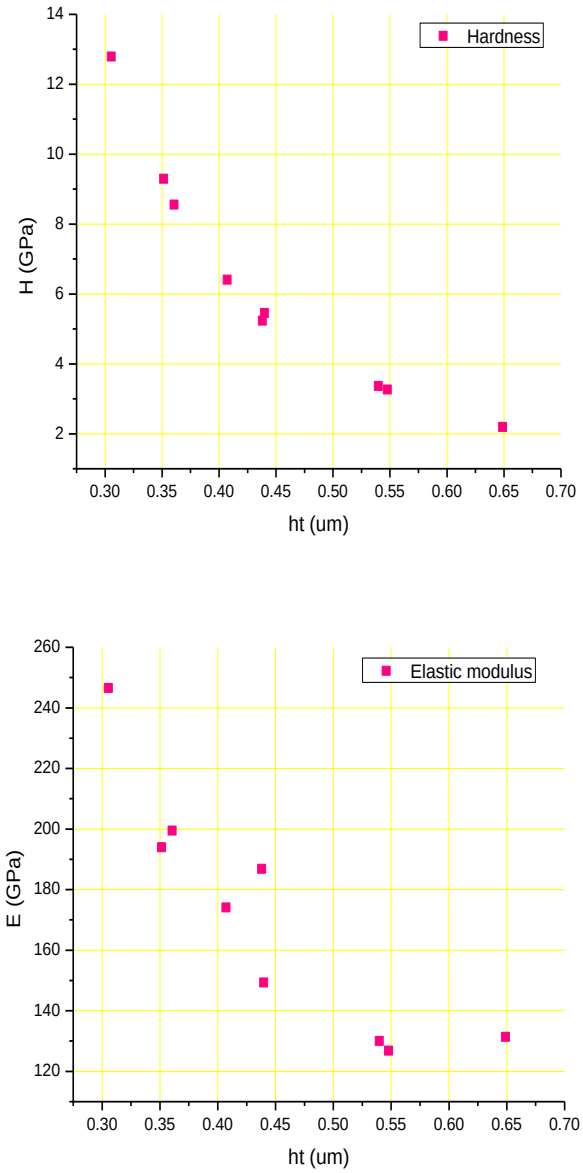

Figure 4.42 Nano hardness and elastic modulus of 200-h ECAP-BP consolidated pellet

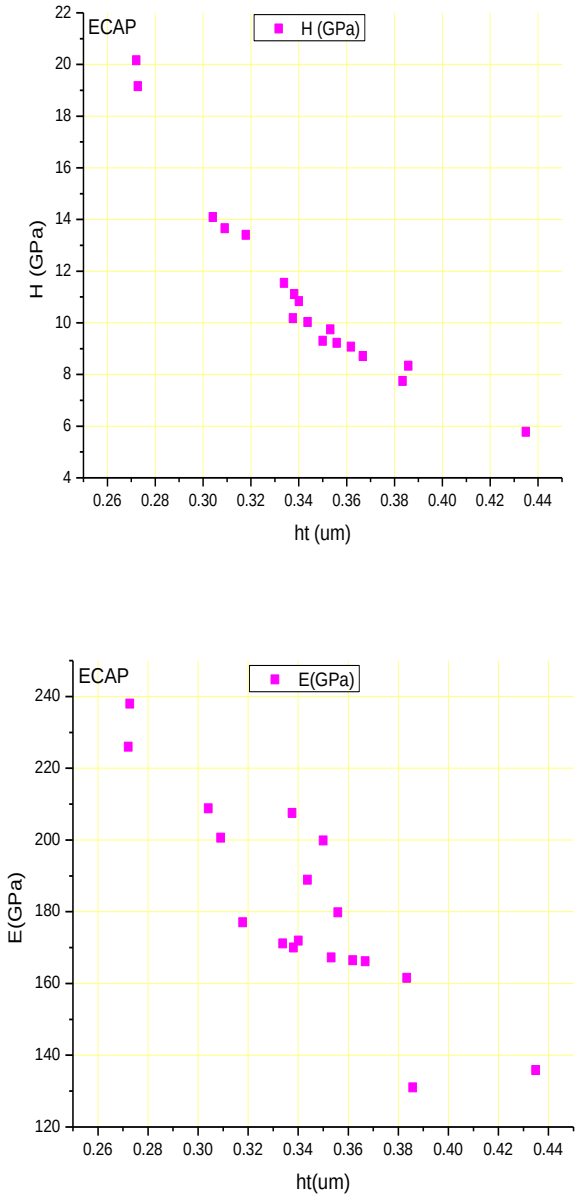

Figure 4.43 Nano hardness and elastic modulus of 400-h ECAP-BP consolidated pellet

4.4.6.5 DSC analysis of the pellets

Thermal effects on the ECAP-BP consolidated pellets are investigated using DSC. The profiles of DSC experiments are presented in Fig.4.44 and 4.45. Following inferences can be drawn from the profiles:

(i) Low temperature exothermic peak at 250 ^{0}C in the DSC curve presented for 100-hour pellet (elemental powders ball milled for 100 hours and consolidated by ECAP-BP) is due to ordering of disordered transitional AlFe alloy. While, a low intensity peak at 380 ^{0}C is due to alloying of elemental phases by diffusion mechanism. Moreover, high temperature peak at 520 ^{0}C could be due to recrystallisation, grain growth and loss of various defects that occurred during milling and subsequent consolidation by ECAP.

(ii) Crystallization trace on the DSC curve is not seen to be prominent as formation of new crystallite phase is not observed during heating in calorimeter. However, DSC curves related to the ECAP-BP pellets of Al_{90}-Fe_{10} system show the visibility of peaks related to the onset of crystallization temperature (Tx) and peak temperature (Tp) of crystallization.

(iii) Pellet consolidated from powder ball milled for 200 hours showed incomplete ordering (LRO=0.65) structure as reported by XRD in section 4.4.6.1. Thus, DSC peaks between 200 ^{0} and 300 ^{0}C is due to transformation of incomplete ordered structure into an ordered intermetallic phase (LRO>0.7) when heated in calorimeter. Similar to the 100-h pellet, high temperature (> 500 ^{0}C) hump is caused by recrystallisation, grain growth and annihilation of defects.

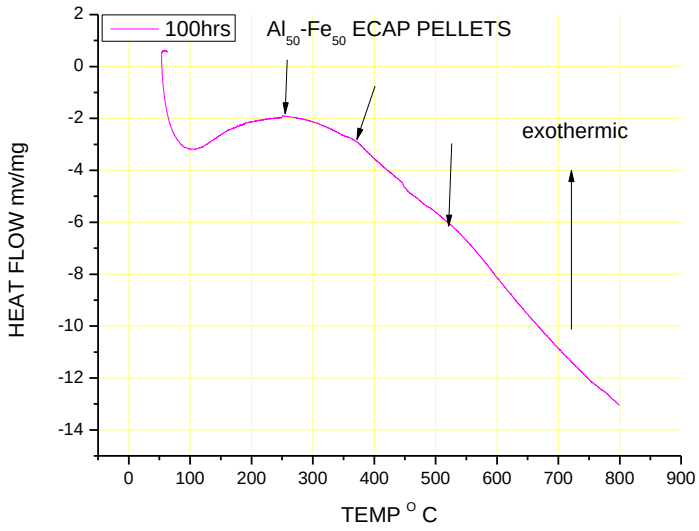

Figure 4.44 DSC curve of heat flow as a function of temperature of ECAP-BP pellet obtained by consolidating powder ball milled for 100 hours

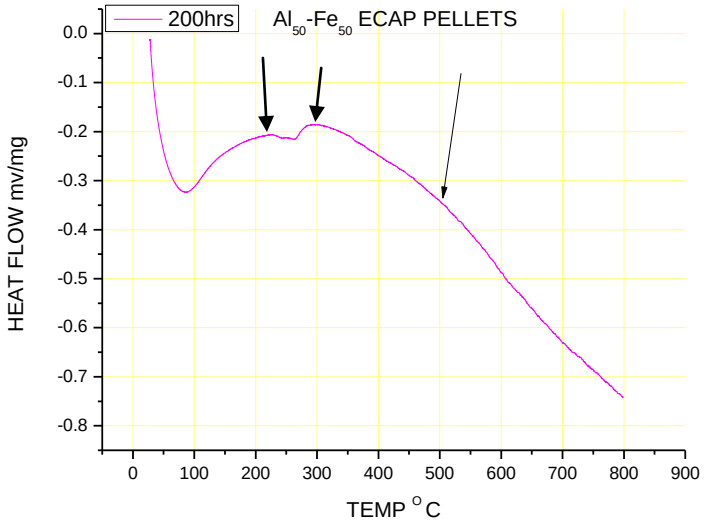

Figure 4.45 DSC curve of heat flow as a function of temperature of ECAP-BP pellet obtained by consolidating powder ball milled for 200 hours of duration.

4.4.6.6 TEM characterization of the pellets

TEM bright field image of pellet consolidated (300 ^{0}C) from powder milled for 300 hours is presented in Fig 4.46. Qualitatively the typical microstructure observed confirms the following inferences:

(i) Porous regions which are heavily deformed and the grains are not clearly defined as seen in Fig 4.46 a.

(ii) While nanocrystalline domain appears to be around 12 nm, thus the mean crystallite size estimated for the pellet using XRD (scherrer equation) and the one observed in TEM are consistent with each other. The microstructure is mainly composed of small crystals from AlFe transition (LRO=0.4) alloy phase.

(iii) By maintaining a low consolidation (ECAP-BP) temperature (300 ^{0}C) and pressure (300 MPa) ensures the potential for achieving finer grain size and inhibition of grain growth. Rapid heating and cooling of die with back pressure suppresses dynamic recrystallisation and reduces mobility of grain boundaries.

(iv) Diffraction rings in the SADP (Fig 4.46 b) relate to nanocrystallites. Moreover, the continous rings indicate the amorphous structure while, the spots refer to crystallinity. Values of d-spacing ('d' hkl) calculated from XRD and the TEM (SADP) rings are compared in Table 4.28. The observed rings corresponds to diffraction from the four most significant planes of the FeAl crystal lattice, i.e. the 110, 200, 211 and 220 planes, thus the results are consistent with the XRD data.

(v) Appearance of amorphous phase could be due to oxide and hydride in addition to disordered AlFe phase (LRO 'S' = 0.4).

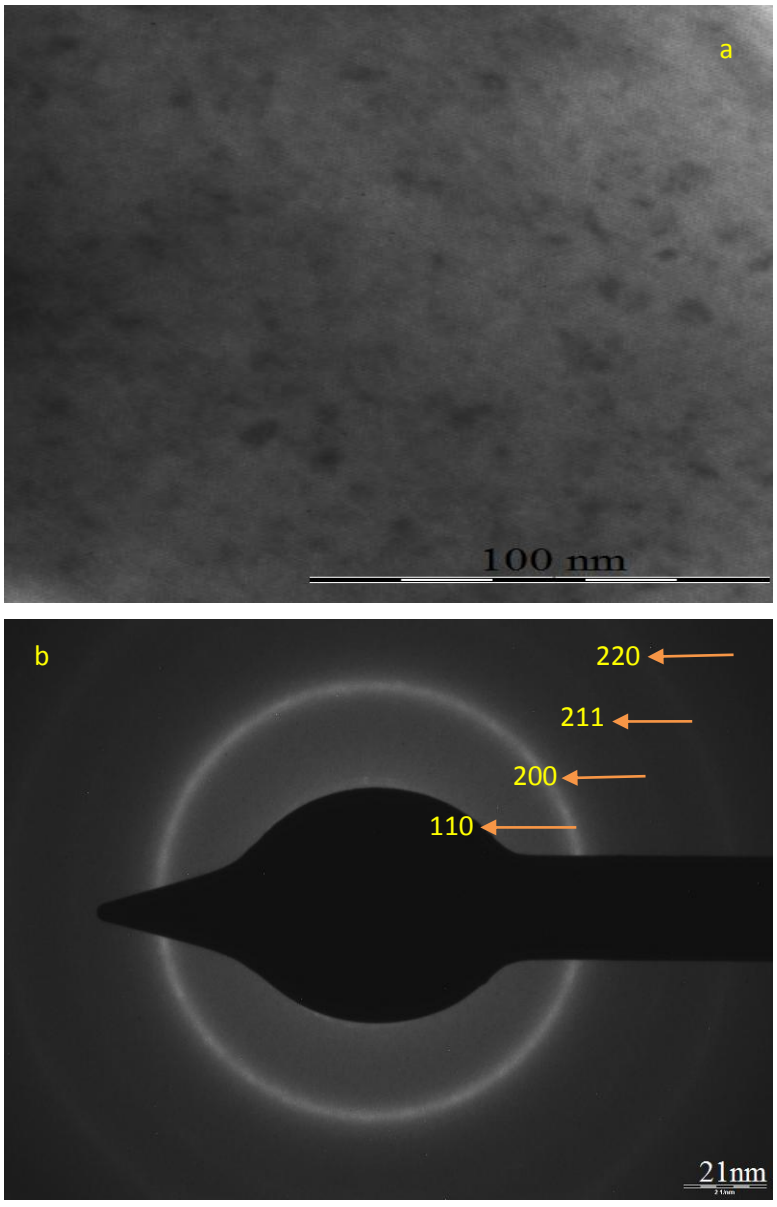

Figure 4.46 TEM micrographs of pellet synthesized by consolidating (300^0 C) powder milled for 300 hours, a) morphology, b) selected area diffraction pattern

Table 4.28 Comparision of 'd'-spacings obtained by XRD and TEM for pellet synthesized by consolidating powder milled for 300 hours

d-Spacing from X-ray diffraction (nm)	d-Spacing from TEM SADP (nm)	d-Spacing for bulk FeAl (nm) in literature	Assignments (hkl)
0.205028	0.204	0.205	110
0.144841	0.144	0.145	200
0.118361	0.118	0.118	211
0.102360	0.103	0.102	220

4.4.6.7 Magnetic properties of the pellets

Room temperature magnetic properties of pellets obtained by ECAP-BP consolidation of mechanically alloyed powders of different ball milling durations are shown in Fig.4.47 and Table.4.29. Accordingly the following inferences could be drawn:

1) The M_S of 100-hour pellet (powder sample ball milled for 100 hour was consolidated by ECAP-BP) analysed from the hysteresis loops (M-H curve) is 30.33 emu/gm which is comparatively much lower than that of 100 hour ball milled powder (Fe_{50}-Al_{50} system) which possessed 72.65 emu/gm. Such large decrease in M_S in the bulk pellet is due to Al diffusion into Fe lattice leading to the formation of AlFe transition alloy phase during consolidation at elevated temperature. Al reduces the direct ferromagnetic interaction between Fe–Fe sites. XRD results reported in section 4.4.6.1 indicate the presence of AlFe/$AlFe_3$ and traces of elemental phases (Al and Fe) in the 100 hr-ECAP-BP pellets. AlFe intermetallic is paramagnetic while $AlFe_3$ intermetallic which possesses DO_3 (Plazaola F. et al. 2012) structure is ferromagnetic.
2) 100-h and 200-h pellets possess M_S of 30.33 emu/gm and 12.44 emu/gm respectively, however 300-h pellet exhibits much higher M_S (44.93 emu/gm) than these two pellets. Higher magnetic behavior is attributed to the presence of disordered AlFe phase (LRO=0.4) (Sebastian V. et al. 2007). In disordered (atomic intermixing) structure, direct ferromagnetic interaction between Fe–Fe sites without the interference of Al atoms is possible causing a magnetic coupling.
3) It is noted that the coercivity of 100-hour pellet is 136.49 Oe, which is greater than the H_C (88.93 Oe) of 100 hours MA (Fe_{50}-Al_{50} system) powder. Such an increase in H_C value in the ECAP-BP consolidated pellet is mainly due to the magnetic anisotropy that appears due to severe plastic deformation (SPD) (Kenichiro Suehiro et al. 2008). Moreover, coercivity enhancement occurs due to an increase in lattice defects like dislocation and

collapsed vacancies after shear strain induced plastic deformation by ECAP-BP at elevated temperature. Such lattice defects are more likely to hinder the movement of magnetic domain walls because of a pinning effect.

4) In general, coercivity increases as particles become finer for lowering the frequency which causes reversal of magnetic domain to a certain extent. However, beyond which if the particle size is smaller compared to the size of magnetic domain, then further reversal of magnetic domain occurs reducing coercivity to zero. It is observed from TEM and XRD that the crystallite size of 10-15 nm in 300-h pellet corresponds to maximum coercivity. Moreover, greater magnetic anisotropy and increased lattice defect due to severe plastic deformation by ECAP-BP has resulted in finer grain size resulting in higher H_C.
5) Pellets (100-h, 200-h and 300-h) possess coercivity of 136.49 Oe, 127.36 Oe and 214.73 Oe respectively exhibiting excellent hard magnetic properties. However, 150-h (85.96 Oe) and 400-h (73.21 Oe) pellets exhibit magnetic properties in between soft and hard magnetic properties. Magnetic anisotropy is greater in disordered (100-h, 200-h and 300-h) pellets whose LRO 'S' is in the range of 0.3 to 0.65. While, the coercivity decrease is attributed to randomly oriented precipitates cancelling out the shape anisotropy effects. Therefore, the orientations of small ferromagnetic precipitates ($Fe/AlFe_3$) after consolidation are important in influencing H_C.
6) In order to function as a source of hard magnetic material, high remanence (M_R) is essential in addition to M_S. While this condition is necessary it is not sufficient, since the squareness ratio (M_R/M_S) must also be as close to 1 as possible. We find that the squareness ratio for all the pellets are much less than 1, thus the remanence in the pellets is quite low. It is observed that only 100 hour and 300 hour pellets possess greater remanence of 3.158 emu/gm and 7.126 emu/gm respectively and to a certain extent 200 hr bulk sample has moderate remanence (1.464 emu/gm).
7) Pellet obtained by consolidating 400 hour ball milled powder at 500 ^{0}C exhibits an intermetallic phase ($AlFe/AlFe_3$), LRO 'S' of 0.75 could trigger a low M_S.
8) Looking into the XRD results, 150-hour and 200-hour pellets show traces of magnetite (Fe_3O_4) and aluminium oxide. Fe_3O_4 structure exhibits **low** saturation magnetization (ferrimagnetic) and Curie temperature. While the Al_2O_3 is a paramagnetic material, when present in small quantities drastically reduces the saturation magnetization.
9) Among all the pellets, no texture is visible in the 400-h pellet contributing to the lowest M_S and H_C. Fairly weak texture with a maximum intensity of 250.5 (Ψ=5.0 & Φ=52.5) is observed in 150-hour pellet processed at 500 ^{0}C with 350 MPa also contributes to lower M_S and H_C.

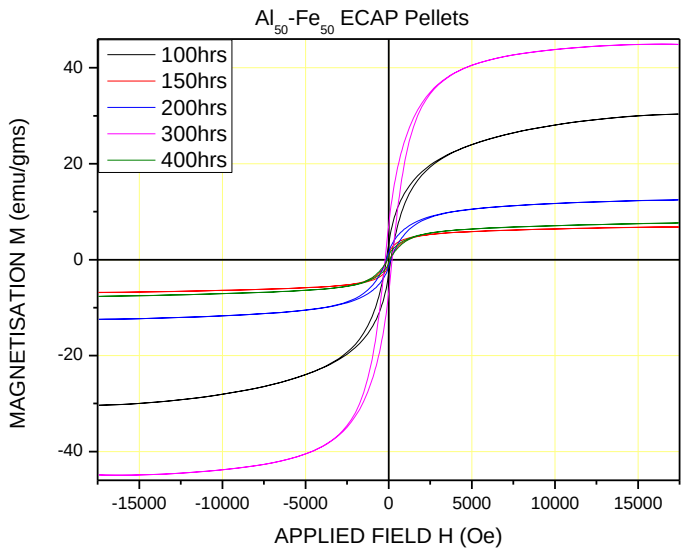

Figure 4.47 Hysteresis loop (M-H curves) of ECAP-BP pellets obtained by consolidating powders ball milled from 100 to 400 hours

Table 4.29 Magnetic properties of ECAP-BP pellets consolidated at various milling time

Sample Name	M_S (emu/gm)	M_R (emu/gm)	Coercivity (Oe) H_C	Sample weight (gms)	Squareness ratio (M_R/M_S)
50Al 100hrs ECAP-BP	30.33	3.158	136.49	0.0352	0.1042
50Al150hrs ECAP-BP	6.833	0.9648	85.96	0.0675	0.1412
50Al200hrs ECAP-BP	12.44	1.464	127.36	0.0434	0.1177
50Al300hrs ECAP-BP	44.93	7.126	214.73	0.0627	0.1586
50Al400hrs ECAP-BP	7.643	0.7327	73.21	0.0427	0.0958

*M_S- Saturation Magnetisation , ie Moment measured in Maximum field, M_R- Remanent Magnetisation

4.4.6.8 Thermo-magnetic properties of the pellets

Temperature dependent magnetization curves of ECAP-BP consolidated pellets are presented in Figure 4.48, from these curves the following inferences could be drawn:

1) The shape of the isotherms indicates the presence of ferromagnetic phase in all the samples at a temperature range of 25 ^{0}C to nearly 550 ^{0}C.

2) Room temperature magnetic properties are low in 150-h, 200-h and 400-h pellets as they possess higher LRO 'S' as indicated in Table 4.27, such a magnetism decreases upon increase in temperature. Magnetite (Fe_3O_4) phase in the 180-h and 200-h pellets cause ferrimagnetic behavior, ionic compounds in the phase is the reason for lower room temperature magnetization. While, Al_2O_3 presence causes weaker magnetism in 150-h pellet.

3) The magnetization of 300 hours pellet decreases continuously beyond 100 ^{0}C, the decrease (beyond 600 ^{0}C is steep) in magnetization with increase in temperature is attributed to the transition to ordered phase, thus causing a decrease in Fe-Fe nearest neighbor. At 750 ^{0}C it possesses slightly less than 5 emu/gm indicates that ferromagnetic phase still prevails at the elevated temperature though it has decreased substantially.

4) Slope of the magnetization curve of 100-h pellet is insignificant at low temperatures (upto 300 ^{0}C) and notably increases (steep) in the range of 450–600 °C. It is observed that the degree of long range order parameter (S) of the pellet sharply increases in the temperature range of 450 ^{0}C-600 ^{0}C; which correlate with the decrease in the proportion of disordered ferromagnetic clusters. Paramagnetic (< 2.0 emu/gm) phase is attained at 660 ^{0}C (Curie temperature, T_C), DSC curves too have shown the exotherm related to the ordered paramagnetic phase.

5) 100-hour pellets, synthesized at different ECAP-BP temperature exhibits unique structural properties as investigated by the XRD results (section 4.4.6.1). Fig 4.48 reveals the variations of LRO 'S' and lattice parameter 'a' at different processing temperature. Degree of long range ordering increases with increasing temperature while simultaneously decrease in lattice parameter is observed. Steep increase in LRO and similar decrease in lattice parameter is observed beyond 450 ^{0}C, such an enhancement in the LRO parameter (> 0.45 to 0.85) 'S' is attributed to cause a steep decline in the thermomagnetic (From 15.5 emu/gm at 450 ^{0}C to paramagnetic (≤ 2 emu/g) at 675 ^{0}C) properties beyond 450 ^{0}C.

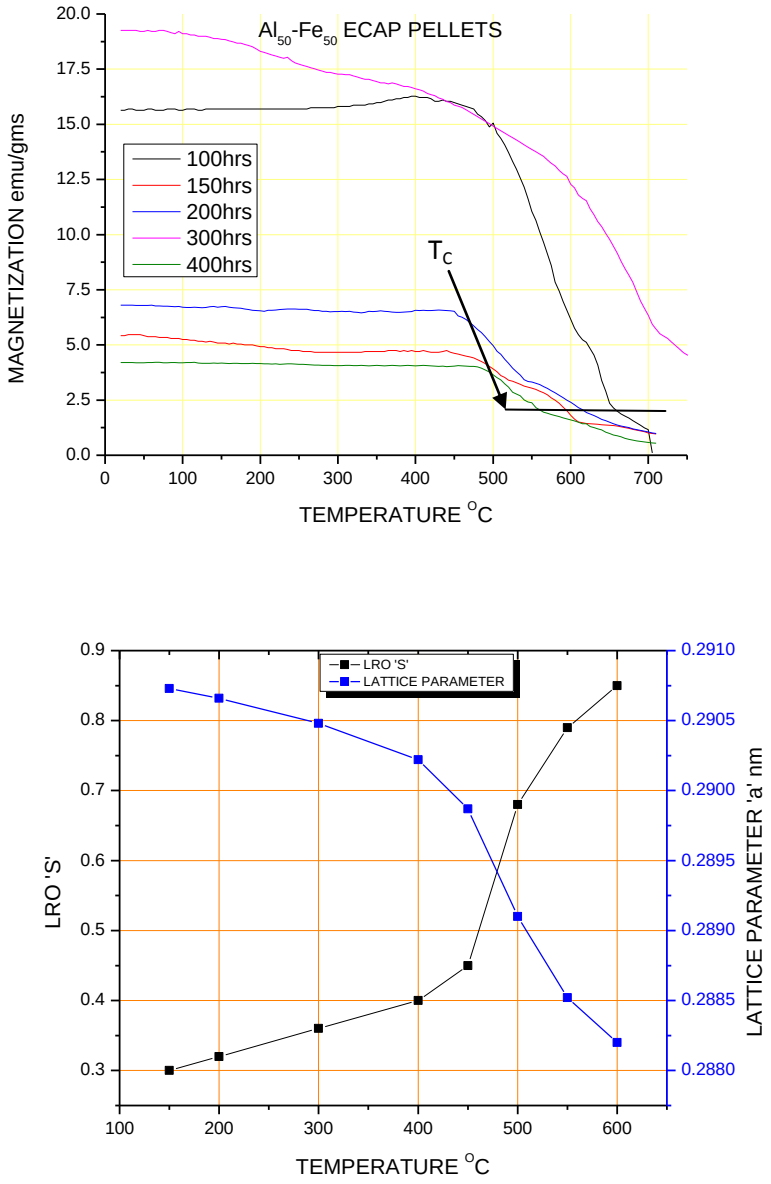

Fig. 4.48 Temperature dependence of magnetization. Structural parameters of ECAP-BP pellets (100-h) processed at various temperature.

4.4.6.9 Texture of ECAP-BP pellets

A study of the nature of evolution of predominant crystallographic orientations resulting from severe plastic deformation (SPD) is of primary importance in ECAP-BP consolidation. Especially since the crystallographic texture has significant effects on many structure-sensitive properties, so that a careful texture analysis makes it possible to estimate the mechanisms responsible for the progress of plastic straining and phase transformations. It is well known that the principle of plastic straining, which is a direct consequence of simple shear, is the basic process underlying the

ECAP-BP consolidation technique. Figures 7.49 to 7.53 in appendix and Fig 4.49 shows pole figures of pellets consolidated by ECAP with back pressure, following inferences could be drawn from these pole figures:

1) Random texture with a maximum intensity of 245.5 ($\Psi = 25^{O}$ and $\Phi = 12.5^{0}$) is observed in 100-h pellet consolidated at 450 ^{0}C. While, the maximum intensity is 312.00 (Ψ=25 & Φ=72.5) in the 100-h pellet consolidated at 150 ^{0}C.

2) The texture of 150-h pellet is fairly weak at a maximum intensity of 250.5 (Ψ=5.0 & Φ=52.5) at a ECAPing temperature of 500 ^{0}C. Though random texture is seen, pole figure of the pellet shows a weak preferred orientation near the centre caused by shear deformation of ECAP process.

3) Pole figure of 180-h pellet shows some preferential alignment with a weak (intensity of 287.5 at Ψ=5.0 & Φ=167.5) fibre texture which resembles the rolling texture seen in some of the alloys. A fibre orientation is observed in the concentration along the extrusion direction (ED) as elliptical bands approximately at Ψ=35° and 90° from the centre in the pole figure. The prevalent texture is caused more due to screw dislocation process during ECAP.

4) Orientation density (at $\Psi = 30^{0}$ and $\Phi = 177.5^{0}$) of the 110 component in 300-h pellet is higher than that of the same component in the 400-h pellet. Both the pellets display shear type texture. The pole figure of 400-h pellet shows almost a random orientation with maximum intensity (181.5) areas are in the circle of ψ=15° and $\Phi = 237.5^{0}$ indicating no texture at ultra fine grain size.

5) The texture of ECAPed pellets is predominantly random although a weak fibre type texture is visible as explained above. The deformation process is associated with random grain rotations during grain boundary sliding (GBS). Thus, shear deformation occurs in the hatched region (Figure 4.50) subtending an angle β at the inner corner of the die, thus the 110 pole figure obtained after ECAP shows no preferred orientation of the initial texture (formed during compaction in the vertical channel along the insertion direction). ID is the insertion direction and ED is the extrusion direction.

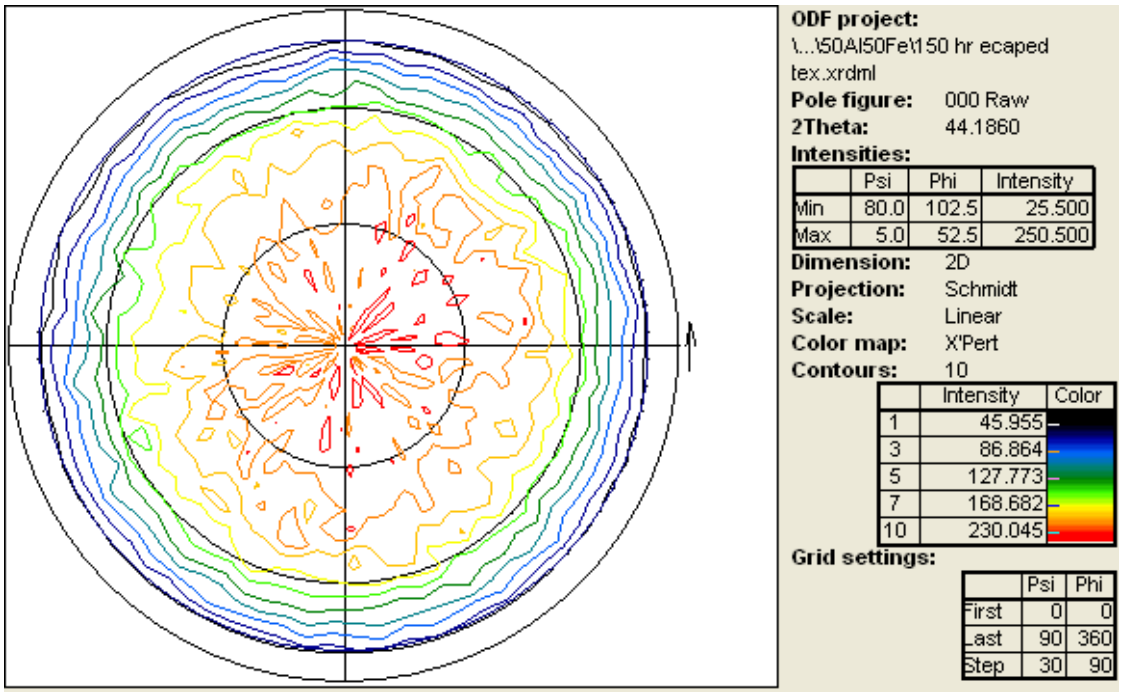

Figure 4.49 Pole figures of 150-h ECAP-BP pellet processed at 500 ^{0}C

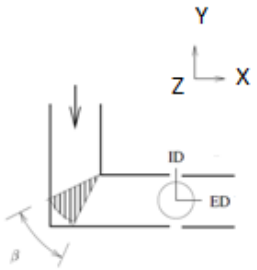

Figure 4.50 Insertion and extrusion direction within the ECAP-BP die.

4.4.7 Consolidation by compaction and sintering

This section concentrates on consolidation of powders ball milled (Al_{50}-Fe_{50} system) in SS-MM by compaction and pressureless sintering. Further, different phases emerged, structural, texture and mechanical properties of sintered **compacts** are compared with those bulk pellets obtained by ECAP-BP consolidation process. The details of room temperature compaction and sintering experiments are explained in section 3.2.2.2. Not all ball milled powder has been consolidated, only a few mechanically alloyed powders have been selected to represent the important metallurgical events that will occur during consolidation by compaction and sintering. Figure 4.51 shows sintered compact hot mounted on a polyfast material for metallography and nanoindentation analysis. Thus, the following **sections** report the investigation of phase transformation, phase

identification, structural parameters, metallography, texture and nanoindentation of sintered compacts.

Figure 4.51 Sintered compact hot mounted on a conductive material (polyfast)

4.4.7.1 XRD analysis of sintered compacts

Mechanically alloyed powders synthesized by ball milling time are consolidated by cold compaction followed by sintering. XRD profiles of such sintered compacts are shown in Fig 4.52 and important structural parameters are indicated in the Table 4.30. Individual XRD profile of each sintered compact is shown in appendix in figures 7.54 to 7.57 while the structural parameters are listed in tables 7.14 to 7.17. From these XRD profiles and tables the following inferences could be drawn:

(i) Compared to the diffraction peaks (110/200 reflections) of mechanically alloyed powder (reported in section 4.4.1), narrower and higher intensity diffraction peaks of Al, Fe and AlFe phases are observed in sintered compacts.

(ii) Accordingly, sintered compact (30-h) exhibits coarser crystallite size and reduced lattice strain of 120 nm and 0.232 % respectively while, greater height (403 counts) and reduced FWHM (0.3660^0) are observed compared to powder ball milled for 30 hours. However, lattice parameter (0.2869/0.4058 nm) of Fe/Al phases in the sintered compact are almost similar to that of ball milled powder but is slightly larger than that of pure unmilled Fe/Al (0.2862/0.4048). Quantitative analysis of Fe, Al and AlN phases are 19 %, 61% and 20 % respectively.

(iii) Powder ball milled for 100 hours showed the presence of AlFe solid solution while sintered compact (100-h) revealed the transition of solid solution to an intermetallic phase. Intermetallic diffraction peak ($2\theta=43.3460^0$) emerges slightly to the left of elemental peak (44.5914^0) and possesses height of 58.67 counts, FWHM of 0.4403^0. Diffraction peaks of intermetallic phase are also observed at Bragg angles of 54.3300^0, 64.5^0, 71.4704^0 and 81.2326^0. Compared Fe(Al) solid solution (100-h ball milled powder) and AlFe intermetallic of 100-h pellet, larger lattice parameter (0.2949 nm) is noted in the AlFe (110 peak) phase of 100-h sintered compact. Such an expanded lattice suggests further diffusion of Al atoms into Fe lattice resulting in the formation of intermetallic during sintering. Thus, elemental phases are reduced quantitatively as shown by XRD profile of 100-h sintered compact. While, increased lattice strain (0.359 %) and finer crystallite size (59 nm) induces broader reflections compared to 30-h sintered compact. Superlattice peaks (100, 111 and 210) confirm the formation of AlFe intermetallic phase.

(iv) Presence of $AlFe_3$ phase in addition to AlFe has been indexed in 150-h sintered compact, thus intermetallic phases increase at the expense of elemental phases.

(v) Sintered (200-h) compact possesses nanostructured AlFe (66 %) intermetallic phase along with AlN, negligible traces of elemental phases and Fe_4N as indicated by XRD profile quantification. The Bragg angle, height, FWHM and lattice parameter of AlFe phase (110 peak) are 43.9424^0, 362.11 counts, 0.6043^0 and 0.2912 nm respectively, results indicate greater lattice strain (0.571 %), finer crystallite size (28 nm) and larger lattice compared to 150-h sintered compact.

(vi) AlN and FeN phases are present due to sintering in nitrogen atmosphere. However, nitride phase almost diminished in sintered compacts produced from powders milled for longer duration of time (200-h) as indicated by quantitative analysis in the profile.

(vii) Inspite of our best efforts to provide a total nitrogen atmosphere during sintering process, traces of oxygen contamination can be found by the presence of Al_20_3 peaks (3) in the 100 hours sintered sample.

(viii) It is contrasting to note that 200-h ECAP-BP pellet possessed only AlFe/$AlFe_3$ phase while, 200-h sintered compact did possess AlFe (66 %), AlN (27 %) along with traces of Al, Fe and Fe_4N. Both the consolidated products were processed from powder ball milled for 200 hours in SS-MM.

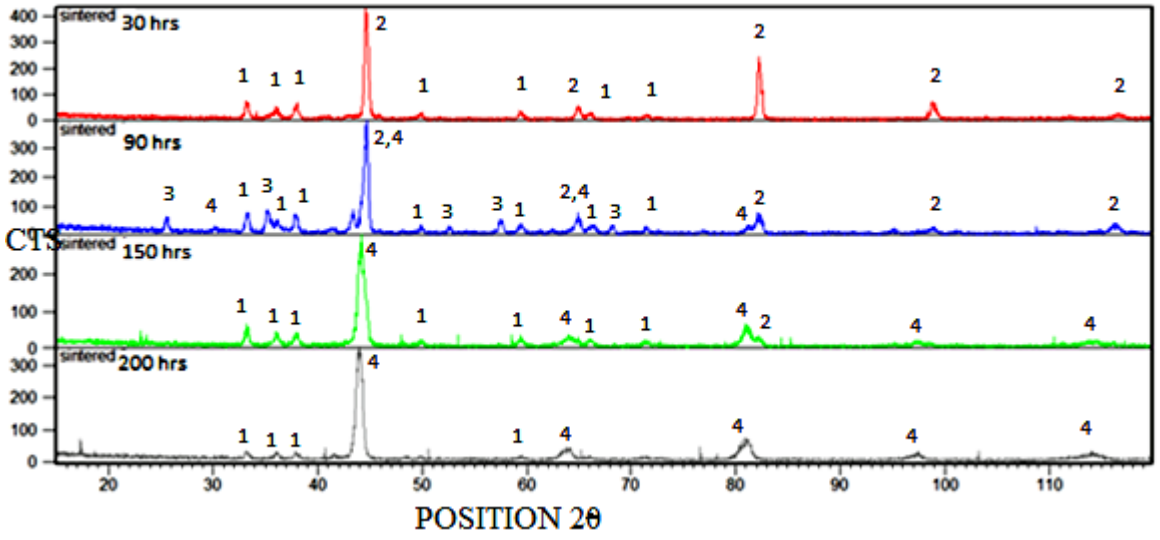

Figure 4.52 XRD profiles of sintered compacts consolidated at various ball milling time. Different peaks in the diffractogram are defined as 1-(AlN), 2-(Al/Fe), 3-(Al_2O_3), 4-(AlFe)

Table 4.30 XRD peaks and Structural parameters of sintered compacts

Sintered compact	Peak Pos (2θ)	Phases	Height counts	FWHM (2θ)	'd' nm	'a' nm	'**D**'nm/ lattice strain %	Rel. intensity
30 hours	33.2176	AlN(100) hexagonal	61.95	0.3618	0.26949			15.36
	37.9363	Al (111)/ AlN (101)	45.57	0.4688	0.23698			11.30
	44.6244	**Fe(110)/ Al (200)**	**403.30**	**0.3660**	**0.20289**	**0.2869/ 0.4058**	**120**/0.232	**100**
100 hours	25.5774	Al_2O_3rho-mbohedral	44.74	0.2909	0.34799			12.92
	30.1490S	AlFe (100)	9.13	0.3081	0.29618			2.64
	33.2507	AlN hexagonal	62.07	0.3782	0.26923			17.92
	37.8715	AlN/Al_2O_3 /Al (111)	60.51	0.3922	0.23737		Al-46 nm	17.47
	43.3460	AlFe **110**/Al_2O_3	58.67	0.4403	0.20858	**0.2949**	**59**/0.359	16.94
150 hours	33.2170	AlN(100) hexagonal	50.44	0.4885	0.26949			19.59
	44.0241	$AlFe_3$ **(220)**/AlFe **(110)**	257.54	0.5587	0.20552	**0.2906**	**33**/0.513	100
	44.3885	Fe110/Al 200	206.18	0.7049	0.20392			80.06
200 hours	33.2175	AlN/Fe_4N *	21.67	0.3904	0.26949			5.98
	37.9264	AlN/Al 111	16.22	0.5572	0.23704			4.48
	43.9424	**AlFe 110**	362.11	0.6043	0.20588	**0.2912**	**28**/0.571	100

*Fe_4N- Simple cube, S-superlattice reflection

4.4.7.2 DSC analysis of sintered compacts

Mechanically alloyed powder subjected to milling time of 100 hours is consolidated by sintering, such a sintered compact is heated in a calorimeter to analyse the elevated temperature behaviour. Typical heat flow curve of a crystalline material is obtained for 100-h sintered compact as presented in Fig 4.53. Superlattice peaks (100 and 111) revealed by XRD also indicates the crystalline (AlFe) phase existing in the sintered compact. Moreover, the curve also represents the alloying of elemental phases triggering the formation of intermetallic.

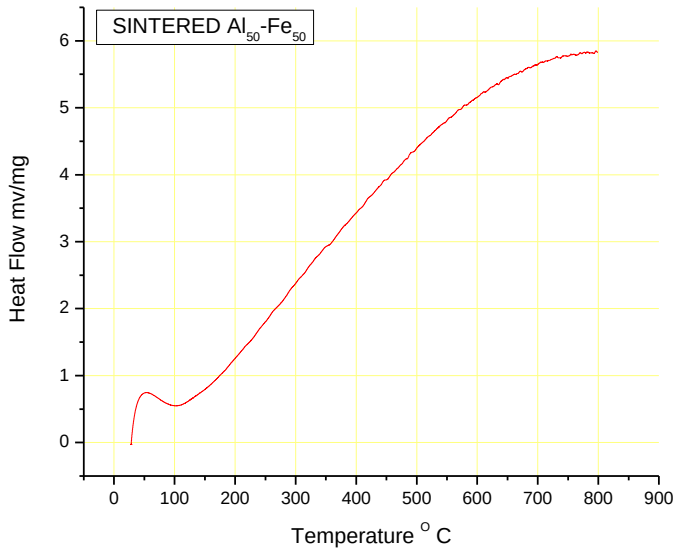

Figure 4.53 DSC curve of sintered compact; heat flow as a function of temperature

4.4.7.3 Nanoindentation of sintered compacts

Three sided Berkovich diamond indenter was used for indentation with an applied peak load of 20 mN. The initial loading (‘a’ in Fig 4.54) segment contained an elastic-plastic displacement while the unloading (‘b’ in Fig 4.54) process is generally considered to be entirely elastic. The loading and unloading rate for the above indentation process was kept constant. Hardness and elastic modulus as a function of penetration depth for 100-h and 200-h compacts are shown in Fig 4.55 to 4.58 respectively. From these figures the following inferences could be drawn:

(i) 200-h sintered compact had the least penetration depth followed by 150-h and 100-h compacts. While, 30-h sintered compact had larger penetration depth among the samples. An arrow, labeled pop in marks the transition from elastic to plastic deformation during the indentation process.

(ii) Nanohardness range varies approximately from 2.9 GPa to a maximum of 7.5 GPa while the elastic modulus varies from 62 GPa to 91 GPa. While the penetration depth varied from 0.42 to 0.82 μm for 100-h sintered compacts.

(iii) However, nanohardness range varies from 5 GPa to 23.5 GPa and the elastic modulus range varies from 135 GPa to 260 GPa in the 200-h sintered compacts. While, the penetration depth varied from 0.25 to 0.45 μm.

(iv) Quantitatively larger regions of AlFe intermetallic (66 %) and AlN (27 %) phases are present in 200-h sintered compacts. In contrast, 100-h sintered compact has lower concentration of AlFe (3 %) and AlN (22 %) phases in addition to Al_2O_3 regions as analysed by XRD. Predominantly covalent bond in addition to metallic bonding prevailing in the intermetallic phase is the cause for higher elastic modulus while, larger portion of AlN is the cause for higher hardness in the 200-h sintered compacts. Elastic modulus is decided by the nature of the bond in the matrix where as hardness is influenced by the nature of second phase particles.

(v) Sintering done under nitrogen atmosphere has a profound influence on nanohardness.

(vi) Among all the sintered compacts, 200-h compact has a more profound texture (maximum intensity of 703.5 at $\Psi=0$ & $\Phi=292.5$) which indicates that the sample with more preferred grain orientation has a higher hardness value.

(vii) Sintered compact (200-h) exhibits higher nanohardness and elastic modulus compared to ECAP-BP consolidated pellets. Such higher mechanical properties are the result of intermetallic and nitride phases prevailing in the sintered compacts in contrast to the transitional phase (incomplete ordering) revealed in most of the pellets as reported by XRD analysis in section 4.4.6.1. More free volume exists in the disordered structure than the crystalline one, thus the interatomic distance in disordered structure is larger than the crystalline structure. As a result the crystalline structure has a higher elastic modulus (Zhao B. et al. 2003).

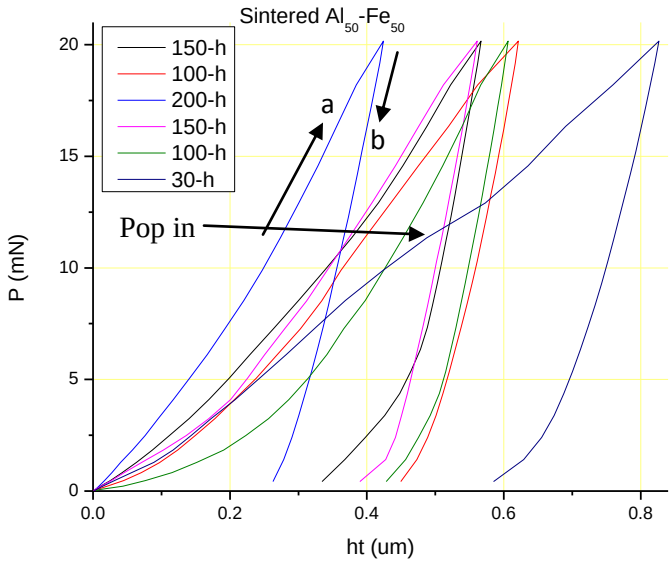

Figure 4.54 load as a function of indentation depth of sintered compacts obtained by consolidating MA powders processed at various ball milling time.

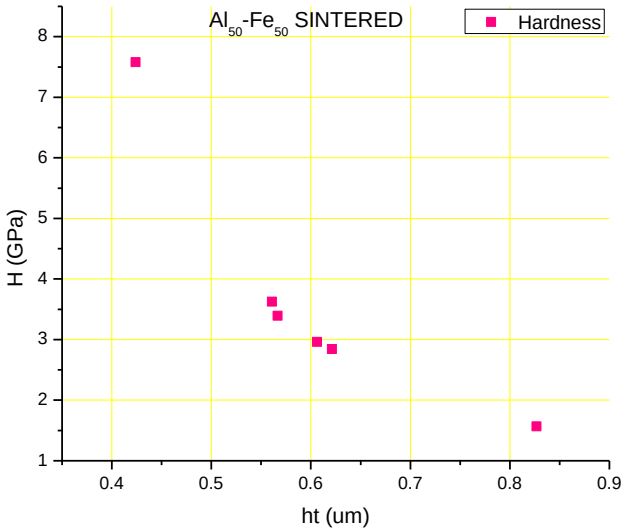

Figure 4.55 nanohardness of sintered compact obtained by consolidating powder ball milled for 100 hours.

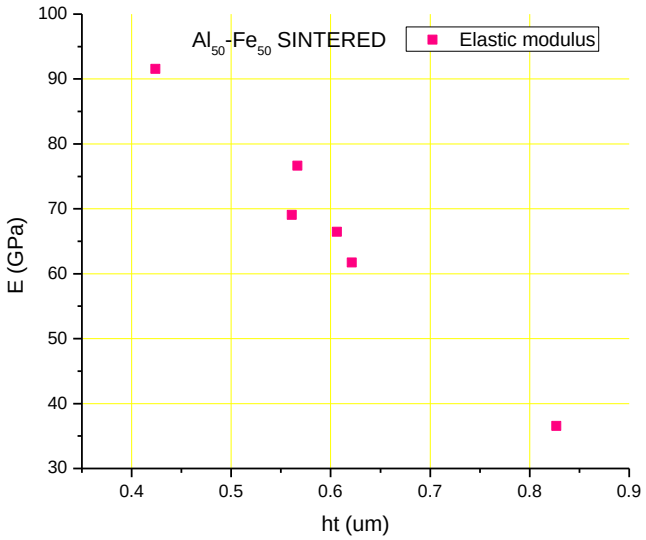

Figure 4.56 nanoindentation (elastic modulus) of sintered compact obtained by consolidating powder ball milled for 100 hours

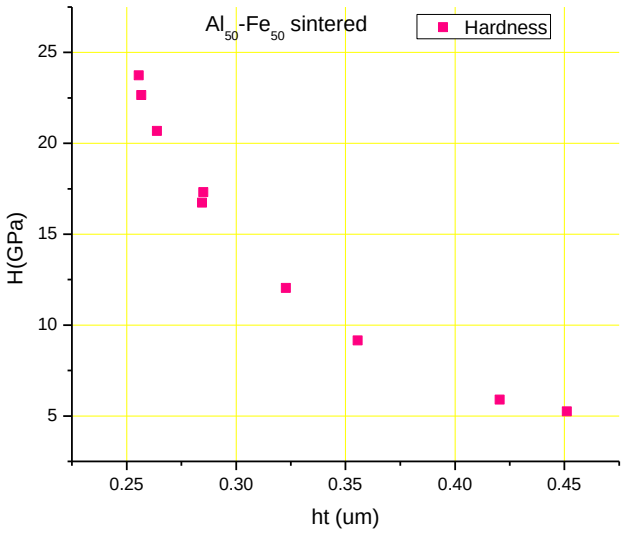

Figure 4.57 nano hardness of sintered compact obtained by consolidating powder ball milled for 200 hours

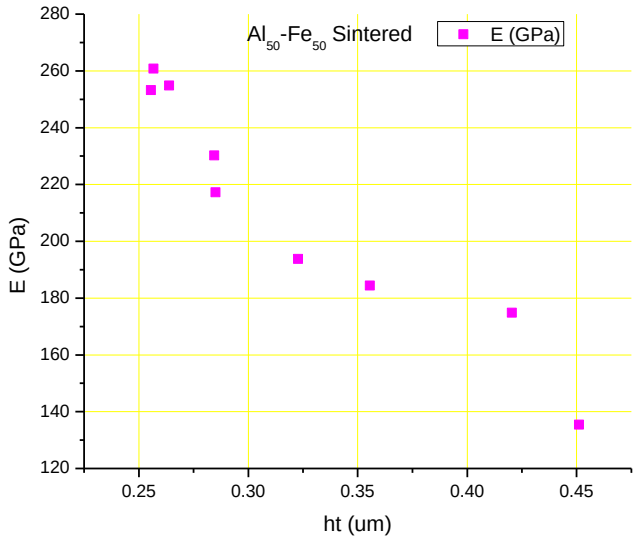

Figure 4.58 nanoindentation (elastic modulus) of sintered compact obtained by consolidating powder ball milled for 200 hours

4.4.7.4 Texture of sintered compacts

Because of the anisotropy of individual crystals, the structural, mechanical and magnetic properties of polycrystalline sintered compacts are dependent upon any preferred orientation or texture which may be developed in the component crystals during cold compaction followed by sintering. The preferred orientation in the sintered compacts (cold compaction and sintered) is best described and quantified by pole figures 4.59 and 4.60, accordingly the following inferences can be drawn:

(i) Weak deformation texture with a maximum relative intensity in the 110 pole figure is 473.5 (at $\Psi=20^{0}$ and $\Phi=212.50^{0}$) for 100-h sintered compact. Such a texture is regarded as being close to a random one.

(ii) However, an enhanced texture is visible in the form of an elliptical contour in 200-h sintered compact with a maximum relative intensity of 703.500 (at $\Psi=0$ and $\Phi= 292.5^{0}$) in the 110 pole figure obtained at a Bragg angle of 44.6630^{0}.

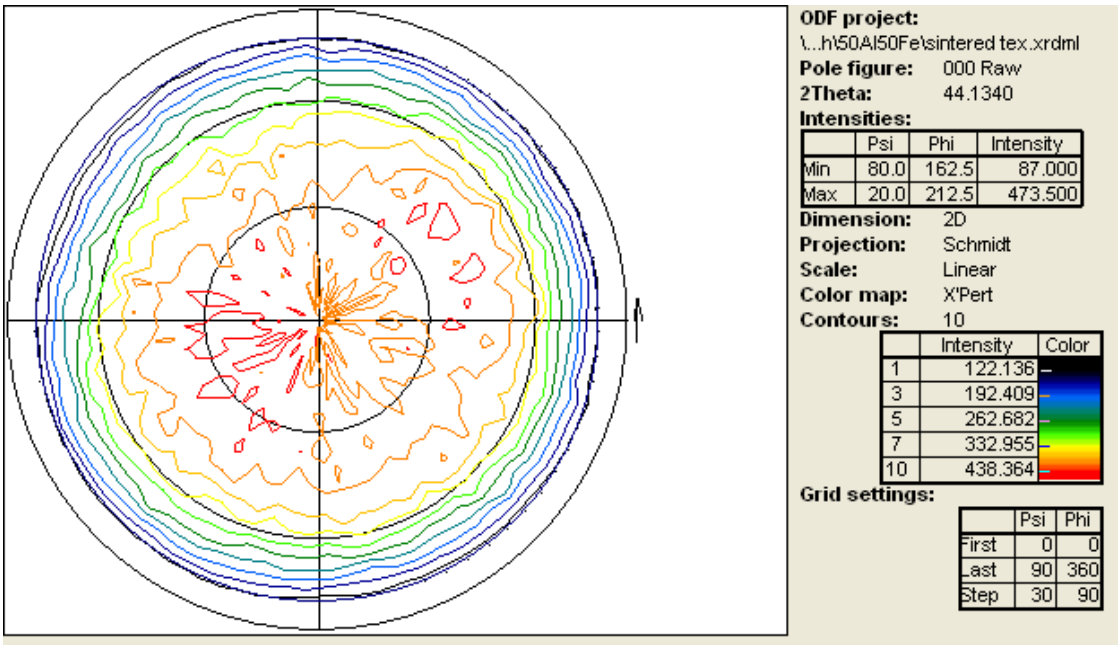

Figure 4.59 XRD pole figure of sintered compact obtained by consolidating powder ball milled for 100 hours

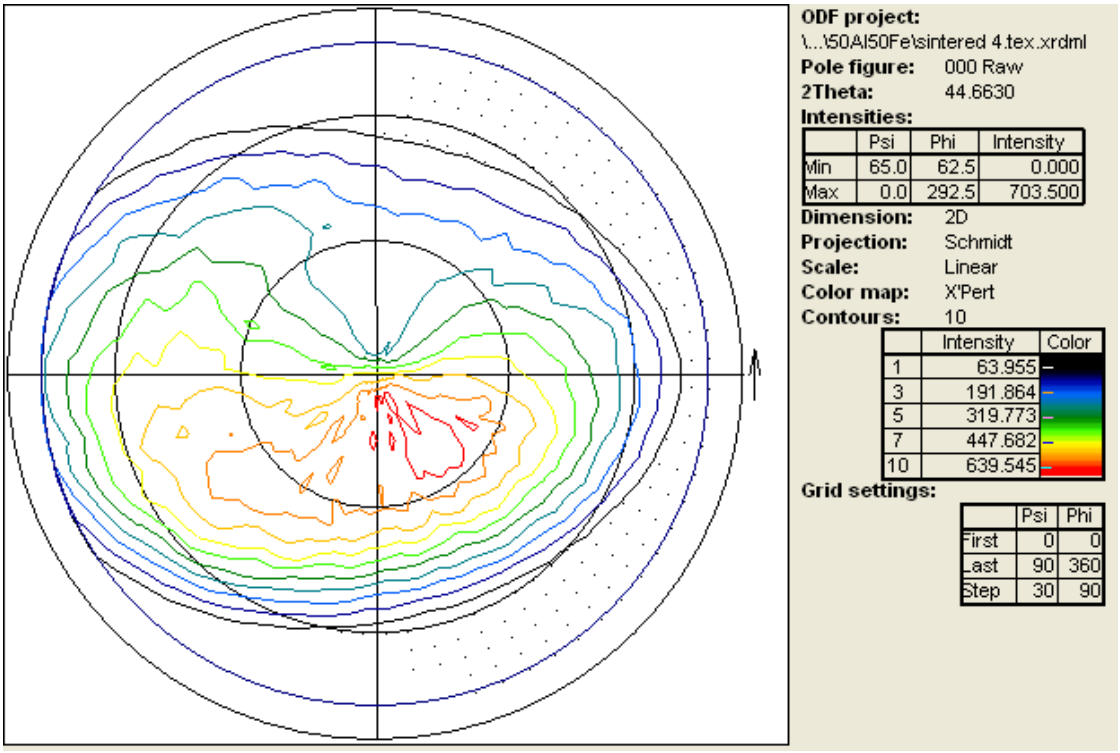

Figure 4.60 XRD pole figure of sintered compact obtained by consolidating powder ball milled for 200 hours.

4.4.7.5 Metallography of sintered compacts

Sintered compacts were subjected to metallographic preparations like wafer slicing, successive fine grinding, etc. Final polishing was done on a MD-Chem polishing pad with OP-S (oxide polishing) suspension in which colloidal silica (SiO_2) is used. Experimental detail is reported in section 3.3.3. Metallographically polished samples are observed and analysed by optical microscopy and SEM, the images are presented in Figure 4.61 to 4.63. From these images following inferences could be drawn:

(i) Al Particle size had a significant effect on the size and distribution of porosity in the sintered compacts. Widespread bimodal porosity size distribution is observed in optical micrographs (Fig 4.61 a), 30-h sintered compact processed at 950 ^{0}C has larger pores as a result of coarser Al crystallite size of 120 nm. In contrast, smaller pores (Fig 4.61 b) are seen in 100-h sintered compact with finer Al crystallite size in the vicinity of 46 nm. Factors which contribute to the porosities in the sintered compacts are; porosities initially present in the green compacts, development of kirkendall porosity (due to imbalanced diffusivities of elemental phases) during the heating stage and presence of agglomerated Al particles. Though the crystallite size in the nano scale cannot be seen in OM.

(ii) With higher processing temperature of 1000 ^{0} C and 1150 ^{0} C in 100-h and 200-h (Fig 4.62) sintered compacts respectively, porosities become finer and are reduced compared to lower processing temperature compacts. Fine needle like shaped AlN phase is distinctly observed in the photomicrograph. In addition, triangular shaped region of stronger bonding and dense structure is seen.

(iii) The bright regions in the secondary electron mode SEM micrograph (Fig. 4.63) indicate the Al_2O_3, AlN and Fe_4N phases while the grey areas represent the AlFe intermetallic phase in the 100-h sintered compact. In addition, pores are visible.

(iv) SEM-EDS analysis is carried out on sintered compact and the results are listed in table 4.31 while, SEM image along with energy dispersive x-ray spectroscopy (EDS) spectra are shown in Fig 4.63 (graph). Typical EDS area analysis shows the presence of Al, Fe, O and N which suggests the formation of AlN, Al_2O_3 and AlFe phases. Possible formation of Fe_4N is not ruled out as analysed by XRD.

Figure 4.61 OM Image of sintered compact synthesised from a) 30 hour ball milled powder b) 100 hour ball milled powder

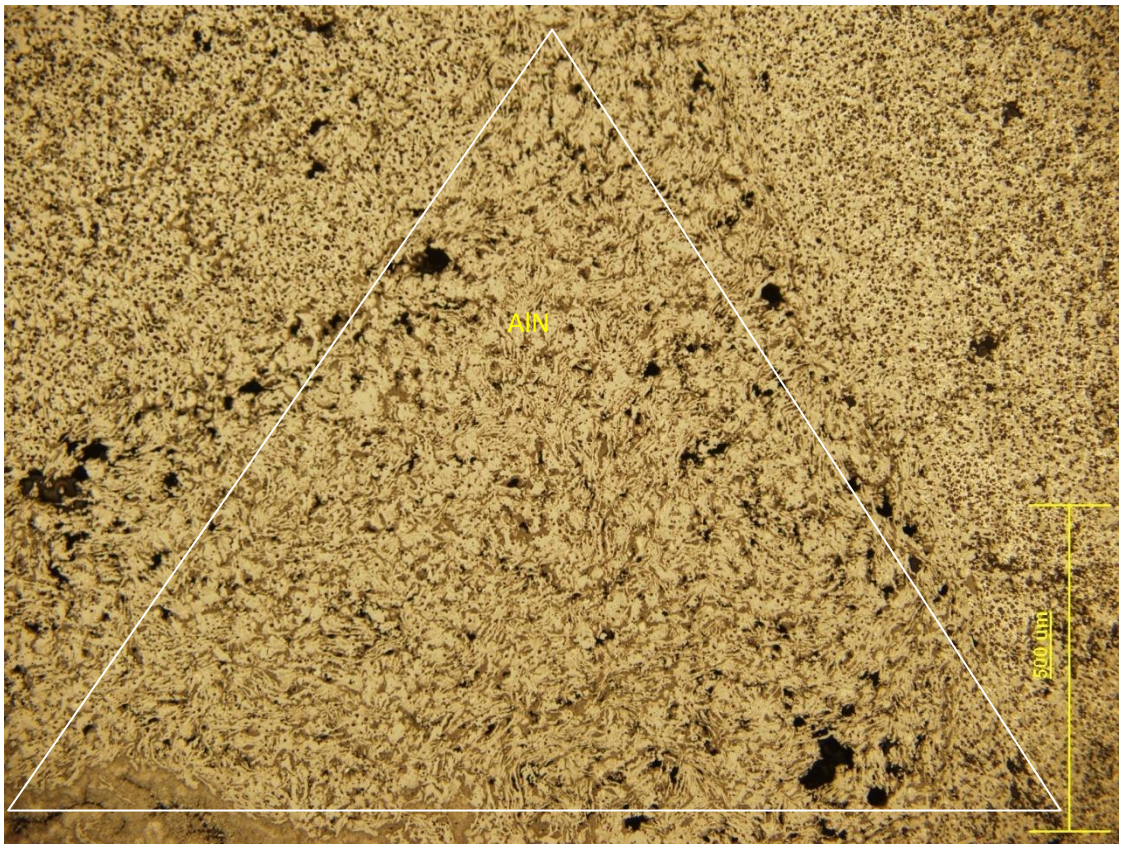

Figure 4.62 OM image of sintered compact synthesized from 200 hours milled powder

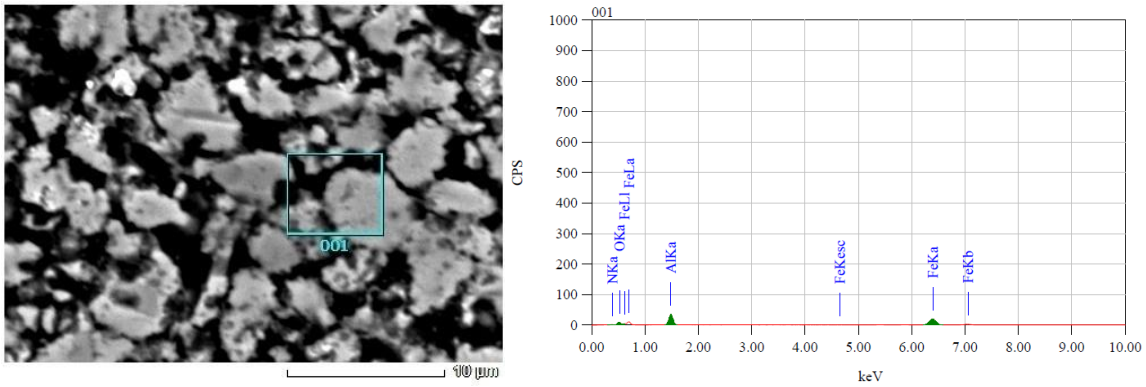

Figure 4.63 a) SEM-EDS micrograph and b) spectra of sintered compact (100 hour milled powder)

Table 4.31 EDS analysis of sintered compacts

Elements	keV	Mass %	Error %	At %
N	0.392	5.03	0.32	11.16
O	0.525	13.70	0.15	26.61
Al	1.486	28.55	0.14	32.89
Fe	6.398	52.73	0.32	29.35
Total		100		100

4.5 Overview of Metallurgical Events in Al_{50}-Fe_{50} System

Elemental powders of Al and Fe (atomic composition of 50 % each) ball milled in tungsten carbide (WC) and toluene milling media (MM) showed the formation of Fe (Al) solid solution with a lattice parameter of 0.29316 nm at the end of 185 hours of milling time. During the course of ball milling, crystallite size (D) got refined to the tune of ≤ 12 nm and some amount of amorphous structure is observed. Disordered solid solution transforms into ordered structure upon heating to a temperature in the vicinity of 350 ^{0}C. Due to progressive alloying of Al in Fe as a consequence of ball milling, saturation magnetisation (M_S) decreases with increase in ball milling time. No atmospheric contamination is observed in the milled product. Further, elemental powder ball milled (WC-MM) for 185 hours has been consolidated to bulk compacts by compaction, sintering and annealing. Such an annealed compact exhibits fully ordered structure. Further, ordered annealed compact is plastically deformed by a range of stresses due to which it undergoes a transition to disorder of varying magnitude. Order to disorder transition is accompanied by lattice expansion, crystallite size refinement, increased M_S and nanohardness (H) and Bragg angle shift to lower 2θ angles.

In order to compare the role of MM during ball milling, elemental powders of Al and Fe (Al_{50}-Fe_{50} system) has been ball milled in stainless steel (SS) milling media in an argon gas envelope to prevent contamination from atmosphere. The onslaught of MA due to ball milling has reduced the crystallite size to 5 nm with a lattice parameter of 0.2934 nm of Fe (Al) solid solution at the end of 400 hour of milling time. DSC analysis has shown the crystallisation from slight amorphous structure attained during the process of long milling time. Thus, possible precipitation of equilibrium phases like AlFe/$AlFe_3$ intermetallics is noticed. The extent of amorphisation attained is less than that found in the powder ball milled in WC-MM. Soft magnetic (H_C < 125 Oe) properties are attained in all the milled powders except powder ball milled for 300 hours. TEM result confirms the nano crystallite size attained during the course of ball milling, while, dislocations are visible. Further, ball milled (SS-MM) powders have been consolidated by ECAP-BP, consolidation has resulted in the formation of AlFe/AlFe3 intermetallic phases in the pellets. Depending on the consolidation temperature, long range order (LRO) 'S' varies from 0.3 for 100-h pellet (processed at 150 ^{0}C) to 0.75 for 400-h pellet (processed at 500 ^{0}C). The lattice parameter of the ECAP-BP pellet consolidated from powder ball milled for 400 hours is 0.2911 nm AlFe/0.58 nm $AlFe_3$. Elongated particles due to plastic deformation, compressed regions and bonding in the pellets are noted from optical micrographs (OM). Intermetallic phases, plastically deformed regions and nucleation of nanoporosities are observed from SEM micrographs of pellets. Mixture of metallic and covalent bonds due to the presence of intermetallic phases is the cause for higher nanohardness and elastic modulus compared to those pellets possessing transitional (partially

ordered) structure. DSC and TEM results indicate the existence of slight amorphous phase in the pellets. Increase in ECAP-BP processing temperature causes partially ordered structure to fully ordered one, triggering simultaneous decrease in lattice parameter associated with an increase in LRO. Such change in structural parameters initiates ferro to paramagnetic transition. Inaddition to ECAP-BP consolidation, ball milled (SS-MM) powders have been consolidated by compaction and sintering. Sintered compacts possess AlFe intermetallic, AlN, Fe_4N phases inaddition to Al_2O_3 due to contamination from atmosphere. Enhanced texture in the sintered compact coupled with the presence of above mentioned phases, they exhibit higher mechanical properties then the pellets.

CHAPTER 5: BALL MILLING AND CONSOLIDATION (Al_{90}-Fe_{10} SYSTEM)

In this chapter, elemental powders with an initial composition of **90** atomic % Al and **10** atomic % Fe (Al_{90}-Fe_{10} system) are ball milled in SS-MM to achieve mechanical alloying. Further, the ball milled powders are characterized by XRD, DSC, VSM and TEM, the results of these characterization techniques are listed and discussed in the following sections.

In another set of experiments, the above mentioned mechanically alloyed powder as a function of ball milling time is consolidated by two different techniques: (i) consolidation by ECAP-BP and (ii) consolidation by cold compaction and sintering. Consolidated solid materials are further characterized by XRD, DSC, VSM, nanoindentation and metallographic examination by optical and scanning electron microscopes. Thus, structural, mechanical and magnetic properties as well as elevated temperature behavior and metallography results are presented and discussed in the following sections.

5.1 XRD Analysis of Unmilled Powder Mixture

Unmilled elemental Al and Fe are mixed with a composition of 90 atomic % Al and 10 atomic % Fe. Such an unmilled mixture of elemental powder is scanned by XRD and the resulting profile is presented in Fig 5.1. Structural parameters obtained from the profile are indicated in Table 5.1, accordingly the following inferences could be drawn from the profile and table:

(i) Individual Al diffraction peaks (111, 311 and 331) and overlapped peaks of Al/Fe (200/110, 220/200, 222/211, 400/220 and 420/310 are narrow indicating typical FCC rich mixture.
(ii) Al (111) and Al/Fe (400/220) diffraction peaks possess highest (1526.21 cts) and least (53.61 cts) intensities (height) respectively.
(iii) The lattice parameter of unmilled Al obtained from 111 reflection is 0.4048 nm, microstrain is 0.03 %, relative intensity is 100 % and its integrated intensity is 162261.39. While, full width half maximum for the reflection is 0.2954^0 and the crystallite size is 60 um.
(iv) Quantitative analysis indicates 81 % of Al and 19 % of Fe, which goes to show the prominent presence of elemental Al.
(v) It is quite evident from the XRD profile analysis that the elemental phases are crystalline.

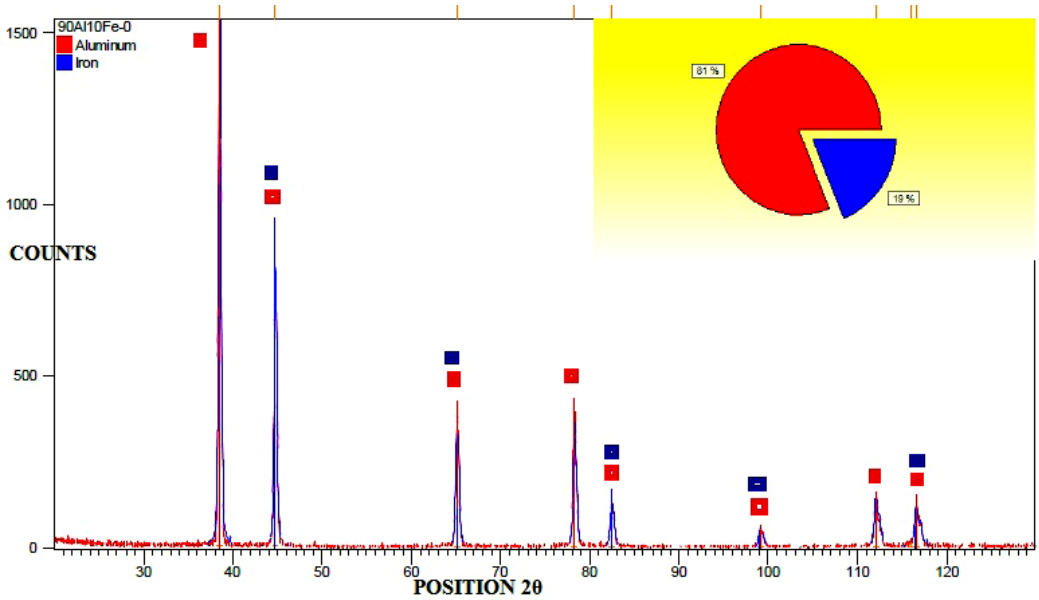

Figure 5.1 XRD pattern of unmilled mixture of elemental Al and Fe powder in an atomic ratio of 90:10

Table 5.1 structural parameters of unmilled powder mixture with an atomic ratio of 90:10

Peak Pos. 2θ	hkl/ phase	Height (cts)	FWHM 2θ	d-spacing (Å)	'D' nm	Micro strain %	Matched by Ref Pattern N0.
38.4883 *	111/ Al	1526.21	0.2954	2.33711	≥60 μm	0.03	03-065-2869
44.7351	**200**/ 110**Al**/ Fe	801.08	0.3211	2.02419	≥60 μm	0.137	03-065-2869; 03-065-4899
65.1131	**220**/ 200**Al**/ Fe	376.74	0.3266	1.43143			03-065-2869; 03-065-4899
78.2457	311/ Al	364.02	0.3169	1.22079			03-065-2869
82.4358	**222**/ 211**Al**/ Fe	130.97	0.3818	1.16902			03-065-2869; 03-065-4899
99.0715	**400**/ 220**Al**/ Fe	53.61	0.4070	1.01247			03-065-2869; 03-065-4899
112.0551	331/ Al	134.19	0.4320	0.92885			03-065-2869
116.5849	**420**/ 310**Al**/ Fe	131.90	0.4000	0.90544			03-065-2869; 03-065-4899

* At 2θ=38.4883^0, lattice parameter 'a'=0.4048 nm and Integrated Inetensity (II)=162261.39

5.2 Ball Milling of Elemental Powders

Elemental powders with an initial composition of 90 atomic % Al and 10 atomic % Fe (Al_{90}-Fe_{10} system) are mechanically alloyed by ball milling in an argon atmosphere using stainless steel grinding balls and milling jar (MM). Ball milling was done using Retsch PM-400 ball mill at 200 rpm while, the maximum length of ball milling time of elemental powder was 400 hours. Ball milling is interrupted at predetermined time interval in order to take out small quantity of powder for characterization purpose. Experimental details have been reported in section 3.2.1.

5.2.1 XRD analysis of ball milled powder

Each mixture of elemental powder subjected to ball milling for different length of milling time is scanned by XRD for θ-2θ scan. XRD profiles obtained from such scan for each ball milled powder sample as a function of milling duration are presented in Figs. 5.2 & 5.3 in addition to Figs. 7.58 and 7.59 in appendix. Structural parameters obtained from each profile are listed in Tables 7.18 to 7.20 in appendix. Further, to index the scanned profiles and identify the phases quantitatively and qualitatively, reference profile (Fig. 7.60 in appendix), list of matching pattern with reference code (table 7.21) along with peak list (Table 7.22) of reference profile from the xpert high score data base are utilised. In addition, a consolidated Table 5.2 is prepared which lists the structural parameters of ball milled powder as a function of milling time. Following inferences could be drawn from the values presented in Table 5.2 and Fig. 5.2:

(i) Al rich supersaturated solid solution (Al (Fe)) is formed as a consequence of ball milling time. Some of the prominent diffraction peaks of solid solution observed after varied ball milling times are 220, 33-2 and 620 (hkl).

(ii) Expansion of Al lattice (0.4055 nm) at the end of 100 hours of milling time compared to unmilled elemental Al (0.4048 nm) is observed indicating the diffusion of Fe atoms into Al lattice causing the formation of solid solution possessing FCC structure. With further increase in ball milling time to 250 hours brings about further lattice expansion (0.4088 nm) which saturates (0.4086 nm) at the end of 400 hours of milling time.

(iii) Compared to the diffraction peaks (FWHM=0.2954^0 & 0.3211^0 of 111 Al and 200/110 Al/Fe respectively) of unmilled powder mixture, broader peaks (FWHM=1.3966^0 & 1.8806^0) are observed in the ball milled powder indicating a profound crystallite refinement (7.6 & 5.4 nm) and increased lattice strain (1.698 & 1.973 %). During MA, the powder particles experience severe plastic deformation which ultimately leads to the particle and crystallite size refinement (5.6 nm from > 300 nm) and increase in the lattice strain (2.195 % from 0.03 %) with increasing milling time. These two effects cause broadening of the XRD peaks and consequent decrease in peak height. Furthermore, formation of **nano-amorphous** phases can significantly broaden the XRD peaks.

(iv) Al (111) diffraction peak shifts to higher Bragg angles (38.7007^0) while Al (Fe) solid solution peak (620) shifts to lower Bragg angle (44.3003^0) as a function of ball milling time compared to unmilled powder mixture. Such changes in structural parameters are due

to depletion of Al/Fe phases causing the growth of metastable supersaturated solid solution (Al(Fe)) as proved by XRD profile quantitative analysis (91 %). In addition, the integrated intensity (3249907.00) of solid solution peak (620) at 250 hours of ball milling time increased compared to the integrated intensity (3178291.5) of 100-hours of ball milled powder, which goes to prove the quantitative increase in solid solution phase.

(v) Furthermore, the decrease in the relative integrated intensity (159586.98) of Al peaks (111 and 200) of ball milled powders compared to the peaks (II=162261.39) of unmilled powder suggests the diminishing of Al phase leading to the growth of solid solution.

(vi) Not all Al is used up in the formation of solid solution at the end of 400 hours of ball milling time as observed from the visibility of Al diffraction peaks in the profile. Compared to Al diffusion in Fe, Fe diffusion in Al is limited to a large extent.

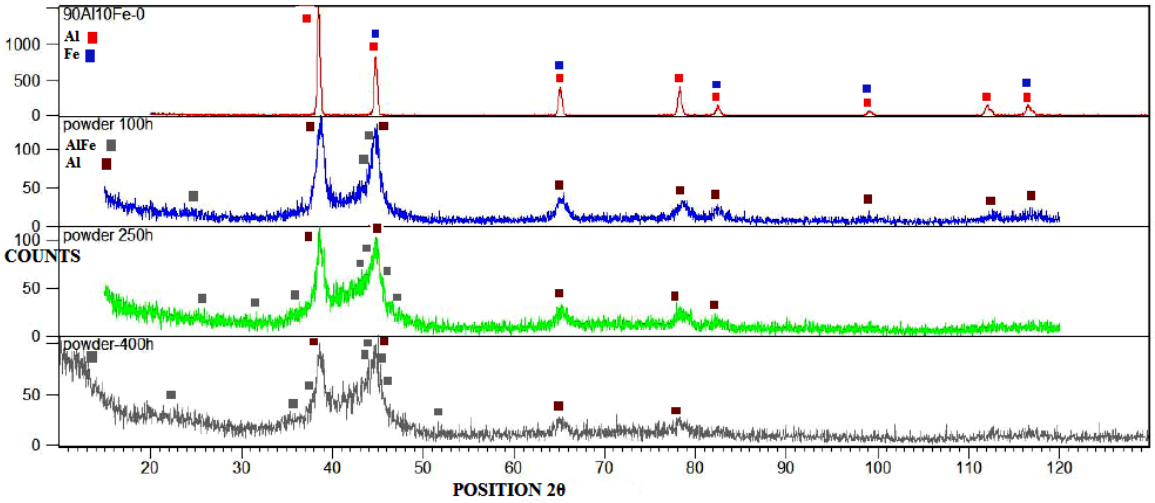

Figure 5.2 XRD pattern of unmilled and ball milled (100, 250 and 400 hours) powders of Al_{90}-Fe_{10} system

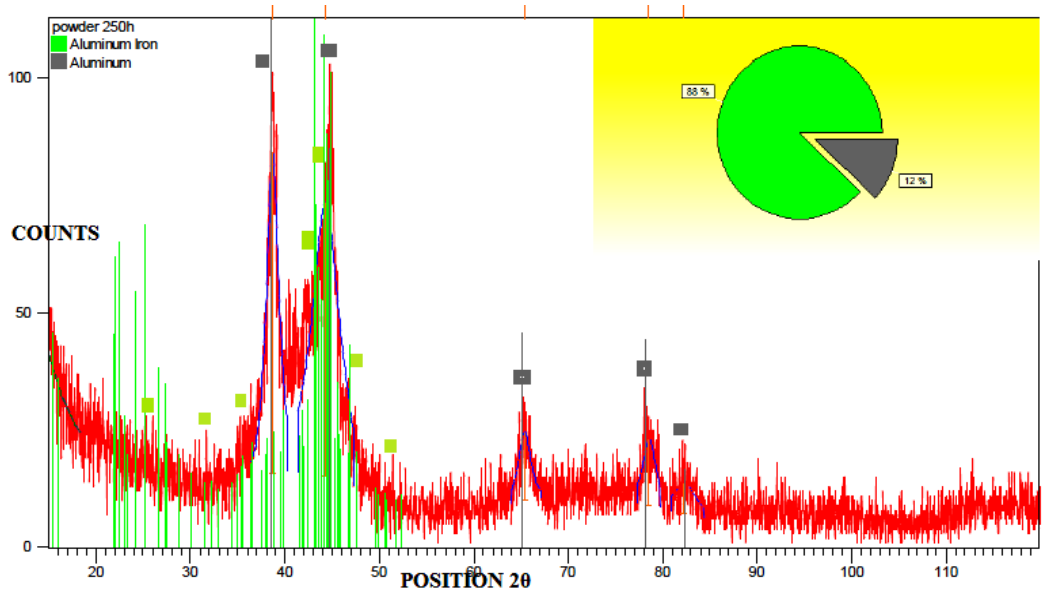

Figure 5.3 XRD pattern of powder MA by ball milling time of 250 hours.

Table 5.2 Structural parameters of MA powder as a function of ball milling time.

Milling time-hr	Peak Pos. 2θ	hkl/phase	Height cts	FWHM	'd' nm	'a' nm	II	'D' nm	Micro strain %
100	25.127	**220 Al(Fe)**			3.54130				
	38.6713	(33-2) Al(Fe)/ **111Al**	123.26	**1.3966**	2.32647		**159895.26**	**7.6**	**1.698**
	42.5493	**(712)/ Al (Fe)**	34.71	1.6877	2.12298				
	44.6665	**620 Al(Fe) / 200Al**	104.65	**1.8806**	2.02714	**0.4055**	**3178291.5**	**5.4**	**1.973**
	65.2228	220Al	33.83	3.7668	1.42929				
250	25.127	**220 Al(Fe)**			3.54130				
	38.6668	(33-2) Al(Fe)/ **111Al**	68.42	**1.5964**	2.32673		159895.26	**6.5**	1.951
	44.2783	**620Al(Fe) /200Al**	58.42	**3.5546**	2.04401	**0.4088**	**3249907.00**		
	65.2977	220Al	14.60	1.5546	1.42783				
400	13.572	111 Al(Fe)			6.51900				
	22.423	003 Al(Fe)			3.96180				
	38.7007	332Al(Fe) /**111Al**	60.92	**1.7912**	2.32477		**159586.98**	5.6	2.195
	44.3003	**620Al(Fe)** /200Al	59.02	**3.3969**	2.04304	**0.4086**	**3247078.6**		
	65.2089	220 Al	13.49	1.6600	1.42956				

5.2.2 DSC analysis of ball milled powder

Thermal effects on the powder mechanically alloyed (by ball milling) in Ar atmosphere utilizing stainless steel milling vials and balls is investigated using DSC. The profiles of DSC experiments are presented in Fig.5.4 and Fig.5.5 and the following inferences could be drawn from the profiles:

1) Mechanical alloying of elemental powders in high energetic ball mill induces amorphous structure as noted by XRD analysis, thus a distinct glass transition temperature prior to crystallisation and a narrow supercooled liquid region can be observed in all the powder samples.

2) The glass transition temperature (Tg), the onset temperature of crystallization (Tx), the peak temperature of the crystallization reaction Tp are indicated in the Fig 5.4. However, the width of the supercooled liquid region ΔTx influences the stability of that phase. The larger the ΔTx (=Tx - Tg), greater is the thermal stability of the super-cooled liquid against crystallization (May J. E. et al. 2004).

3) Slight shift in the exothermic peak (T_P) is observed with increase in ball milling duration from 100-h to 400-h, such a shift in peak is due to the significant amount of Al present in the ball milled powder, nanosized Al crystallites serve as nucleating sites for crystallization.

4) The exothermic peak (T_P) is attributed to the precipitation of $Al_{76}Fe_{24}$ intermetallic from the amorphous phase. Meanwhile, the endothermic peak at 700^0 C could be due to the melting of Al.

5) Peak (320^0 C) related to alloying of elemental phases almost vanished after ball milling time of 400 hours compared to lower milling time, which suggests the presence of minute quantity of elemental phases in the powder processed at higher milling time.

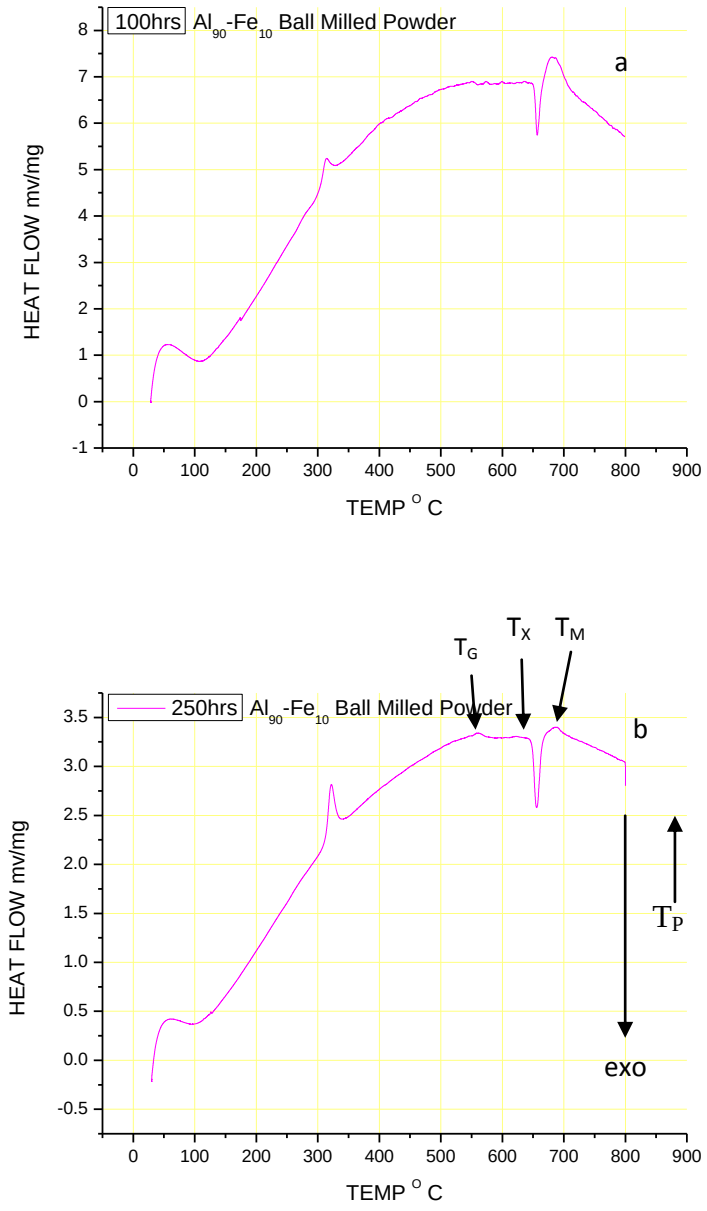

Figure 5.4 DSC curves of heat flow as a function of temperature of ball milled powders, a) milled for 100 hours and b) milled for 250 hours

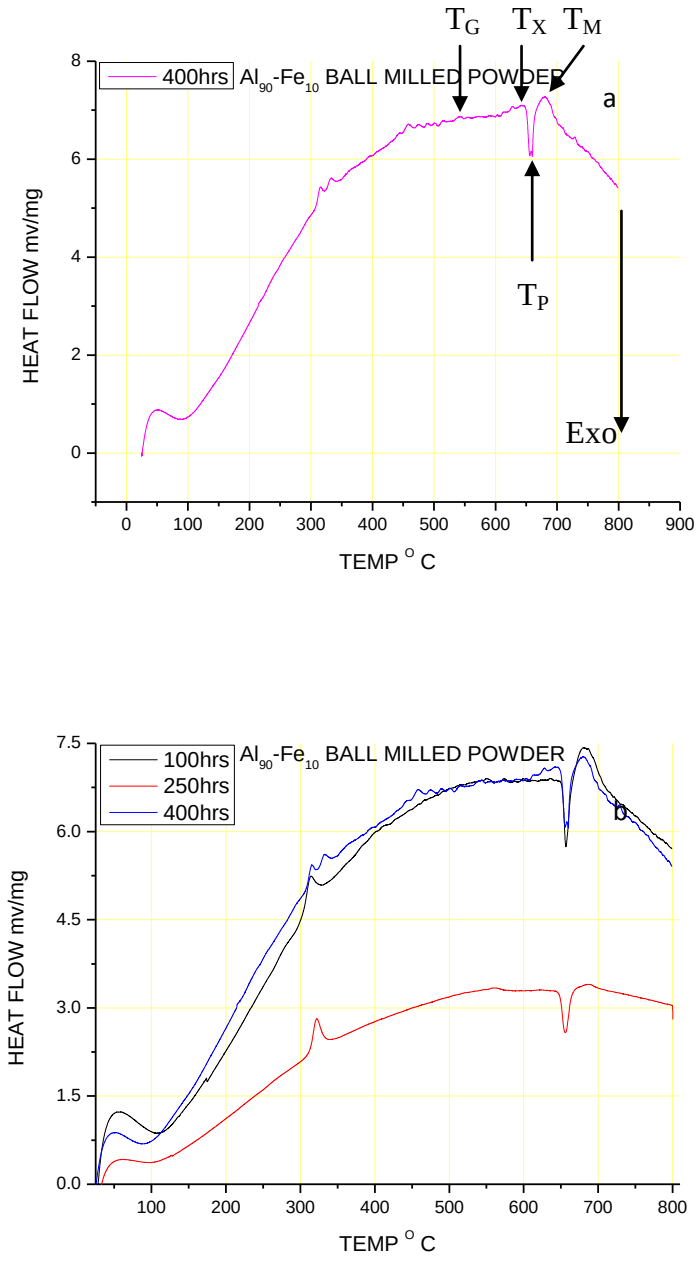

Figure 5.5 DSC curves of heat flow as a function of temperature of ball milled powders, a) milled for 400 hours and b) combined curves of all three ball milled powders

5.2.3 Magnetic features of ball milled powder

Room temperature magnetic properties of ball milled powder as a function of milling time is obtained by utilizing VSM, the results are obtained as hysteresis loops (M-H curves) shown in Fig 5.6 and Fig.5.7. Magnetic parameters (Table 5.3) like M_S, H_C and M_R are obtained by analysing M-H (M-magnetisation, H-applied field) curves. By analyzing M-H curves and magnetic parameters, the following inferences could be drawn:

(i) Coercivity (H_C) obtained at 100-h of ball milling time was 418.52 Oe, reaching a maximum value of 444.15 Oe at the end of 250-h of milling time only to decrease to a value of 294.10 Oe at 400-h of milling time. These results show that all the MA powder samples possess excellent higher ($H_C \geq 294.10$ Oe) hard magnetic properties (H_C >125.664 Oe) with low M_S. The low value of M_S ($\leq$ 8.432 emu/gms) is due to the higher atomic percent (90 %) of Al in the mechanically alloyed Al-Fe solid solution. Another possible reason for the lower M_S is the presence of small quantities (9 %) of unalloyed Al even after mechanical alloying to 400 hours of milling duration as reported in section 5.2.1.

(ii) Longer ball milling time of 400 hours resulted in lower H_C (294.10 Oe) among the ball milled powders, such an observation suggests lower percent of elemental phases (Fe) as well as crystallite size (5.6 nm) for the powder is well below critical particle size.

(iii) However, among the powder samples ball milled in toluene liquid and tungsten carbide milling media of Fe_{50}-Al_{50} system, only 30-h, 40-h, 50-h and 65-h powders possess H_C greater than 125.664 Oe. The H_C increases from 128.5 Oe at 30-h of milling time to 203 Oe at the end of 50-h of milling time, only to decrease to a value of 191 Oe at 65-h of milling time. Thus, these ball milled powders too possess hard magnetic properties but on the lower side of H_C ($\leq$ 203 Oe). In addition, higher M_S is observed as reported in section 4.2.3. The higher M_S ($\geq$ 76.5 emu/gms) is attributed to the higher atomic % (50 %) of Fe and disordered phase prevailing in the mechanically alloyed Fe-(Al) solid solution powder.

(iv) Contrary to the previous powders, sample ball milled for 300 hours in argon atmosphere with stainless steel milling media is the lone exception exhibiting hard magnetic property (low H_C of 151.64 Oe and high M_S of 67.38 emu/gms) among the ball milled powders in its category (Fe_{50}-Al_{50} system).

(v) Broader M-H curves presented in Figure 5.6 indicate that the ball milled powders (Al_{90}-Fe_{10} system) are magnetically hard compared to narrow M-H curves of Al_{50}-Fe_{50} system shown in section 4.2.3 and 4.4.3. Increasing the aluminium percentage from 50 to 90 atomic % during ball milling of elemental (Al & Fe) powder, induces a transition from soft magnetic properties to magnetically hard one, although 300-hours (Al_{50}-Fe_{50} argon and stainless steel media) in addition to 30-h, 40-h, 50-h and 65-hours (Al_{50}-Fe_{50}, toluene and tungsten carbide media) ball milled powders show exception with hard magnetic properties on the lower side ($H_C \leq 203$ Oe).

(vi) Higher H_C in the Al_{90}-Fe_{10} system is due to finer grain size (5-8 nm), greater magnetic anisotropy attained as a result of more severe lattice defects introduced in the form of dislocations as observed in the TEM images presented in Figs 5.9 and 5.10.

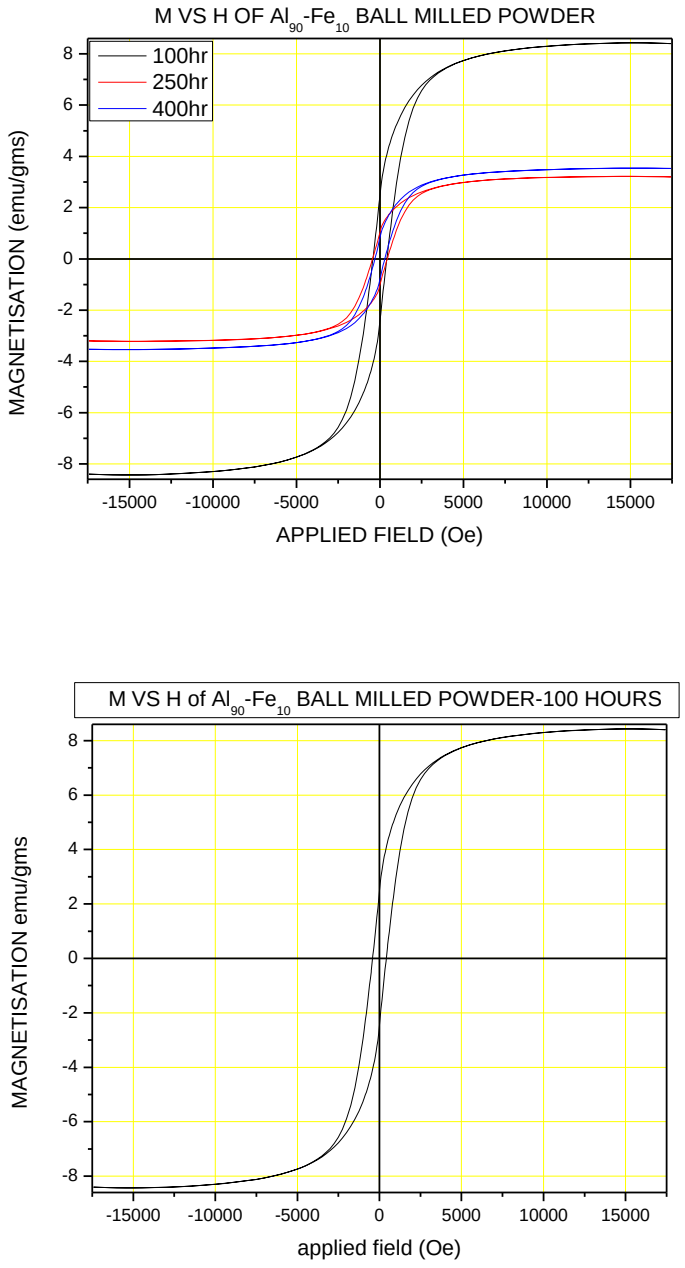

Figure 5.6 room temperature hysteresis loops of; combination of the three ball milled powders and powder ball milled for 100 hours

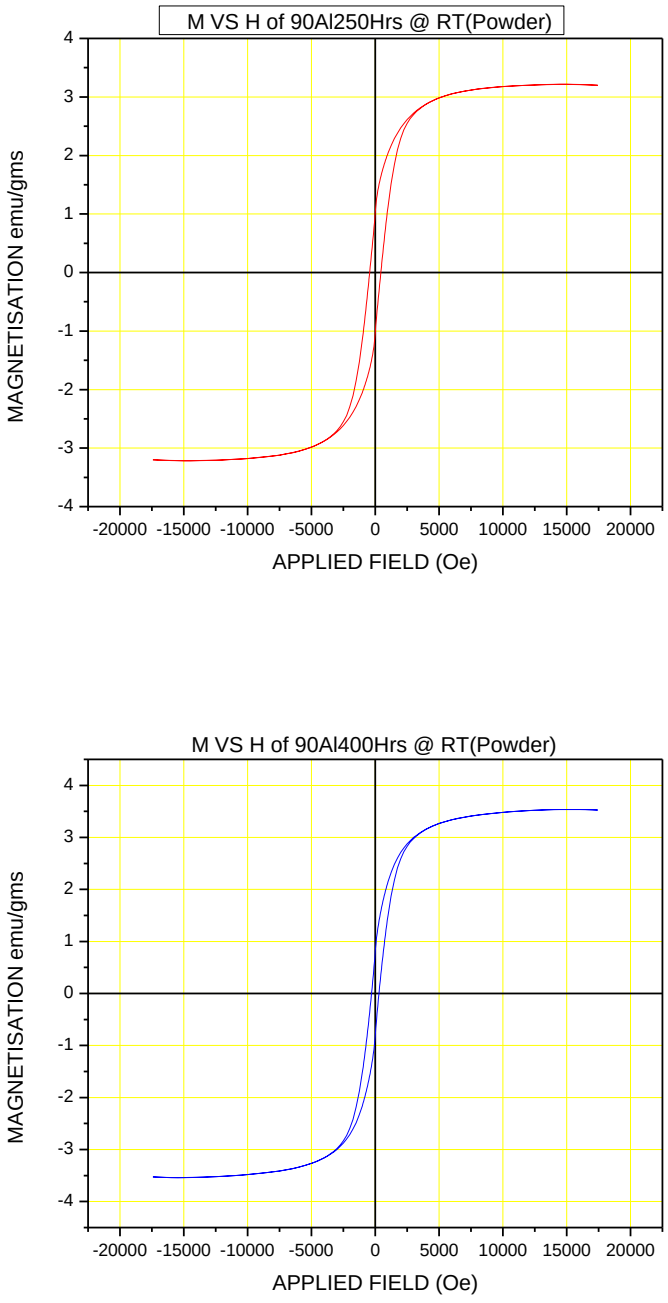

Figure 5.7 Room temperature hysteresis loops of; powder ball milled for 250 hours and powder ball milled for 400 hours

Table 5.3 Room temperature magnetic parameters of MA powders as a function of ball milling duration

Sample Name	Saturation Magnetisation (M_S) , ie Moment measured in Maximum field (emu/gm)	Remanent Magnetisation (M_R) (emu/gm)	Coercivity-H_C (Oe)	Sample weight (gms)
90Al100hrs Powder	8.432	2.467	418.52	0.0452
90Al250hrs Powder	3.216	1.039	444.15	0.0611
90Al400hrs Powder	3.539	0.8207	294.10	0.0537

5.2.4 Elevated temperature magnetic analysis of milled powder

Temperature dependent magnetization curves of mechanically alloyed powder at different ball milling time are shown in Fig 5.8. From these curves following inferences can be drawn:

(i) Less than 220 ^{0}C, there is not much variation in magnetization for all the ball milled powder samples; such low temperature may not cause any changes in the existing phases.

(ii) Magnetic variation begins at 220 ^{0}C in the form of decreasing low slope in 100-h milled powder, while the decreasing slope is steep beyond 320 ^{0}C reaching a paramagnetic phase at 375 ^{0}C. Presence of higher amount of unalloyed elemental Al and Fe is the main cause for higher magnetization at lower temperature compared to other ball milled powder samples. Alloying of elemental phases by diffusion (Fe atoms migrate into Al lattice) causes a steep reduction in magnetization beyond 320 ^{0}C. Thus, Al atoms act as an obstacle between Fe atoms hindering the direct ferro-magnetic coupling between Fe-Fe atoms causing a decrease in magnetism.

(iii) Not much variation in magnetization is seen less than 300 ^{0}C in 250-h and 400-h ball milled powders, however beyond 330 ^{0}C steep decrease is observed in 250-h ball milled powder due to alloying of elemental phases. While decrease is not that steep due to low amount (9 %) of elemental phases prevailing in the 400-h milled powder.

(iv) Greater percentage of Al rich solid solution is the reason for lower magnetism in 250-h and 400-h ball milled powder compared to higher percent of unalloyed elemental phases in 100-h milled powder. However, greater disorder/amorphous solid solution in 400-h milled

powder could be the reason for slightly higher magnetism compared to 250 hour ball milled powder.

(v) Infact, all the ball milled powders possess paramagnetic phase throughout the temperature range measured, transition of solid solution to intermetallic phase coupled with Al rich solid solution at room temperature and Al rich intermetallic phase at elevated temperature could be the reason for such a magnetic behavior.

(vi) DSC analysis (section 5.2.2) has shown the formation of intermetallic (600 ^{0}C) as well as alloying of elemental phases. While XRD analysis (5.2.1) has identified elemental as well as solid solution phases.

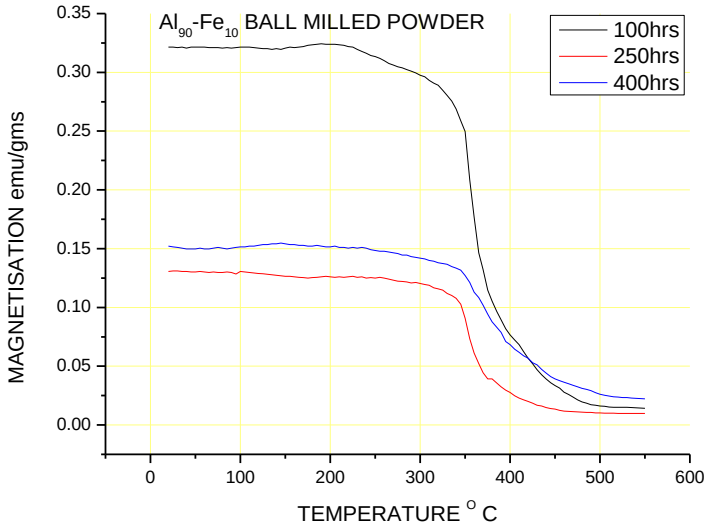

Figure 5.8 ball milled powders: Variation of magnetization with temperature

5.2.5 TEM analysis of ball milled powder

Figures 5.9 (a and b) shows TEM micrographs of MA powders synthesized at 100-hours and 250-hours of ball milling time respectively. Micrographs indicate severe plastically deformed structure with the possible appearance of dislocations with high angle grain boundaries in the form of needles. The average crystallite size (grain boundary to boundary) observed from the TEM micrograph is around 15 nm, thus the crystallite size estimated is almost identical with the XRD result. The morphology of ball milled powder looks like cellulose-cotton like structure (Fig. 5.10 a) which is almost an amorphous one, SADP obtained by TEM in Figure 5.10 b shows broad diffuse halo rings indicating an amorphous structure. It appears as though the structure is not

entirely amorphous but does contain grain boundaries and dislocations as observed from the micrographs. The XRD results also indicate such a structure in the MA powder samples (ball milled duration of > 100-h).

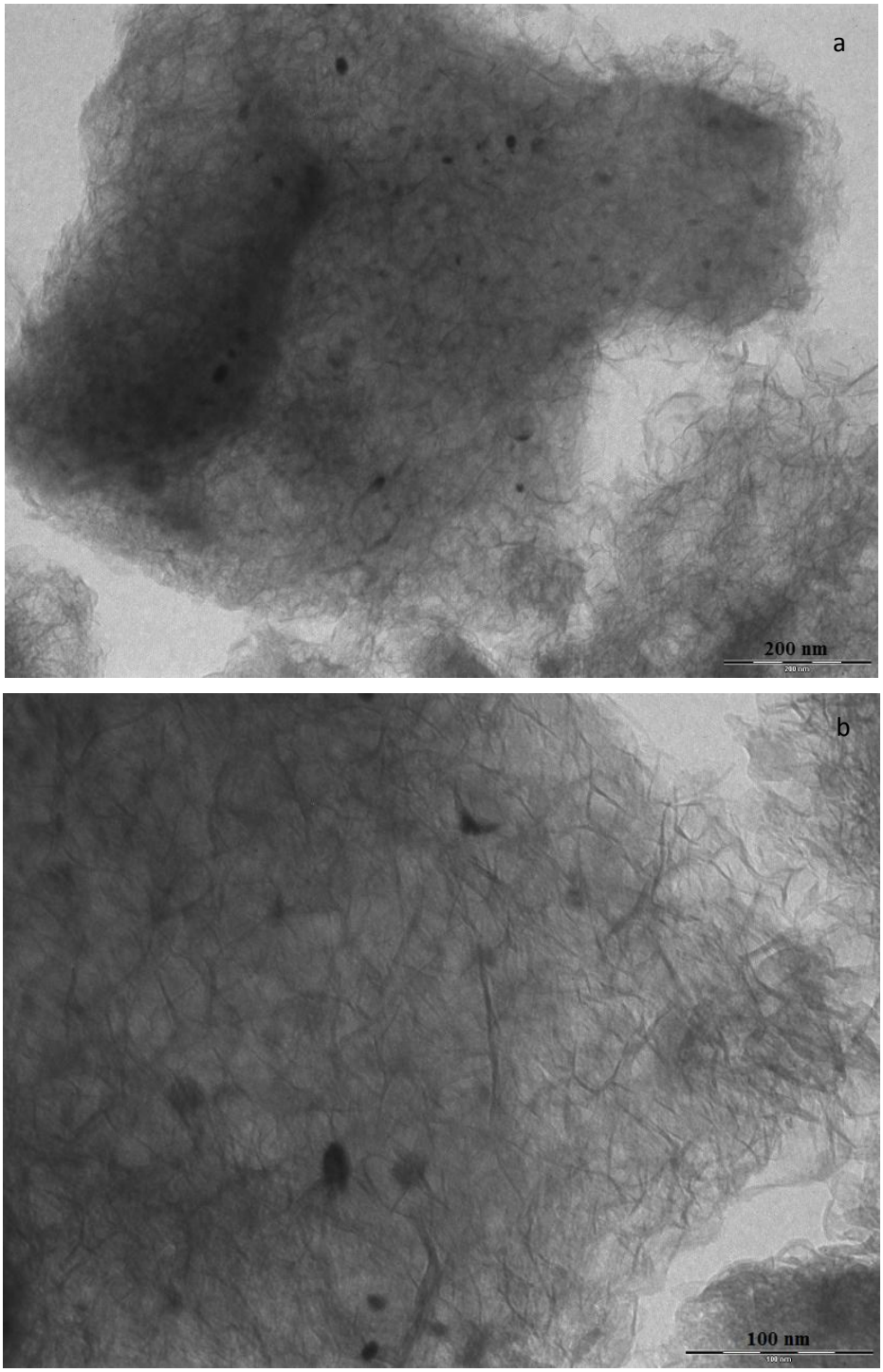

Figure 5.9 TEM images of ball milled powders; **a)** Large regions (dark) of unalloyed Fe as well as alloyed Fe along the grain boundaries 100-h MA powder sample. **b)** Presence of Fe along the grain boundaries in 250-h MA powder sample.

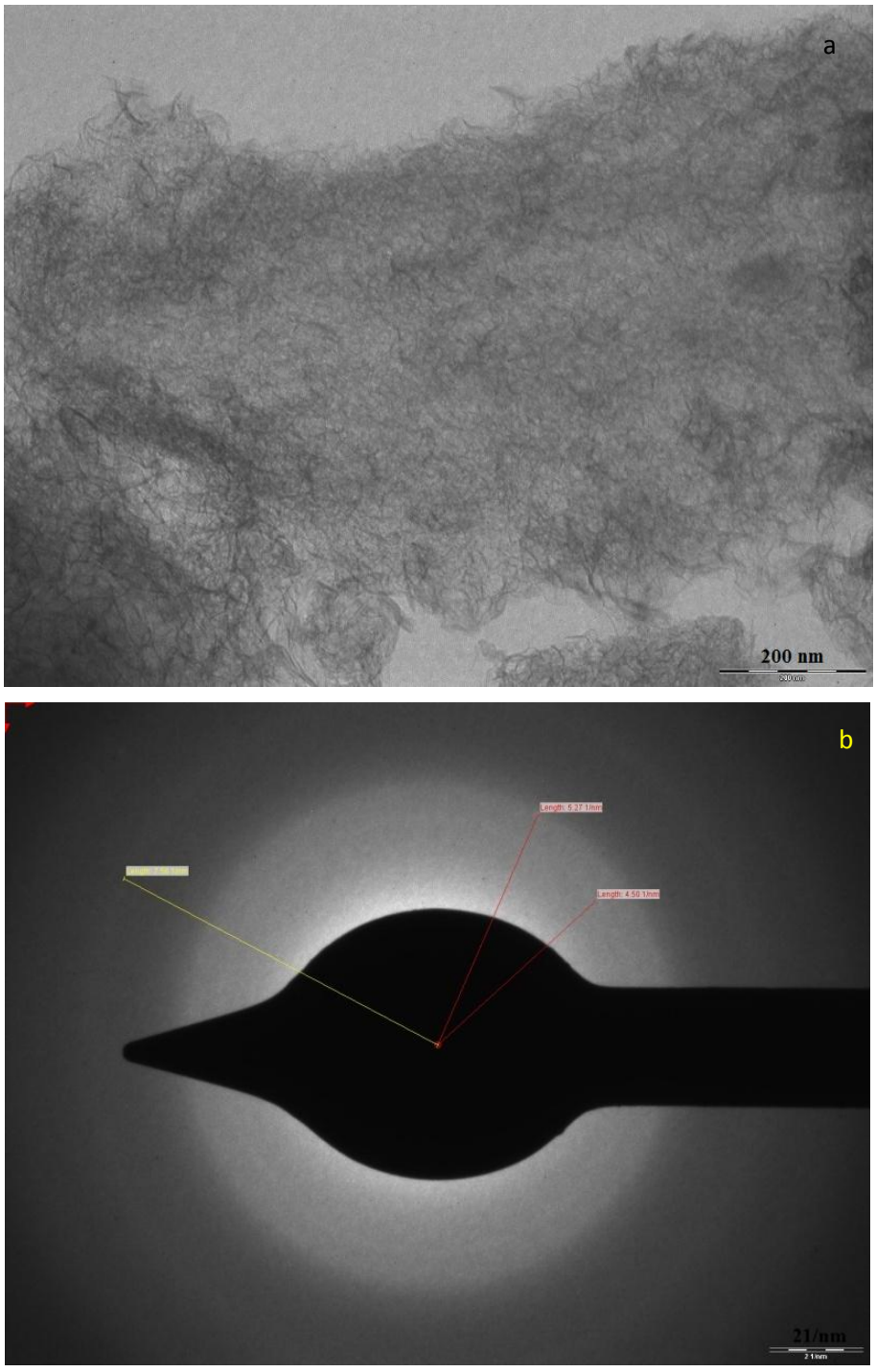

Figure 5.10 TEM images; **a)** cotton like amorphous structure of powder MA for 400-h. **b)** Selected area diffraction pattern

5.2.6 Consolidation by ECAP-BP

Mechanically alloyed nanostructured powders synthesized by ball milling have limited practical applications. Thus, ball milled powders have been consolidated into bulk solid form for useful practical applications. However, the challenge in front of the researchers is to retain the nanostructure and non equilibrium metastable phases in the consolidated solid material. Bulk solid

material possessing nanostructured non equilibrium phases are superior in structural, mechanical, and magnetic properties compared to microcrystalline counterparts. Thus, this section concentrates on ECAP-BP consolidation of mechanically alloyed powders (synthesized by ball milling). Many interesting and critical metallurgical events could unfold during the consolidation process, this research work captures such important events. Ball milled powders synthesized at different duration of milling time (100-h, 250-h and 400-h) and their characterizations are reported in section 5.2; these mechanically alloyed powders are consolidated by ECAP-BP as reported experimentally in section 3.2.2.1. The consolidated pellets (Fig. 5.11 'a') are subjected to XRD, DSC, VSM and nanoindentation analyses to investigate phase changes, structural, texture, magnetic and mechanical properties. Further, the pellets are subjected to metallography preparations (Fig. 5.11 'b') and then analysed by OM and SEM with EDS to investigate the phases, morphology, plastic deformation and composition. The results of the above mentioned analysis is reported and discussed in the following sections:

Figure 5.11 a) ECAP-BP consolidated pellets, b) Portion of the pellet hot mounted on polyfast for various analyses

5.2.6.1 XRD analysis of pellets

ECAP-BP consolidated **pellets** are subjected to XRD experiments resulting in three profiles presented in Figure 5.12 and 5.13. Analysing these profiles, various structural parameters are obtained as tabulated in tables 7.23 to 7.25 in appendix for each category of pellets. From the XRD profiles and structural parameters (Table 5.4), following inferences could be drawn:

- Metastable solid solution phase of ball milled powder transforms to a more stable $Al_{76}Fe_{24}$ compound of monoclinic structure in all the pellets.

- Diffraction peaks related to compound (2θ=44.5830, FWHM=1.0937^0) and elemental Al (2θ=38.4063, FWHM=0.4395^0) are much narrow and shift to lower Bragg angles compared to 100-h ball milled powder as a consequence of transformation.

- However, lattice contraction (0.4062 nm) of Al is observed in the pellet compared to that of ball milled (MA) powder (0.4088 nm), contraction of lattice triggers grain growth and ordering

- In addition, lattice expansion occurs compared unmilled elemental Al (0.4048 nm), such an expansion suggests Fe diffusion into Al lattice and formation of Al rich compound.

- The intensity (77.85 %) of elemental Al peak (111) has been reduced relative to the intensity (100 %) of AlFe peak (040) which has increased.

- Above mentioned changes in structural parameters are observed in all the three analysed pellets.

- The narrow diffraction peaks in addition to the formation of $Al_{76}Fe_{24}$ compound is due to the elevated temperature processing involved during ECAP-BP consolidation of ball milled powder.

- Integrated intensities (162983.93 and 163087.14) in all the pellets are greater than the ball milled powders as a consequence of peak narrowing. Such changes are due to increased crystallinity, grain growth (10 nm) and decreased lattice strain (1.259 %).

- AlO formation is due to the oxygen contamination during the consolidation. Quantitative analysis of the profiles indicates that the $Al_{76}Fe_{24}$ phase is the largest among the ingredients in the pellets.

- XRD profiles exhibit slight halo related to amorphous structure, thus the pellets (250-h and 400-h) are not entirely crystalline ($Al_{76}Fe_{24}$) but slightly amorphous (Al and AlO) too.

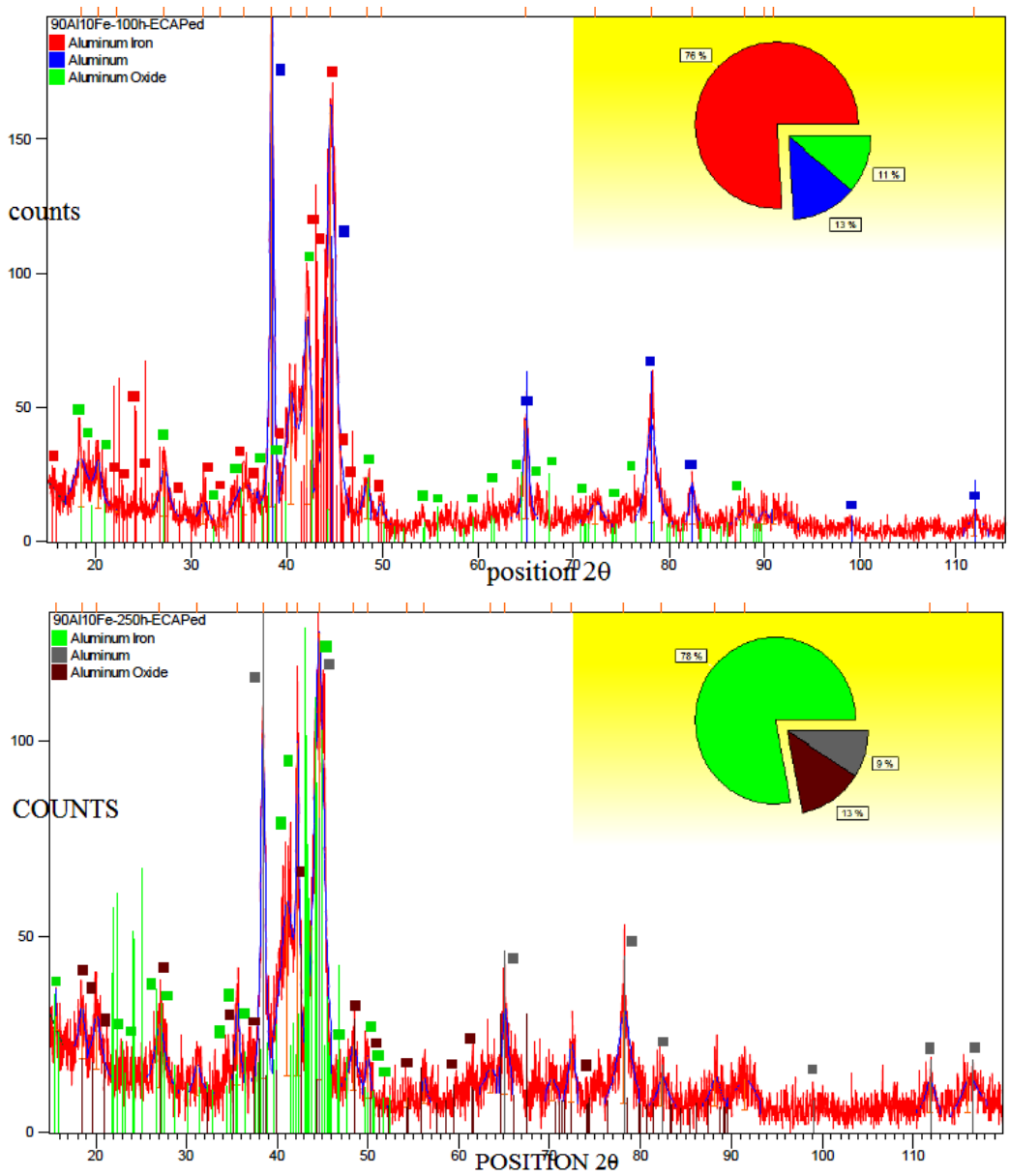

Figure 5.12 XRD pattern of pellets synthesized by ECAP-BP consolidation of powder ball milled for 100, and 250 hours

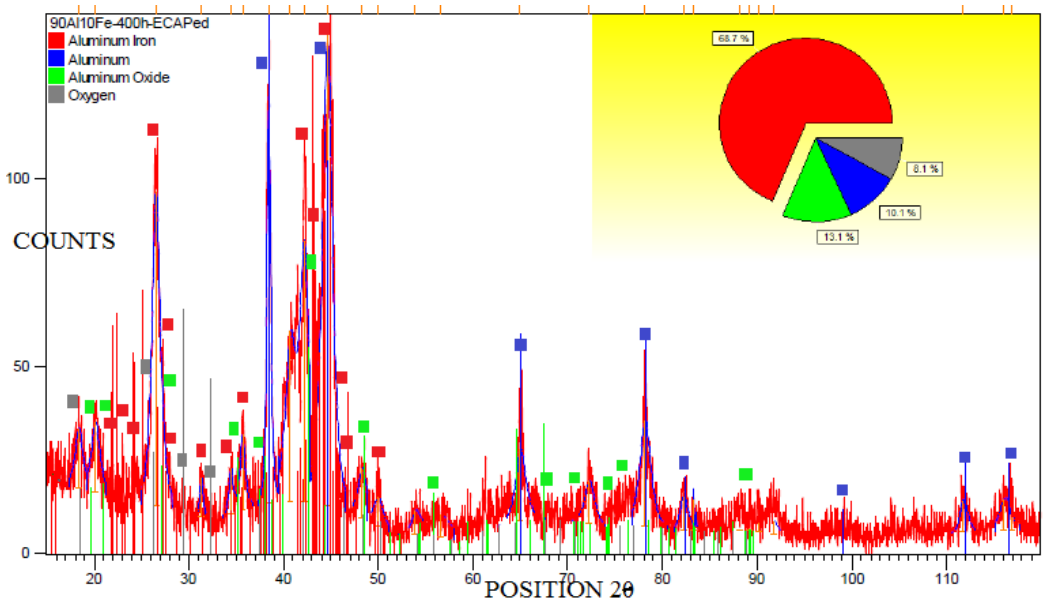

Figure 5.13 XRD pattern of pellet synthesized by ECAP-BP consolidation of powder ball milled for 400 hours

Table 5.4 Structural parameters of ECAP-BP ($Al_{90}Fe_{10}$ system) consolidated pellets

Type of pellet	Peak Pos. $2\theta^0$	phase	FWHM $2\theta^0$	'd' nm	'a' nm	II*	'D' nm	Micro strain %	Rel Int %
100-h	38.4063	111Al	0.4395	0.234191	0.4056	162983.93			100.00
	44.5830	040Al Fe/**Al 200**	1.0937	0.203074	**0.4062**		**10.7**	**1.122**	**82.19**
250-h	38.3986	111Al	0.5567	0.234237	0.4057	163087.14			77.85
	44.5718	040AlFe/ **Al 200**	**1.2440**	0.203123	**0.4063**		**9.0**	**1.287**	**100.00**
400-h	38.4019	Al111	0.4525	0.234217	0.4057	163087.14			86.19
	44.5931	040AlFe/ **Al200**	**1.2194**	0.203030	**0.4061**		**9.3**	**1.259**	**100.0**

*II- Integrated Intensity, a-lattice parameter, D-crystallite size, d-planar spacing. FWHM-full width half maximum

5.2.6.2 DSC analysis of ECAP-BP pellets

It can be seen from the Differential Scanning Calorimeter (Fig. 5.14) curves that crystallization of the partially amorphous phase occurs as indicated by the temperature (T_X), which is the onset of crystallization. While there is no glass transition (T_G) prior to crystallization as was the case during heating of the ball milled powders (section 5.2.2) in a calorimeter. The absence of glass transition is attributed to the elevated temperature (450^0 C) attained during ECAP-BP consolidation resulting in a decrease in amorphous content in the pellets. The endothermic peak (T_M) around 700^0 C could be due to the melting of Al during heating. T_P is the exothermic peak temperature (660^0 C) at which crystallization reaction occurs.

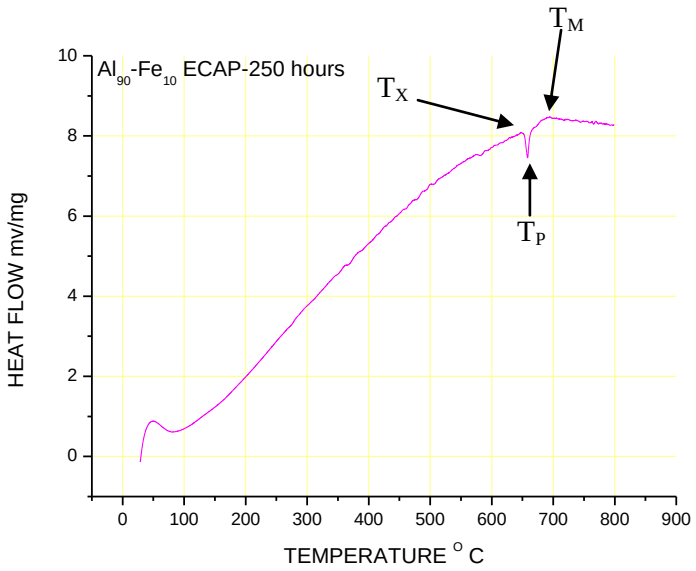

Figure 5.14 DSC; heat flow as a function of temperature curve of ECAP-BP consolidated pellet

5.2.6.3 Magnetic properties of pellets

Hysteresis loops in Fig 5.15 and magnetic parameters listed in Table 5.5 were obtained using VSM, these results form the basis for the inference that can be drawn as follows:

(i) The H_C decreases from 107.63 Oe for 100-h pellet to 92.70 Oe for 250-h pellet to remain almost constant at 92.84 for 400-h pellet. While M_S shows a different trend as it decreases from 0.4336 emu/gm for 100-h pellet to 0.2931 emu/gm for 250-h pellet and subsequently increases to 0.6582 emu/gm for 400-h pellet. From these results and also from the shape of the M-H curves, it is evident that all the pellets possess soft magnetic (H_C < 125.64 Oe) properties. In comparision, the ball milled powders (Al_{90}-Fe_{10} system) from which these pellets were consolidated possessed hard magnetic properties (section 5.2.3). Such differences in magnetic properties are due to the compound formed by additional heating done under pressure during consolidation process. However, defects such as pores and powder interfaces in the structures formed in the pellets contribute to decreased M_S and H_C.

(ii) Low values of M_S ($\leq$ 0.6582) in the consolidated pellets compared to ball milled powder is also due to the reduction in elemental Fe as a consequence of diffusion into Al lattice by plastic deformation during elevated temperature powder consolidation by ECAP-BP.

(iii) Ball milled powders possess higher amount of magnetic amorphous solid solution in addition to elemental phases (Fe and Al). While, the pellets possess higher amount of paramagnetic compound ($Al_{76}Fe_{24}$) in addition to minute quantities of elemental phases.

(iv) Finer crystallite size (≤ 7.6 nm) in ball milled powders compared to coarser crystallite size (≥ 9 nm) of pellets could also be the reason for possible reduction in H_C and M_S. Among the pellets, higher H_C (107.63 Oe) in 100-h pellet is due to some magnetic anisotropy prevailing as a result of least lattice strain (1.122 %) introduced during consolidation.

(v) ECAP-BP pellets of Al_{50}-Fe_{50} system possess higher magnetic properties than pellets of Al_{90}-Fe_{10} system due to disordered AlFe and ferromagnetic $AlFe_3$ phases present.

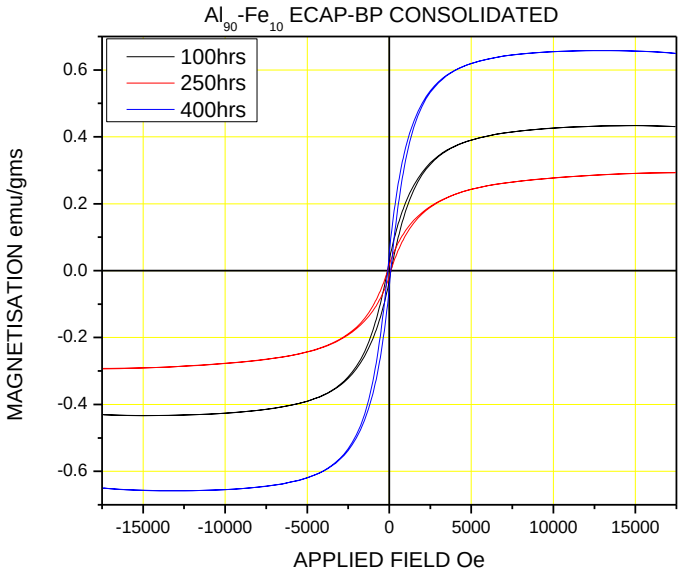

Figure 5.15 Hysteresis loops (M-H curves) of ECAP-BP consolidated pellets.

Table 5.5 Room temperature magnetic parameters of ECAP-BP consolidated pellets

Sample Name	Saturation Magnetisation , ie Moment measured in Maximum field (emu/gm) (M_S)	Remanent Magnetisation (emu/gm)	Coercivity (Oe) H_C	Sample weight (gms)
90Al100hrs Solid	0.4336	0.02885	107.63	0.0248
90Al250hrs Solid	0.2931	0.01615	92.70	0.0500
90Al400hrs Solid	0.6582	0.0499	92.84	0.0196

5.2.6.4 Elevated temperature magnetic analysis of pellets

Temperature dependent magnetization curves of ECAP-BP consolidated pellets are shown in Fig 5.16, these curves were obtained using VSM and the following inferences could be drawn from these curves:

(i) Slight enhancement of magnetisation is observed in the temperature range of 100 ^{0} - 320 ^{0}C. Such a magnetic trend is probably due to the elongated shaped precipitates ($Al_{76}Fe_{24}$ compound). Presence of elongated precipitates shown in Fig 5.16 will increase the directional magnetization component in proportion to the external field.

(ii) Among the pellets, 400-h pellet possesses highest room temperature magnetization probably due to greater amorphisation as indicated in the XRD profile. The decrease in magnetization below 350 ^{0}C is low while it is steep beyond 350 ^{0}C.

(iii) The amorphous and crystalline phases of the pellets are shown in XRD profiles and also indicated in the SEM micrographs. Approximately in the temperature range of 600 ^{0} to 650 ^{0}C, amorphous phase in the pellets undergo a transition to paramagnetic intermetallic phase. The DSC curves have indicated an exothermic peak related to the crystallization reaction from an amorphous phase at a temperature of 660 ^{0}C (T_P) and the onset of crystallization temperature (T_X) at 630 ^{0}C. The alloying of unalloyed elemental phases too contributes to the decrease in magnetization with increase in temperature.

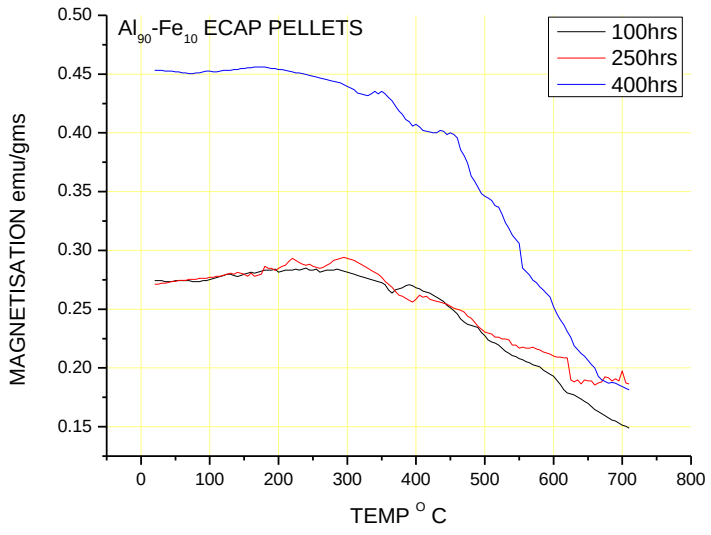

Figure 5.16 Temperature dependent magnetization curves of ECAP-BP consolidated pellets

5.2.6.5 Optical microscopy characterization

Optical micrograph of 100-h pellet is shown in Fig.5.17 (a), minute pores along with compacted regions is observed in the vertical channel when the forward pressure is less than the backward pressure. However, in the same figure, fractured equiaxed particles along with larger pores are observed. Compaction produced in the vertical channel moves to horizontal channel when the forward pressure exceeds the preset back pressure causing fracture of fragmented powder to fine particles and increase in pore size.

Higher consolidation temperature (450 ^{0}C) and back pressure (300 MPa) causes severe shear plastic deformation in the horizontal channel in addition to higher compaction of powder in the vertical channel. Therefore greater compaction pressure in the vertical channel ensures reduced porosity with increased bonding between the particles. Thus, finer grains in nanosize regime along with increased grain boundary areas are formed in the horizontal channel which is not visible in the optical micrographs of 250-h pellet in Fig 5.17 (b)

Shearing exposed fresh and clean surfaces of the particles and compressive stress ensured good contact between them while bonding occurred spontaneously without needing extremely high temperatures and high pressure as seen in Fig 5.18 (a). Improvement of relative density of compact produced in the vertical channel is associated with localized fragmentation, mechanical interlocking and realignment of particles. Further, reduction in the porosity due to shear deformation is clearly visible qualitatively by optical microscopy.

Microstructure (Fig. 5.18 (b)) mainly consists of $Al_{76}Fe_{24}$ compound, elemental Al, Fe and oxides in the 400-h pellet, quantitative analysis indicates 68.7 % of compound phase compared to other phases. Reduced processing temperature (300 ^{0}C) causes greater porosities and less dense structure.

ECAP-BP consolidation induces compaction and fracture of the compacted particles in the two (vertical and horizontal) channels as shown in Fig 5.19.

Present research has demonstrated beyond doubt that excellent bonding between particles can be achieved at low temperatures 450^0 C with back pressure of 300 MPa, much lower than normal sintering temperature. No canning and pre-compacting of powder were needed before ECAP-BP.

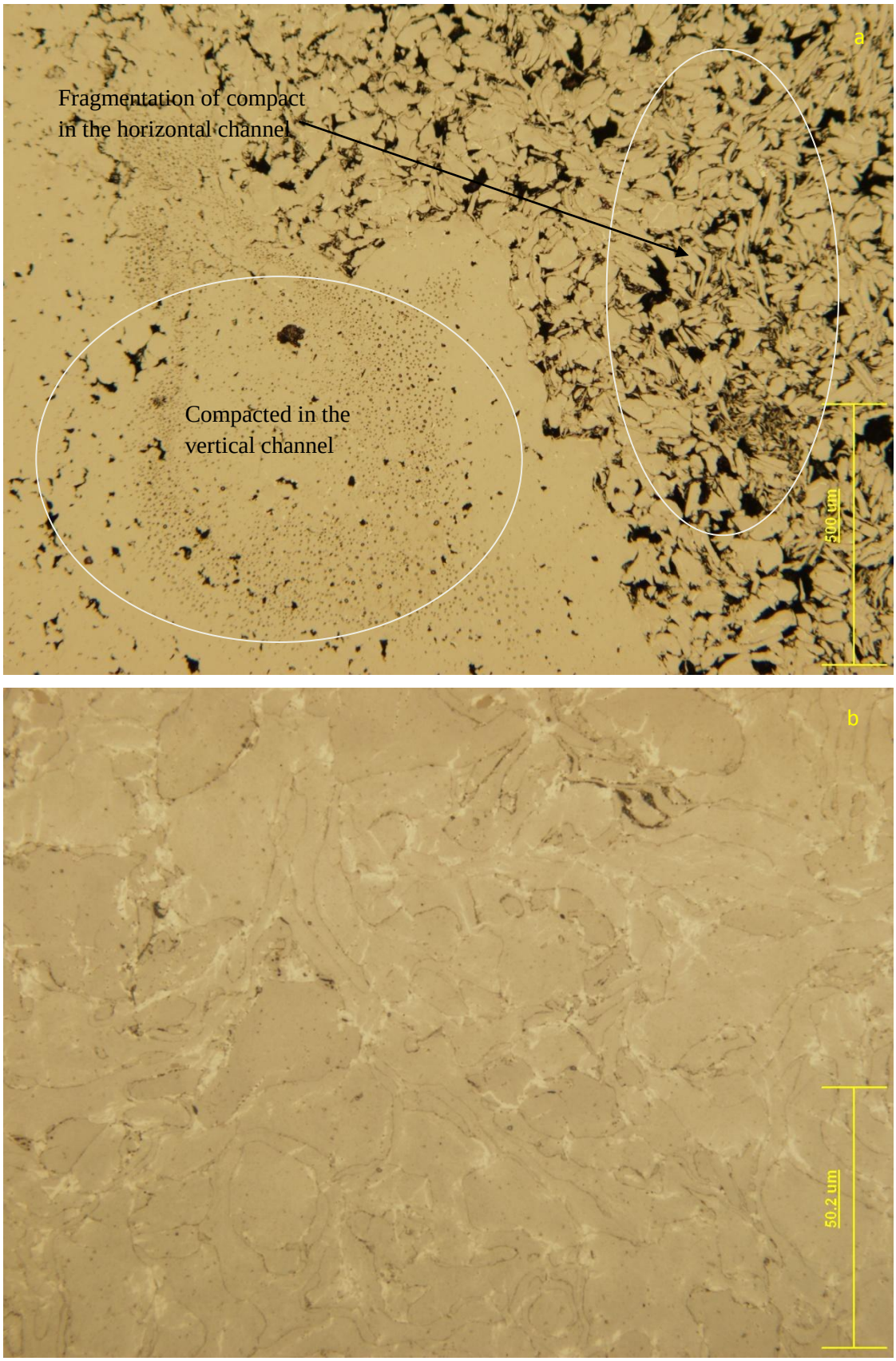

Figure 5.17 Optical micrographs of ECAP-BP consolidated pellets a) consolidated from powder milled for 100-h b) consolidated from powder milled for 250-h

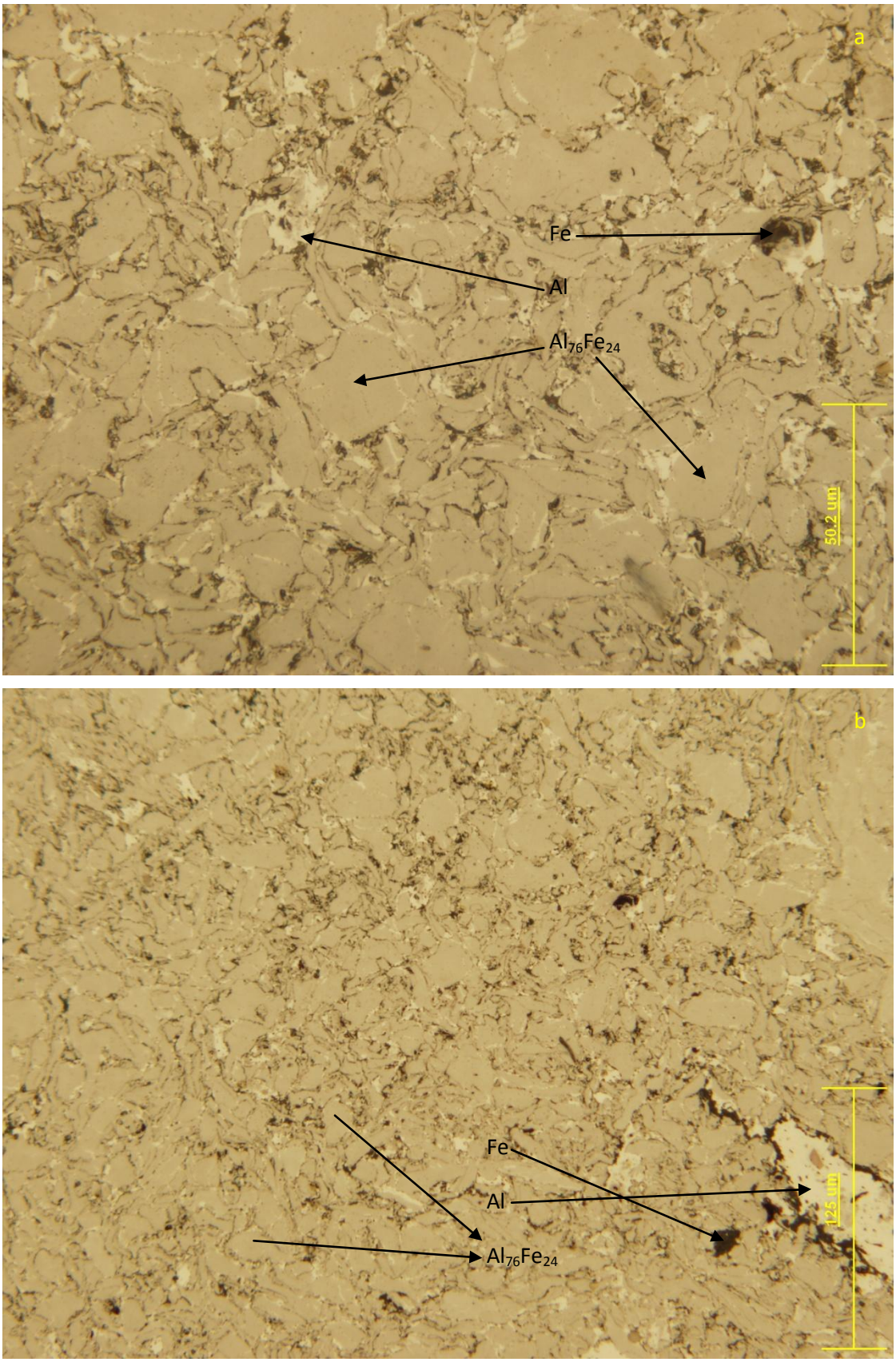

Figure 5.18 Optical micrographs of ECAP-BP consolidated pellets a) consolidated from powder milled for 400-h at 450 ^{0}C with 300 MPa b) consolidated from powder milled for 400-h at 300 ^{0}C with 300 MPa.

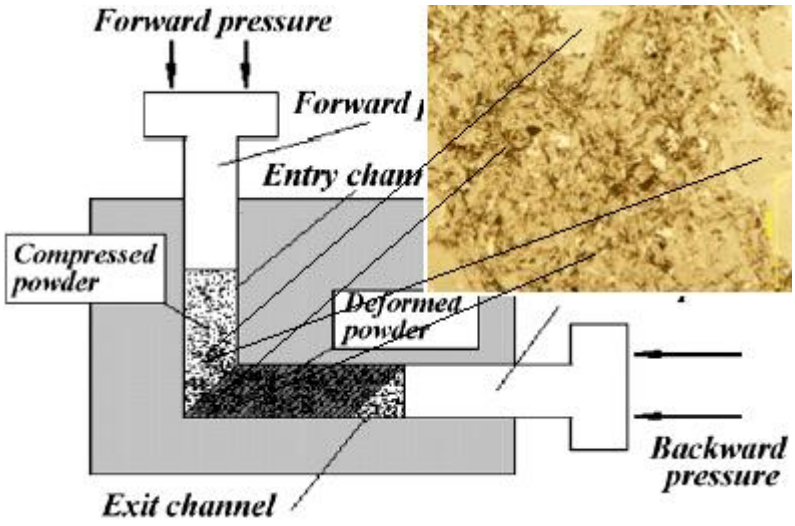

Figure 5.19 compaction, fragmentation and different phases formed at different regions in the ECAP-BP die during consolidation.

5.2.6.6 SEM characterization of pellets

Scanning electron microscopy (SEM) with field emission gun (FEG) was used to characterize the ECAP-BP consolidated pellets. Following inferences could be drawn from the micrographs shown in Figures 5.20 and 5.21 (a and b) and 5.22:

(i) Amorphous structure present in the ball milled powder has not been totally crystallized during ECAP-BP consolidation as noticed in SEM micrograph in Fig. 5.20. Both perforated amorphous (Al) as well as crystalline ($Al_{76}Fe_{24}$ compound) structures are observed in the pellet consolidated by ECAP-BP. XRD results (section 5.2.6.1) too showed the presence of both these structures.

(ii) Compaction which occurs in the vertical channel undergoes severe shear plastic deformation in the horizontal channel in the form of elongated shaped precipitates of alternate bright and dull grey colored phases observed in Fig 5.21 (a). Bright color indicates amorphous structure of Al phase while the dull grey colored phase is due to $Al_{76}Fe_{24}$ compound phase.

(iii) The volume fraction of $Al_{76}Fe_{24}$ phase in the 100-h and 250-h consolidated pellets are quantitatively analysed by XRD as 76% and 78% respectively.

(iv) Different compaction layers and nano sized grain boundaries are visible (Fig. 5.21 (b)) in the 400-h pellet, while the porosities are not visible even at a very high magnification. Small amount of amorphous phase retained along the grain boundaries, indicates the high stability of the phase even after undergoing shear deformation at elevated temperature. Such unusual stable amorphous phase can affect the observed grain growth kinetics and accordingly properties. Layer by layer diffusion which might have occurred during MA is noticed.

(v) Porosities, compaction, and plastically elongated regions are seen in the micrograph (Fig. 5.22) of 100-h pellet (consolidated from 100 hour ball milled powder with a back pressure of 50 MPa and at a temperature of 200 ^{0}C). Moreover, oxygen contamination causes the formation of oxide impurities (AlO) during elevated temperature consolidation of ball milled powder into pellets.

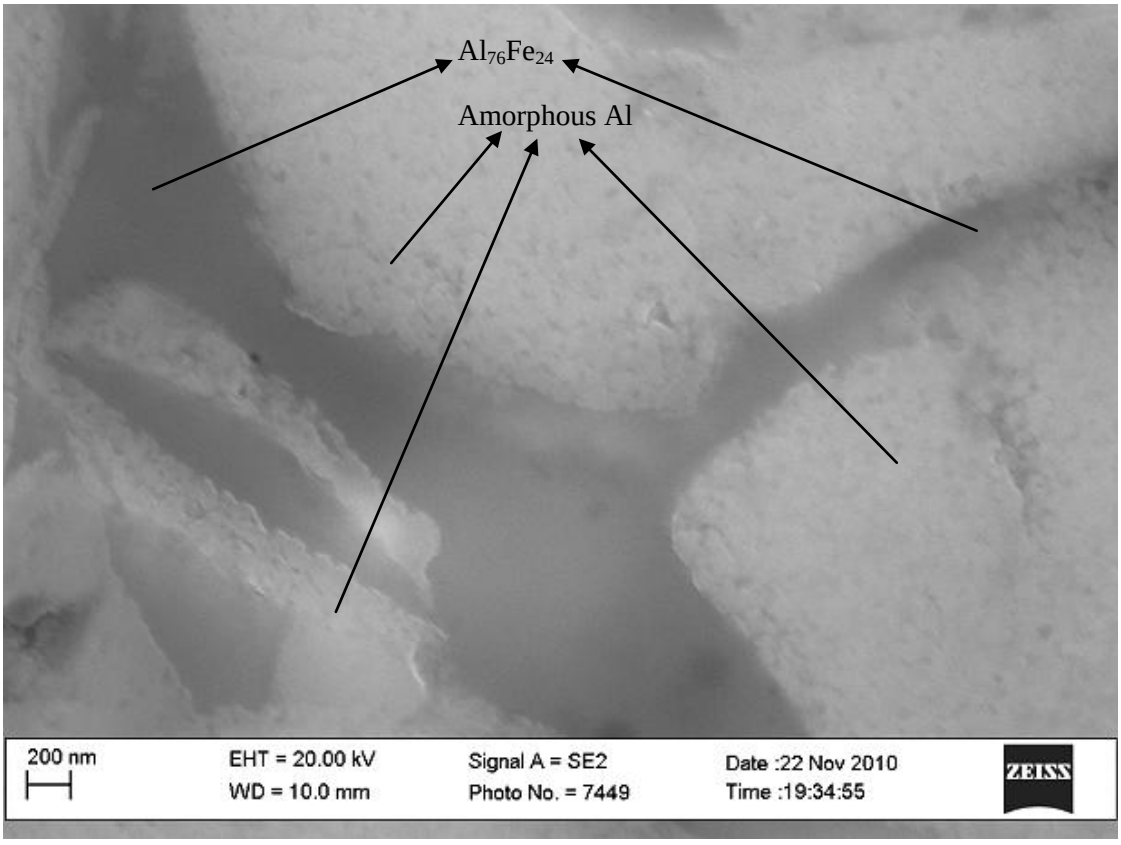

Figure 5.20. FEG-SEM micrograph of ECAP-BP pellet consolidated from powder ball milled for 100 hours.

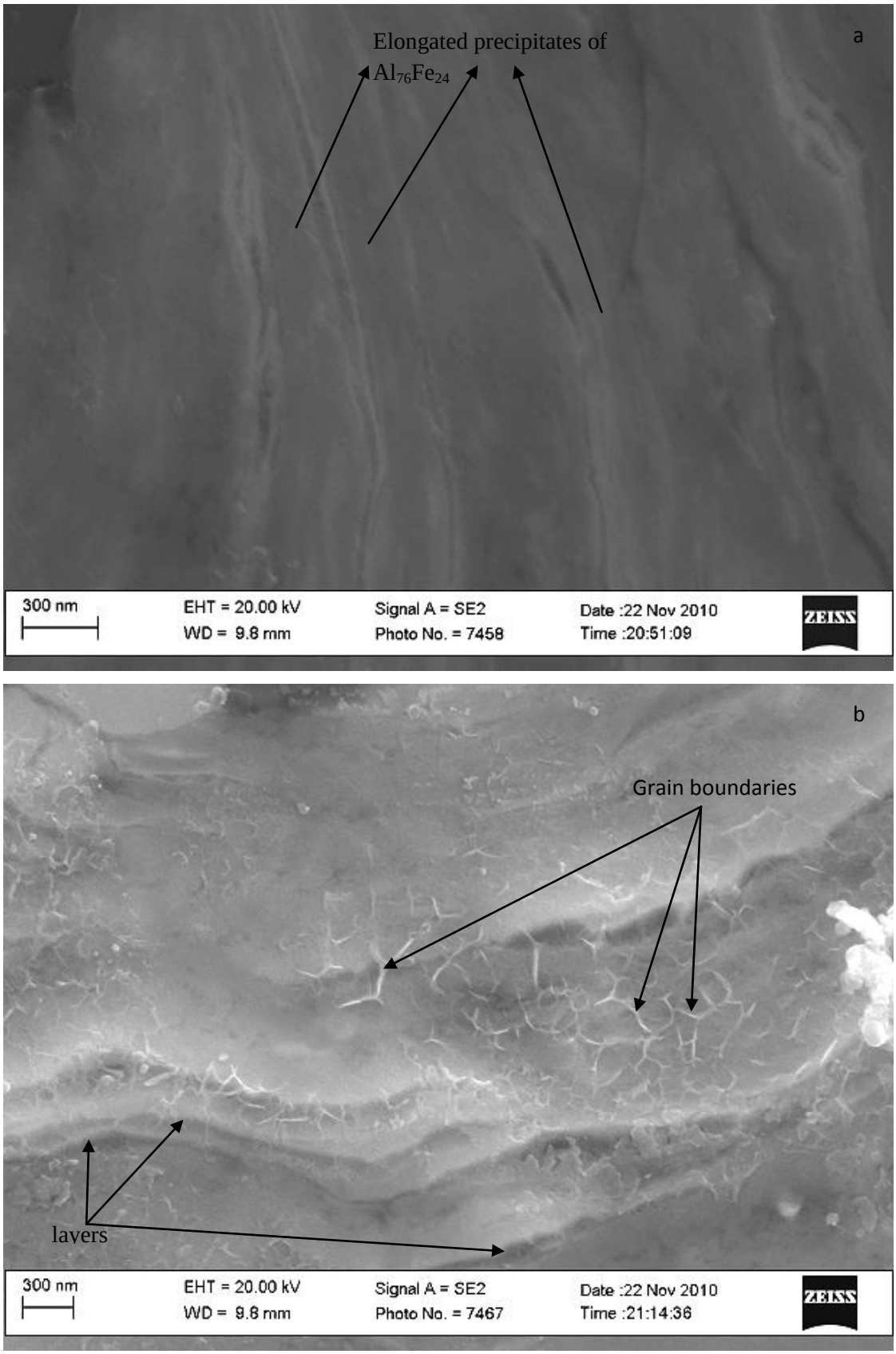

Figure 5.21. FEG-SEM micrographs of ECAP-BP pellets consolidated from powder ball milled for a) 250 hours, and b) 400 hours

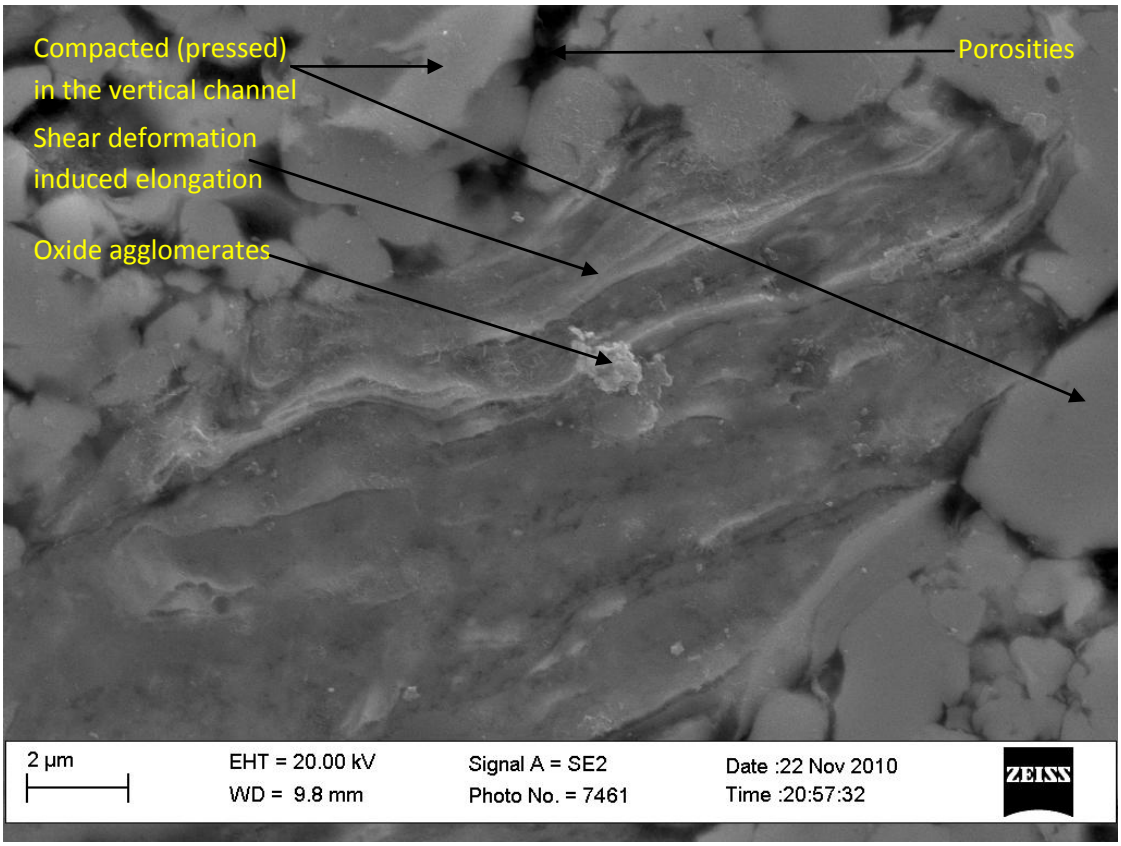

Figure 5.22. FEG-SEM micrograph of ECAP-BP pellet consolidated (200 ^{0}C and 50 MPa) from powder ball milled for 100 hours.

5.2.6.7 Nanoindentation of the pellets

Load (force) as a function of indentation depth (displacement (µm)) curves is shown in Fig. 5.23, the indentation depth limit is 700 nm with a maximum applied load of 20 mN. Such curves are used to obtain hardness and elastic modulus values. Following inferences could be drawn from these curves as well as nano hardness and elastic modulus shown in figures 5.24 and 5.25:

(i) Most of the load-displacement curves of consolidated pellets (ECAP-BP 250h and 400-h) are overlapping; this reflects the homogeneous nature of the phases present in these pellets and also uniform bonding between the grains.

(ii) Pop-in behaviour is observed in 250-h pellet (consolidated from powder ball milled for 250 hours). Such a behavior is due to sudden jump in displacement of the indenter associated to large-scale dislocation nucleation at the onset of plastic deformation and it is a function of pre-existing dislocation density (Baltazar Hernandez V. H. et al. 2010). Pop in phenomena also reveals the porosity existing below the indenter causing reduced elastic modulus and nanohardness.

(iii) Nano-hardness varies from 2.4 to 7.4 GPa while Elastic modulus varies from 55 to 160 GPa for 100-h pellet. Range of mechanical properties is quite wide due to different compositions of various phases in the consolidated pellet. When indented at different positions on the sample surface, the response to the indentation by various phases (elemental, $Al_{76}Fe_{24}$ and AlO phases) existing beneath the indenter is quite different due to the fact that the load induced deformation is dominated by the local phase composition rather than the bulk mechanical properties.

(iv) Lower elastic modulus of 55 GPa could be due to Al phase while a higher elastic modulus of 160 GPa is due to $Al_{76}Fe_{24}$ compound. Higher elastic modulus implies stronger covalent bonding in the intermetallic compound.

(v) In addition to the bonding effect, resistance of the material to indentation gradually increases with finer crystallite size. Thus, 250-h and 400-h pellets (consolidated from powder ball milled for 400 hours) possess finer crystallite size than 100-h pellet (consolidated from powder ball milled for 100 hours) which goes to show the higher mechanical properties in the 250-h pellet (Fig 5.25).

(vi) Nishtha Gupta et al (2012) have produced bulk Al 2024 alloy by consolidating the MA powder using ECAP process with a theoretical density of 97 %. The elastic modulus and hardness reported for the bulk sample are 86 GPa and 0.46 GPa respectively. However, ECAP-BP (Al_{90}-Fe_{10}) consolidated pellets reported in this research work show higher nano hardness and elastic modulus implying higher density than Al 2024 bulk samples.

(vii) Compared to the two categories of ECAP-BP consolidated pellet systems, nano hardness and elastic modulus of Al_{90}-Fe_{10} pellets are lower than Al_{50}-Fe_{50} pellets (11 GPa and 181.5 GPa).

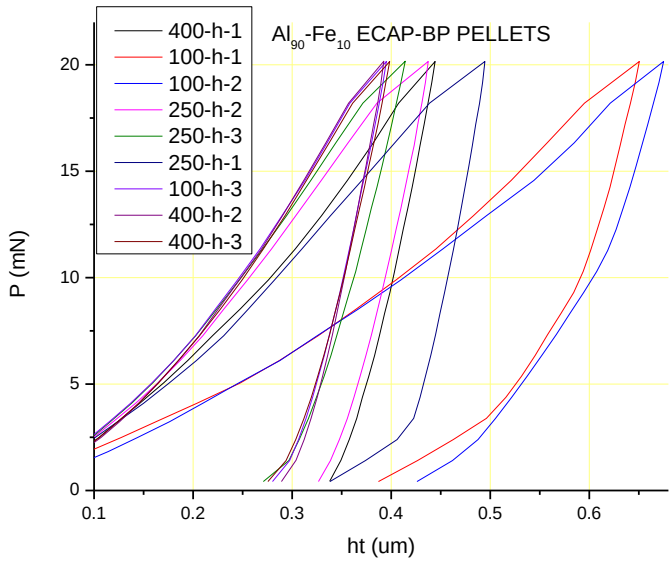

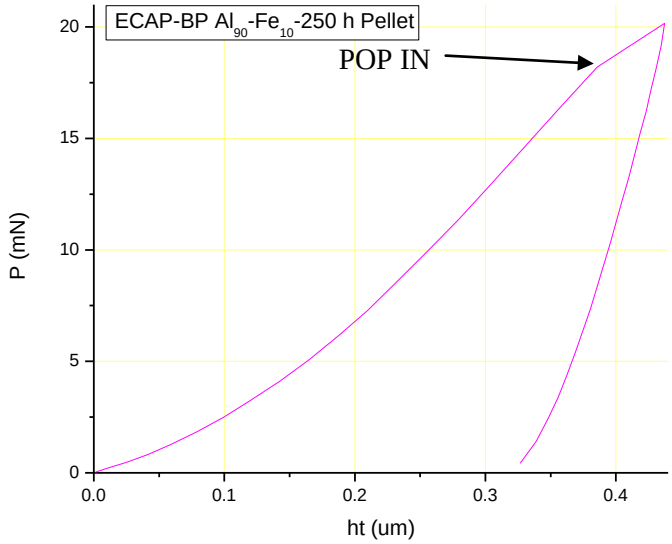

Figure 5.23 top: Load as a function of penetration depth (μm) and pop in observed in the nanoindentation curve of 250-h pellet

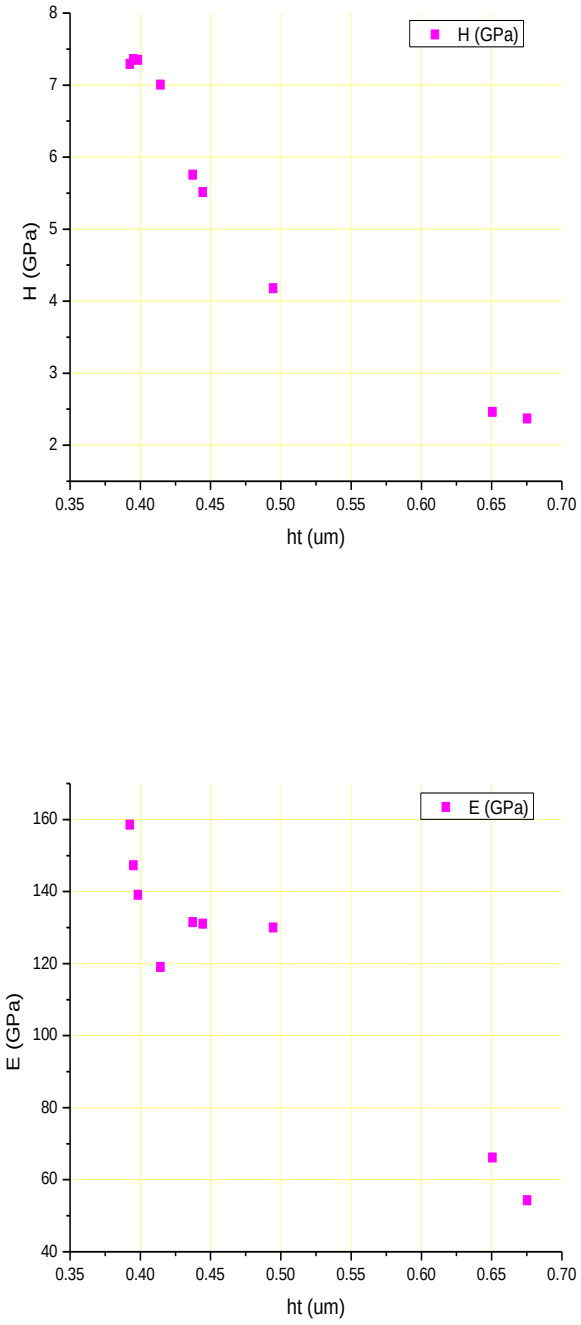

Figure 5.24 Nano hardness and elastic modulus of ECAP-BP pellet consolidated from powder ball milled for 100 hours

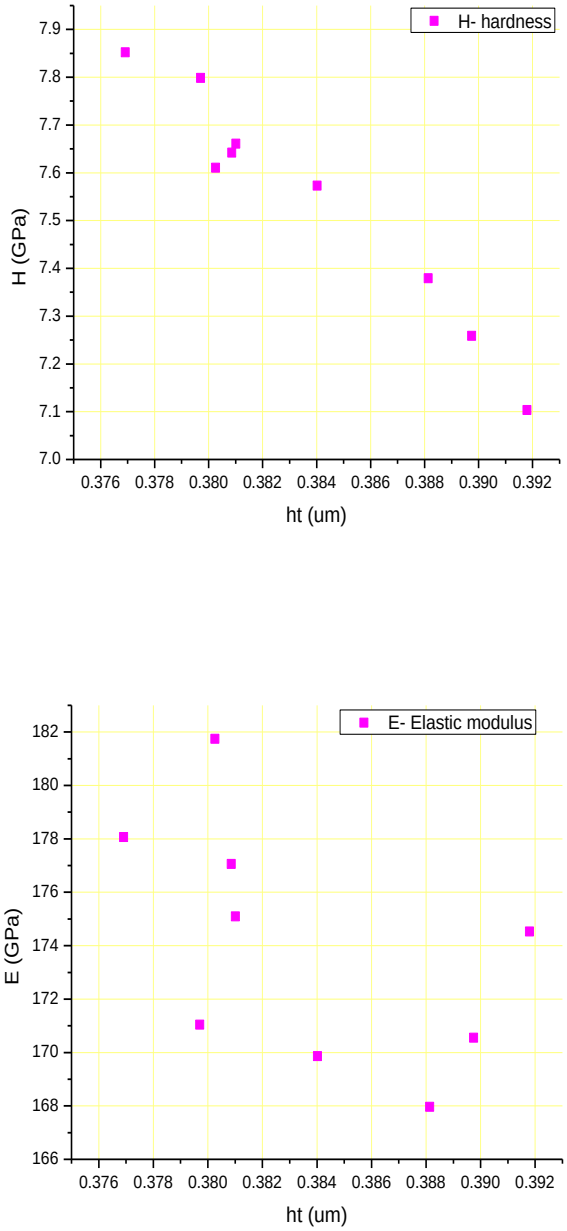

Figure 5.25 Nano hardness and elastic modulus 250–h ECAP-BP consolidated pellet

5.2.6.8 Texture of pellets

Texture analysis was performed by Panalytical X-Ray diffraction equipment, the resulting pole figures of various pellets synthesized by ECAP-BP consolidation is shown in Figures 5.26 and 5.27. From these pole figures, following inferences could be drawn:

(i) Texture in 100-h pellet processed at 450^0 C shows a weak texture near the centre of the pole figure (a) with a maximum intensity (242.5) located in the third quadrant (Φ=207.5 and Ψ=10.0) Fig 5.26 (a).

(ii) The texture shows a further weakening in the 100-h pellet processed at 300^0C, possibly due to lowering of the consolidation temperature down to 300^0C. The weak texture is located in the third quadrant with a maximum intensity of 212.5 (Φ=217.5 & Ψ=5.0) as shown in Fig 5.26 (b).

(iii) Pellets (250-h and 400-h) consolidated at 450^0 C with a back pressure of 300 MPa exhibit certain percent of preferred orientation as shown in Fig.5.27 (a & b).

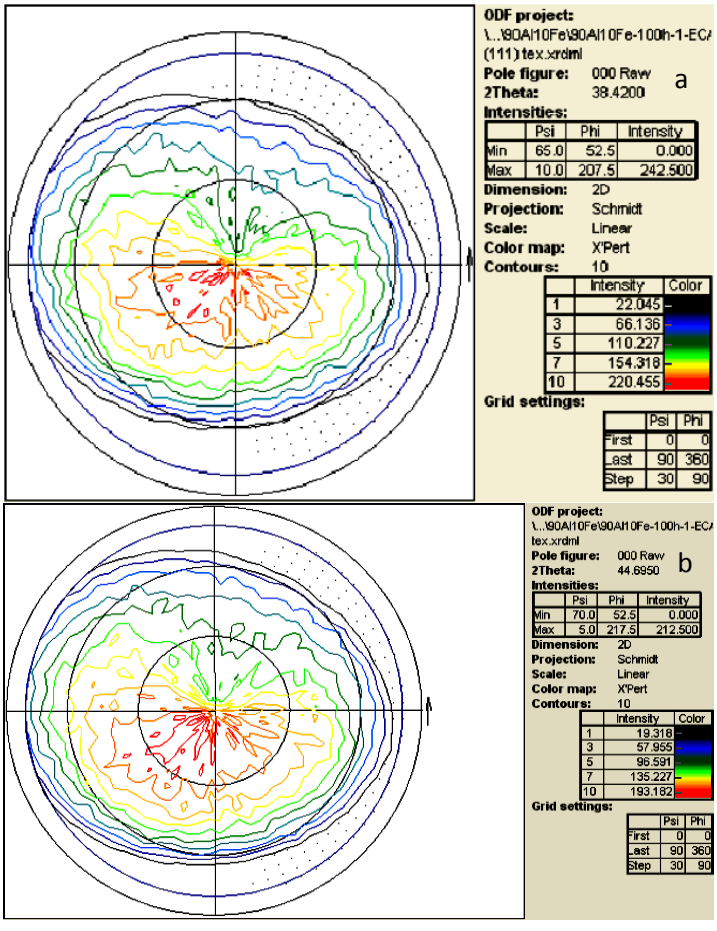

Figure 5.26 Pole figures of ECAP-BP pellets produced by consolidating powders ball milled at a) 100 hours at 450 ^{0}C, b) 100 hours at 300 ^{0}C

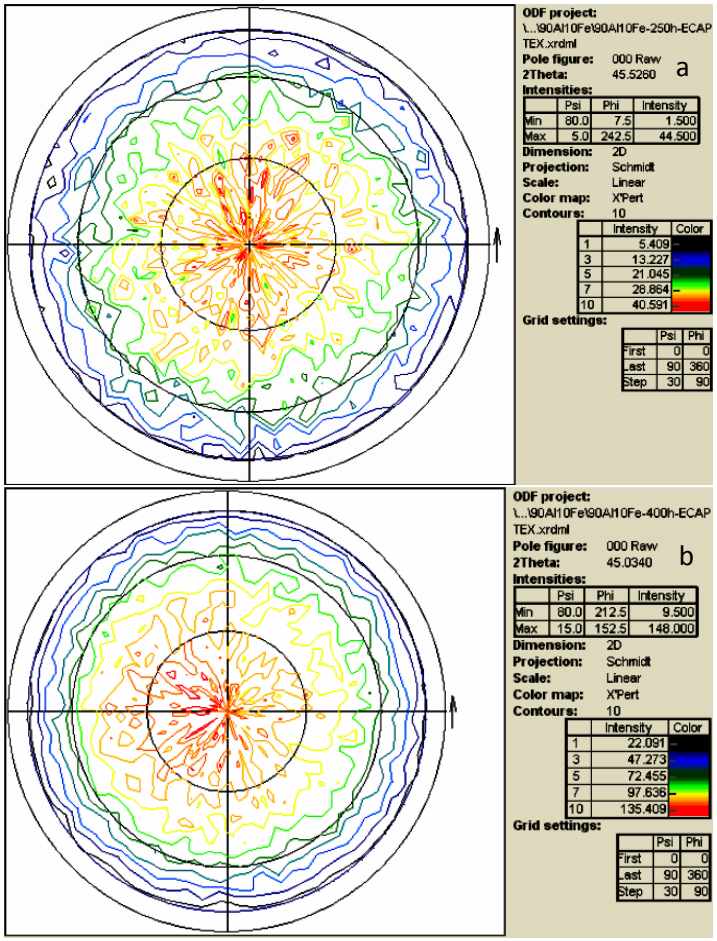

Figure 5.27 Pole figures of ECAP-BP pellets produced by consolidating powders ball milled at, a) 250-h pellet, b) 400-h pellet.

5.2.7 Consolidation by compaction and sintering

An alternative to ECAP-BP consolidation process is compaction and sintering. Thus this section of the chapter concentrates on the consolidation of ball milled powders by compaction and sintering at different temperatures. Moreover, sintering in a nitrogen atmosphere is attempted in this research work, as nitrides formed during the consolidation process could have an impact on microstructure, mechanical properties and atmospheric contamination.

Sintering occurs when packed particles are heated to a temperature where there is sufficient atomic motion to grow bonds between the particles. The conditions that induce sintering depend on the material, its melting temperature, particle size, and a host of processing variables. It is common for sintering to produce a dimensional change, typically shrinkage, where the powder compact densifies, leading to significant strengthening. Microstructure coarsening is inherent to sintering, most evident as grain growth, but it is common for pore growth to occur as density increases. Thus, the aim of this section is to consolidate the nanostructured mechanically alloyed (by ball

milling) Al-Fe powder synthesized in this research work by cold compaction and sintering. Elemental powders of Al_{90}-Fe_{10} system has been ball milled by high energetic planetary ball mill and as a result of such a processing; mechanical alloying has been achieved to a large extent. The ball milled powders have been extensively characterized by various techniques as reported in section 5.2 of this chapter. Such a ball milled powder has been consolidated by compaction and sintering to produce bulk material for various practical applications. In addition, the various metallurgical events associated with the process of consolidation (compaction and sintering) as mentioned earlier in this paragraph has been investigated and critically examined. Retaining the nanostructure produced during mechanical alloying by ball milling is critical during the consolidation process. As nanostructured bulk materials offer a wide range of property enhancement compared to bulk material of coarser grained structure. The sintered compacts are investigated for phase transformation, structural and mechanical properties in addition to metallographic (Fig.5.28 shows sintered compact hot mounted for metallographic analysis) and texture examination. The results and discussions are elaborately reported in the following sections. While, the experimental details regarding compaction and sintering were reported in section 3.2.2.2 of chapter 3.

Figure 5.28 Sintered compacts hot mounted on a polyfast

5.2.7.1 XRD analysis of sintered compacts

Sintered compacts as a function of ball milling time (elemental powder ball milled for various time duration have been consolidated by compaction followed by sintering) are subjected to XRD analysis. Profiles of sintered compacts scanned by X Ray diffractogram are presented in Figures 7.61 to 7.63 in appendix. Accordingly, structural parameters analysed from these profiles of various sintered compacts are listed in tables 7.26, 7.28 and 7.29 in appendix. While, table 7.27 shows the matching patterns (reference code etc,) for 100-h sintered XRD profile shown in Fig

7.61 in appendix. From the consolidated XRD profiles in Fig 5.29 and structural parameters listed in Table 5.6, following inferences could be drawn:

1) In all the three sintered compacts, crystalline phases of $Al_{76}Fe_{24}$ compound and Al in addition to AlN are present. Thus, amorphous Al-Fe solid solution in ball milled powder transforms to an intermetallic compound upon sintering. While, a distinct ECAP-BP pellets possessed $Al_{76}Fe_{24}$ compound and an amorphous Al.
2) Further, Al phase in the sintered compacts underwent lattice expansion to **0.4109 nm** compared to the lattice parameters of pure Al unmilled (0.4048 nm), ball milled (0.4088 nm) powder and ECAP-BP processed pellet (0.4063 nm). Such an expansion in lattice is an evidence of Fe diffusion into Al lattice and the formation of Al rich intermetallic during sintering.
3) However, Al also reacts with nitrogen during sintering forming AlN, such a phase formed depends on the quantity of Al present in the ball milled powder.
4) Moreover, 100-h sintered (consolidated by sintering from powder ball milled for 100 hours) compact exhibits peak narrowing (FWHM=**0.3991)**, Al lattice expansion (a=**0.4104 nm)**, decrease in the height/integrated intensity (**54.59 counts)** of elemental (Al) peaks coupled with increase in the height / integrated intensities (II) of intermetallic (**398.18 counts)** and AlN peaks compared to 100-h ball milled powder.
5) Such structural parameters indicate grain growth (coarser crystallites), decreased lattice strain and intermetallic / AlN formation at the expense of elemental phases when compared to ball milled powder. Similar results are also observed in 250-h and 400-h sintered compacts.
6) Grain growth (85 nm, 20 nm and 135 nm) and decreased lattice strain (0.329, 0.819 and 0.253 %) due to sintering occurs in all the compacts (100-h, 250-h and 400-h) compared to ball milled powder.
7) Larger quantity (74%) of $Al_{76}Fe_{24}$ compound crystallises in the 400-h sintered compact compared to other sintered products. Greater percentage of solid solution in the 400-h ball milled powder could be the possible reason for such large quantity.
8) Compared to ECAP-BP processed pellets, larger lattice parameter of Al in the sintered compacts suggests higher diffusion of Fe in Al leading to the formation of larger percentage of intermetallic compound. Compound formed is at the expense of elemental phases.

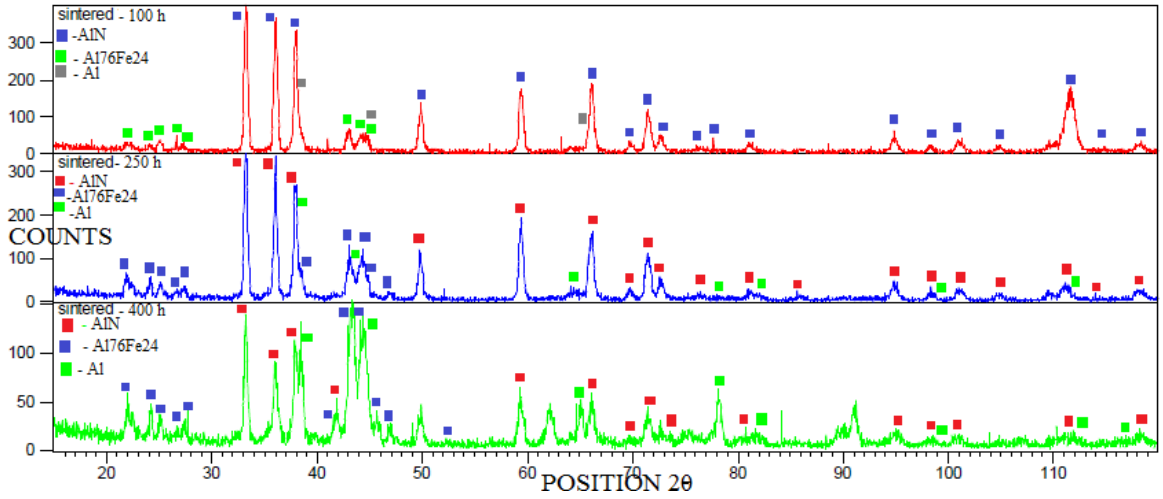

Figure 5.29 Combined XRD pattern of sintered compacts consolidated from powders ball milled at 100-h, 250-h and 400-h

Table 5.6 Structural parameters of unmilled and milled powders and sintered compacts (Al_{90}-Fe_{10} system)

Sample type	$2\theta^0$	hkl/phase	Ht 'cts'	FWHM	'a' nm/'d'nm	II/ Rel Int/ strain%	'D' nm	Micro Strain %
Unmilled powder (0-h)	38.4883	111/Al	1526.21	0.2954	0.4048/ 0.233711	162261.39	60 µm	0.03
	44.7351	200/110Al/Fe	801.08	801.08	0.202419		317 nm	0.137
100 –h powder	38.6713	(33-2) Al(Fe)/111Al	123.26	1.3966	0.232647	159895.26	7.6	1.698
	44.6665	620Al(Fe)/200Al	104.65	1.8806	**0.4055**/0.202714	3178291.5	5.4	1.973
250-h powder	38.6668	(33-2) Al(Fe)/111Al	68.42	1.5964	0.232673	159895.26	6.5	1.951
	44.2783	620Al(Fe)/200Al	58.42	3.5546	**0.4088**/0.204401	3249907		
400-h powder	38.7007	33-2Al(Fe)/111Al	60.92	1.7912	0.232477	159586.98	5.6	2.195
	44.3003	620Al(Fe)/200Al	59.02	3.3969	0.204304/**0.4086**	3247078.6		
100-h sintered	33.2284	$Al_{76}Fe_{24}$/AlN	398.18	0.3325	2.69405	/100.00 %		
	38.5171	$Al_{76}Fe_{24}$/AlN/Al	54.59	0.3991	2.33543/**0.4104**	/13.71 %	85	0.329
250-h sintered	33.2121	$Al_{76}Fe_{24}$/AlN	341.49	0.3408	2.69534	/100.00 %		
	38.0873	$Al_{76}Fe_{24}$/AlN/Al	170.26	0.7144	2.36079/**0.4109**	/49.86%	20.3	0.819
400-h sintered	33.2040	$Al_{76}Fe_{24}$/AlN	117.17	0.3637	2.69598	/79.77 %		
	38.4587	Al76Fe24/AlN/Al	95.14	0.3618	2.33884 /**0.4106**	/64.78%	135.7	0.253

*II-Integrated Intensity, d-planar spacing, 2θ-Bragg angle, Ht-height in counts, FWHM-full width half maximum, a-lattice parameter, D- crystallite size, Al(Fe)=$Al_{76}(Fe_{24})$

The following are some of the important unique structural parameters and phases identified in the sintered components of the two systems ($Al_{90}Fe_{10}$ and $Fe_{50}Al_{50}$):

- AlFe intermetallic was formed in sintered compacts of Fe_{50}-Al_{50} system while $Al_{76}Fe_{24}$ intermetallic is formed in Al_{90}-Fe_{10} system.

- The AlN peak (170 counts) formed was of high intensity and the quantitative analysis too suggests the larger quantity of such nitride phase compared to sintered compacts (60 counts) of Fe_{50}-Al_{50} system.
- Lattice (0.4109 nm) dilation of Al occurred forming Al rich intermetallic phase of monoclinic structure in the Al_{90}-Fe_{10} system while Fe (0.2949 nm) lattice dilation occurred forming Fe rich intermetallic phase of bcc structure.
- The lattice parameters of $Al_{76}Fe_{24}$ and AlFe intermetallic phase obtained as a consequence of sintering are larger than the lattice parameters of respective solid solutions (0.4088 nm and 0.2933 nm) obtained as a result of mechanical alloying.
- Such expansion in lattice parameter suggests alloying of elemental phases occurred by diffusion during sintering process.
- The crystallite size of intermetallic ($Al_{76}Fe_{24}$) phase varies from 85 nm to 135 nm for 100-h and 400-h sintered compacts with a low of 20 nm in the 250-h sintered compact.
- While, the crystallite size varies from 59 nm to 28 nm in 100-h and 200-h sintered compacts for AlFe intermetallic phase of Fe_{50}-Al_{50} system.
- Fe_4N phase is present in the 200-h sintered compact of Fe_{50}-Al_{50} system while no such iron nitride phase is present in the sintered components of Al_{90}-Fe_{10} systems.

5.2.7.2 Nanoindentation of sintered compacts

Smooth nanoindentation curves generated as a result of load (P) as a function of indenter penetration depth (ht-μm) are shown in Fig. 5.30. Nano-hardness and elastic modulus obtained from analyzing these curves are shown in Fig 5.31. Maximum applied load is 20 mN while, the maximum penetration depth did not exceed 700 nm. From these figures, following inferences could be drawn:

(i) Sintered compacts (400-h) produced by consolidating 400 hours of ball milled powder shows minimum depth of penetration followed by 250-h sintered compacts. While, the 100-h sintered compacts have the largest penetration depth among the sintered products.

(ii) Even though larger amount of AlN (61 %) and $Al_{76}Fe_{24}$ (36 %) compound phases are present, less dense structure with greater porosities (Fig. 5.34 a) in the 100-h sintered compact accounts for lower hardness. While, finer crystallite size with dense structure (Fig. 5.34 b) along with larger amount of $Al_{76}Fe_{24}$ compound (74 %) and AlN (19 %) phases in the 400-h sintered compacts is the reason for higher hardness. However, higher processing temperature caused higher hardness and elastic modulus in all the compacts.

(iii) Nanohardness varies from 2.5 GPa to 37.5 GPa, such wide distribution is the result of dispersed porosity and intermetallic regions. Indentation on the intermetallic surface has resulted in higher hardness; strong deformation texture coupled with crystalline structure has resulted in the higher hardness in 400-h sintered compacts compared to others.

(iv) The elastic modulus range varies from 75 GPa to 275 GPa, the higher elastic modulus is the result of covalent bond existing in the intermetallic phase while the lower hardness / elastic modulus is due to the elemental Al phase in addition to the porosities.

(v) Another reason for higher mechanical properties in 400-h sintered compacts is due to greater deformation texture compared to all other sintered products.

(vi) Compared to sintered products of Al_{50}-Fe_{50} system, 400-h sintered compacts (Al_{90}-Fe_{10} system) possess higher nano-hardness and elastic modulus to the tune of 2.5 to 37.5 GPa and 80 to 275 GPa respectively. Such higher mechanical properties in Al_{90}-Fe_{10} system are due to stronger texture (maximum intensity of 6556.00) and larger amount of AlN (117.17 counts at FWHM=0.3637^0) phase in addition to $Al_{76}Fe_{24}$ compound. Moreover, Al_{50}-Fe_{50} system possesses weak texture (maximum intensity of 703.500) and lower amount of AlN (62.07 counts at FWHM=0.3738^0).

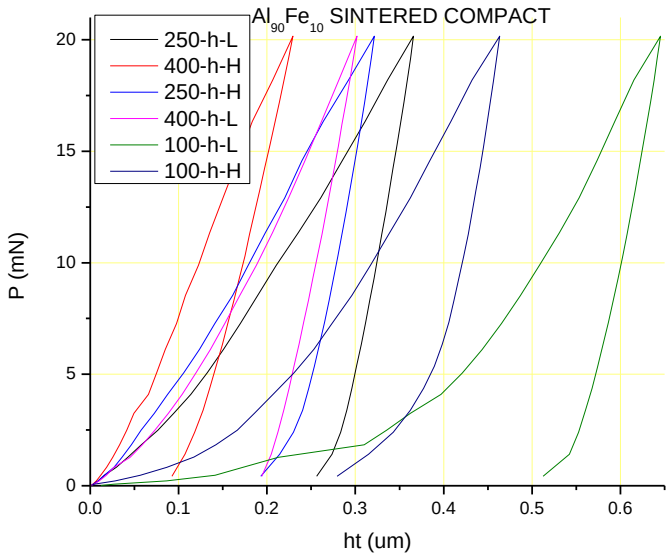

Figure 5.30 Nanoindentation of sintered compacts; loading and unloading curves vs penetration depth (μm). L-lower processing temperature (800 ^{0}C), H-higher processing temperature (1020 ^{0}C)

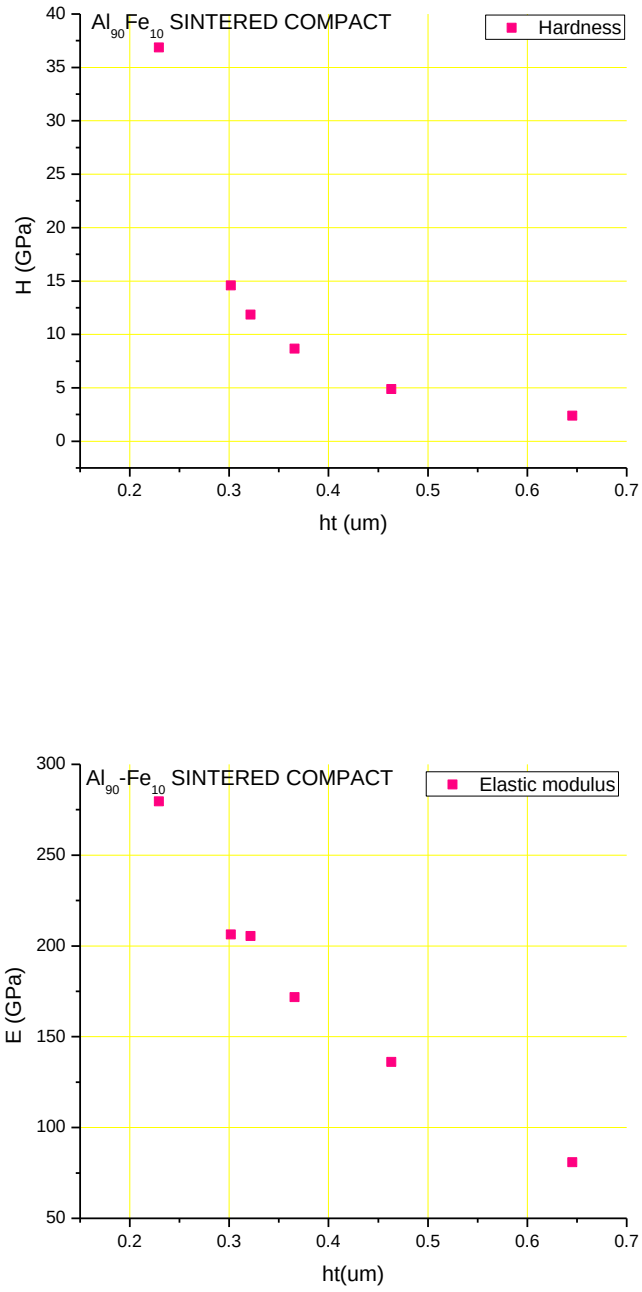

Figure 5.31 Nanoindentation; hardness and elastic modulus 400-h sintered compact

5.2.7.3 Optical microscopy of sintered compacts

Optical micrographs show the agglomerated powder in the sintered compacts presented in Figures 5.32 (a and b) and 5.33 (a and b). Observations from these images suggest that there are two types of pores, large pores between the agglomerates and smaller pores within the agglomerates. The smaller pores vanish quickly upon increasing the sintering temperature while the larger pores are

slow to contract. By increasing the sintering temperature, establishes good bonding between the particles decreasing the size and volume of pores (Fig. 5.32 (b)). Fine acicular needle shaped AlN particles and also second phase particles (intermetallics) are visible in the OM images (Fig. 5.32 (a & b)). In addition, early trend of engloving (Fig. 5.33 (a & b)) is observed in the micrographs in which the second phase particles are surrounded by softer Al, however Al could be oxidized on the surface.

5.2.7.4 SEM analysis of sintered compacts

Sintered compact produced by consolidating 100 hour ball milled powder at 800^0 C show poor bonding between the particles: A lot of processing defects such as porosity and voids are indicated by arrows in the SEM micrograph shown in Fig. 5.34 (a). Powder MA for 400 hours of ball milling duration is sintered at 1020 ^{0} C, the bonding between the particles has greatly improved and very few isolated porosity and voids are present (Fig. 5.34 (b)). The major cause for poor particle bonding, porosities and voids could be due to high particle strength; MA as a result of long duration (100 to 400 hours) of ball milling induces strain hardening increasing the strength of the powder. Thus, because of high particle strength, the particles may not be sufficiently compressed during cold compaction to establish complete contact between the particles. AlN, oxide, Al and second phase particles are indicated in the images, such phases have been identified by XRD quantitatively and qualitatively too. While, very fine acicular AlN and second phase particles of nano size formed during the process is observed in OM and SEM micrographs. While, the EDS analysis in Fig. 5.35 (a & b) shows SEM micrograph along with the spectrum, indicating the composition (Table 5.7) of acicular needle shaped structure as AlN in the 100-h sintered compact. Moreover, the grey color in the micrograph (Fig. 5.36 (a & b)) indicates the composition (Table 5.8) of Al-Fe intermetallic phase in the 400-h sintered compact.

5.2.7.5 Texture of sintered compacts

The texture prevalent in the 100-h sintered compact measured by XRD pole figure in Fig. 5.37 (a) shows minimum intensity (at 14.000 at Ψ=80 and Φ=297.5) and maximum intensity of 231.500 (at Ψ=25 and Φ=297.5). The analysis indicates predominantly random or weak texture in the sintered compact, the pole figure was obtained for the diffraction peak (2θ=37.9130^0) of $Al_{76}Fe_{24}$ phase.

The 400-h sintered compact has a minimum intensity of 17.500 (at Ψ=80 and Φ=352) while, the maximum intensity of 6556.00 (at Ψ=5.0 and Φ=342.5) is observed indicating a strong deformation texture shown in Fig. 5.37 (b).

However, the 100-h and 200-h sintered compacts of Fe_{50}-Al_{50} system possess maximum intensities of 473.5 and 703.50 respectively (reported in section 4.4.7.4), the pole figures were obtained from 110 diffraction peaks of AlFe phase.

Sintered compact (400-h) of Al_{90}-Fe_{10} system has stronger deformation texture compared to sintered products of Fe_{50}-Al_{50} system.

Further, it is also observed that the 400-h **sintered** sample (Al_{90}-Fe_{10} system processed at 1020^0 C) has stronger deformation texture than the pellets obtained by ECAP-BP consolidation process of both Fe_{50}-Al_{50} as well as Al_{90}-Fe_{10} systems. Thus, the texture results of ECAP-BP consolidated pellets of both the systems are summarised below:

- In the **$Fe_{50}Al_{50}$** system, the pellet (180-h) consolidated by ECAP-BP process at 450^0 C shows some preferred alignment with a fibre texture resembling the rolling texture (maximum intensity of 287.500 at Ψ=5.0 and Φ=167.5 from 110 peak of AlFe phase).
- While, the 200-h ECAP-BP pellet shows slightly greater deformation texture (maximum intensity of 306.500 at Ψ=15.0 and Φ=222.5 from 110 peak of AlFe/$AlFe_3$ phase) among the ECAP-BP consolidated pellets in its class.
- The texture in 100-h ECAP-BP pellet of **$Al_{90}Fe_{10}$** (processed at 450^0C) shows weak texture near the centre of the pole figure (2θ=38.42^0 of $Al_{76}Fe_{24}$ phase) with a maximum intensity (242.5) located in the third quadrant (Φ=207.5 and Ψ=10.0).
- While, the 400-h ECAP-BP pellet exhibits further weakening of the texture in the Al_{90}-F_{10} system. The pole figure obtained (at 2θ=45.03^0) for the $Al_{76}Fe_{24}$ phase shows a maximum intensity of 148.00 (Ψ=15.00 and Φ=152.5).

The above summary of results confirms the stronger texture prevailing in the 400-h sintered compact of Al_{90}-Fe_{10} system.

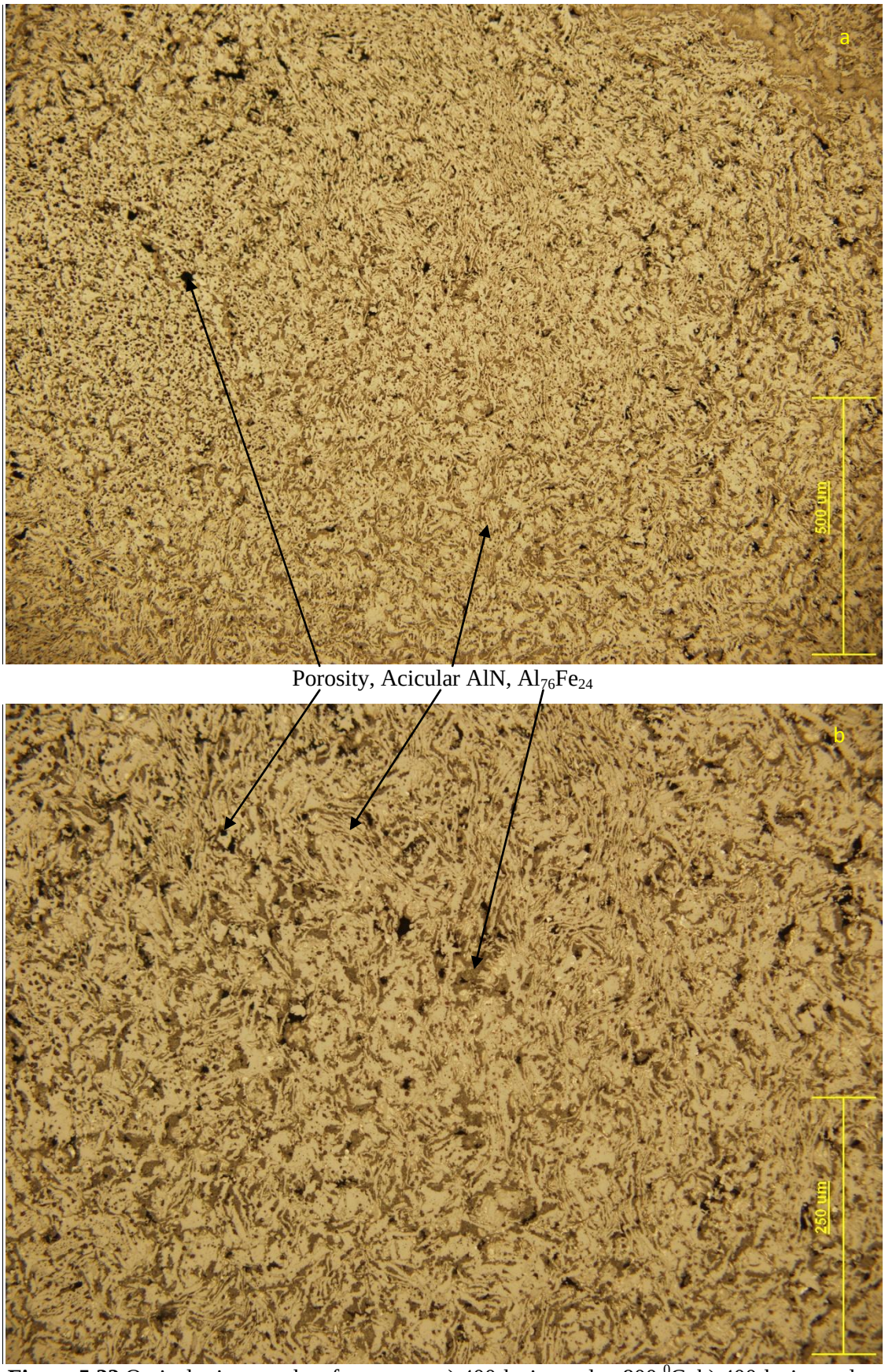

Figure 5.32 Optical micrographs of compacts a) 400-h sintered at 800 ^{0}C, b) 400-h sintered at 1020 ^{0}C

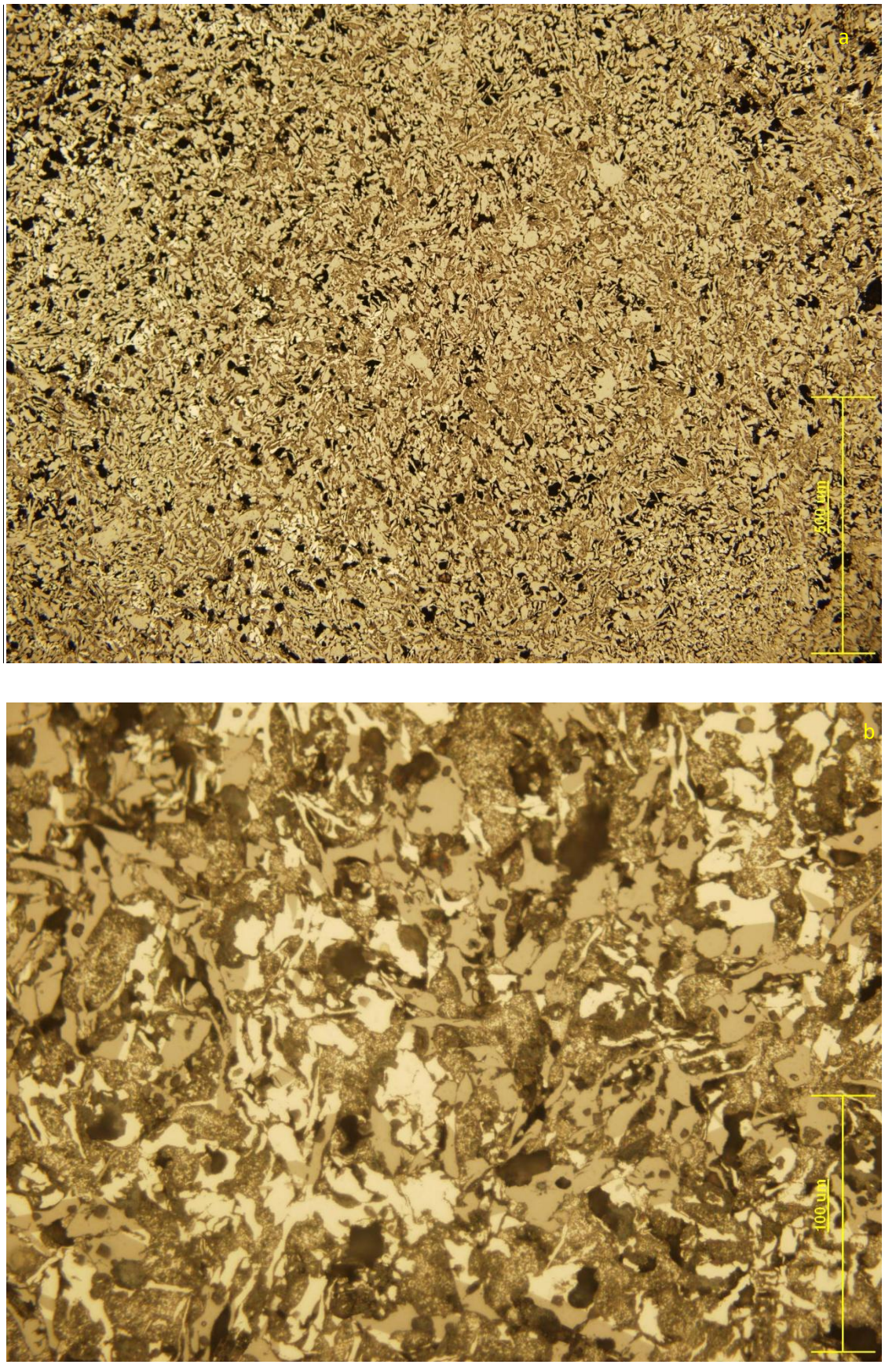

Figure 5.33 Optical micrographs of compacts, a) 250-h sintered at 800^0 C, b) 250-h sintered at 1020^0 C

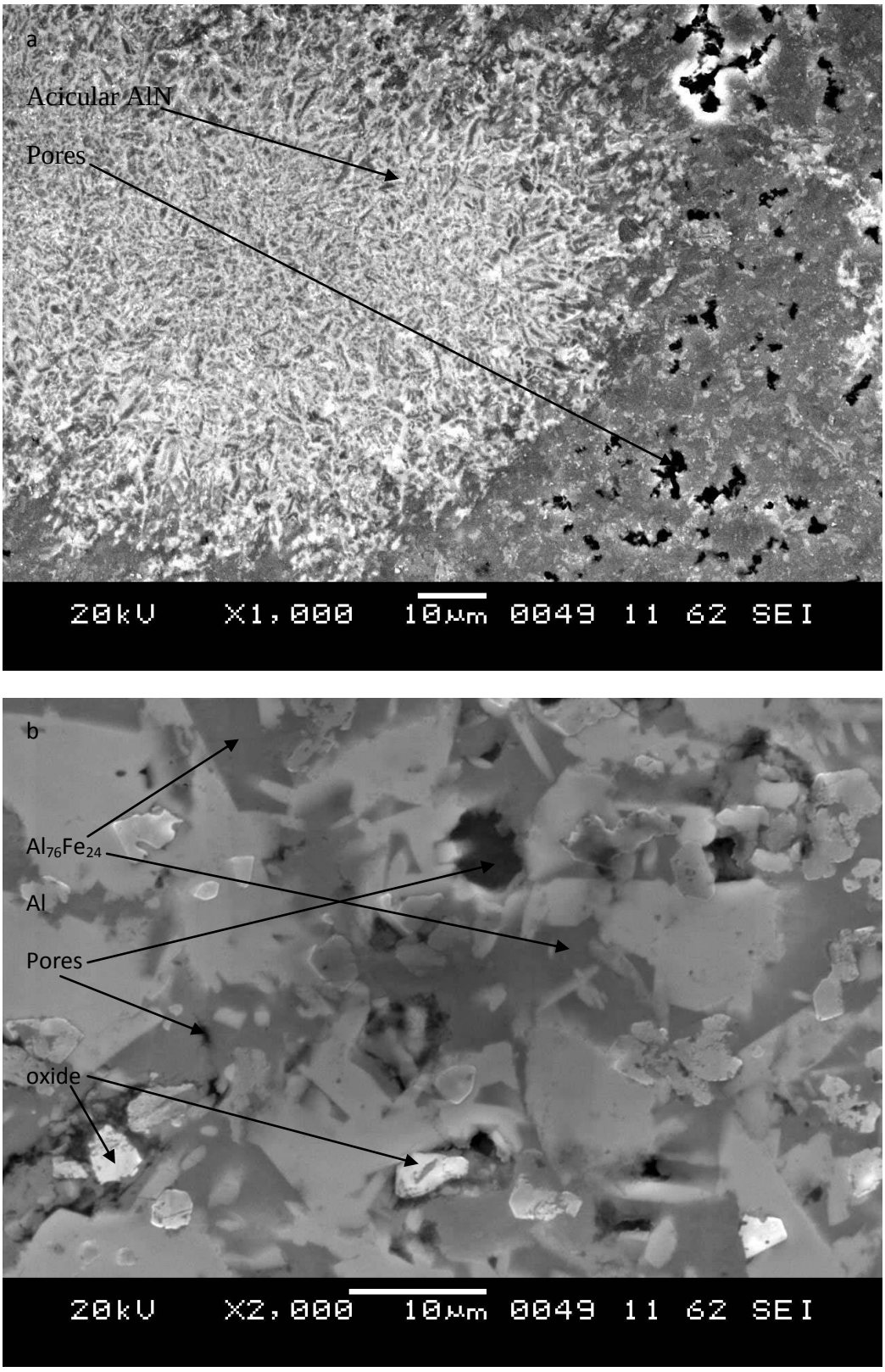

Figure 5.34 SEM micrographs of compacts, a) 100-h sintered at 800^0 C b) 400-h sintered at 1020^0 C

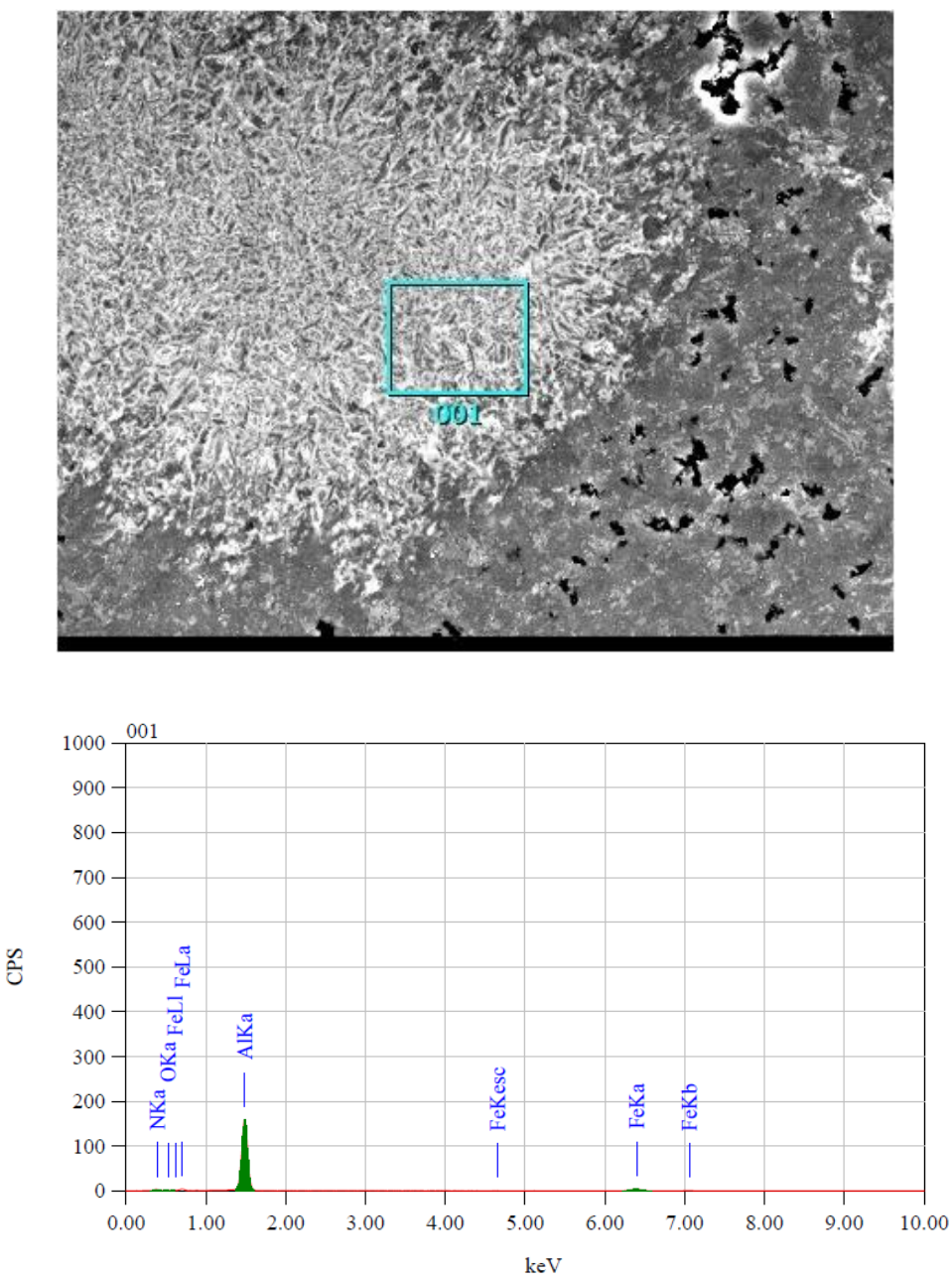

Fig. 5.35 EDS-SEM micrograph and spectra of 100-h sintered compact

Table 5.7 EDS analysis of 100-h sintered compact

Element	(keV)	mass%	Error %	At % Compound mass%	Cation K
N K	0.392	17.27	1.59	**29.47**	19.0231
O K	0.525	2.27	0.92	**3.39**	1.3708
Al K	1.486	71.43	0.29	**63.28**	70.2419
Fe K	6.398	9.04	1.12	**3.87**	9.3642
Total		100.00		**100.00**	

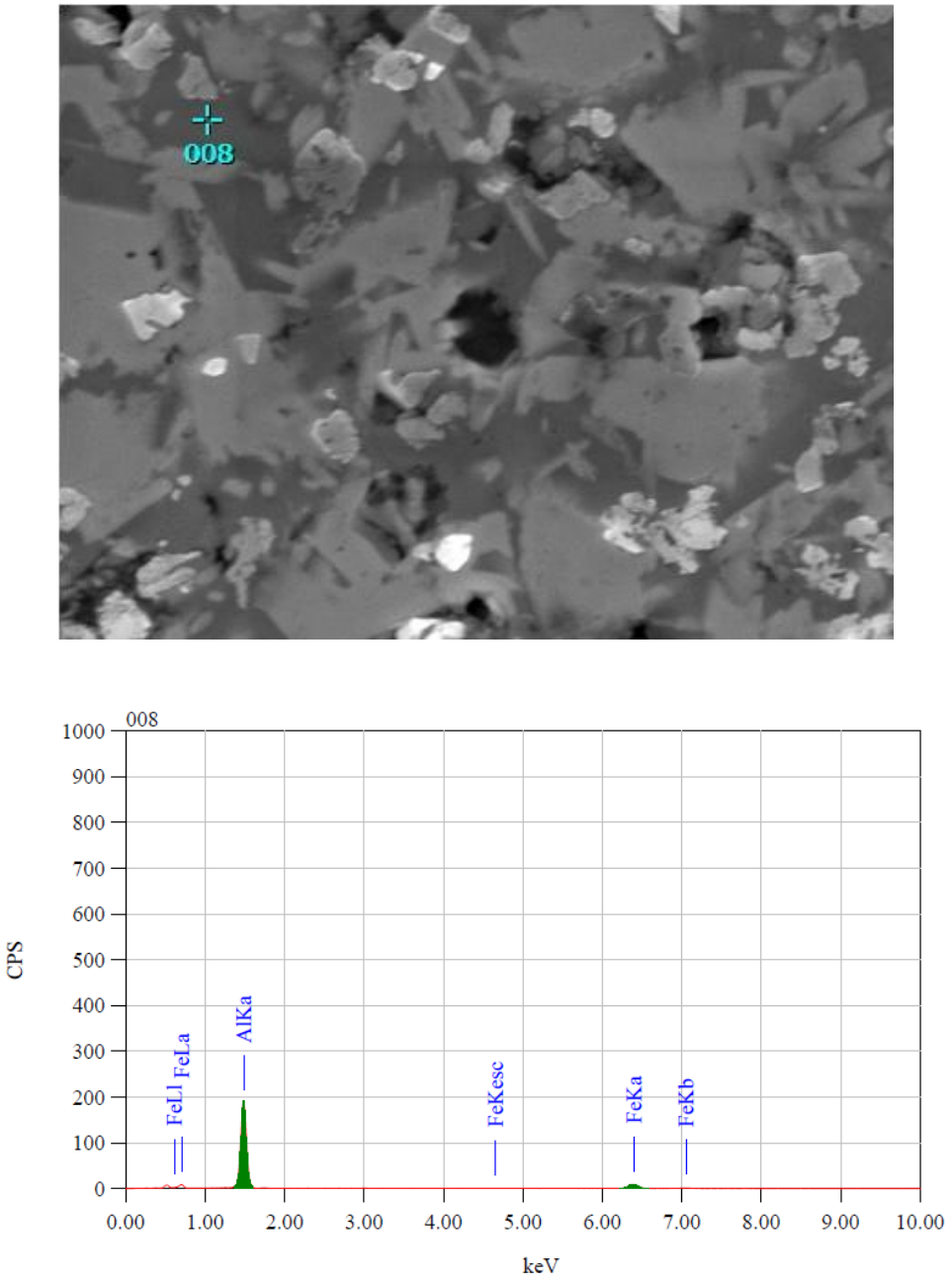

Fig. 5.36 EDS-SEM micrographs and spectra of 400-h sintered compact.

Table 5.8 EDS analysis of 400-h sintered compact

Element	(keV)	mass%	Error %	At% Compound mass%	Cation K
Al K	1.486	81.20	0.39	**89.94**	79.4342
Fe K	6.398	18.80	1.43	**10.06**	20.5658
Total		100.00		**100.00**	

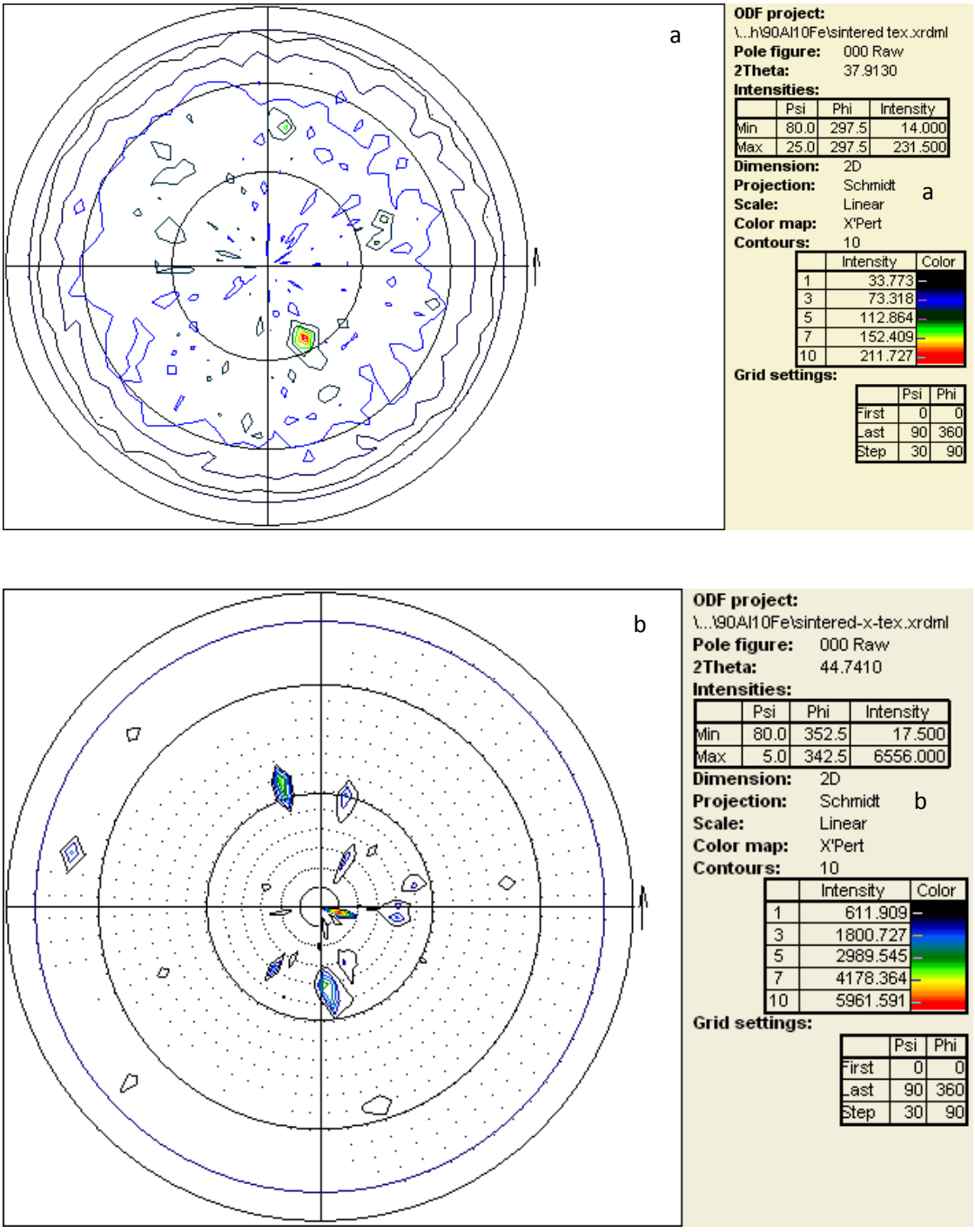

Figure 5.37 XRD Pole figures of compacts, a) 100-h sintered, and b) 400-h sintered

5.3 An Overview of Metallurgical Events in Al_{90}-Fe_{10} System

Ball milling of elemental powders resulted in the formation of Al rich supersaturated solid solution of Al (Fe) of FCC structure. Not all Al is used up in the formation of solid solution as indicated by the presence of elemental Al by XRD analysis, even after extending the milling time to 400 hours. The maximum size of the lattice parameter 'a' of Al (200 reflection) phase is 0.4088 nm attained after undergoing milling for 200 hours. Amorphous nature of the ball milled powder is noted in the XRD profile. DSC curves have revealed the glass transition temperature prior to crystallisation with a narrow super cooled liquid region observed in all the ball milled powder which goes to indicate the amorphous content in the milled powder. Selected area diffraction pattern of TEM image too showed amorphous structure in the ball milled powder. Hard magnetic ($H_C \geq 125$ Oe) properties with a broader hysteresis loops are noted in all the ball milled powders notably due to the crystallite size reduction to finer size (< 8 nm). Dislocations and nano sized grain boundaries are visible in the heavily deformed ball milled structure.

Upon consolidating the ball milled powders by ECAP-BP process, supersaturated solid solution transforms to a more stable intermetallic phase ($Al_{76}Fe_{24}$) of monoclinic structure. Presence of elemental Al (a = 0.4063 nm for 200 reflection) in the consolidated pellets is noted, however, phases are not entirely crystalline as slight amorphous structure is still retained in some of the pellets. DSC curves of pellets have shown slight amorphous nature as there is no glass transition prior to crystallisation which was the case with ball milled powders. Due to slight grain growth (10 nm) in the pellets, soft magnetic ($H_C \leq 125$ Oe) properties are observed. OM have shown fragmentation of larger particles into finer ones and dense structure compared to pellets of Al_{50}-Fe_{50} system. In addition, intermetallic and elemental phases have been identified. Amorphous and crystalline phases are noted in field emission SEM images. Elongation of second phase particles due to plastic deformation along with nano sized grain boundaries and oxygen contamination are also observed from SEM analysis.

Sintered compacts possess $Al_{76}Fe_{24}$ intermetallic, AlN and elemental phases, lattice expansion (0.4109 nm) of Al is noted during the consolidation process. Crystallite size of the compacts varied from 20 nm to 135 nm depending on the sintering parameters and milling duration of the precursor powder. Sintered compact (400-h) possesses stronger texture (Maximum intensity 6556.00), larger amount of AlN (19 %) and intermetallic (74 %) phases, thus the compact has higher nanohardness and elastic modulus compared to all types of consolidated bulk materials investigated in this research work. Fine acicular needle shaped AlN and second phase particles are found in the optical micrographs (OM), engloving is also observed both in SEM images as well as in OM.

CHAPTER 6: CONCLUSIONS

The process of mechanical alloying of Al and Fe using planetary high energetic ball mill is able to produce nano crystalline materials with short range order (SRO) / disorder nature which possess special structural, mechanical and magnetic properties when consolidated through different modes like equal channel angular pressing with back pressure and cold compaction followed by sintering routes. The results of the experiments carried out with the mixtures of 50 % Al and 50 % Fe (atomic %) of Al_{50}-Fe_{50} system has offered following conclusions:

1) From the results it is evident that the phases present in the unmilled mixture of powder at pre-mechanical alloying stage are elemental Al and Fe, no strain is induced in the powder and neither any solid solution phase is present.

2) Ball milling has resulted in progressive alloying of Al and Fe converting powder particles of the size of 60 μm to nano crystallites of the size of < 50 nm.

3) Lattice expansion is characterised by disordered structure while lattice contraction accompanies SRO phase. Ordered structure is thermodynamically more stable and offers greater resistance to crystallite refinement than the disordered state which is a metastable one.

4) Partial amorphisation and short range order (SRO) were noted when milling was carried out for a minimum duration of 125 and 30 hours respectively using tungsten carbide and toluene milling media (MM). However, the same phenomena appeared at a milling duration of 200 and 300 hours respectively in the case of stainless steel and argon MM.

5) SRO in the milled material is due to migration of vacancies as a result of Al diffusion in Fe lattice. SRO could also be caused by the increased micro-temperature attained during ball milling.

6) As the ball milling proceeds, crystallite size refinement associated with increase of microstrain takes place. The crystallite size refinement and increase in microstrain observed when milled in tungsten carbide and toluene media is to the tune of 12 nm and 1.021 % respectively at 65 hours of ball milling. While the crystallite size refinement and increase in micro strain when milled in stainless steel and argon media was 4.9 nm and 2.215 % respectively at 400 hours of ball milling.

7) At the end of 65 hours of milling (tungsten carbide MM) there is no visible change in composition of powder indicating that further change in energy of milling would be utilised for various metallurgical events to happen inside individually alloyed finely communited powder particles.

8) Metallurgical events taking place during ball milling in stainless steel and argon media are qualitatively not different compared to that carried out in tungsten carbide and toluene media except for the fact that maximum lattice expansion (0.2880 nm) of **Fe** at 20 hours of ball milling using tungsten carbide and toluene media is greater than the maximum lattice expansion (0.2869 nm) obtained at 100 hours of ball milling in stainless steel and argon media from 110 reflection.

9) Fe rich BCC solid solution (Fe (Al)) with a lattice parameter of 0.29316 nm was formed at the end of 185 hours of ball milling duration using tungsten carbide and toluene milling media (MM). However, such a solid solution with a lattice parameter of 0.2934 nm was observed at 400 hours of ball milling time using stainless steel and Argon MM.

10) Agglomeration of nano-sized crystalline particles, amorphisation to certain extent, destruction of grain boundaries, and formation of dislocation cells are evident in the TEM images of ball milled (stainless steel MM) powder.

11) Lattice expansion of solid solution (0.2927 nm) relates to the production of antisite defects. Complete alloying of elemental phases coupled with the formation of SRO could be the possible reasons for low M_S (21.37 emu/gm) in the 400 hour ball milled powder.

12) Ball milling beyond 30 hours using tungsten carbide and toluene MM causes hard (H_C > 125 Oe) magnetic properties. However, when stainless steel and argon MM was used, ball milled powders showed soft magnetic properties with the exception of 300 hours milled powder.

13) Decrease in M_S is mainly due to the progressive alloying of Al in Fe while, lattice expansion induced disordering due to ball milling causes ferromagnetism.

14) Mechanically alloyed powder transforms into ordered intermetallic (AlFe) of paramagnetic phase upon heating in the temperature range of 500 ^{0} to 700 ^{0}C. However, intermetallic $AlFe_3$ structure is ferromagnetic mainly because of its atomic structure.

15) Based on the present investigations, it is obvious that the magnetization can be modified by crystallite size and lattice parameter. Ball milling introduces vacancies, partial order within the disordered domain (antisite defects) and lattice expansion which contribute significantly to magnetic properties.

16) Results demonstrate the increase in M_S during the plastic deformation of annealed compacts to factors like applied stress, LRO parameter and lattice expansion. M_S increase is attributed to the simultaneous increase of both antisite atoms and lattice expansion. The M_S increase is low during initial stress range (0 to 3 GPa) predominantly because the deformed compact possess varying degree of ordering (LRO of ≥ 0.3), while the increase is steep for compact stressed between 3 GPa to 4 GPa, because of transition to complete disorder (LRO ≤ 0.2).

17) Order to disorder transition during low stress range caused by the increase in the occupancy of atoms in the wrong atomic sites influences the hardening phenomena. Crystallite size refinement leads to an increase in grain boundary area, grain boundaries act as barriers of metal flow during hardness indentation, thus, leading to increased hardness values.

18) Transitional alloy (AlFe) / Intermetallic compound ($AlFe_3$) are seen to be formed from Al-Fe solid solution when mechanically alloyed powders produced in stainless steel and argon MM are consolidated by ECAP-BP at different processing temperatures and back pressure.

19) Since grain growth is a diffusional process during elevated temperature consolidation, back pressure assisted ECAP decreases the diffusional coefficient thereby restricting the grain boundary mobility. Thus, grain growth which occurred during ECAP process is negligible, as, crystallite size (D=13.4 nm) of the pellet synthesized from powder ball milled for 100-hours is still in the nano range.

20) Pellet consolidated at higher temperature of 450 ^{0}C and with a higher back pressure of 480 MPa possesses better density with almost no porosities; compared to those consolidated at lower temperature and back pressure.

21) Metallurgical features like honeycomb structure, nucleation of nanopores, precipitation of second phase particles, plastic deformation and undeformed zones are observed in the photomicrographs of pellets.

22) ECAP-BP pellets of Al_{50}-Fe_{50} system possessed higher magnetic properties than pellets of Al_{90}-Fe_{10} system due to transitional (order to disorder) AlFe and ferromagnetic $AlFe_3$ phases.

23) Comparing the two categories of ECAP-BP consolidated pellet systems, nano hardness and elastic modulus of Al_{90}-Fe_{10} pellets were found to be lower than that of Al_{50}-Fe_{50} pellets.

24) Similar to hardness, the nature of bond between the atoms is responsible for change in elastic modulus of ECAP-BP pellets. The solid solution (having LRO $\leq$ 0.45) which consists of metallic bond records lower elastic modulus compared to AlFe/$AlFe_3$ intermetallic phases which consists of predominantly covalent bond apart from metallic bonds.

25) Wider (scattered) distribution of nano-indentation profiles is due to the fact that the load induced deformation is dominated by the local phase composition rather than the bulk mechanical properties.

26) Pop in phenomenon observed in the load-displacement curve for the pellet is associated with large scale dislocation motion with the onset of plastic deformation. Presence of a pore or collapsed vacancies below the advancing indenter could also be the possible reason for such a phenomenon.

27) TEM image of pellets indicate heavily deformed regions while SADP refers to amorphous as well as crystalline regions.

28) Oxygen contamination has caused the formation of Fe_3O_4 (magnetite) and Al_2O_3 formation in the pellets. Fe_3O_4 is ferrimagnetic while Al_2O_3 is paramagnetic.

29) Increase of H_C in the ECAP-BP pellets is mainly due to the magnetic anisotropy that appears due to severe plastic deformation. In addition, coercivity enhancement also occurs due to an increase in lattice defects like dislocation and collapsed vacancies as a consequence of SPD by ECAP-BP.

30) M_S of the pellets are lower than that of ball milled powders. However, H_C of the pellets are much higher than that of ball milled powders.

31) Consolidation of mechanically alloyed powder by compaction followed by sintering in a nitrogen atmosphere has resulted in the formation of AlN to a considerable extent. In addition, phases like AlFe, $AlFe_3$, AlN and Fe_4N are present in the sintered compact

32) Lattice dilation (by 0.4109 nm) of Al induced the formation of Al rich intermetallic phase of monoclinic structure in the Al_{90}-Fe_{10} system. Fe lattice dilation (by 0.2949 nm) induced the formation of Fe-rich intermetallic phase of Bcc structure in Al_{50}-Fe_{50} during sintering.

33) Sintered compact (200-h) exhibits higher nanohardness and elastic modulus compared to ECAP-BP consolidated pellets. Higher mechanical properties are due to the intermetallic (AlFe) and nitride phases (AlN and Fe_4N) prevailing in the sintered compacts in contrast to the transitional phase (partially ordered) revealed in most of the pellets.

34) Sintered compact (200-h) with enhanced texture (maximum intensity of 703.500 at Ψ=0 and Φ=292.5) than the ECAP-BP pellets, exhibits higher nanohardnes. In addition, larger crystallites (28 to 120 nm) have been identified in the sintered compacts compared to the crystallite size (9 to 13 nm) of pellets.

The results of the experiments carried out with the mixtures of 90 % Al and 10 % Fe (atomic %) have offered the conclusions that many of the metallurgical events occurred during mechanical alloying followed by consolidation processes are same as with 50 % Al and 50 % Fe, qualitatively. However, there are some specific differences in the case where a mixture of 90 % Al and 10 % Fe (Al_{90}-Fe_{10} system) is taken for investigation. Those conclusions are presented below:

1) The extent of amorphisation is substantially greater in the case of 90 % Al and 10 % Fe mixture compared to that of 50 % Al and 50 % Fe one when mechanical alloying is carried out under similar conditions.

2) Distinct glass transition temperature prior to crystallisation and a narrow supercooled liquid region are observed in all the powder samples of Al_{90}-Fe_{10} suggesting greater amorphous structure than those of Al_{50}-Fe_{50}.

3) Increasing the aluminium percentage from 50 to 90 atomic % during ball milling of elemental (Al & Fe) powder, induced a transition from soft magnetic properties to hard magnetic one.

4) Al is found to be present in elemental form without entering into alloying process even when milling is carried out for a longer duration of 400 hours in the present case. Similarly, Al is present in the elemental form along with intermetallic and AlN in all the sintered products.

5) Mechanical alloying has resulted in the dilation of Al lattice (0.4088 nm) in the present case in contrast to that of Fe lattice (0.2869/0.2880 nm in the case of stainless steel MM/tungsten carbide MM) in the case of 50 % Fe and 50 Al mixture.

6) Regions of crystallites (intermetallic compound of chemical formula $Al_{76}Fe_{24}$) along with undissolved elemental Al and aluminium oxide are formed from the matrix of amorphous solid solution of Al-Fe when mechanically alloyed powder is consolidated by ECAP-BP.

7) Slight amorphous structure in the pellets is indicated by the DSC analysis, the amount of amorphous structure is much less than that found in the ball milled powders.

8) Good bonding with minimum porosities is achieved in 400-h ECAP-BP consolidated pellet processed with a back pressure of 300 MPa and at a temperature of 450 ^{0}C in the present instance. While, in the 50 % Al and 50 % Fe, greater back pressure and temperature was needed to achieve the same quality.

9) No canning and pre-compaction of mechanically alloyed powder is necessary for ECAP-BP consolidation while pre-compaction is required for pressureless sintering process. However, canning is required for consolidation by ECAP without back pressure.

10) Some of the porosities in the pellets are in the nano scale regime, although, pellets consolidated at a low back pressure of 50 MPa and temperature of 200 ^{0}C showed

maximum sized porosities in the range of 2μm. However, pressureless sintered products showed larger sized (5 μm) porosities at a processing temperature of 800 ^{0}C and 1020 ^{0}C.

11) In addition to the lattice dilation observed during mechanical alloying, further dilation of Al lattice (0.4109 nm) was seen after sintering, such an expanded lattice is larger than the lattice dilation observed during mechanical alloying.

12) 400-h sintered compact (Al_{90}-Fe_{10} system) possessed highest nano-hardness and elastic modulus compared to other sintered compacts/pellets of both the systems. Such higher mechanical properties were due to stronger texture, larger amount of fine acicular AlN phase, and nanocrystalline $Al_{76}Fe_{24}$ compound present in the compact.

13) Strong deformation texture (maximum intensity of 6556.00 at Ψ=5.0 and Φ=342.5) of high intensity was observed in 400-h sintered product compared to all other consolidated products. Due to such higher preferred orientation of crystallites, highest nanohardness (37.5 GPa) was seen in the sintered product.

APPLICATIONS OF NANOSTRUCTURED Al-Fe ALLOYS

Nanostructured Al-Fe alloys are nearly 10 times higher in mechanical properties than conventional Al-Fe alloys. They are lighter and stronger and very promising material for application in transportation, small engines in automotive and aerospace application

The alloy finds application in car engines that consume less energy and can keep running on low oil, lead-free plumbing fixtures, and army tanks that are light enough to be airlifted, but are just as rugged as the much heavier varieties.

Mechanically alloyed nanostructured AlFe pellets can also be used as hard and soft magnetic materials in electrical and mechanical motors; high-power electromotors, computer and telecommunication industry, magnetic high density recording, navigation, aviation and space operations, automation micromechanics, medicine, sensor techniques, magneto caloric refrigeration, materials testing and household applications.

REFERENCES

Alexandrov I. V, Zhang K, Kilmametov A. R, Lu K and Valiev R. Z, (1997). *Materials Science and Engineering A*, 234 – 236, pp. 331 - 334.

Amils X, Nogues J, Surinach S et al., (1999), *Nanostructured materials*, **11**(6), pp. 689-695.

Amils X, Nogues J, Surinach S, Baro M. D, Munoz-Morris M. A, Morris D. G, (2000). *Intermetallics* 8, pp. 805±813.

Apinaniz E, Garitaonandia J. S and Plazaola F. (2001), *Journal of Non-crystal Solids*, **287**, pp. 302-307.

Apinaniz E, Plazaola F and Garitaonandia J. S, (2004). *J. Magn. Magn. Mater*. 94 (7), pp. 272–276.

Asgharzadeh H, Simchi A, and Kim H S, (2011). "Hot deformation of ultrafine-grained Al6063/Al_2O_3 nanocomposites," *Journal of Materials Science*, vol. 46, no. 14, pp. 4994–5001,

Badan B, Magrini M, Zambon A. (1996). *Scripta Mater*. (35), 13.

Baltazar Hernandez V. H, Panda S. K, Kuntz M. L, Zhou Y. (2010). *Materials Letters* 64, pp. 207–210.

Basavaraju S, Baker I. A. (2004). "Comparison of the microstructure and magnetic properties of mechanically alloyed and mechanically milled noncrystalline Fe50Co50 powders". *Mat Res Soc Symp Proc.*

Bernard F, Le Gallet S, Spinassou N, Paris S, Gaffet E, Woolman J. N, and Munir Z. A. (2004). *Science of Sintering*, 36, pp. 155-164.

Bettina Voutou, Eleni-Chrysanthi Stefanaki, (2008). *Physics of Advanced Materials Winter School.*

Bob hafner. (2007) *Characterization Facility*, University of Minnesota—Twin Cities 4/16/.

Bonneti E, Scipione G, Enzo S, Frattini R, Schiffini L. (1995). *Nanostructured Materials*, vol 6, pp 397-400.

Calka A, Radlinski A. P. (1991). *Mater Sci and Engineering A* 134:1350±3.

Cherif S. M, Bouziane K, Roussigne Y, Al-Busaidy M. (2007). *Materials Science and Engineering B* xxx xxx–xxx.

Cullity B. D, (1972). "Introduction to Magnetic Materials", *Addison-Wesley Publishing Company, Inc*.: Reading, MA,

Donachie M. J Jr. (2000). *Titanium*. A Technical Guide, second ed., ASM International,

Eelman D.A. Dahn J.R. Mackay G.R. and Dunlap R.A. (1998), *J. Alloys Compd*. **266**, pp. 234-240.

Esaki, H.; Ameyama, K.; Tokizane, M. (April 1989). *Materials Science and Technology*, Volume 5, Number 4, pp. 369-376(8).

Fabrizio M, Giorgi C, Morso A, (2009). *Int. J. Eng Sci*. 47, pp. 821-839.

Froes F. H, Suryanarayana C, Eliezer D. (1992). *Journal Mater Sci*. (27), 5113.

German R.M. (1994). "Powder Metallurgy Science"; 2nd Ed.; *Metal Powder Industries Federation: Princeton*, New Jersey, 562–567.

Goussous S, Xu W, Wu X, Xia K. (2009). *Composites Science and Technology* 69, pp. 1997–2001.

Hashii M. (1999), *Mater. Sci. Forum*. 312-314, pp. 139-144.

Hernando A, Amils X, Nogues J, Surinach S, Baro M. D and Ibarra M. R. (1998). *Physical Review B*, Volume 58, Number 18.

Hong S. J, Kim T. S, Kim H. S, Kim W. T, and Chun B. S, (1999). "Microstructural behavior of rapidly solidified and extruded Al–14 wt.%Ni–14 wt.%Mm (Mm: Misch metal) alloy powders"**,** *Mater. Sci. Eng. A*, vol. 271, pp. 469-476.

Hongwei Shi, Debo Guo and Yifang Ouyang, (2007), *Journal of Alloys & Comp.*

Huang B. Ishihara K.N. and Shingu P.H. (1997), *Mater. Sci.Eng*. A**231**, pp. 72-79.

Inoue A. (1998). "Amorphous, nanoquasicrystalline and nanocrystalline alloys in Al-based systems", *Prog. Mater. Sci*. Vol. 43, pp. 365-520.

Iwahashi Y, Horita Z, Nemoto M, Langdon T. G, (1997). *Acta mater* 45, pp. 4733 - 4741.

Izadi S, Akbari G. H, Janghorban K, Salahinejad E. (2010). *Journal of Alloys and Compounds*, pp 1-20.

Jartych E, Zurawicz J. K, Oleszak D and Pekala M. (1999), *Nano Structured Materials*, **12**, pp. 927-930.

Joint Committee of Powder Diffraction Standards (JCPDS). (1999). *International Centre for Diffraction Data (ICDD)*. 10-0425.

Jozef Miskuf, Kornel Csach, Alena Jurikova, Elena Tabachnikova, Vladimir Bengus, Aleksey Podolskiy and Vladimir Nesterenko. (2009). *Key Engineering Materials.* Vol. 409, pp 358-361.

Kenichiro Suehiro, Shunichi Nishimura and Zenji Horita. (2008). *Materials Transactions*, Vol. 49, No. 1, pp. 102 to 106.

Kim H. S. (2001) "Hardening behaviour of partially crystallised amorphous Al alloys", *Mater. Sci. Eng. A.* (Vols. 304 & 306), pp. 327-331.

Kim Y. B, Park H. M, Jeung W. Y, and Bae J. S, (2004). "Vacuum hot pressing of gas-atomized Ni–Zr–Ti–Si–Sn amorphous powder"**,** *Mater. Sci. Eng. A.* Vol. 368, pp. 318-322.

Klaus-Dieter Liss, Ross E. Whitfield, Wei Xu, Thomas Buslaps, LaReine A. Yeoh, Xiaolin Wu, Deliang Zhang and Kenong Xiab. (2009). *Journal of Synchrotron Radiation*, 16, 825–834.

Knibloe J. R, Wright R. N, Sikka V. K. (1990). In: Andreotti ER, McGreehan PJ, editors. "Advances in powder metallurgy". Princeton, NJ: *Metal Powder Industries Federation*. pp. 219.

Knobel M, Vazquez M, Kraus L, (2003). *Handbook of magnetic materials*, edited by K. H. J. Buschow, Vol. 15, Elsevier Science B.V., Amsterdam.

Koch C. C. (1992). *Mater. Sci. Forum* (243), 88-90.

Kolesnichenko V. G, Varchenko V. T, Zgalat-Lozynskyy O. B, Herrmann M, Ragulya A. V. (2012). *Proceedings of the International Conference Nanomaterials*: "Applications and Properties" Vol. 1 No 3, 03CNN07 (2pp).

Krasnowski M, Grabias A, Kulik T. (2006). *J. Alloys Compd*. (424), pp 119–127.

Krasnowski M, Kulik T. J. (2007). *Intermetallics*. (15), pp 201–205.

Krasnowski M, Kulik T. *Scripta Materialia* 48 (2003) 1489–1494.

Krasnowski M, Matyja H. (2001). *Mater Sci Forum*. (433), 360–362.

Lee K. J and Woo K. D, (2011). "Effect of pre-aging conditions on bake-hardening response of Al-0.4 wt % Mg-1.2 wt % Si-0.1 wt % Mn alloy sheets," *Journal of Korean Institute of Metals and Materials*, vol. 49, no. 6, pp. 448 453.

Levy J. C. S, (1986). *J. Magn. Mag. Mater*. 54- 47, pp. 277-278.

Lu L and Lai M. O. (1998). "Mechanical Alloying", *Kluwer Academic Publishers*.

Luo P, Xie H, Paladugu M, Palanisamy S, Dargusch M. S and Xia K. (2010). "Ultra Fine Grained Materials". *Journal of Material Science*.

May J. E, De Oliveira M. F, Afonso C. R. M, Sa Lisboa R. D, Kuri S. E. (2004). *Journal of Non-Crystalline Solids* 348, pp. 250–257.

McKamey C. G, Devan J. H, Tortorelli P. F, Sikka V. K. (1991). "A review of recent developments in Fe_3Al-based alloys". *Journal of Material Research* (6), 1779–1805.

Metallographic hand book (2010). Copy right by PACE technologies.

Meyers M. A, Mishra A and Benson D. J, (2006). *Prog. Mater. Sci*., 51, pp. 427.

Mhadhbi M, Khitouni M, Escoda L, Sunol J. J, and Dammak M. (2010). *Journal of Nanomaterials* Volume, p 8.

Miki M, Yamasa ki T, Ogono Y. (1995). *Mater Sci Forum*. (307), pp 179–181.

Morris D. G, Amils X, Nogues J, Surinach S, Baro M. D, and Munoz-Morris M. A. (2002). *Int. J. Non-Equilib. Process*. 11, pp. 379.

Morris-Munoz M. A, Doge A and Morris D. G, (1999). *Nanostruct. Mater.* **11, pp.** 873.

Morsi K, Goyal S. (2007). *Journal of Alloys and Compounds* 429, L1–L4.

Murty B. S and Ranganathan S, (1998). *International Material Reviews*, 43, pp. 101 - 141.

Nayak S. S, Chang H. J, Kim D. H, Pabi S. K, Murty B. S. (2011). *Material Science and Engineering A*. (528), 5967-5973.

Nayak S. S, Kim D. H, Pabi S. K, Murty B. S. (2006). *Trans. Ind. Inst. Met*. (59), 193.

Nayak S. S, Murty B. S, Pabi S. K. (2008). *Bull. Mater. Sci*. (31), 449.

Nayak S. S, Wollgarten M, Banhart J, Pabi S. K, Murty B. S. (2010). *Mater. Sci. Eng. A*. (527), 2370.

Negri D, Yavari A.R and Deriu A. (1999). *Acta Mater.* **47**(18), pp. 4545-4554.

Nishtha Gupta**,** S.Ramesh Kumar, B.Ravisankar and S.Kumaran. (2012). "World Academy of Science", *Engineering and Technology*, 61.

Nogueira R. N, Schon C. G. (2005), *Intermetallics.* (13), pp 1233–1244.

Nogues J, Apinaniz E, Sort J, Amboage M, D'Astuto M, Mathon O, Puzniak R, Fita I, Garitaonandia J. S, Surinach S, Munoz J. S, Baro M. D, Plazaola F and Baudelet F. (2006). *Phys. Rev. B* 74 024407.

Nogués J *et al.* (2006). *Phys. Rev. B* 74, 024407.

Oleszak D. and Shingu P.H., (1994), *Mater.Sci.Eng. A* 181-182, pp. 1217-1221.

Oleszak D and Shingu P. H, (1997). *Mater. Sci. Forum.* 235–238, 91.

Omori M, (2000). *Mater. Sci. Eng. A* 287, pp. 183 - 188.

Padmanabham K. A. (2001). *Mater Sci Eng A*. (200), 304–6.

Paydar M. H, Reihanian M, Bagherpour E, Sharifzadeh M, Zarinejad M, Dean T. A. (2009). *Materials and Design* 30, pp. 429–432.

Perepezko J. H, Wu R. I, Hebert R and Wilde G. (2000). MRS Fall Meeting.

Pfullmann T. H, Oehring M, Bohn R, Bormann R. (1996). *Mater Sci Forum*. (757), 225–7.

Pithawalla Y. B, Samy El-Shall M, Deevi S. C, (2000). *Intermetallics* 8, 1225.

Pithawalla Y. B, Samy El-Shall M, Deevi S. C, Strom V and Rao K. V. (2001). *The Journal of Physical Chemistry B* 11 vol 105. pp 2085-2090.

Plascak J. A, Zamora L. E, Alcazar G. A. P. (2000). *Phys Rev B*; 61:3188–91.

Plazaola F, Apiñaniz E, Martin Rodriguez D, Legarra E and Garitaonandia J. S (2012). "Fe-Al Alloys Magnetism". *Advanced Magnetic Materials*, pp. 133-170.

Qi Zeng, Ian Baker. (2007). *Intermetallics*. 15, pp. 419-427.

Rafiei M, Enayati M. H, Karimzadeh F. (2009). Journal of Alloys and Compounds 480, pp. 392–396.

Raviprasad K, Chattopadhyay K. (1992). *Philos Mag Lett*; 65:255–9.

Rico M. M, Greneche J. M and Perez A.G.A, (2005), *Journal of Alloys and Compounds*, 398, pp. 26-32.

Run-Hua Fan, Jia-Tao Sun, Hong-Yu Gong, et al., (2005), *Powder Tech.*, 149, pp. 121-126.

Sasaki T. T, Ohkubo T, Hono K. (2009). *Acta Mater*. (57), 3529.

Sebastian V, Lakshmi N and Venugopal K. (2007), *Intermetallics*, pp. 1-7.

Senkov O. N, Senkova S. V, Scott J. M, Miracle D. B. (2005). *Mater Sci Eng A*; 393:12.

Siegel R. W. (1993). *Mater. Sci. Eng. A*. 168, 189.

Sikka V. K. (1991). In: *Proceedings of the 5th Annual Conf*. on "Fossil Energy Materials". Oak Ridge, TN, p. 197.

Sort J, Ile D. C, Zhilyaev A. P, Concustell A, Czeppe T, Stoica M, Surinach S, Eckert J, Baro M. D. (2004). *Scripta Materialia* 50, pp. 1221–1225.

Stoloff N. S, Liu C. T, Deevi S. C. (2000). "Emerging applications of intermetallics". *Intermetallics*. (8), pp 1313–1320.

Stolyarov V. V, Lapovok R, Brodova I. G, Thomson P. F. (2003). *Materials Science and Engineering A*. 357, pp. 159-167.

Sung-Chul Lim, Kyung-Hoon Kim, Hung-Bok Lee. (2007). *Material Science Forum*. Vols. 534-536, pp 281-284.

Suryanarayana C. (2001). *Progress in Materials Science*. (46), 1 - 184.

Tavoosi M, Karimzadeh F, Enayati M. H, and Kim H. S. (2012). *Journal of Nanomaterials*. Volume 2012, Article ID 814915, 10 pages.

Thakur Prasad Yadav, Ram Manohar Yadav, Dinesh Pratap Singh, (2012). *Nanoscience and Nanotechnology*, 2(3): 22-48.

Thummler F, Oberacker R. (1993) In: "Introduction to powder metallurgy". London, UK: *The Institute of Materials*, p. 12.

Thierry Grosdidier, Gang Ji, Frederic Bernard, Eric Gaffet, Zuhair A. Munir, Sebastien Launois. (2006). *Intermetallics* 14, 1208-1213.

Thierry Grosdidier, Gang Jia, and Sebastien Launois. (2007). *Scripta Materialia*. 57, 525–528.

Valiev R. Z and Langdon T. G (2006). *Rev. Adv. Mater. Sci*. 13, pp. 15-26.

Valiev R. Z. (2004). *Nature Mater* 3:511.

Victor Abdelsayed, Samy El-Shall M, Takafumi Seto. (2006). *Journal of Nanoparticle Research*. Volume 8, Issue 3-4, pp 361-369.

Viswanathan, Laha T, Balani K, Agarwal A, Seal S, (2006). *Materials Science and Engineering R*. 54, 121–285.

Wu D, Baker I, and Munroe P.R. (2004), *Intermetallics*, **12**, pp. 851-858.

www.struers.com (2012).

Xia K, Wu X, Honma T, Ringer S. P. (2007). *J Mater Sci*. 42:1551–1560.

Xia K, Wu X. (2005). *Scripta Materialia*. 53, pp. 1225–1229.

Xiaoyin Cheng, Yifang Ouyang, Hongwei Shi, Xiaping Zhong, Yong Du, Xiaoming Tao. (2006). *Journal of Alloys and Compounds* 421, pp. 314–318.

Xi S. Q, Zhou J. G, Wang, X. T. (December 2007). *Powder Metallurgy*, Volume 50, Number 4, pp. 367 373 (7).

Xu W, Honma T, Wu X, Ringer S. P and Xia K. (2007). *Applied Physics Letters*. 91, 031901.

Xu W, Wu X, Sadedin D and Xia K. (2008). *Materials Forum*. Vol 32.

Yezdi B. Pithawalla, Sarojini Deevi. (2004). *Materials Research Bulletin*. 39, 2303–2316.

Yoritoshi Minamino, Yuichiro Koizumi, Nobuhiro Tsuji, Naoko Hirohata, Kiyoshi Mizuuchi, Yoshihira Ohkanda. (2004). *Science and Technology of Advanced Materials*. (5), 133-143.

Zeng Q. and Baker I. (2006), *Intermetallics*, **14**, pp. 396-405.

Zhang B. Q, Lu L, Lai M. O. (2003). *Physica B*. 325, 120-129.

Zhang M. X, Huang H, Spencer K, Shi Y. N. (2010). *Surface & Coatings Technology*. 204, 2118–2122.

Zhang W. S, Bruck E, Li W. F, Si P. Z, Geng D. Y and Zhang Z. D. (2005). *Physica B*. 370, pp. 131–136.

Zhao B, Gao Y, Zeng F, Pan F. (2003). "Nuclear Instruments and Methods" in *Physics Research B.* 211, pp. 339–345.

Zhilyaev A. P, Langdon T. G (2008). *Prog Mater Sci*. 53: 893.

Zhou F, Luck R, Scheer M, Lang D, and Lu K, (1999). "The crystallization process of amorphous Al80Fe20 alloy powders prepared by ball milling". *J. Non-Crystal. Solids*, vol. 250-252, pp. 704-708.

APPENDIX I

Graphs and Tables for ball milling and consolidation (Al_{50}-Fe_{50} system) characterization results

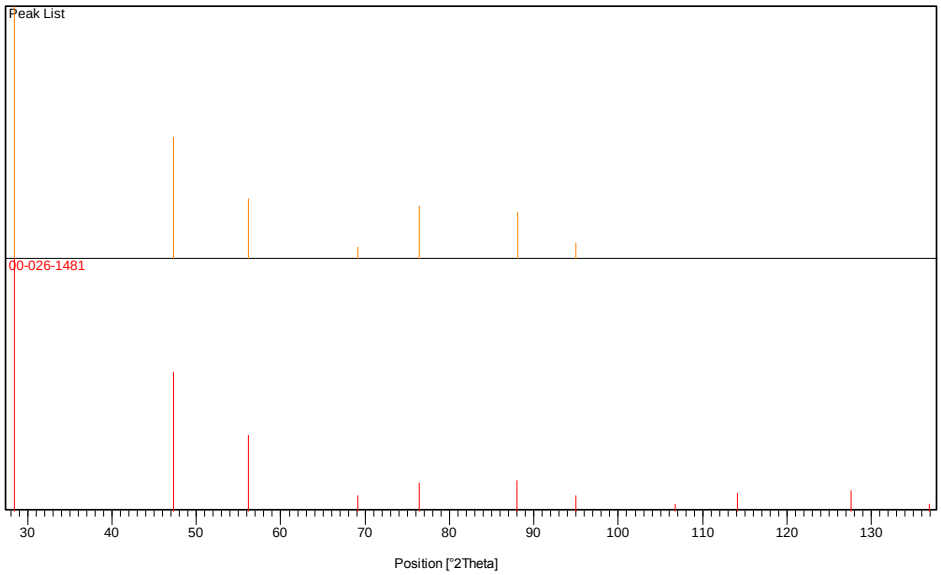

Fig 7.1 XRD matching pattern of silicon standard

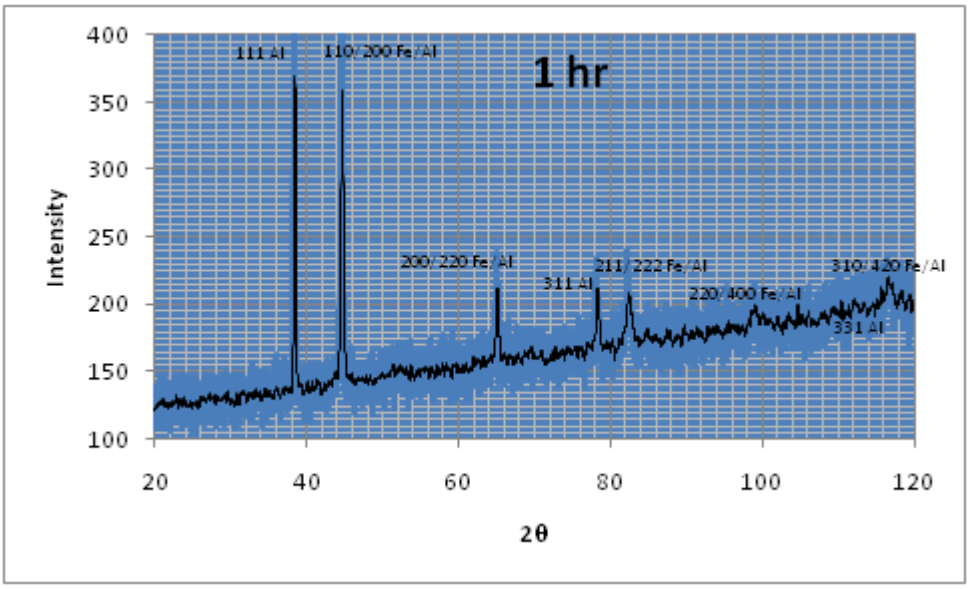

Figure 7.2 XRD pattern of powder ball milled for 01 hr.

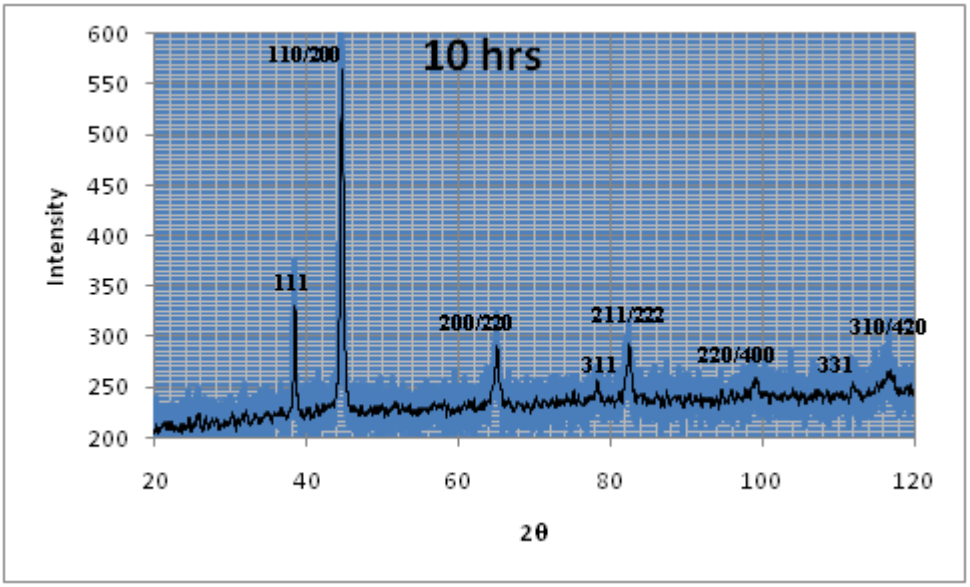

Figure 7.3 XRD pattern of powder ball milled for 10 hr.

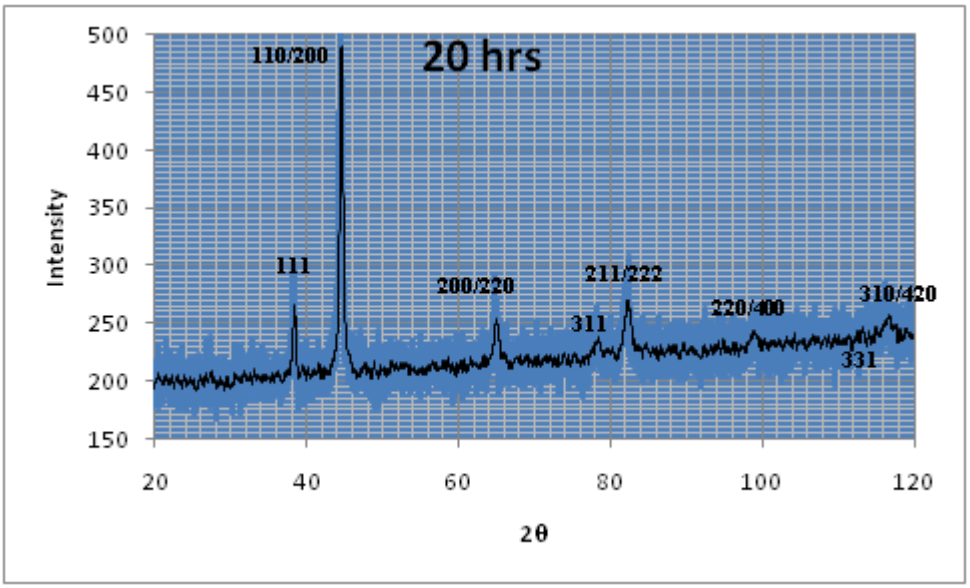

Figure 7.4 XRD pattern of powder ball milled for 20 hr.

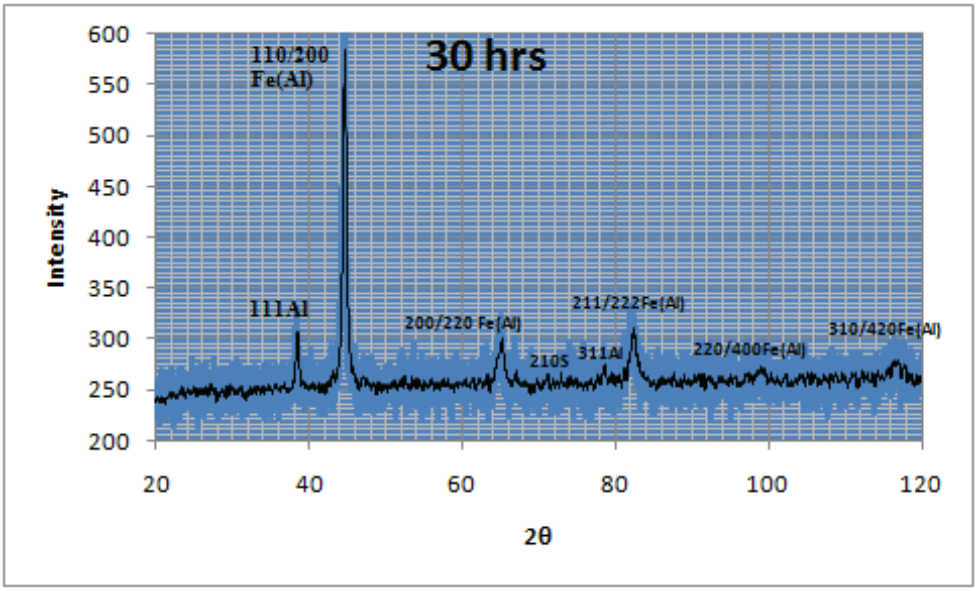

Figure 7.5 XRD pattern of powder ball milled for 30 hr.

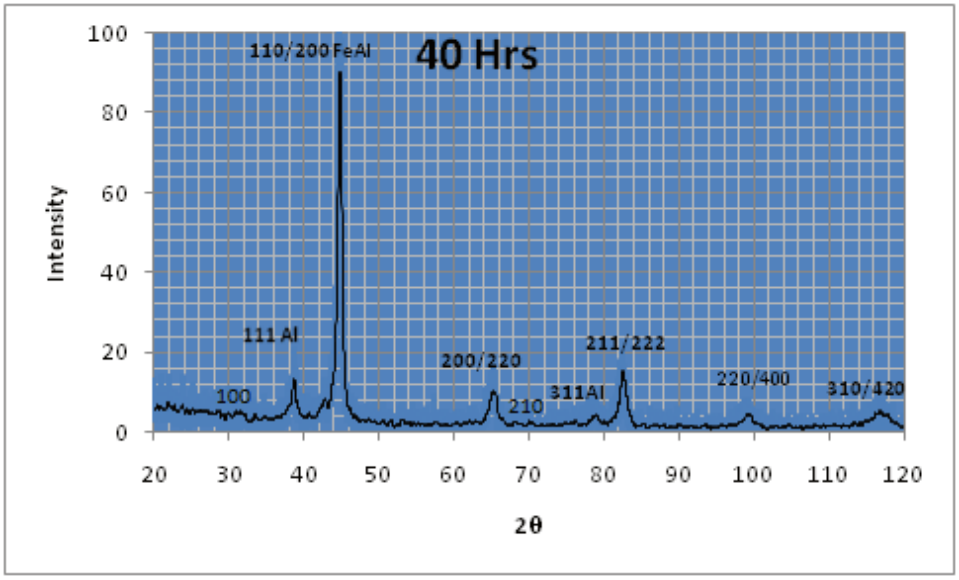

Figure 7.6 XRD pattern of powder ball milled for 40 hr.

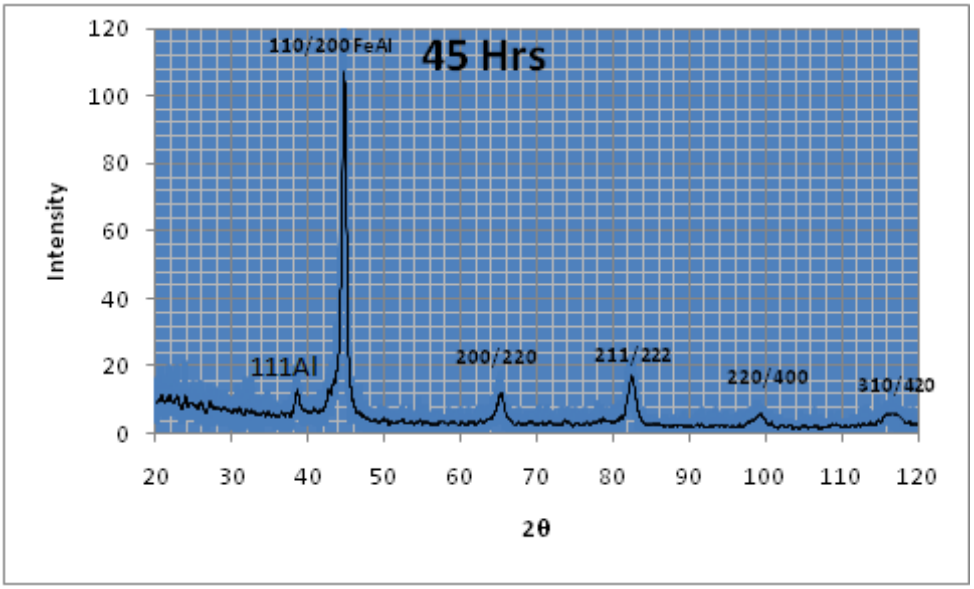

Figure 7.7 XRD pattern of powder ball milled for 45 hr.

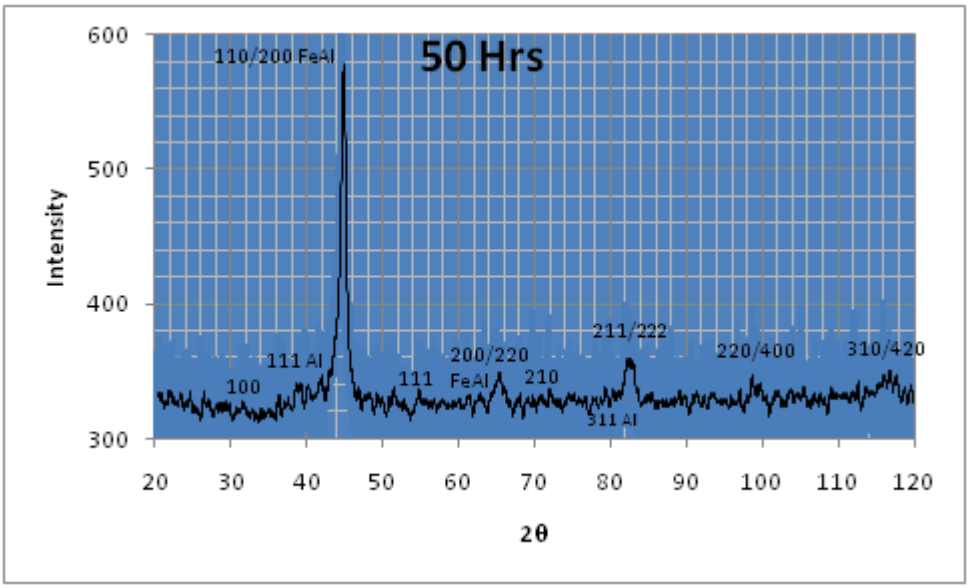

Figure 7.8 XRD pattern of powder ball milled for 50 hr.

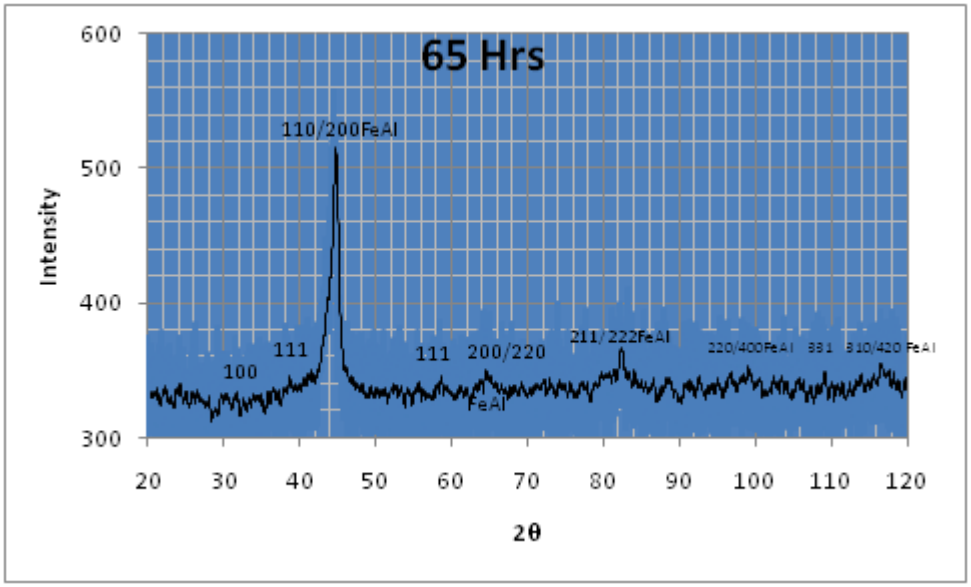

Figure 7.9 XRD pattern of powder ball milled for 65 hr.

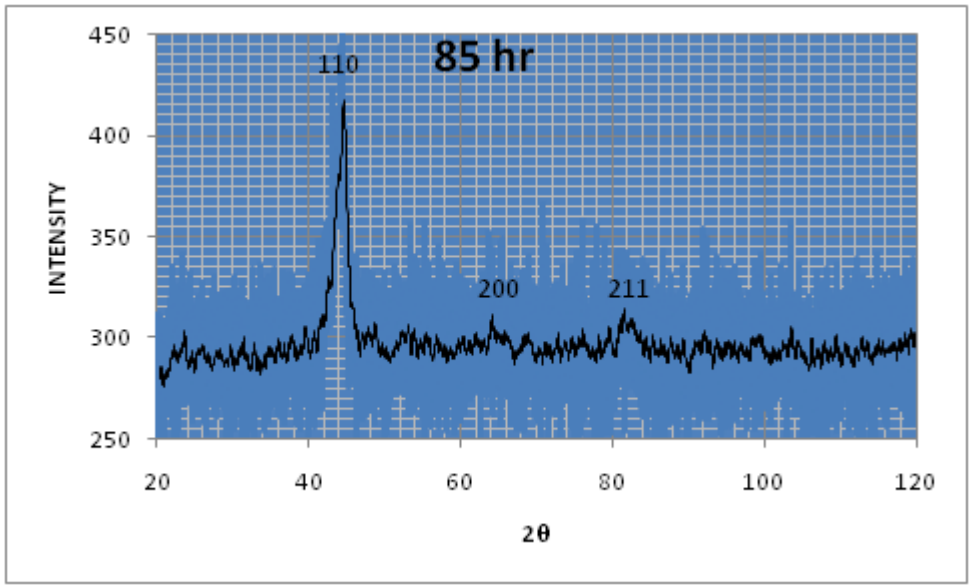

Figure 7.10 XRD pattern of powder ball milled for 85 hr.

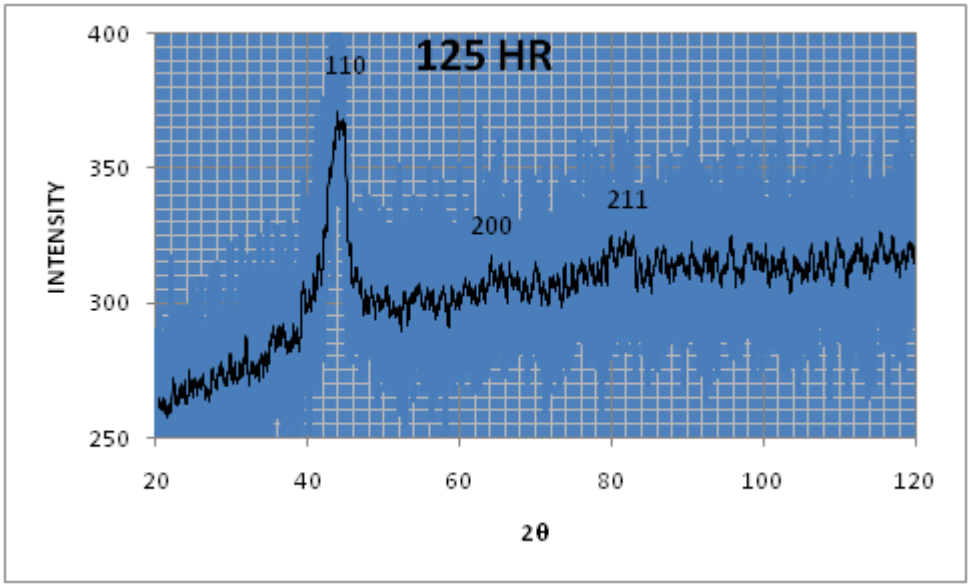

Figure 7.11 XRD pattern of powder ball milled for 125 hr.

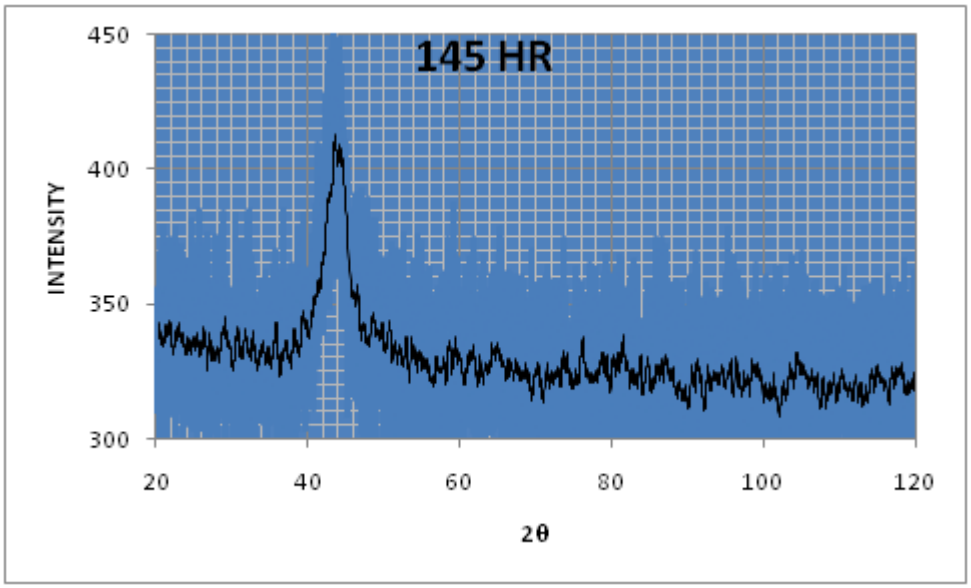

Figure 7.12 XRD pattern of powder ball milled for 145 hr.

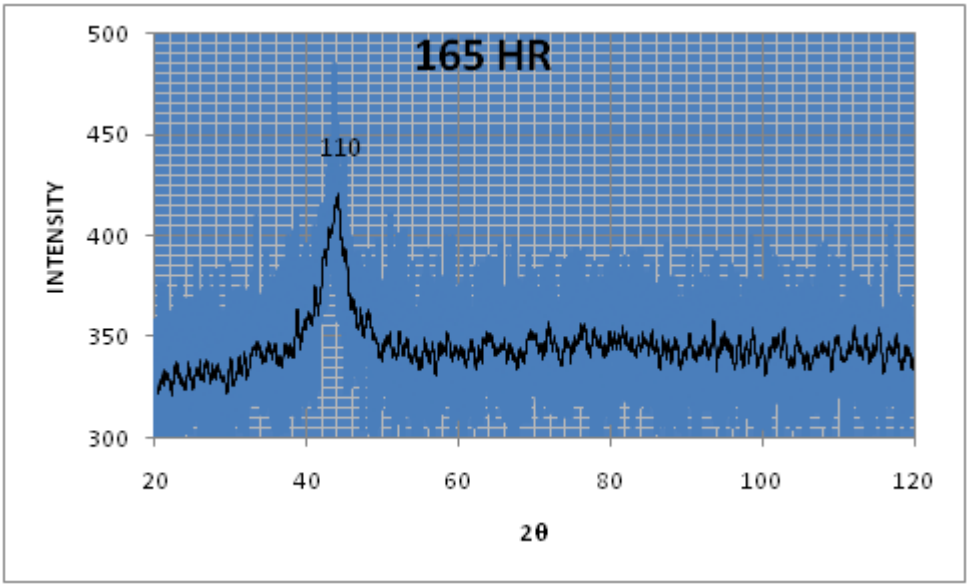

Figure 7.13 XRD pattern of powder ball milled for 165 hr.

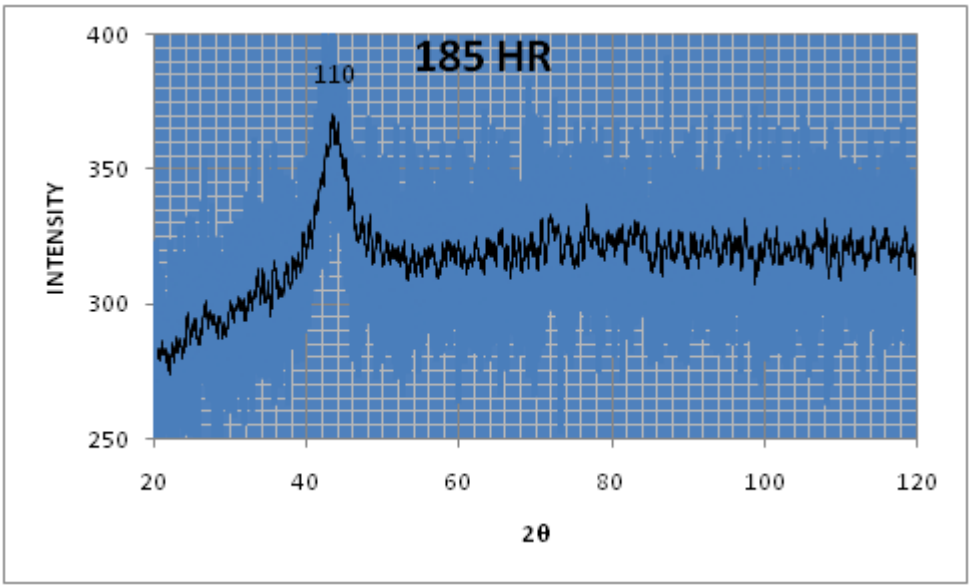

Figure 7.14 XRD pattern of powder ball milled for 185 hr.

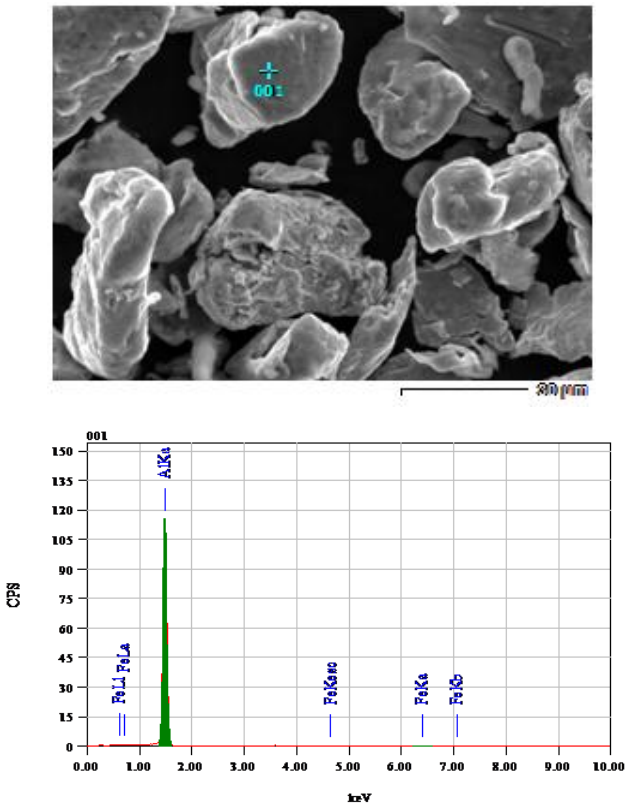

Figure 7.15 One (01) hr ball milled powder.

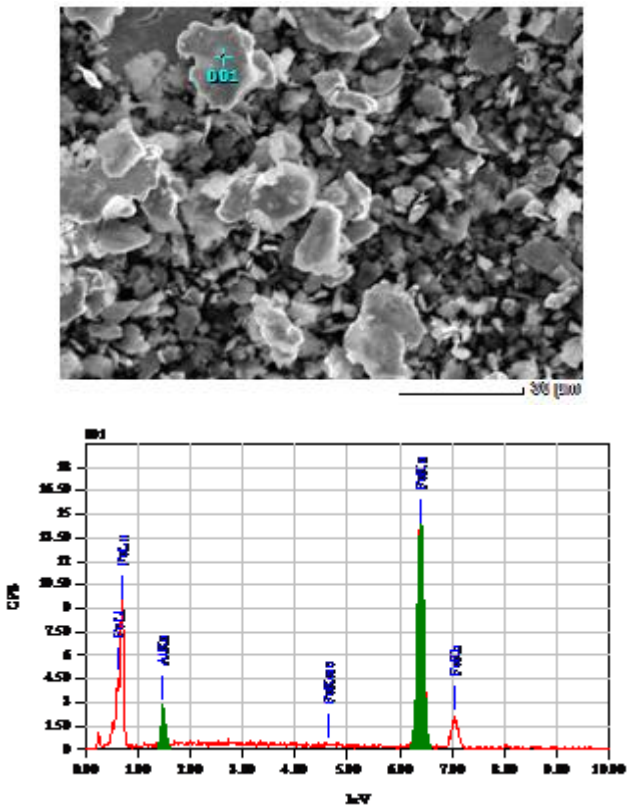

Figure 7.16 Ten (10) hr ball milled powder.

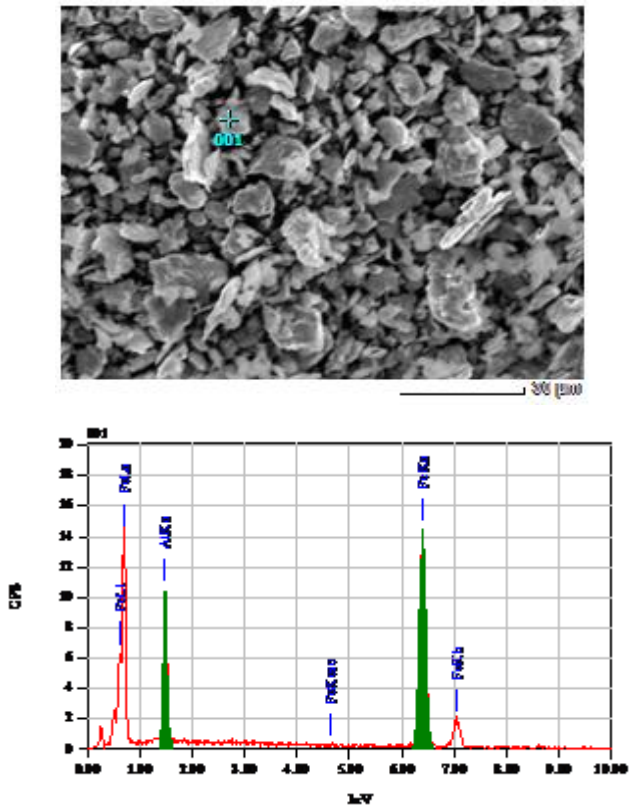

Figure 7.17 Twenty (20) hr ball milled powder.

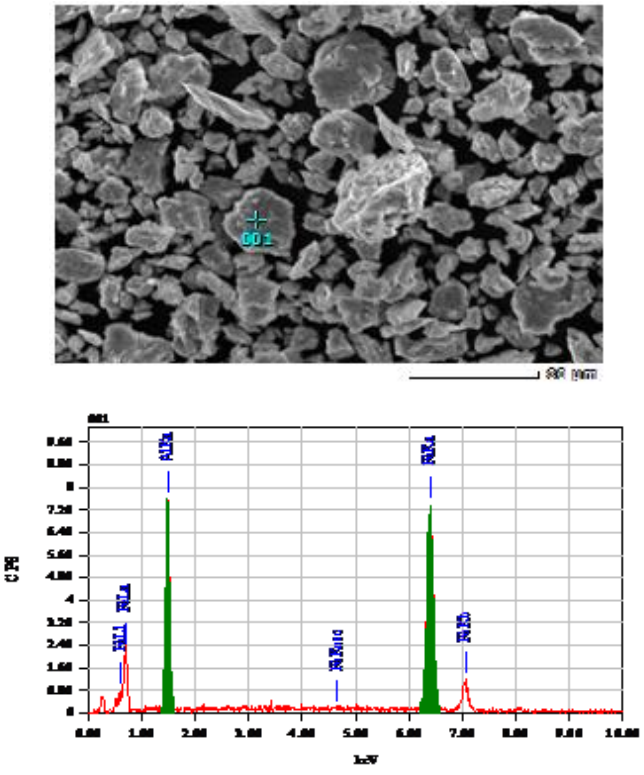

Figure 7.18 Fourty (40) hr ball milled powder.

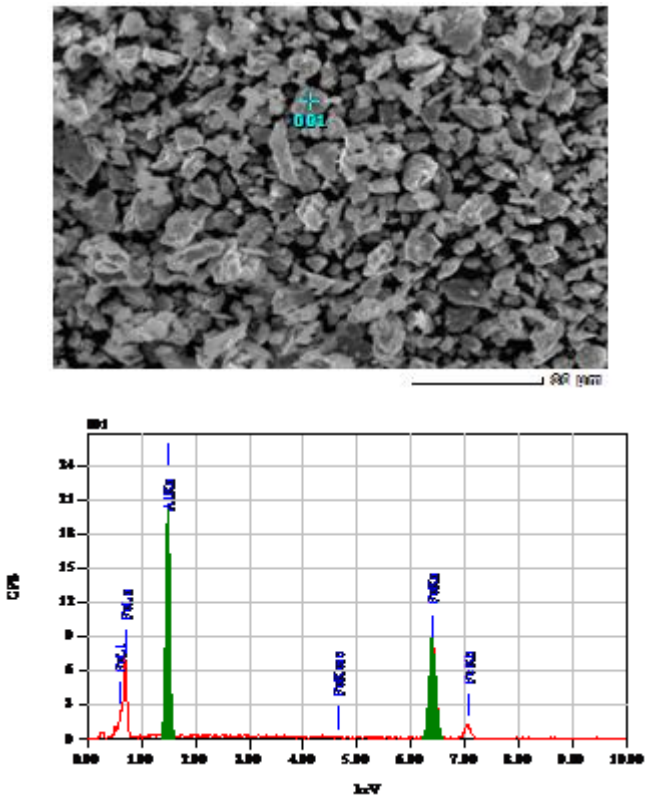

Figure 7.19 Fifty (50) hr ball milled powder.

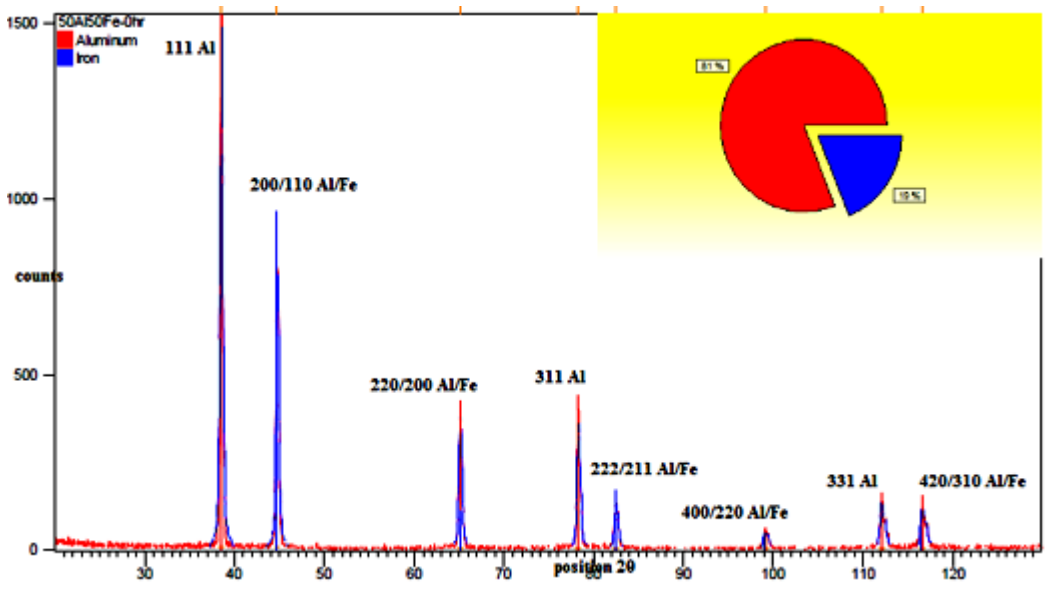

Figure 7.20 XRD pattern of elemental Al/Fe mixture of unmilled powder.

Table 7.1 Peak list of pattern no 03-065-2869 of Al and pattern no 03-065-4899 of Fe

Peaks	hkl	d(A)	2θ	I(%)	peaks	hkl	d(A)	2theta(deg)	I(%)
1	111	2.33810	38.471	100.0	1	110	2.02728	44.663	100.0
2	200	2.02485	44.720	47.8	2	200	1.43350	65.008	11.5
3	220	1.43178	65.095	26.1	3	211	1.17045	82.314	17.7
4	311	1.22103	78.227	26.8	4	220	1.01364	98.917	4.7
5	222	1.16905	82.434	7.5	5	310	0.90662	116.344	6.4
6	400	1.01242	99.078	3.3					
7	331	0.92906	112.015	9.9					
8	420	0.90554	116.565	9.4					

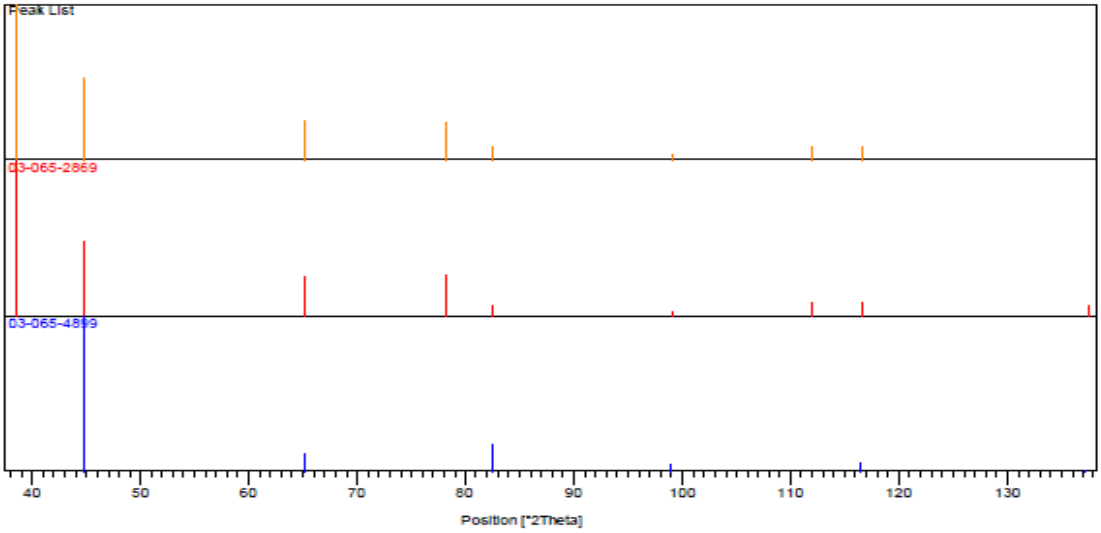

Figure 7.21 Matching patterns obtained for unmilled XRD pattern.

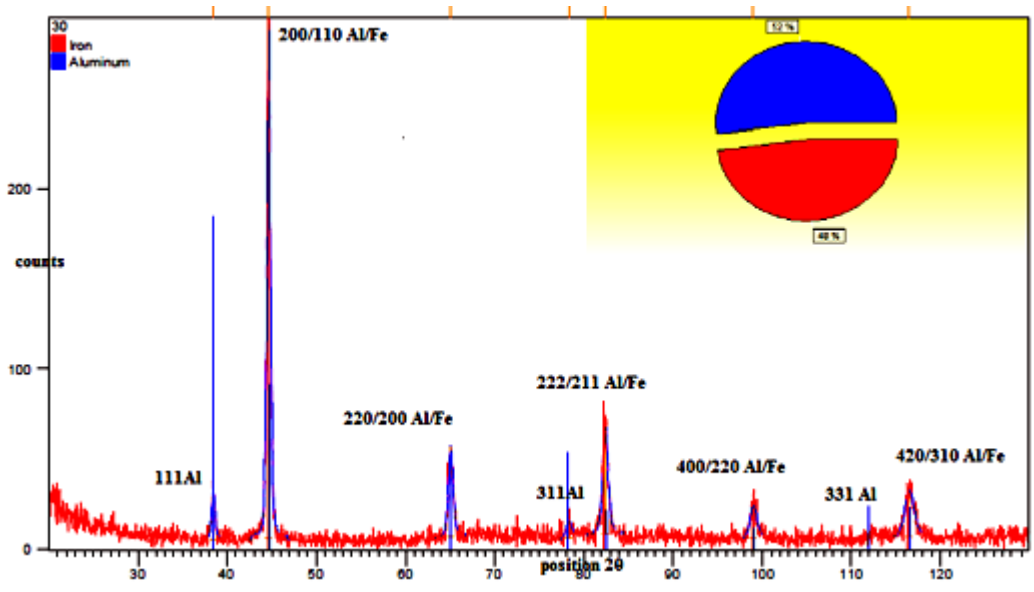

Figure 7.22 XRD profile of elemental powder ball milled for 30 hours.

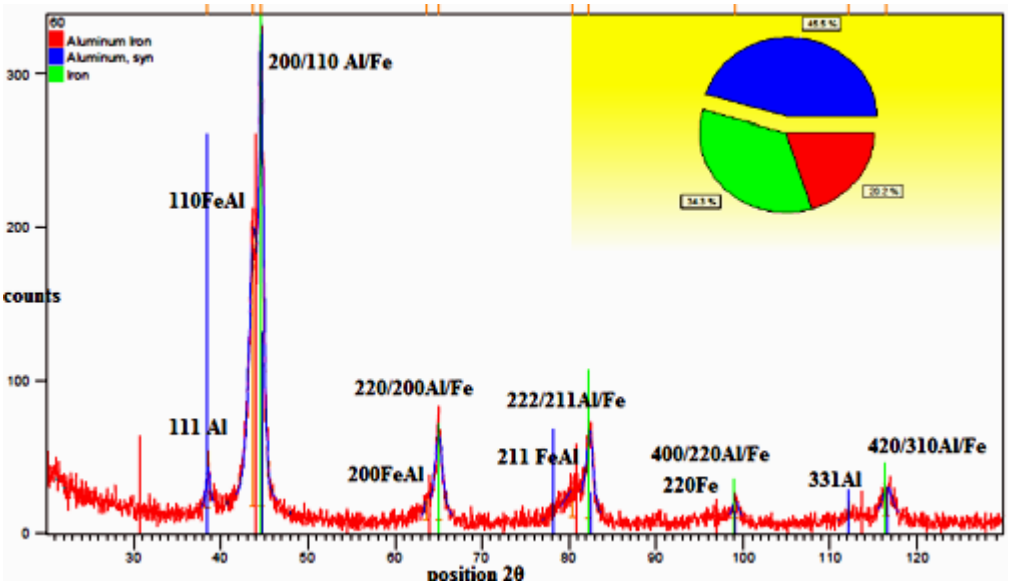

Figure 7.23 XRD profile of elemental powder ball milled for 60 hours.

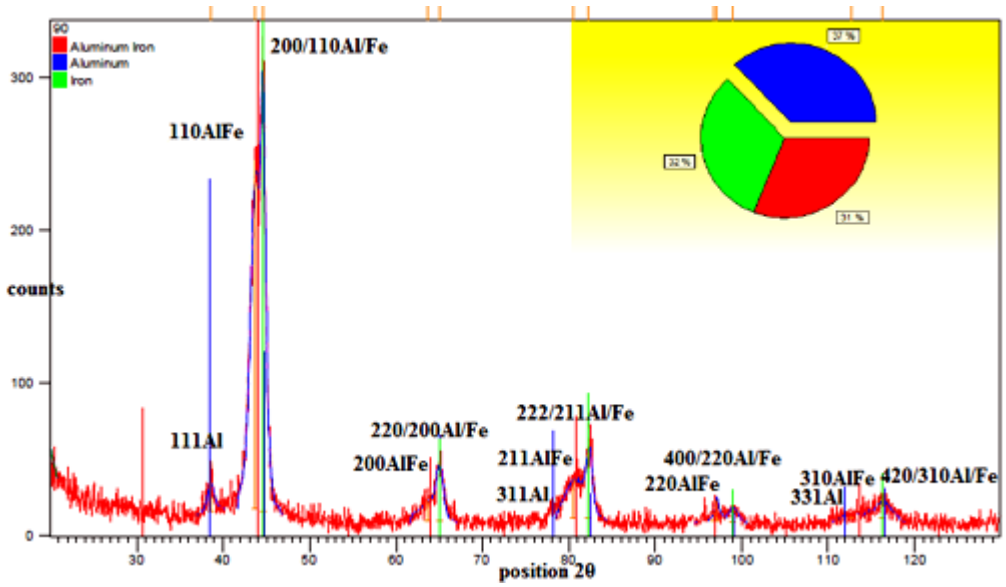

Figure 7.24 XRD pattern of elemental powder ball milled for 100 hours duration.

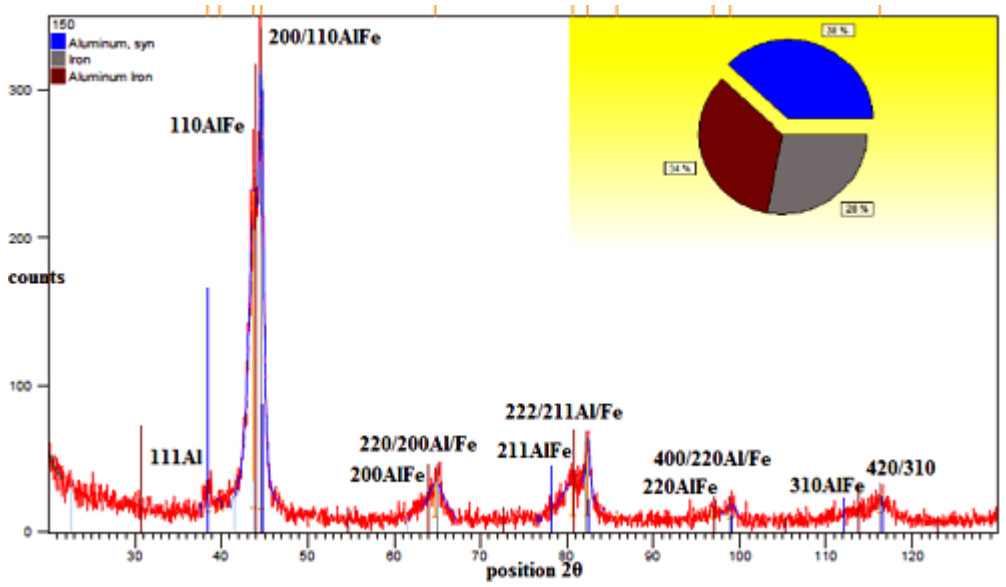

Figure 7.25 XRD pattern of elemental powder ball milled for 150 hours duration.

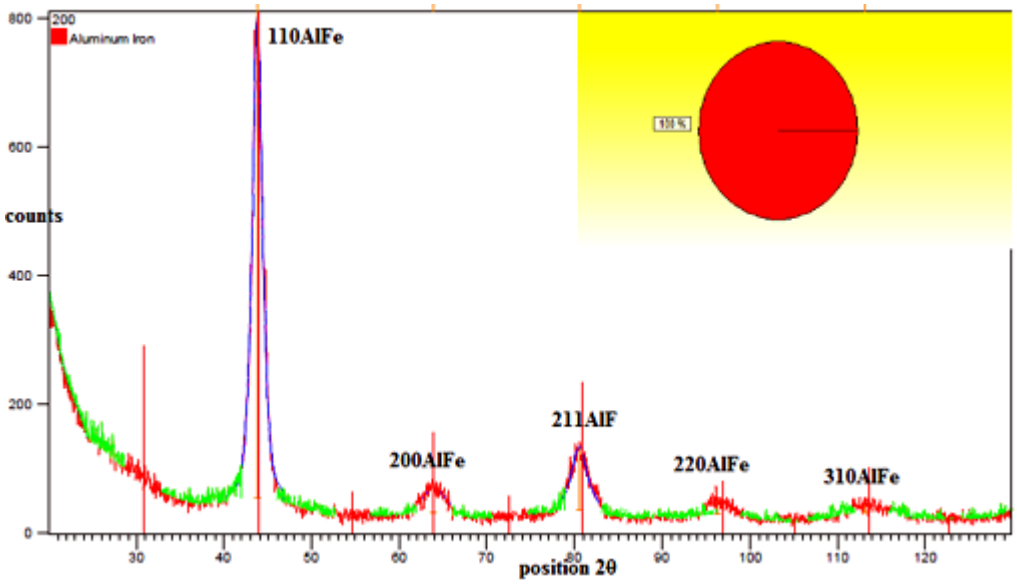

Figure 7.26 XRD pattern of elemental powder ball milled for 200 hours duration.

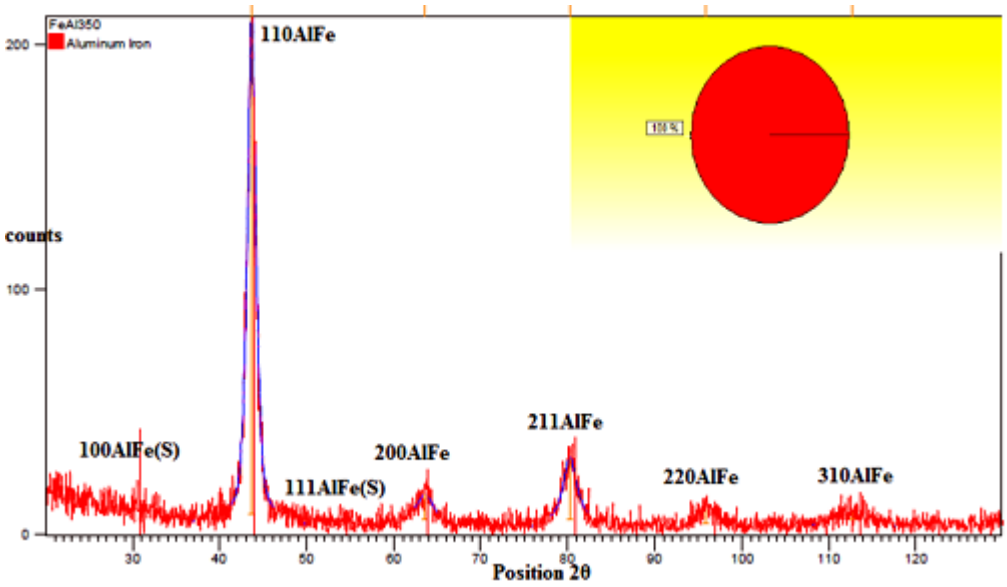

Figure 7.27 XRD pattern of elemental powder ball milled for 300 hours duration.

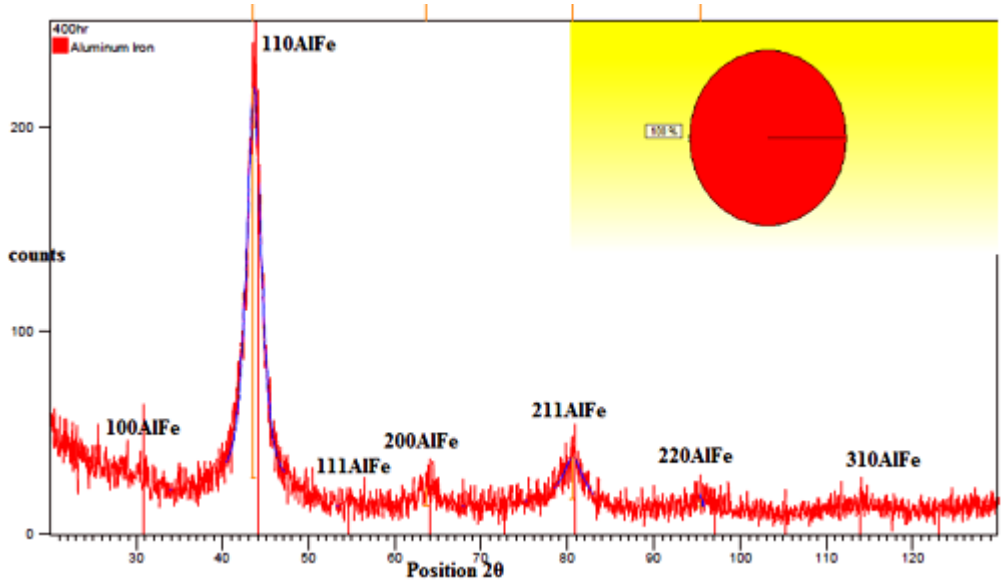

Figure 7.28 XRD pattern of elemental powder ball milled for 400 hours duration.

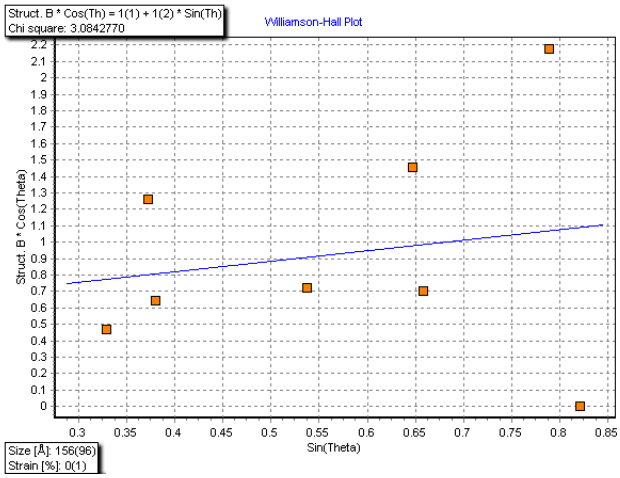

Figure 7.29 Hall-Williamson plot obtained for 30 hours ball milled powder sample.

Table 7.2 Peak list of AlFe (matching pattern no; 03-065-0985) and Al (no; 00-004-0787) for 60 hours ball milled powder

peak	hkl	d(A)	2theta(deg)	I(%)	peak	hkl	d(A)	2theta(deg)	I(%)
1	100	2.91000	30.699	20.2	1	111	2.33800	38.473	100.0
2	110	2.05768	43.969	100.0	2	200	2.02400	44.740	47.0
3	111	1.68009	54.579	3.6	3	220	1.43100	65.135	22.0
4	200	1.45500	63.932	12.3	4	311	1.22100	78.230	24.0
5	210	1.30139	72.585	3.1	5	222	1.16900	82.438	7.0
6	211	1.18800	80.842	19.7	6	400	1.01240	99.081	2.0
7	220	1.02884	96.957	5.1	7	331	0.92890	112.046	8.0
8	300	0.97000	105.145	1.0	8	420	0.90550	116.574	8.0
9	310	0.92022	113.666	6.8					
10	311	0.87740	122.789	0.7					

Table 7.3 Fe 03-065-4899-60 hrs

peak	hkl	D(A)	2theta(deg)	I(%)
1	110	2.02728	44.663	100.0
2	200	1.43350	65.008	11.5
3	211	1.17045	82.314	17.7
4	220	1.01364	98.917	4.7
5	310	0.90662	116.344	6.4

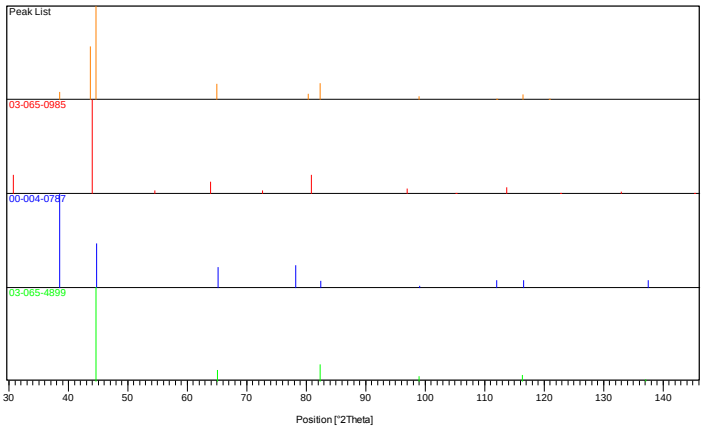

Figure 7.30 Matching pattern obtained for XRD pattern of 60 hours ball milled powder.

Table 7.4 Pattern No: 03-065-6132 of AlFe-150 hr

peak	hkl	d(A)	2theta(deg)	I(%)
1	100	2.90760	30.725	19.5
2	110	2.05598	44.007	100.0
3	111	1.67870	54.628	3.4
4	200	1.45380	63.991	12.1
5	210	1.30032	72.654	3.1
6	211	1.18702	80.923	19.4
7	220	1.02799	97.064	5.0
8	300	0.96920	105.269	1.0
9	310	0.91946	113.811	6.7
10	311	0.87667	122.963	0.6

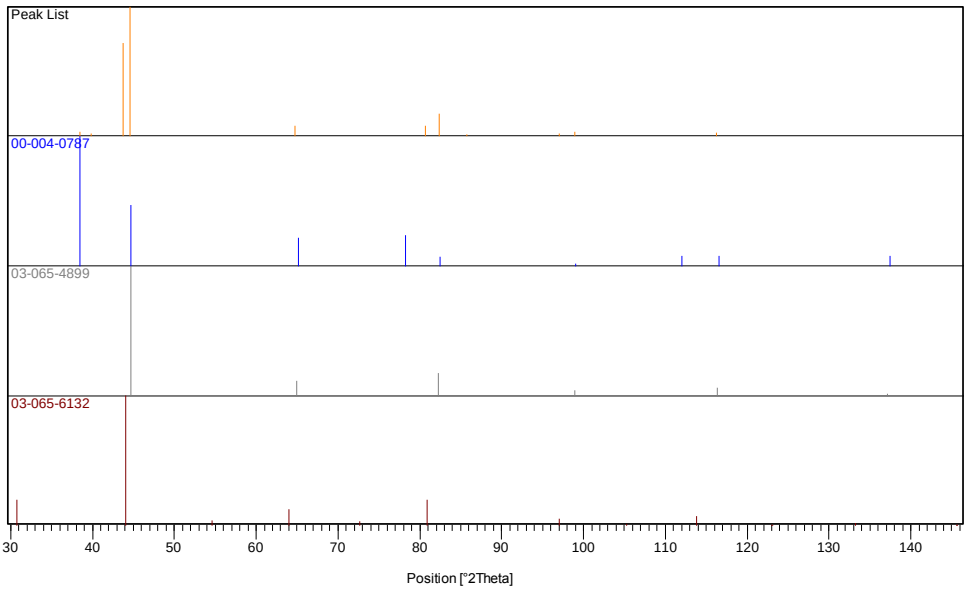

Figure 7.31 Matching pattern obtained for XRD pattern of 150 hours ball milled powder.

Table 7.5 Peak list & Plot of Identified Phase AlFe-200 hrs

peak	hkl	d(A)	2θ	I(%)
	100	**2.91000**	**30.699**	**20.2**
	110	2.05768	43.969	100.0
	111	1.68009	54.579	3.6
	200	1.45500	63.932	12.3
	210	1.30139	72.585	3.1
	211	1.18800	80.842	19.7
	220	1.02884	96.957	5.1
	300	0.97000	105.145	1.0
	310	0.92022	113.666	6.8
	311	0.87740	122.789	0.7

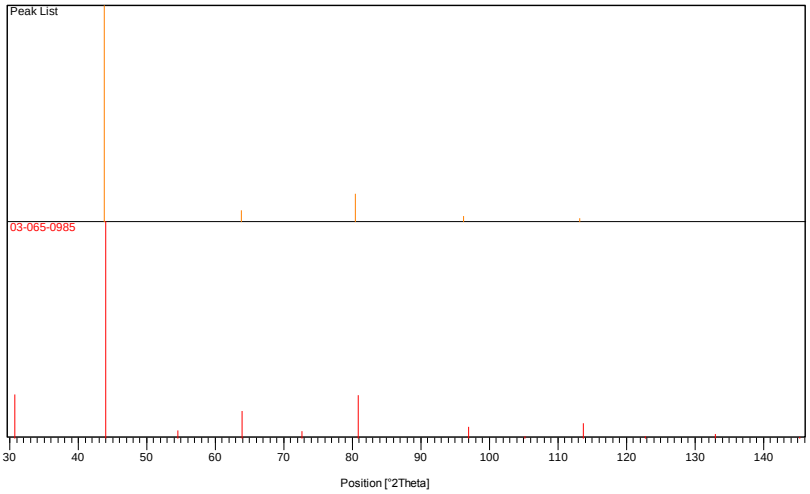

Figure 7.32 Matching pattern obtained for XRD pattern of 200 hours ball milled powder.

Table 7.6 Peak list & Plot of Identified PhaseFeAl-300 hrs

peak	hkl	d(A)	2θ	I(%)
1	**100**	2.91000	30.699	20.2
2	**110**	**2.05768**	**43.969**	100.0
3	111	1.68009	54.579	3.6
4	**200**	**1.45500**	**63.932**	12.3
5	210	1.30139	72.585	3.1
6	**211**	**1.18800**	**80.842**	19.7
7	**220**	**1.02884**	**96.957**	5.1
8	300	0.97000	105.145	1.0
9	**310**	**0.92022**	**113.666**	6.8
10	311	0.87740	122.789	0.7

Table 7.7 400 hrs-Plot of Identified Phases: Peak list

peak	hkl	d(A)	2θ	I(%)
1	100(S)	2.90760	30.725	19.5
2	110	2.05598	44.007	100.0
3	111(S)	1.67870	54.628	3.4
4	200	1.45380	63.991	12.1
5	210(S)	1.30032	72.654	3.1
6	211	1.18702	80.923	19.4
7	220	1.02799	97.064	5.0
8	300(S)	0.96920	105.269	1.0
9	310	0.91946	113.811	6.7
10	311	0.87667	122.963	0.6

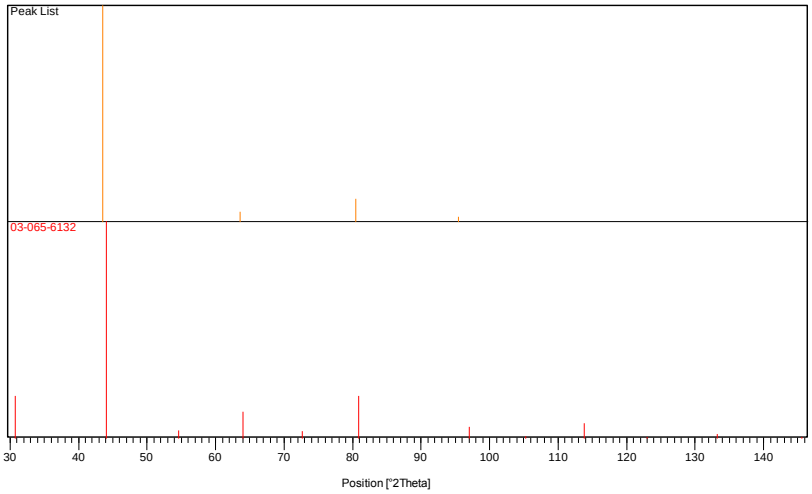

Figure 7.33 Matching pattern obtained for XRD pattern of 400 hours ball milled powder.

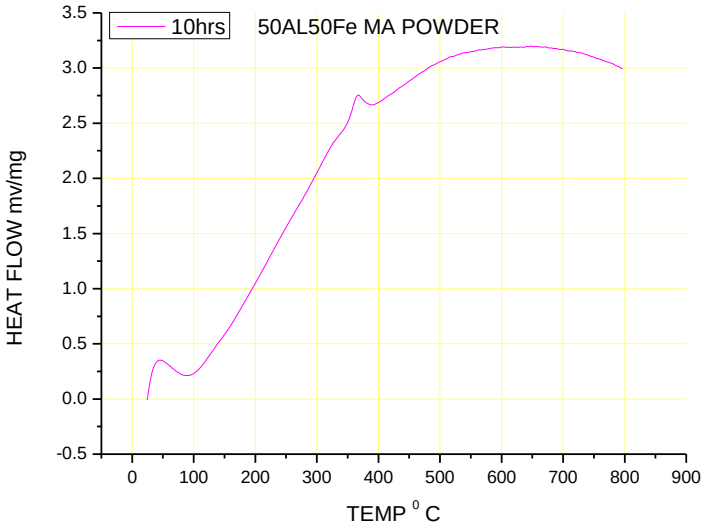

Figure 7.34 DSC curve of powder ball milled for 10 hours

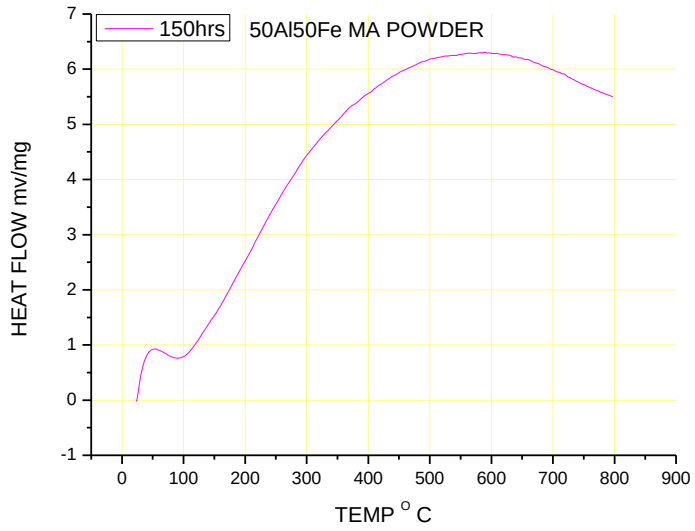

Figure 7.35 DSC curve of powder ball milled for 150 hours

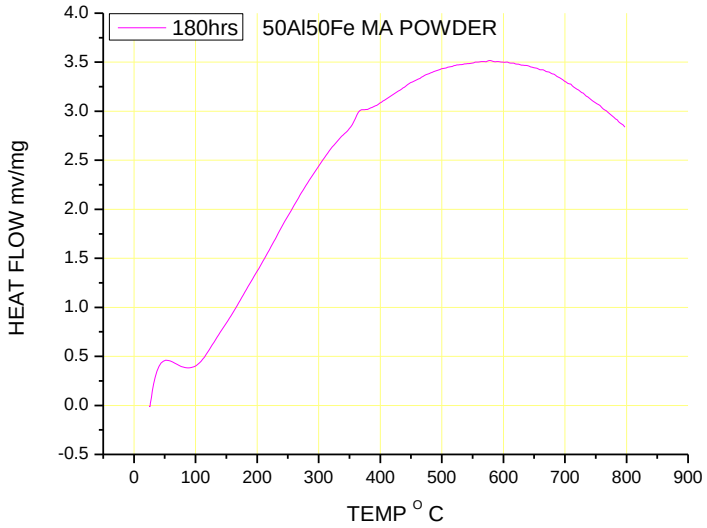

Figure 7.36 DSC curve of powder ball milled for 180 hours

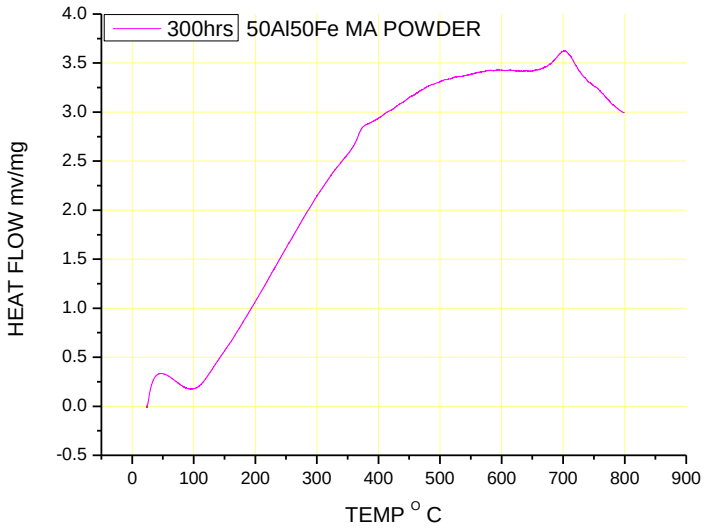

Fig 7.37 DSC curve of powder ball milled for 300 hours

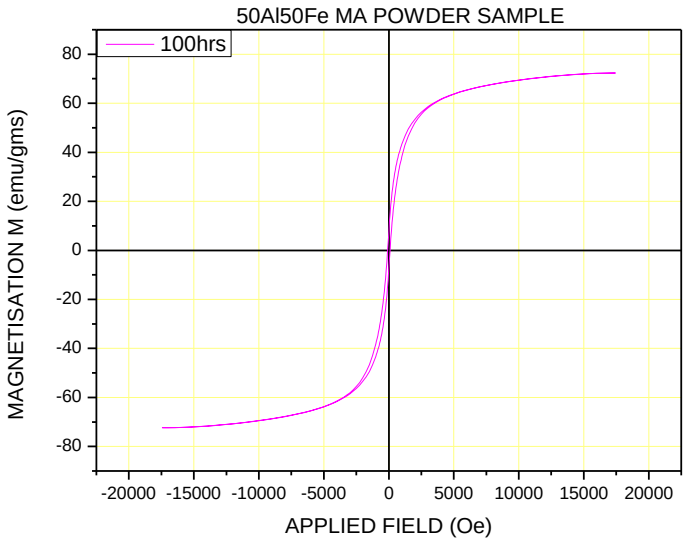

Figure 7.38 Magnetic hysteresis loop of 100 hour ball milled powder

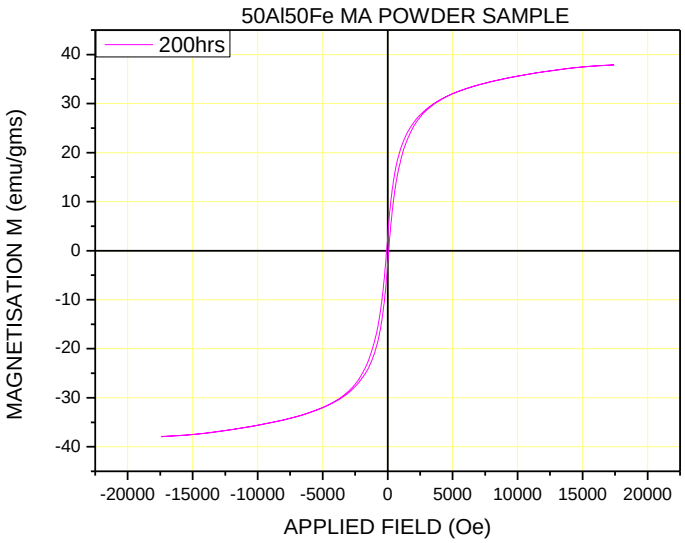

Figure 7.39 Magnetic hysteresis loop of 200 hour ball milled powder

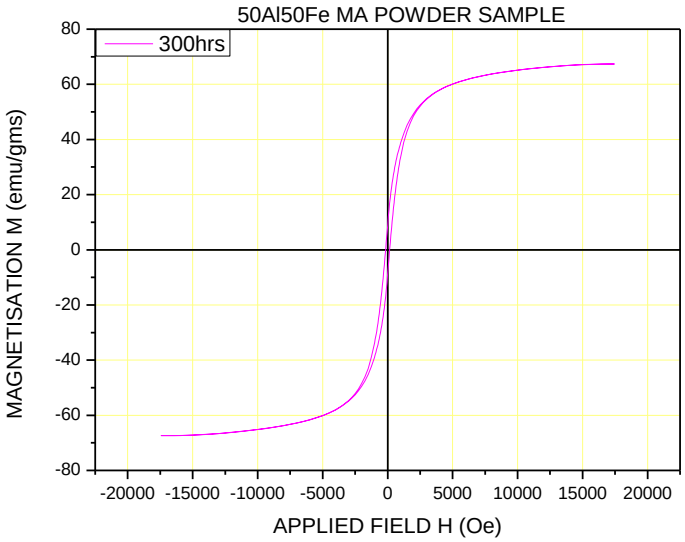

Figure 7.40 Magnetic hysteresis loop of 300 hour ball milled powder

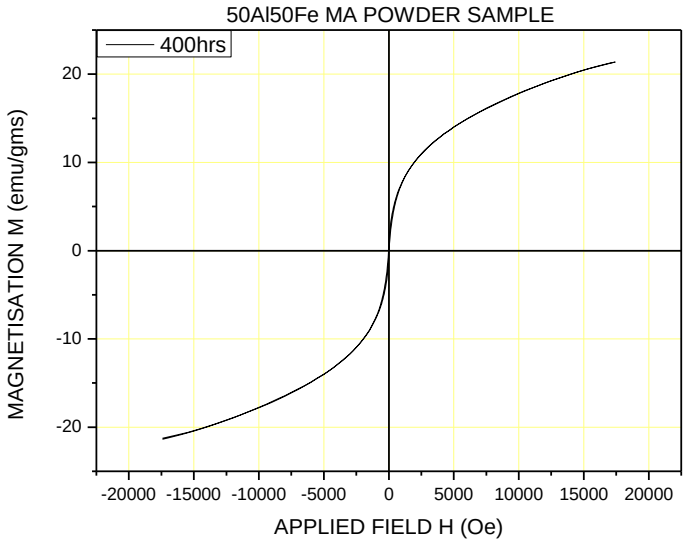

Figure 7.41 Magnetic hysteresis loop of 400 hour ball milled powder

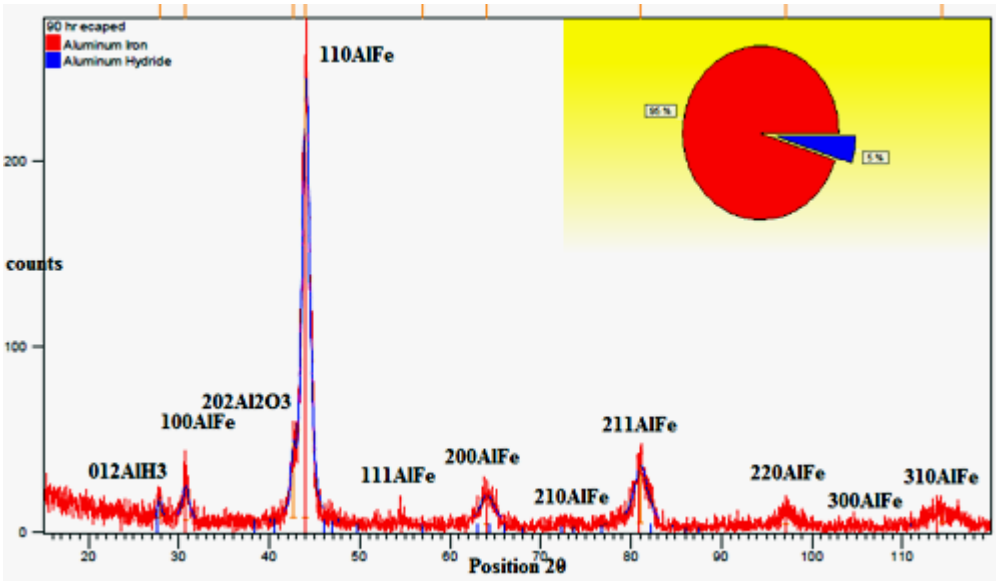

Figure 7.42 XRD pattern of ECAP-BP pellet obtained by consolidating MA powders processed at 100 hours of ball milling duration at 300^0 C. Shows AlFe, AlH_3 and Al_2O_3 phases. AlFe phase is ordered (100,111, 210 and 300 superlattice peaks). AlH_3 is rhombohedral and Al_2O_3 is hexagonal crystal structures

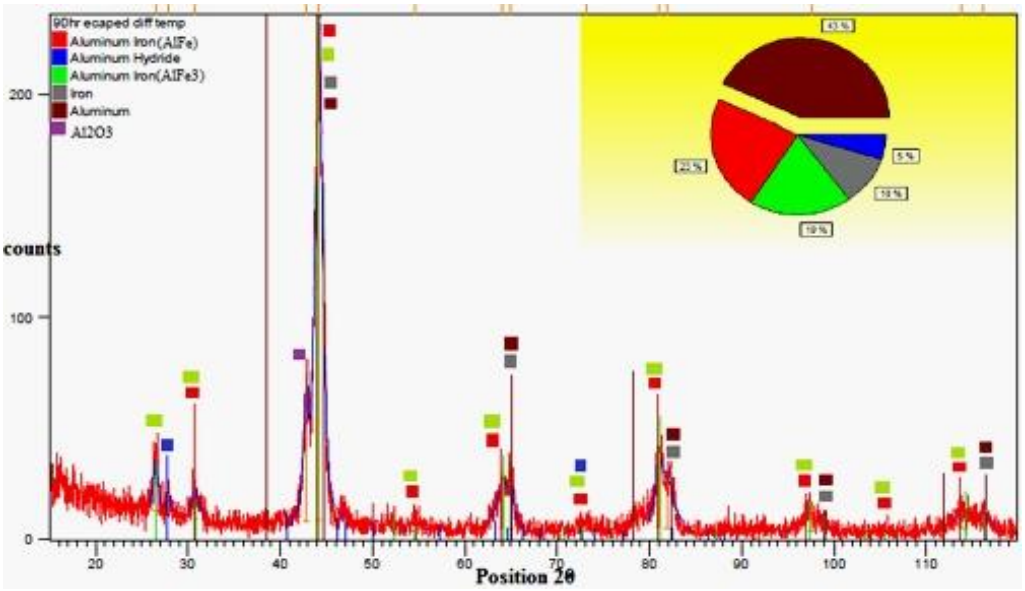

Figure 7.43 XRD pattern of ECAP-BP pellet obtained by consolidating MA powder at 500^0 C, MA is done at 100 hours of ball milling duration. Shows AlFe, $AlFe_3$, AlH_3, Al, Fe and Al_2O_3 phases.

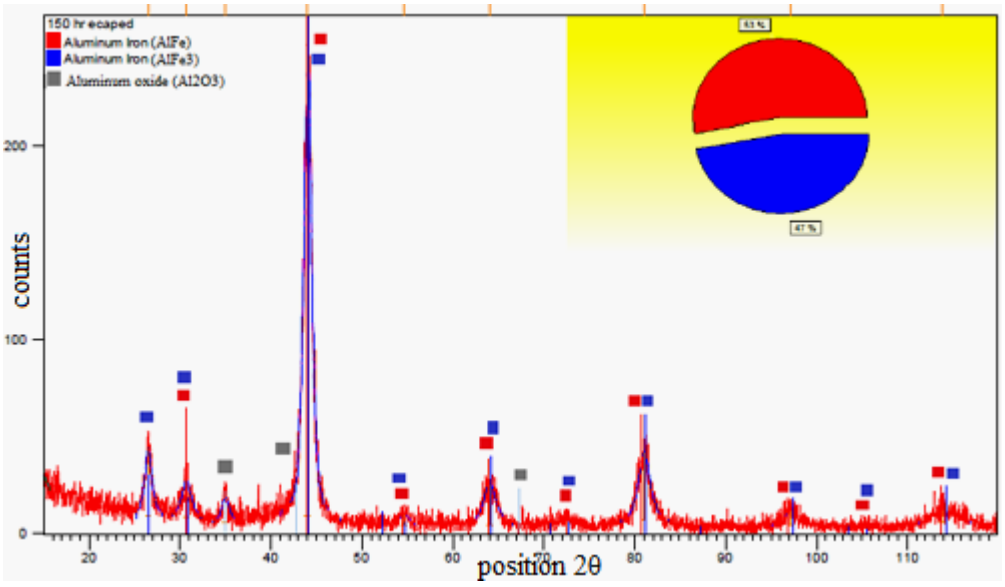

Figure 7.44 XRD pattern of ECAP-BP pellet obtained by consolidating MA powder at 500^0 C, MA is done at 150 hours of ball milling duration.

Table 7.8 Structural parameters of ECAP-BP pellet synthesized by consolidating ball milled powder (100 hours of MA duration) at 500 ^{0}C

Peak Pos. 2θ	hkl/phase	Height [cts]	FWHM 2θ	d-spacing [Å]	'a' nm	'D' nm	Lattice strain %	Matched by Ref. pattern
26.4539	111$AlFe_3$	24.17	0.5985	3.36657				03-065-4419
27.8320	012AlH_3	8.89	0.4751	3.20291				01-071-2422
30.7304	**100AlFe** 200$AlFe_3$	13.99	0.9047	2.90711				03-065-3201; 03-065-4419
42.7390	202Al_2O_3	60.05	0.6107	2.11399				
44.1482*	**110AlFe** 220$AlFe_3$	**227.36**	**0.9340**	**2.04973**	**0.2891/ 0.57975**	**13.5**	**0.952**	03-065-3201; 03-065-4419; 03-065-4899; 03-065-2869
54.6162	111AlFe 222$AlFe_3$	4.98	1.5102	1.67903				03-065-3201; 03-065-4419
64.0690	200AlFe 400$AlFe_3$	21.14	1.5925	1.45222				03-065-3201; 01-071-2422; 03-065-4419; 03-065-4899; 03-065-2869
64.9946	**Al/Fe 220/200**	23.32	0.4894	1.43376				03-065-3201; 01-071-2422; 03-065-4419; 03-065-4899; 03-065-2869
73.2399	210AlFe 420$AlFe_3$	2.95	3.0083	1.29135				03-065-3201; 01-071-2422; 03-065-4419
80.9746	211AlFe 422$AlFe_3$	33.52	0.8264	1.18639				03-065-3201; 03-065-4419
81.9651	**Al/Fe 222/211**	22.14	1.6772	1.17454				03-065-3201; 01-071-2422; 03-065-4419; 03-065-4899; 03-065-2869
97.5697	220AlFe 440$AlFe_3$	7.45	2.5297	1.02401				03-065-3201; 03-065-4419; 03-065-4899
105.2	221AlFe 600$AlFe_3$							
113.8522	310AlFe 620$AlFe_3$	8.27	1.8146	0.91925				03-065-3201; 03-065-4419

*Integrated Intensity (II) = 102613.67 at 2θ = 44.1482 for 110AlFe

Table 7.9 Structural parameters of ECAP-BP pellet synthesized by consolidating ball milled powder (150 hours of MA duration)

Peak Pos. 2θ	hkl/ phases	Height [cts]	FWHM 2θ	d-spacing [Å]	'D' nm	Lattice strain %	Integrated intensity	Matched by Ref. pattern
26.4735	111$AlFe_3$	34.81	0.9559	3.36411				03-065-4419
30.6583	200/**100** $AlFe_3$/**AlFe**	18.75	1.2612	2.91378			19922.03	03-065-0985; 03-065-4419
34.9483	Al_2O_3	12.77	0.9488	2.56530				
44.0110*	220/**110** $AlFe_3$/**AlFe**	**238.26**	**1.0076**	**2.05580**	**12.0**	**1.041**	103845.88	03-065-0985; 03-065-4419
52.269	311 $AlFe_3$			1.74877				
54.6065	222/111 $AlFe_3$/AlFe	5.94	1.0715	1.67931				03-065-0985; 03-065-4419
64.0034	400/200 $AlFe_3$/AlFe	21.11	1.6908	1.45355				03-065-0985; 03-065-4419
70.747	331$AlFe_3$			1.33061				
72.8	420/210 $AlFe_3$/AlFe							
80.9824	422/211 $AlFe_3$/AlFe	35.80	1.4734	1.18630				03-065-0985; 03-065-4419
97.0956	440/220 $AlFe_3$/AlFe	6.80	2.0088	1.02774				03-065-0985; 03-065-4419
105	600/300 $AlFe_3$/AlFe							
113.8649	620/310 $AlFe_3$/AlFe	6.30	3.1564	0.91918				03-065-0985; 03-065-4419

*__Lattice parameter 'a'__= 0.5815/__0.29074 nm__ of 220/__110__ $AlFe_3$/__AlFe__ phases at 2θ = 44.0110 and the Rel. Intensity for the reflection is 100 %

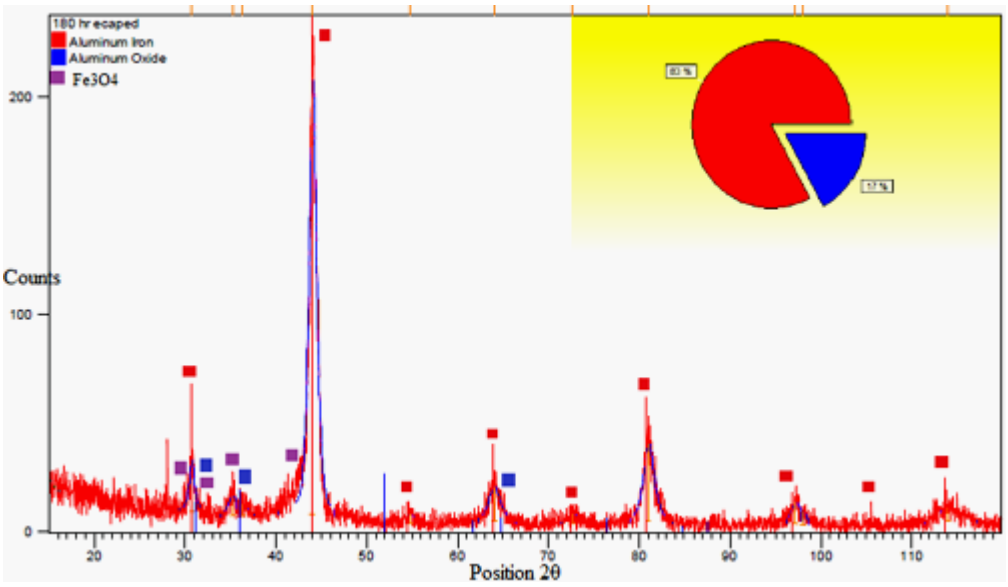

Figure 7.45 XRD pattern of ECAP-BP pellet obtained by consolidating MA powder at 450^0 C, MA is done at 180 hours of ball milling duration.

Table 7.10 Structural parameters of ECAP-BP pellet synthesized by consolidating ball milled powder (180 hours of MA duration)

Pos. [°2Th.]	hkl/phase	Height [cts]	FWHM [°2Th.]	d-spacing [Å]	Rel. Int. [%]	Integrated Intensity (I)	Matched by Ref. pattern
30.168	Fe_3O_4			2.96000	20.0		
30.6961	**S**100AlFe	23.83	0.7081	2.91028	12.01	19825.3	03-065-0985; 01-075-0277
31.080	111Al_2O			2.87520	22.2		
32.054	Fe_3O_4			2.79000	10.0		
35.452	Fe_3O_4			2.53000	18.0		
36.2428	200 Al_2O	5.14	1.5195	2.47660	2.59		01-075-0277
43.254	Fe_3O_4			2.09000	20.0		
44.0402*	**110** AlFe	**198.46**	**0.9684**	**2.05450**	**100.00**	103685.5	03-065-0985
54.7063	**S**111 AlFe	4.77	1.1570	1.67648	2.40		03-065-0985
64.0055	200 AlFe	16.33	1.5340	1.45350	8.23		03-065-0985; 01-075-0277
64.800	222 Al_2O			1.43760	10.6		
72.6636*	**S** 210AlFe	4.16	1.2743	1.30017	2.10		03-065-0985
81.0186	211 AlFe	35.65	1.3754	1.18586	17.97		03-065-0985
97.2162	220 AlFe	9.87	1.3028	1.02679	4.97		03-065-0985
98.0499		5.85	0.7555	1.02027	2.95		03-065-0985
113.9825	310 AlFe	6.70	2.6250	0.91857	3.38		03-065-0985

*S-Super Lattice, lattice parameter 'a' = **0.29055** nm, crystallite size 'D'=**12.7** nm, lattice strain=**0.995**% and Rel. Intensity=100% at 2θ=44.0402 for **110 AlFe** reflection

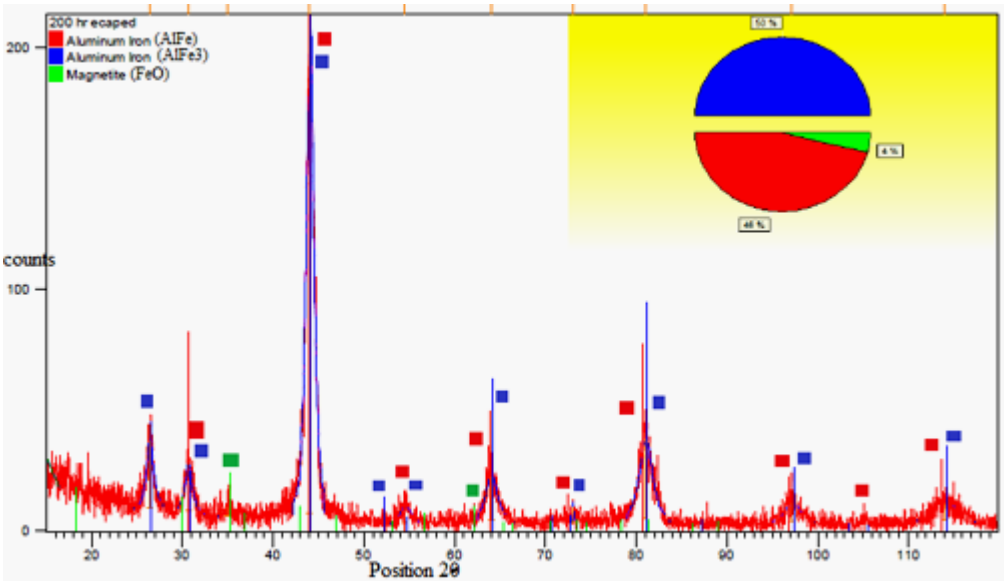

Figure 7.46 XRD pattern of ECAP-BP pellet obtained by consolidating MA powders processed at 200 hours of ball milling duration.

Table 7.11 Structural parameters of ECAP-BP pellet synthesized by consolidating ball milled powder (200 hours of MA duration)

Pos. [°2Th.]	hkl/phase	Height [cts]	FWHM [°2Th.]	'd'spacing [Å]	Integrated intensity	Rel. Int. [%]	Matched by Ref. pattern
26.4119*	**S**111/$AlFe_3$	28.03	0.9339	3.37181		13.71	03-065-4419
30.6622*	200/**S100** $AlFe_3$/**AlFe**	19.81	0.8857	2.91342	19914.32	9.69	03-065-0985; 03-065-4419; 01-086-1351
35.0086	Fe_3O_4	3.52	1.1637	2.56103		1.72	01-086-1351
44.0416*	220/**110** $AlFe_3$/**AlFe**	**204.44**	**0.9588**	**2.05444**	103721.13	**100.00**	03-065-0985; 03-065-4419; 01-086-1351
52.269*	**S**311 $AlFe_3$			1.74877		2.3	
54.5129*	222/**S**111 $AlFe_3$/AlFe	6.95	1.4473	1.68197		3.40	03-065-0985; 03-065-4419
64.0298	400/200 $AlFe_3$/AlFe	18.32	1.5147	1.45301		8.96	03-065-0985; 03-065-4419; 01-086-1351
73.0031*	420/**S**210 $AlFe_3$/AlFe	6.02	0.0557	1.29496		2.94	03-065-0985; 03-065-4419; 01-086-1351
81.0274	422/211 $AlFe_3$/AlFe	33.27	1.6148	1.18575		16.27	03-065-0985; 03-065-4419; 01-086-1351
97.1736	440/220 $AlFe_3$/AlFe	7.81	1.9431	1.02712		3.82	03-065-0985; 03-065-4419
114.0801	620/310 AlFe/$AlFe_3$	6.98	3.1809	0.91806		3.42	03-065-0985; 03-065-4419

*S-superlattice peaks. Lattice parameter 'a'=0.5811/**0.29054** nm at 2θ =44.0416^0 for 220/**110** $AlFe_3$/**AlFe** reflection, crystallite size 'D'=**12.9** nm, lattice strain=**0.985**% at a Rel.Intensity = 100 %

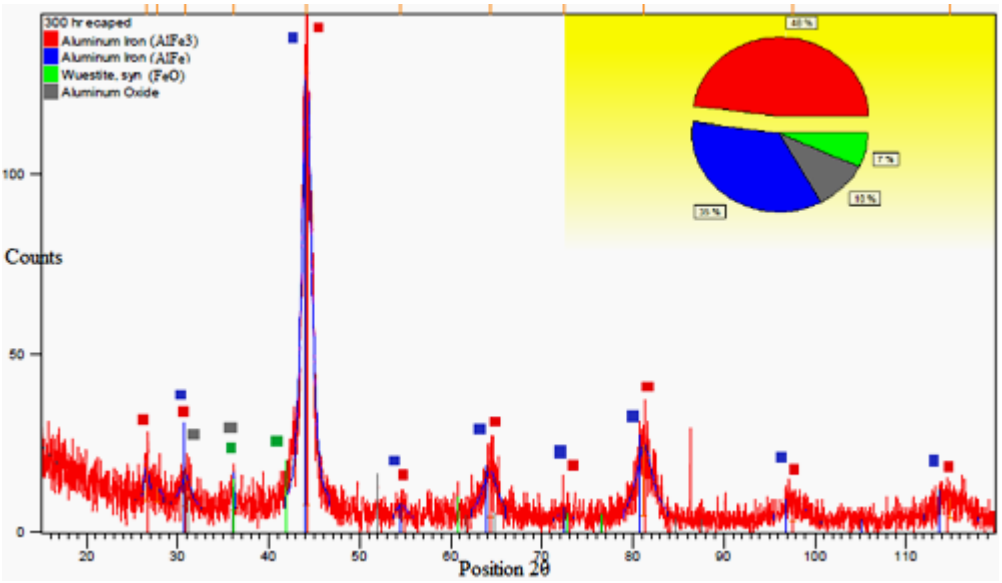

Figure 7.47 XRD pattern of ECAP-BP pellet obtained by consolidating MA powders processed at 300 hours of ball milling duration.

Table 7.12 Structural parameters of ECAP-BP pellet synthesized by consolidating (300^0 C) ball milled powder (300 hours of MA duration)

Pos. [°2Th.]	Hkl/phase	Height [cts]	FWHM [°2Th.]	d-spacing [Å]	Integrated Intensity	Rel. Int. [%]	Matched by Ref. pattern
26.5436*	S111AlFe$_3$	11.69	0.4955	3.35539		9.48	03-065-5188
30.8129*	**S100AlFe**/ 200AlFe$_3$/1 11Al$_2$O	8.62	1.3435	2.89951	19601.863	7.00	03-065-5188; 03-065-0985; 01-075-0277
36.1717	200Al$_2$O/1 11FeO	6.40	0.0389	2.48130		5.20	01-075-1550; 01-075-0277
44.1356*	**110AlFe**/2 20AlFe$_3$	**123.22**	**1.2257**	**2.05028/ 2.04743**	**102702.36**	**100.00**	03-065-5188; 03-065-0985
54.5125*	S111AlFe/ 222AlFe$_3$	4.11	1.1547	1.68198		3.33	03-065-5188; 03-065-0985
64.2573	200AlFe/4 00AlFe$_3$/22 2Al$_2$O	12.80	2.0296	1.44841		10.39	03-065-5188; 03-065-0985; 01-075-0277
72.4440*	S210AlFe/ 420AlFe$_3$	3.02	1.5233	1.30357		2.45	03-065-5188; 03-065-0985; 01-075-1550
81.2048	211AlFe/4 22AlFe$_3$	19.80	1.9990	1.18361		16.07	03-065-5188; 03-065-0985
97.6218	220AlFe/4 40AlFe$_3$	5.29	3.2834	1.02360		4.29	03-065-5188; 03-065-0985
114.8398	310AlFe/6 20AlFe$_3$	5.58	3.8875	0.91415		4.53	03-065-5188; 03-065-0985

Lattice parameter 'a'=**0.28995**/0.57910 nm, crystallite size 'D'=**9 nm** and lattice strain=**1.281**% at 2θ=44.1356^0 for **110AlFe**/220AlFe$_3$ reflection. S-Superlattice reflection

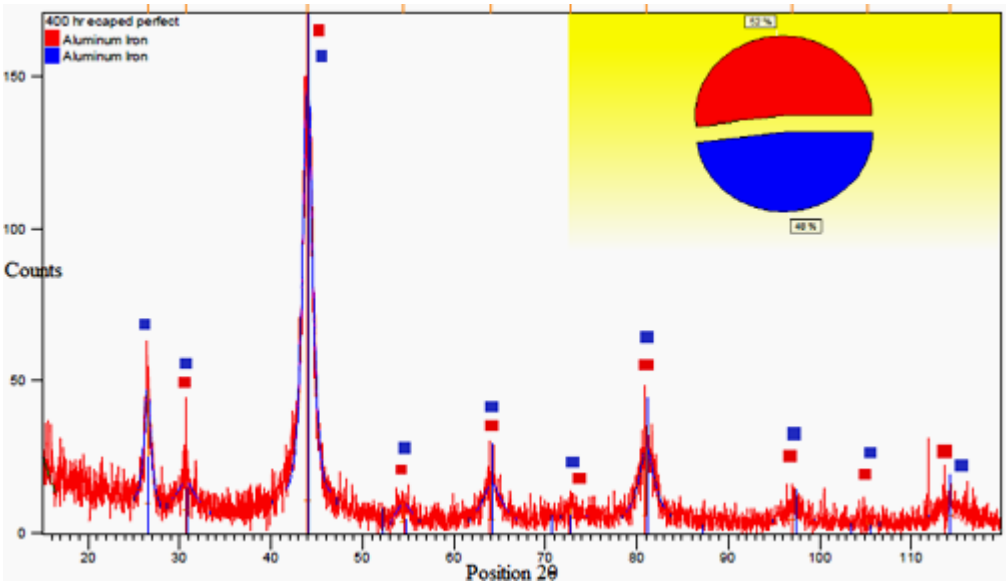

Figure 7.48 XRD pattern of ECAP-BP pellet obtained by consolidating MA powders processed at 400 hours of ball milling duration.

Table 7.13 Structural parameters of ECAP-BP pellet synthesized by consolidating (500^0 C) ball milled powder (400 hours of MA duration)

Peak Pos. 2θ	Hkl/phase	Height (cts)	FWHM 2θ	d-spacing (Å)	Integrated Intensity	Rel. Int. (%)	Matched by Ref pattern
26.4524	S111AlFe$_3$	37.66	0.8824	3.36675		27.01	03-065-4419
30.6177	S100/200AlFe/AlFe$_3$	9.47	2.3393	2.91756	19968.33	6.79	03-065-3201; 03-065-4419
43.9566*	**110/220AlFe/AlFe$_3$**	**139.45**	**1.2836**	**2.05822/2.05061**	**104255.78**	**100.00**	03-065-3201; 03-065-4419
54.3998	S111/222AlFe/AlFe$_3$	6.71	1.8095	1.68520		4.81	03-065-3201; 03-065-4419
64.0713	200/400AlFe/AlFe$_3$	12.04	2.2522	1.45217		8.64	03-065-3201; 03-065-4419
72.7367	S210/420AlFe/AlFe$_3$	3.13	2.0023	1.29904		2.24	03-065-3201; 03-065-4419
81.0069	211/422AlFe/AlFe$_3$	22.48	1.8680	1.18600		16.12	03-065-3201; 03-065-4419
96.9975	220/440AlFe/AlFe$_3$	4.80	2.0812	1.02852		3.44	03-065-3201; 03-065-4419
105.3926	S221/600AlFe/AlFe$_3$	2.65	2.2188	0.96840		1.90	03-065-3201; 03-065-4419
114.3128	310/620AlFe/AlFe$_3$	3.42	3.3087	0.91685		2.46	03-065-3201; 03-065-4419

Lattice parameter 'a'=**0.2911**/0.58 nm, crystallite size 'D'=**8.7** nm, lattice strain=**1.351**% at 2θ=43.9566^0 for **110AlFe**/220AlFe$_3$ reflection

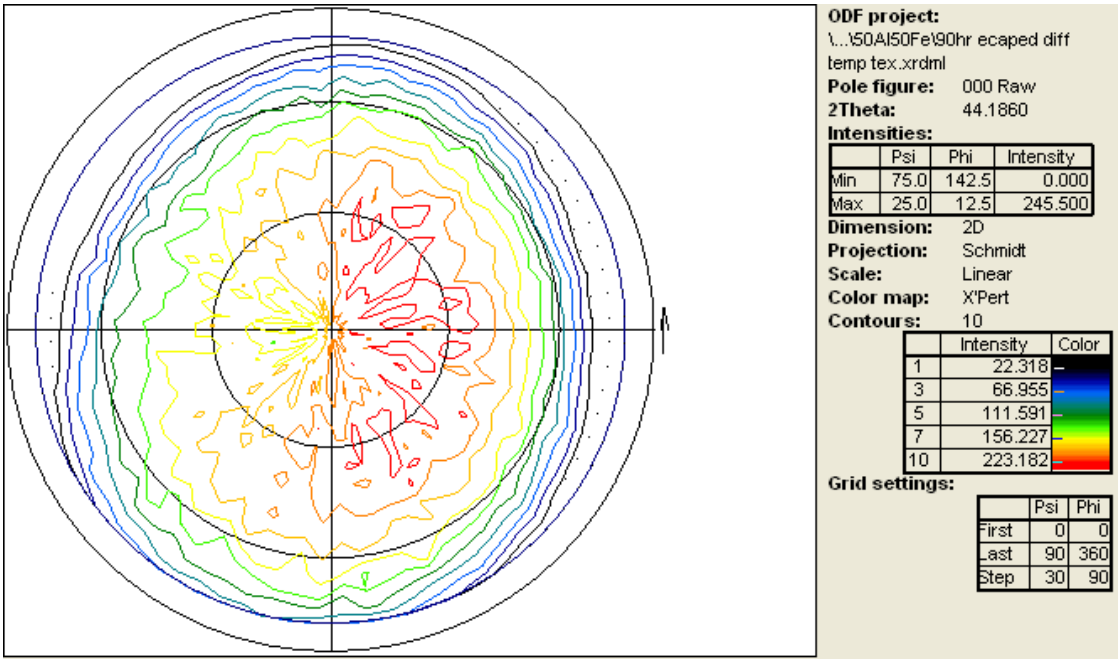

Figure 7.49 pole figures of 100-h ECAP-BP processed (450^0 C) pellet

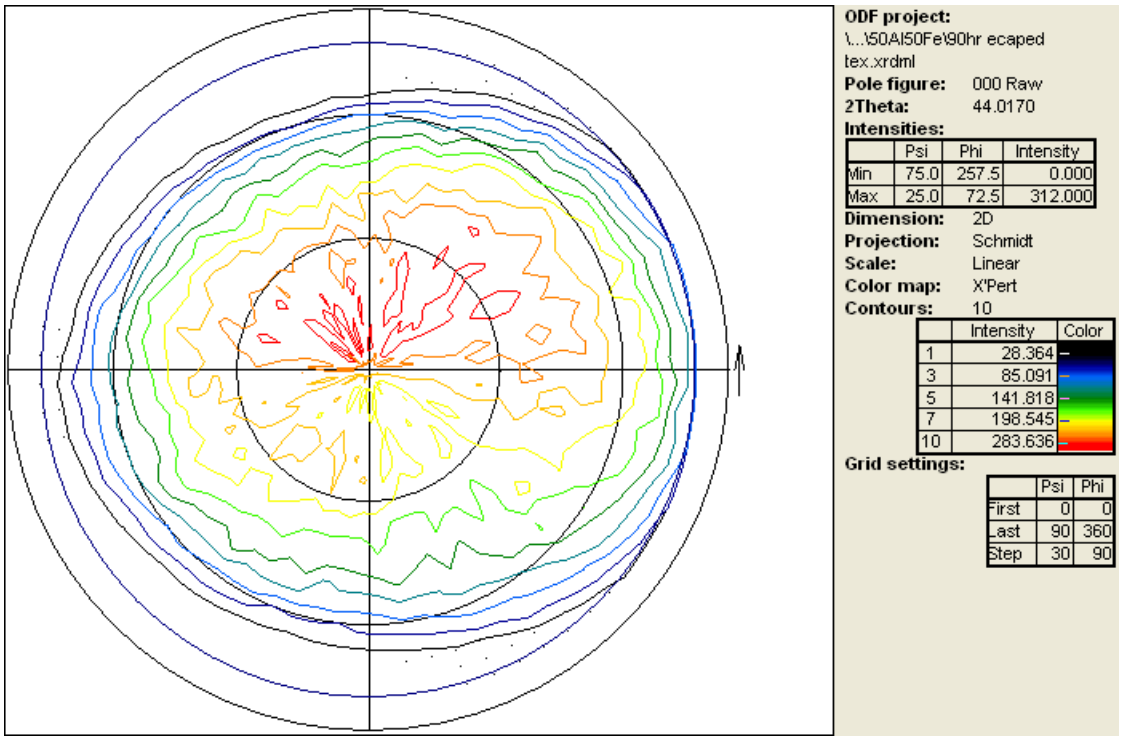

Figure 7.50 pole figures of 100-h ECAP-BP processed (150^0 C) pellet

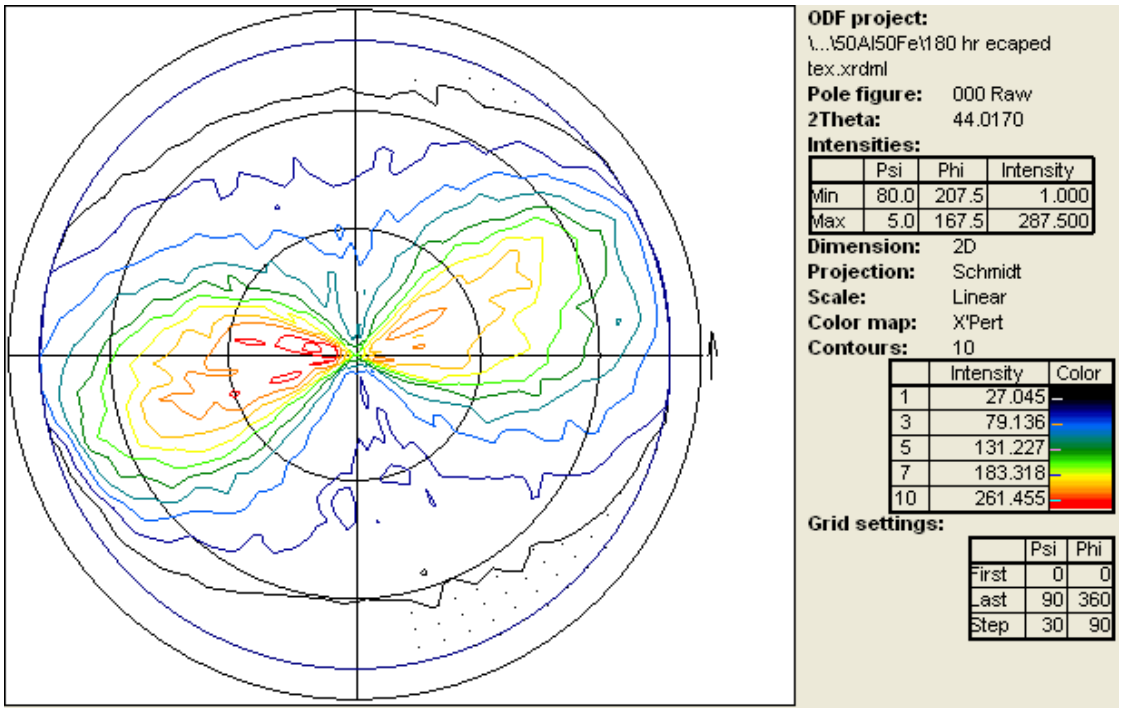

Figure 7.51 pole figures of 180-h ECAP-BP processed (450^0 C) pellet

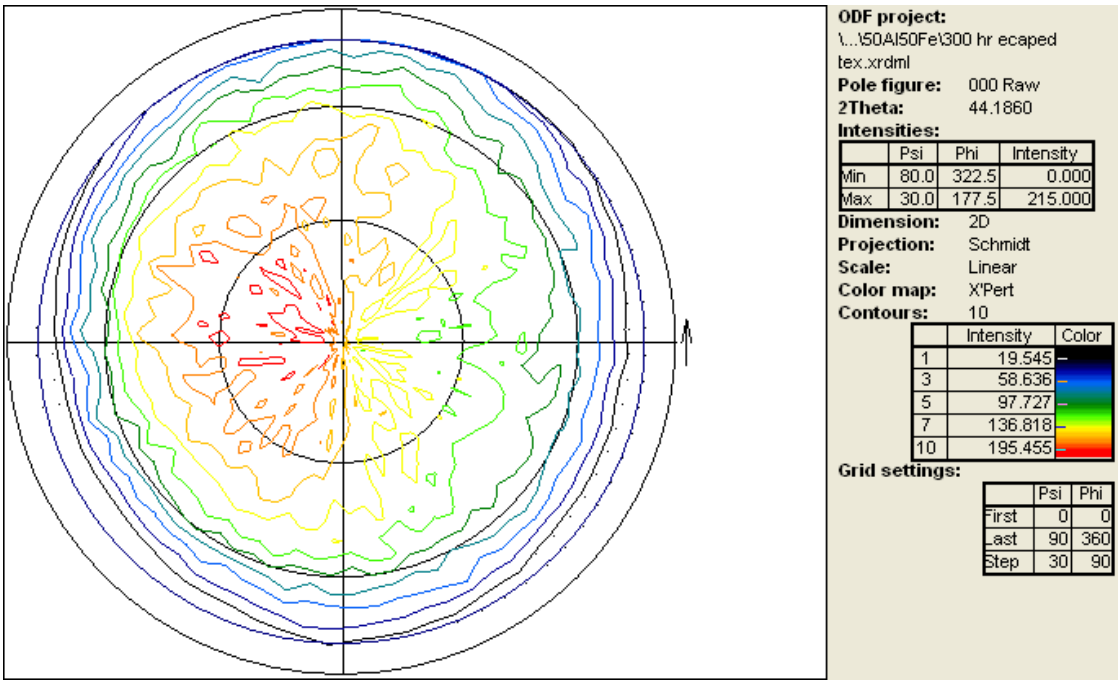

Figure 7.52 pole figures of 300-h ECAP-BP processed (300^0 C) pellet

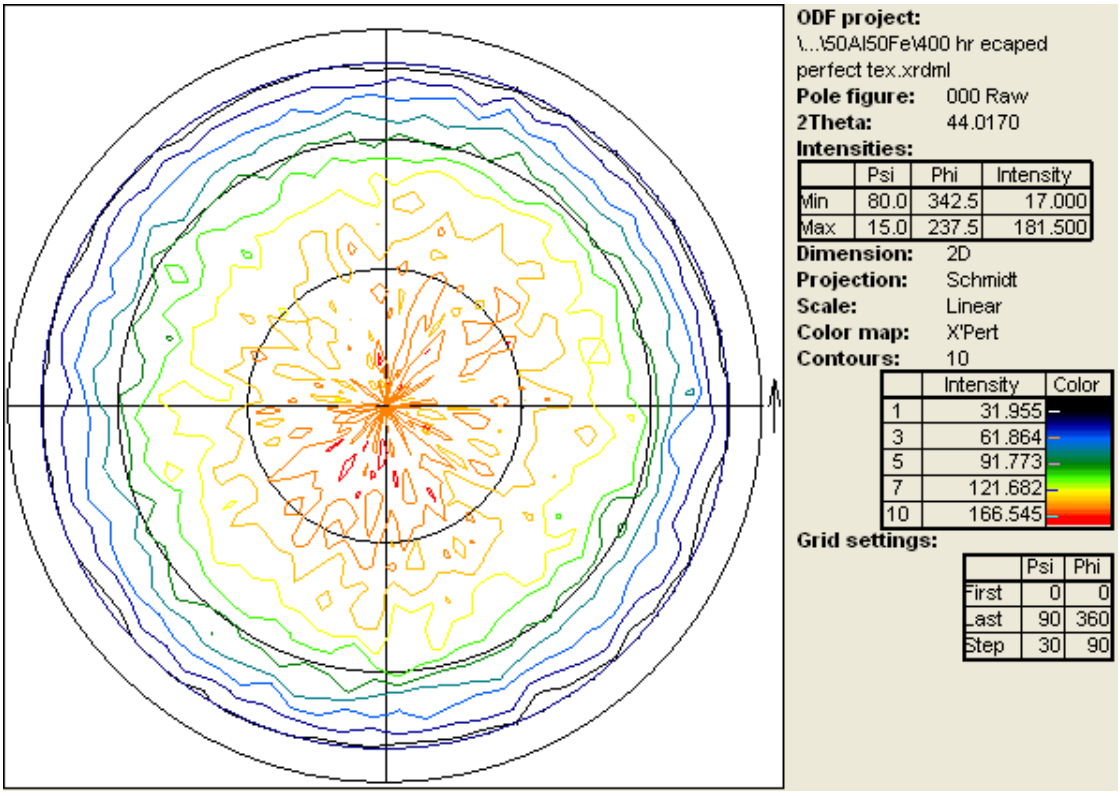

Figure 7.53 pole figures of 400-h ECAP-BP processed (500^0 C) pellet

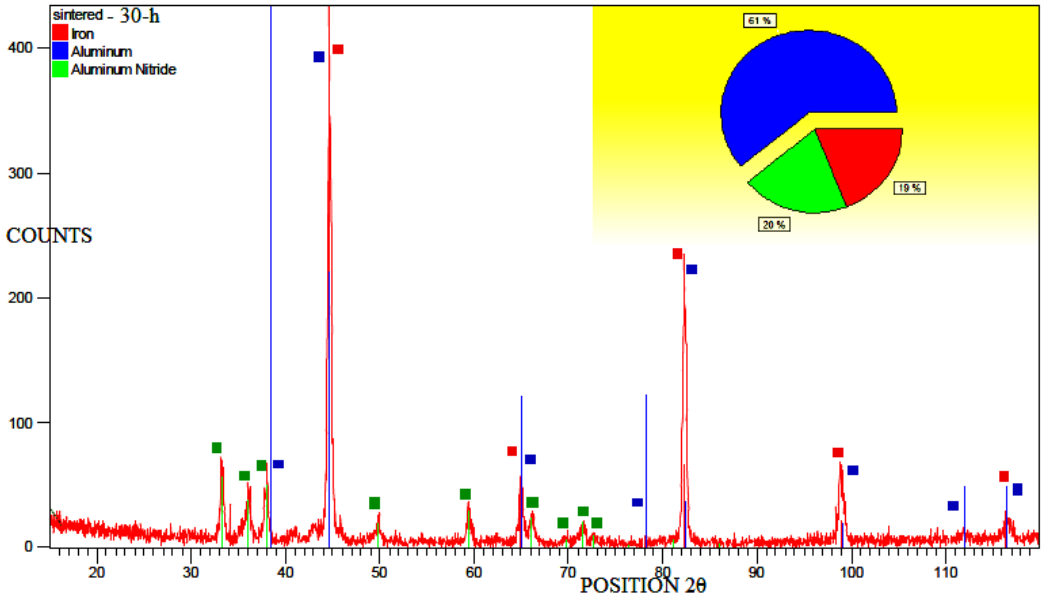

Figure 7.54 XRD profile of sintered compact obtained by consolidating MA powder ball milled for 30 hours of duration

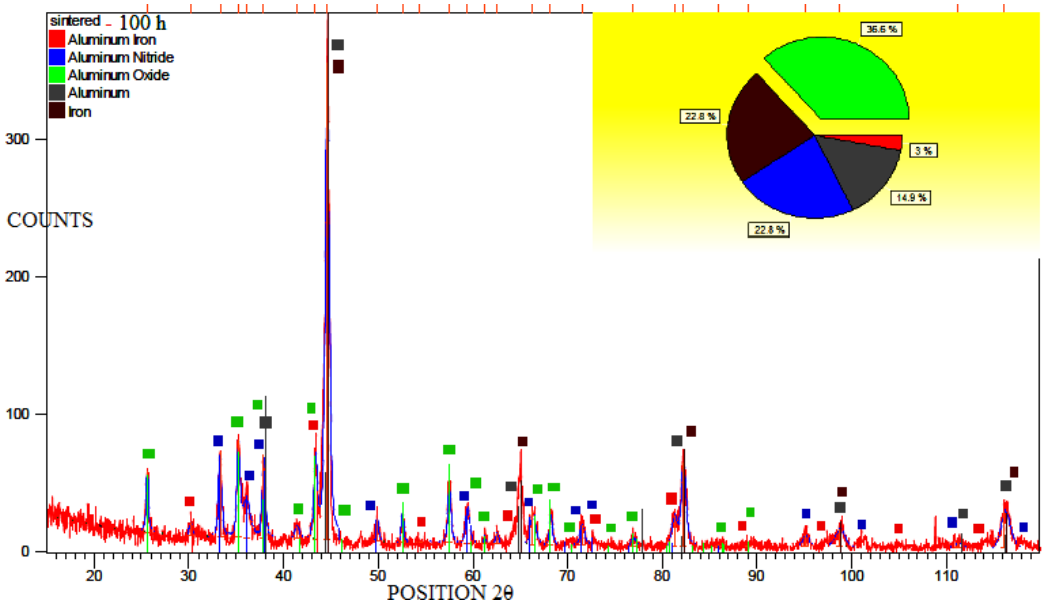

Figure 7.55 XRD profile of sintered compact obtained by consolidating MA powder ball milled for 100 hours of duration.

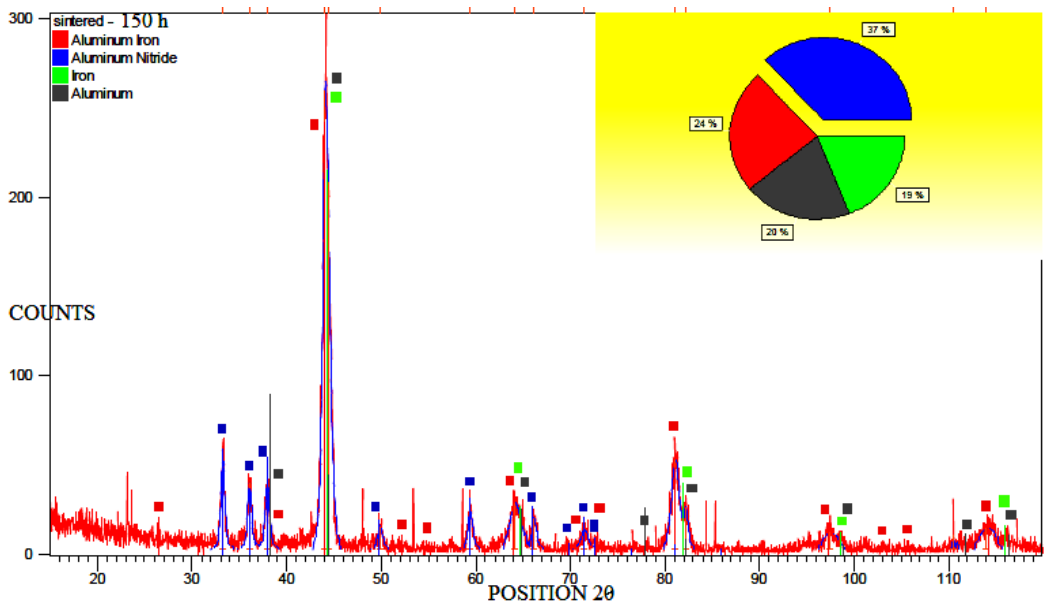

Figure 7.56 XRD pattern of sintered compact obtained by consolidating MA powder ball milled at 150 hours of duration

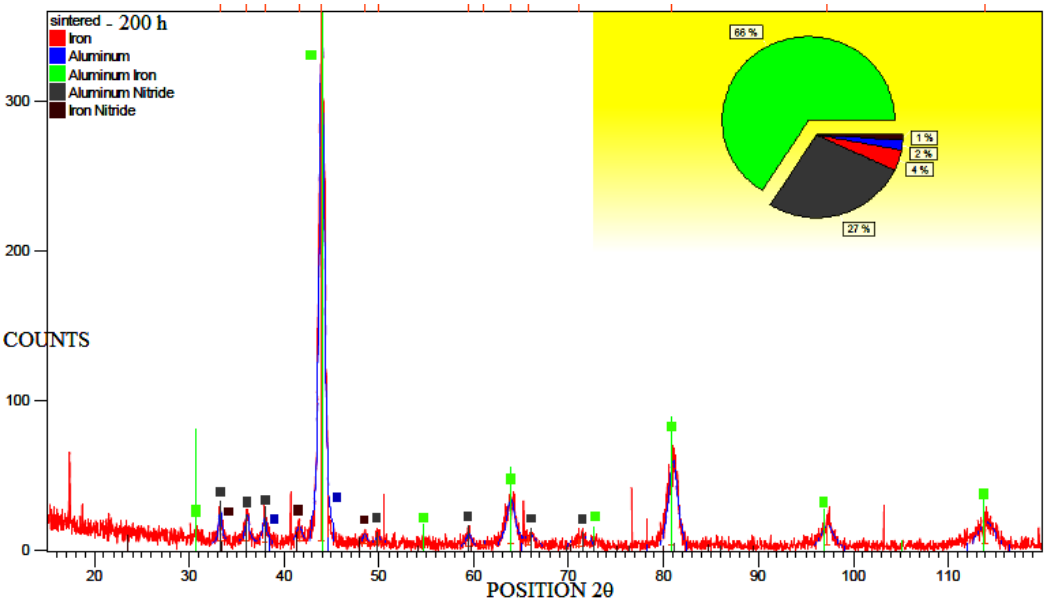

Figure 7.57 XRD pattern of sintered compact obtained by consolidating MA powder ball milled at 200 hours of duration

Table 7.14 Structural parameters of 30-h MA powder consolidated by compaction and sintering

Peak Pos. 2θ	phase	Height (cts)	FWHM 2θ	d-spacing (Å)	'a' nm	'D'nm/ Lattice strain %	Rel. Int. (%)	Matched by Ref. pattern
30.8	AlFe100							
33.2176	AlN(100) Hexagonal	61.95	0.3618	2.69490			15.36	01-076-0565
36.0086	AlN(002)	32.46	0.6722	2.49217			8.05	01-076-0565
37.9363	Al(111)/ AlN (101)	45.57	0.4688	2.36984			11.30	03-065-2869; 01-076-0565
44.6244	Fe(110)/ Al(200)	403.30	0.3660	2.02896	0.2869/ 0.4058	120/ 0.232	100.00	03-065-4899; 03-065-2869
49.7748	AlN(102)	14.84	0.6586	1.83040			3.68	01-076-0565
59.3712	AlN(110)	25.06	0.4446	1.55541			6.21	01-076-0565
64.9291	Fe(200)/ Al(220)	44.97	0.4514	1.43504			11.15	03-065-4899; 03-065-2869
66.0884	AlN(103)	21.71	0.5154	1.41265			5.38	01-076-0565
71.4506	AlN(112)	13.47	0.5469	1.31923			3.34	01-076-0565
72.6592	AlN(201)	5.29	0.3859	1.30024			1.31	01-076-0565
82.2442	Fe(211)/ Al(222)	219.17	0.3003	1.17126			54.34	03-065-4899; 03-065-2869

'a'-lattice parameter, 'D'-crystallite size. FWHM-full width half maximum

Table 7.15 Structural parameters of 100-h MA powder consolidated by compaction and sintering

Peak Pos. 2θ	Phase	Height (cts)	FWHM 2θ	d-spacing (Å)	'a' nm	'D'nm/ Lattice strain%	Matched by Ref pattern
25.5774	Al2O3 Rhombohedral	44.74	0.2909	3.47991			01-075-1864
30.1490	AlFe(100)S	9.13	0.3081	2.96183			03-065-0985
33.2507	AlN Hexagonal	62.07	0.3782	2.69230			01-075-1620
35.1980	Al2O3	70.47	0.3706	2.54768			01-075-1864
36.0340	AlN	29.78	0.9722	2.49046			01-075-1620
37.8715	AlN/ Al2O3/Al(111)	60.51	0.3922	2.37375			01-075-1620; 01-075-1864; 03-065-2869
41.3680	Al2O3	8.42	0.5947	2.18083			01-075-1864
43.3460	**AlFe**(110)/Al2 O3	58.67	0.4403	2.08579	**0.2949**	59/0.359	03-065-0985; 01-075-1864
44.5914	Al(200)/Fe(11 0)	346.35	0.4806	2.03038	**0.2872**	46/0.405	03-065-2869; 03-065-4899
52.5232	Al2O3	22.02	0.2699	1.74091			01-075-1864
54.3300	**AlFe**(111)bcc S	1.16	4.0000	1.68720	**0.2923**		03-065-0985
71.4704	AlFe(210)S/ AlN	14.92	0.4968	1.31891			03-065-0985; 01-075-1620
81.2326	AlFe(211)/AlN / Al2O3	22.38	0.6193	1.18327			01-075-1620; 01-075-1864; 03-065-2869

*S- superlattice parameter

Table 7.16 Structural parameters of 150-h MA powder consolidated by compaction and sintering

Peak Pos. 2θ	Phase	Height (cts)	FWHM 2θ	d-spacing (Å)	'a' nm	Rel. Int. (%)	Matched by Ref. pattern
33.2170	AlN(100) Hexagonal	50.44	0.4885	2.69495		19.59	01-076-0702
36.0441	AlN(002)	37.63	0.4980	2.48979		14.61	01-076-0702
37.9139	AlN(101)/Al(111)	36.09	0.5555	2.37119		14.01	01-076-0702; 03-065-2869
44.0241*	AlFe3(220)/AlFe (110)bcc	257.54	0.5587	2.05522	0.2906	100.00	03-065-4419; 03-065-4899; 03-065-2869
44.3885	Fe(110)/Al(200)	206.18	0.7049	2.03919	0.2884	80.06	03-065-4419; 03-065-4899; 03-065-2869
49.8409	AlN(102)	12.94	0.6207	1.82813		5.03	01-076-0702
59.3798	AlN(110)	21.63	0.5581	1.55520		8.40	01-076-0702
64.1495	AlFe3(400)/AlFe (200)/Fe(200)/ Al(220)	26.19	1.3984	1.45059	0.2901	10.17	03-065-4419; 03-065-4899; 03-065-2869
66.0959	AlN(103)	17.64	0.5437	1.41251		6.85	01-076-0702
71.4171	AlN(112)	11.18	0.8535	1.31977		4.34	01-076-0702
81.0360	AlFe3(422)/AlN (202)/Fe	50.80	0.9419	1.18565		19.72	03-065-4419; 01-076-0702; 03-065-4899
82.1977	Fe(211)/Al(222)	24.13	0.4337	1.17181		9.37	03-065-4899; 03-065-2869

*Crystallite size 'D' =**33** nm and lattice strain=**0.513**% at 2θ=**44.0241^0 for 110AlFe/220AlFe$_3$**

Table 7.17 Structural parameters of 200-h MA powder consolidated by compaction and sintering

Peak Pos. 2θ	Phase	Height (cts)	FWHM 2θ	d-spacing (Å)	'a' nm	Rel. Int. (%)	Matched by Ref. pattern
33.2175	AlN/Fe4N	21.67	0.3904	2.69491		5.98	01-076-0565; 01-086-0231
36.0654	AlN Hexagonal	17.34	0.4338	2.48837		4.79	01-076-0565
37.9264	AlN/ Al(111)	16.22	0.5572	2.37044		4.48	03-065-2869; 01-076-0565
41.5471	Fe4N simple cube	10.31	0.5839	2.17184		2.85	01-086-0231
43.9424	AlFe(110) bcc	362.11	0.6043	2.05885	0.2912	100.	03-065-4899; 03-065-3201
48.4373	Fe4N	5.33	0.5350	1.87777		1.47	01-086-0231
49.8579	AlN	4.79	0.9834	1.82754		1.32	01-076-0565
59.3816	AlN/Fe4N	7.77	0.6120	1.55516		2.14	01-076-0565; 01-086-0231
63.8314	AlFe(200)	33.66	1.0192	1.45705	0.2914	9.30	03-065-3201
65.8433	AlN/ Al(220)	6.06	1.7775	1.41731		1.67	03-065-2869; 01-076-0565
71.1724	AlN	4.69	4.0000	1.32370		1.30	01-076-0565
80.9330	AlFe(211)	57.24	1.0476	1.18690		15.81	03-065-3201; 01-076-0565

Crystallite size '**D**' =**28** nm and lattice **strain**=**0.571**% at 2θ=43.9424^0 for **110 AlFe** reflection

APPENDIX II

Graphs and Tables for ball milling and consolidation (Al_{90}-Fe_{10} system) characterization results

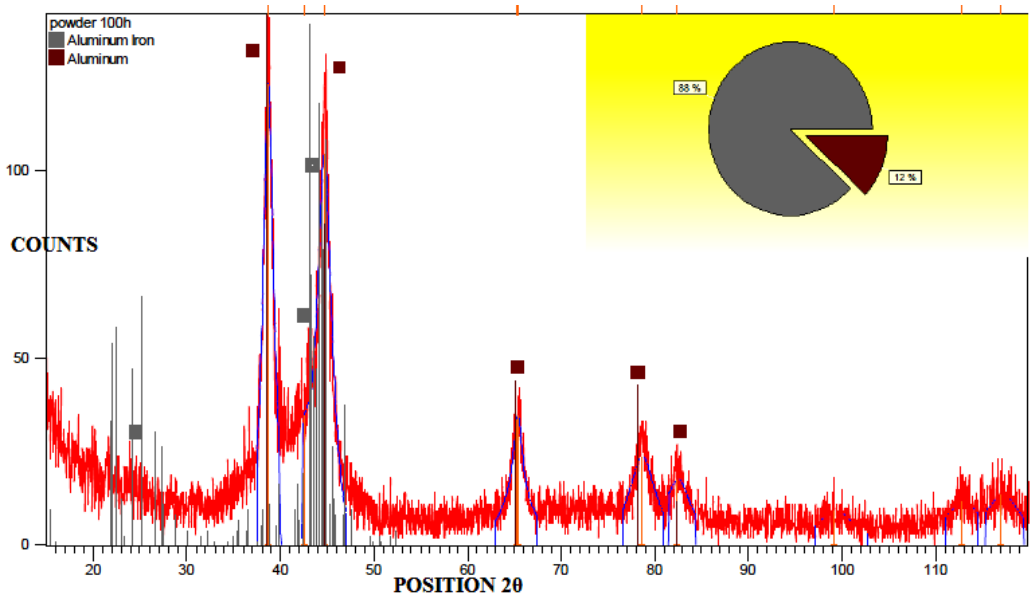

Figure 7.58 XRD pattern of powder MA by ball milling duration of 100 hours

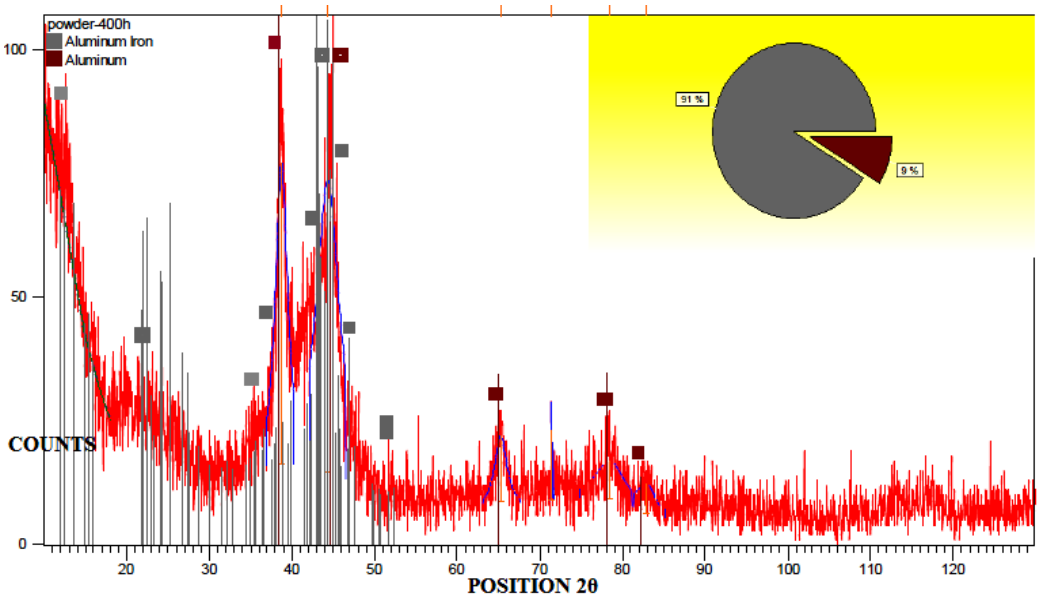

Figure 7.59 XRD pattern of powder MA by ball milling duration of 400 hours

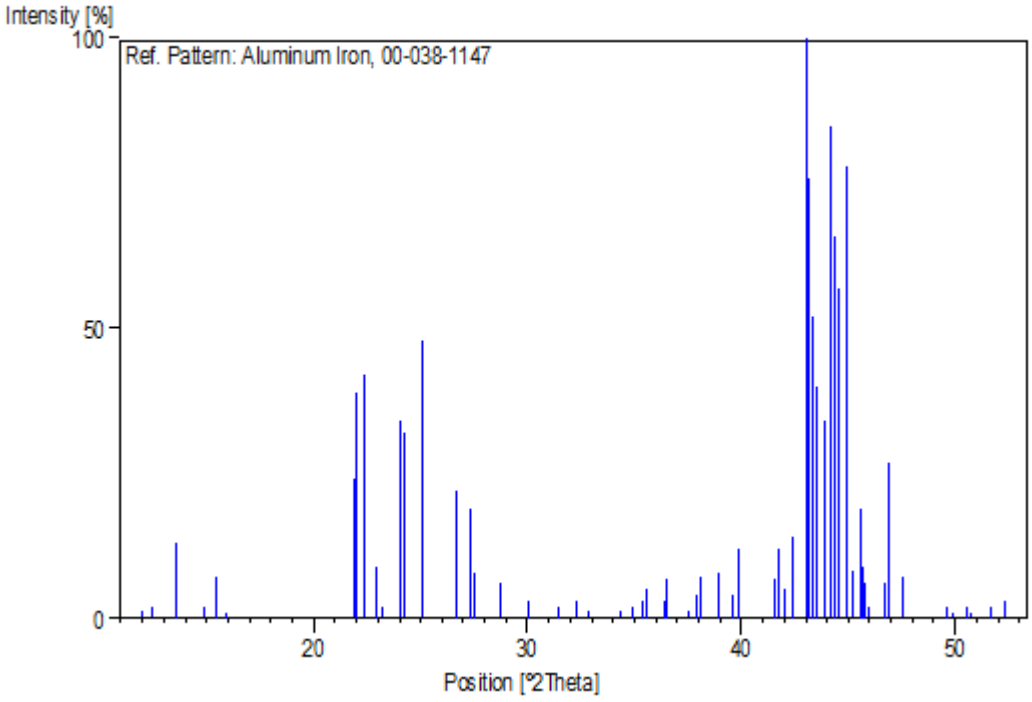

Figure 7.60 AlFe Matching XRD Pattern

Table 7.18 structural parameters of MA powder obtained at a ball milling duration of 100 hours

Peak Pos. 2θ	hkl/phase	Height (cts)	FWHM 2θ	d-spacing (Å)	Integrated Intensity (I_I)	'D' nm	Micro strain %	Matched by Ref. pattern
25.127	**220Al(Fe)**			3.54130				00-038- 1147
38.6713	(33-2) Al(Fe)/**111 Al**	123.26	**1.3966**	2.32647	**159895.26**	**7.6**	**1.698**	00-038- 1147; 01- 085-1327
42.5493	**(71-2)/Al(Fe)**	34.71	1.6877	2.12298				00-038- 1147
44.6665*	**620Al(Fe) / 200Al**	104.65	**1.8806**	2.02714	**3178291.5**	**5.4**	**1.973**	00-038- 1147; 01- 085-1327
65.2228	220Al	33.83	3.7668	1.42929				01-085- 1327
78.5817	311Al	23.71	3.5448	1.21641				01-085- 1327
82.3775	222Al	17.64	3.6215	1.16970				01-085- 1327
99.1424	400Al	9.50	4.0000	1.01194				01-085- 1327
112.7916	331Al	11.79	4.0000	0.92486				01-085- 1327
116.9770	420Al	13.54	4.0000	0.90354				01-085- 1327

*Lattice parameter 'a'=**0.4055** nm at 2θ=44.6665 of 200 Al phase

Table 7.19 structural parameters of MA powder obtained at a ball milling duration of 250 hours

Pos. [°2Th.]	hkl/phase	Height [cts]	FWHM [°2Th.]	d-spacing [Å]	'a'nm	Integrated Intensity (II)	Matched by Ref. pattern
25.127	**220Al(Fe)**			3.54130			00-038- 1147
38.6668	(33-2) Al(Fe)/**11 1Al**	68.42	**1.5964**	2.32673		159895.26	00-038- 1147; 01- 085-1327
44.2783	**620Al(Fe) /200Al**	58.42	**3.5546**	2.04401	**0.4088**	**3249907.00**	00-038- 1147; 01- 085-1327
65.2977	220 Al	14.60	1.5546	1.42783			01-085- 1327
78.5202	311 Al	13.92	1.6582	1.21721			01-085- 1327
82.2477	222 Al	6.34	2.9683	1.17122			01-085- 1327

Crystallite size 'D'=**6.5** nm, lattice strain=**1.951**% and Rel Intensity=100% at 2θ=38.6668^0 for **111Al** reflection

Table 7.20 structural parameters of MA powder obtained at a ball milling duration of 400 hours

Peak Pos. 2θ	hkl/phase	Height (cts)	FWHM 2θ	d-spacing (Å)	'a'nm	II	Rel. Int. (%)	Matched by Ref. Pattern
13.572	11-1 Al(Fe)			6.51900				00-038- 1147
22.423	003 Al(Fe)			3.96180				00-038- 1147
38.7007 *	33-2 Al(Fe)/ **111Al**	60.92	**1.7912**	2.32477		**159586.98**	100.00	00-038- 1147; 01- 089-2837
44.3003	**620 Al(Fe)** / 200Al	59.02	**3.3969**	2.04304	**0.4086**	**3247078.6**	96.88	00-038- 1147; 01- 089-2837
65.2089	220 Al	13.49	1.6600	1.42956			22.15	01-089- 2837
78.3626	311 Al	7.89	4.0000	1.21926			12.95	01-089- 2837
82.8287	222 Al	5.97	3.0161	1.16447			9.81	01-089- 2837

Lattice strain=**2.195**% and crystallite size 'D'=**5.6** nm at 2θ=38.7007 for **111Al** reflection

Table 7.21 matching patterns for XRD profile of ball milled powder (100-h) using Xpert High Score Plus software

Visible	Ref. Code	Score	Compound Name	Displaceme nt [°2Th.]	Scale Factor	Chemical Formula
*	00-038- 1147	41	Aluminum Iron	0.000	0.672	Al76 Fe24
*	01-085- 1327	71	Aluminum	0.000	0.909	Al

Table 7.22 Peak list with relative intensity (I) and indexing of matching pattern of AlFe phase (00-038-1147)

No.	h k l	d (A)	2θ (deg)	I (%)
1	2 0 0	7.39400	11.960	1.0
2	1 1 0	7.08500	12.483	2.0
3	1 1 -1	6.51900	13.572	13.0
4	0 0 2	5.95400	14.867	2.0
5	1 1 1	5.73050	15.450	7.0
6	2 0 1	5.56220	15.921	1.0
7	2 0 2	4.06320	21.857	24.0
8	2 0 -3	4.03990	21.984	39.0
9	0 0 3	3.96180	22.423	42.0
10	4 0 -1	3.87620	22.925	9.0
11	0 2 1	3.82150	23.258	2.0
12	4 0 0	3.69060	24.095	34.0
13	4 0 -2	3.67550	24.195	32.0
14	2 2 0	3.54130	25.127	48.0
15	0 2 2	3.33910	26.676	22.0
16	2 2 1	3.26440	27.298	19.0
17	1 1 3	3.25830	27.350	18.0
18	4 0 -3	3.23600	27.542	8.0
19	2 0 -4	3.10130	28.763	6.0
20	0 0 4	2.97000	30.064	3.0
21	5 1 -2	2.84210	31.451	2.0
22	5 1 0	2.77320	32.254	3.0
23	4 2 0	2.72130	32.886	1.0
24	1 1 4	2.60470	34.403	1.0
25	3 1 3	2.56670	34.929	2.0
26	4 2 1	2.53380	35.397	3.0
27	4 2 -3	2.52460	35.530	5.0
28	2 2 3	2.46620	36.401	3.0
29	2 2 -4	2.45910	36.510	7.0
30	0 2 4	2.39280	37.559	1.0
31	1 3 2	2.37070	37.922	4.0
32	4 0 3	2.36070	38.089	7.0
33	3 3 -2	2.31310	38.904	8.0
34	4 2 -4	2.27640	39.557	4.0
35	1 3 -3	2.25860	39.882	12.0
36	3 3 -3	2.17190	41.546	7.0
37	1 1 5	2.15980	41.790	12.0
38	1 3 3	2.14760	42.038	5.0
39	7 1 -2	2.12980	42.406	14.0
40	6 2 0	2.10090	43.019	100.0
41	6 2 -3	2.09490	43.148	76.0
42	2 0 5	2.08460	43.372	52.0
43	2 0 -6	2.07770	43.523	40.0
44	6 0 2	2.06250	43.861	34.0
45	6 0 -5	2.04810	44.185	85.0
46	7 1 0	2.04090	44.349	66.0
47	4 2 -5	2.03060	44.586	57.0
48	0 4 0	2.01800	44.880	78.0
49	3 1 -6	2.00270	45.242	8.0
50	5 3 0	1.98900	45.571	19.0
51	1 1 -6	1.98330	45.709	9.0
52	0 0 6	1.98080	45.770	6.0
53	6 2 -4	1.97410	45.934	2.0

Table 7.23 Structural parameters of 100-h ECAP-BP ($Al_{90}Fe_{10}$) pellet

Peak Pos. 2θ	phase	FWHM 2θ	d-spacing (Å)	'a' nm	'D' nm	Micro strain %	Rel. Int. (%)	Matched by Ref. pattern
18.4122		1.6780	4.81478				9.63	01-073- 1199
20.2509		0.9623	4.38158				9.59	01-073- 1199
22.1719		0.0321	4.00610				0.44	00-038- 1147
27.1667		1.1409	3.27983				10.15	00-038- 1147; 01-073-1199
31.3043		1.1474	2.85511				4.60	00-038- 1147; 01-073-1199
33.0400		1.2981	2.70898				1.46	00-038- 1147; 01-073-1199
35.4323		2.2329	2.53137				6.63	00-038- 1147; 01-073-1199
38.4063*	**111 Al**	**0.4395**	**2.34191**	**0.4056**			**100.00**	00-038- 1147; 03-065-2869; 01-073-1199
40.4072		1.1113	2.23044				22.70	00-038- 1147; 01-073-1199
42.0902		1.1228	2.14507				38.14	00-038-1147; 01-073-1199
44.5830	040Al Fe/**Al 200**	1.0937	2.03074	**0.4062**	**10.7**	**1.122**	**82.19**	00-038-1147; 03-065-2869; 01-073-1199
48.3235		0.9894	1.88193				7.16	00-038-1147; 01-073-1199
49.8574		0.6590	1.82756				4.22	00-038-1147; 01-073-1199
64.9770		0.6308	1.43410				20.20	03-065-2869; 01-073-1199
72.2955		1.5633	1.30588				4.68	01-073-1199
78.0893		1.2727	1.22284				19.98	03-065-2869; 01-073-1199
82.3270		0.5613	1.17029				8.08	03-065-2869; 01-073-1199
87.8596		1.4598	1.11030				3.11	01-073-1199
89.8338		0.9958	1.09095				2.59	01-073-1199
90.9883		3.2294	1.08009				3.45	01-073-1199
111.9163		2.1487	0.92961				3.67	03-065-2869

*Integrated intensity (II) = 162983.93 at $2\theta=38.4063^0$ for 111Al phase

Table 7.24 Structural parameters of 250-h ECAP-BP ($Al_{90}Fe_{10}$) pellet

Peak Pos. 2θ	phase	FWHM 2θ	d-spacing (Å)	'a'nm	I_I	Rel. Int. (%)	Matched by
15.6308		0.0125	5.66470			2.90	00-038- 1147
18.4760		0.8811	4.79829			11.15	01-073- 1199
20.1204		1.0901	4.40969			11.93	01-073- 1199
27.0739		1.3411	3.29086			14.16	00-038- 1147; 01- 073-1199
31.1473		1.0529	2.86914			7.08	00-038- 1147
35.5911		0.6012	2.52043			18.12	00-038- 1147; 01- 073-1199
38.3986	**111Al**	**0.5567**	**2.34237**	**0.4057**	163087.14	**77.85**	00-038- 1147; 03- 065-2869; 01-073- 1199
41.0737		2.0043	2.19578			39.03	00-038- 1147
42.2246		0.3609	2.13855			74.59	00-038- 1147; 01- 073-1199
44.5718	040 AlFe/ **Al 200**	**1.2440**	2.03123	**0.4063**		**100.00**	00-038- 1147; 03-

Crystallite size 'D'=9 nm and lattice strain=1.287% at 2θ=44.5718 for 200 Al reflection

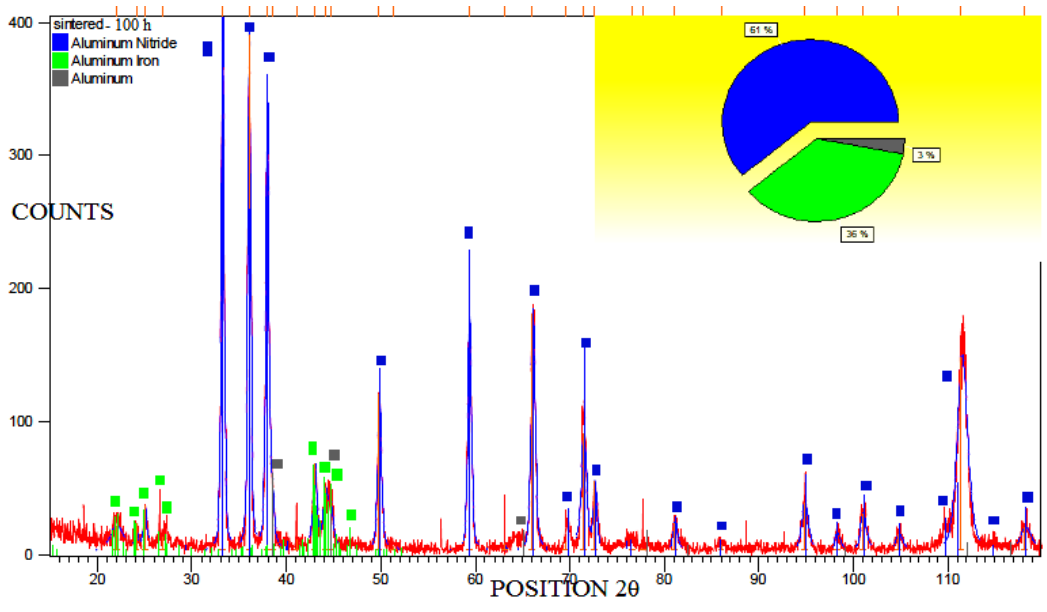

Figure 7.61 XRD profile of sintered compact synthesized from powder ball milled for 100 hours

Table 7.25 Structural parameters of 400-h ECAP-BP ($Al_{90}Fe_{10}$) pellet

Peak Pos. 2θ	phase	Height (cts)	FWHM 2θ	d-spacing (Å)	'a' nm	I_I	Rel. Int. (%)	Matched by
18.3793		16.02	1.0037	4.82334			12.77	01-073- 1199; 01- 073-0229
20.1295		18.84	1.1068	4.40773			15.02	01-073- 1199
26.5288		83.52	1.0653	3.35722			66.57	00-038- 1147; 01- 073-1199; 01-073- 0229
31.3177		10.26	0.3937	2.85392			8.17	00-038- 1147; 01- 073-1199; 01-073- 0229
34.4198		12.16	0.4864	2.60348			9.69	00-038- 1147; 01- 073-1199
35.6319		20.29	0.6727	2.51765			16.17	00-038- 1147; 01- 073-1199
38.4019	**Al111**	108.13	0.4525	2.34217	**0.4057**	163087.14	86.19	00-038- 1147; 03- 065-2869; 01-073- 1199; 01- 073-0229
40.7178		45.43	1.3302	2.21414			36.21	00-038-1147; 01-073-1199
42.1731		69.69	1.1299	2.14104			55.55	00-038-1147; 01-073-1199; 01-073-0229
44.5931	040AlFe/**Al200**	**125.46**	**1.2194**	2.03030	**0.4061**		**100.00**	00-038-1147; 03-065-2869; 01-073-1199
48.2885		13.33	1.0719	1.88321			10.63	00-038-1147; 01-073-1199; 01-073-0229
49.9287		7.59	1.2640	1.82512			6.05	00-038-1147; 01-073-1199; 01-073-0229
53.9164		6.64	1.0027	1.69916			5.29	01-073-1199; 01-073-0229
56.5225		6.15	2.9679	1.62684			4.91	01-073-1199; 01-073-0229
64.9884		19.36	1.2715	1.43388			15.43	03-065-2869; 01-073-1199; 01-073-0229
72.2456		11.58	1.1916	1.30666			9.23	01-073-1199
78.1116		27.91	1.3329	1.22255			22.25	03-065-2869; 01-073-1199; 01-073-0229
82.1951		9.14	0.9247	1.17184			7.29	03-065-2869; 01-073-1199; 01-073-0229
83.2915		8.28	0.0508	1.15918			6.60	03-065-2869; 01-073-1199; 01-073-0229
88.0938		0.21	4.0000	1.10795			0.16	01-073-1199; 01-

Crystallite size 'D'=9.3 nm and lattice strain=1.259% at $2\theta=44.5931^0$ for **040AlFe/200 Al reflection**

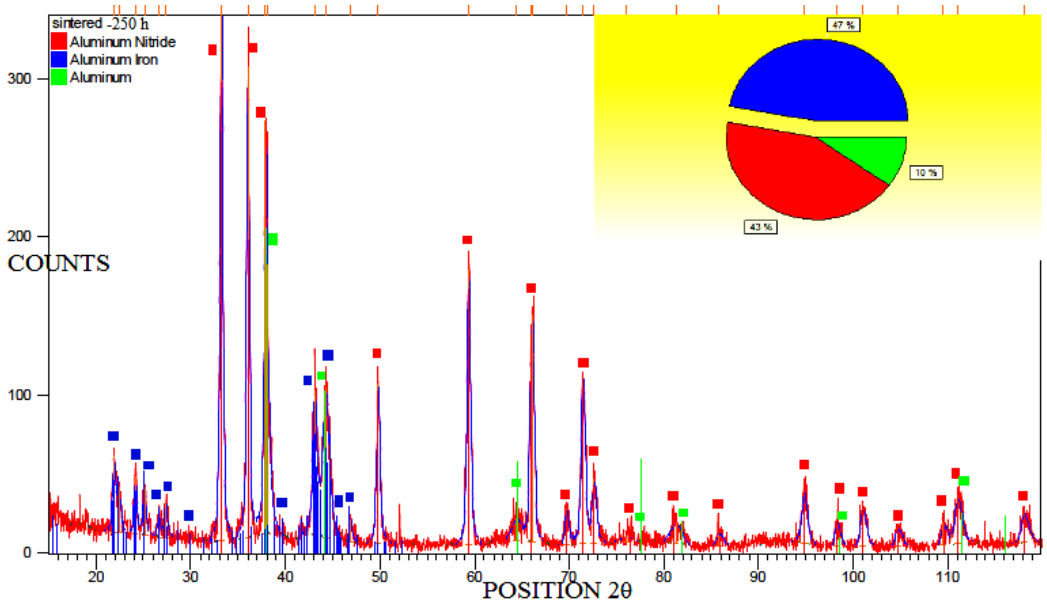

Figure 7.62 XRD profile of sintered compact synthesized from powder ball milled for 250 hours

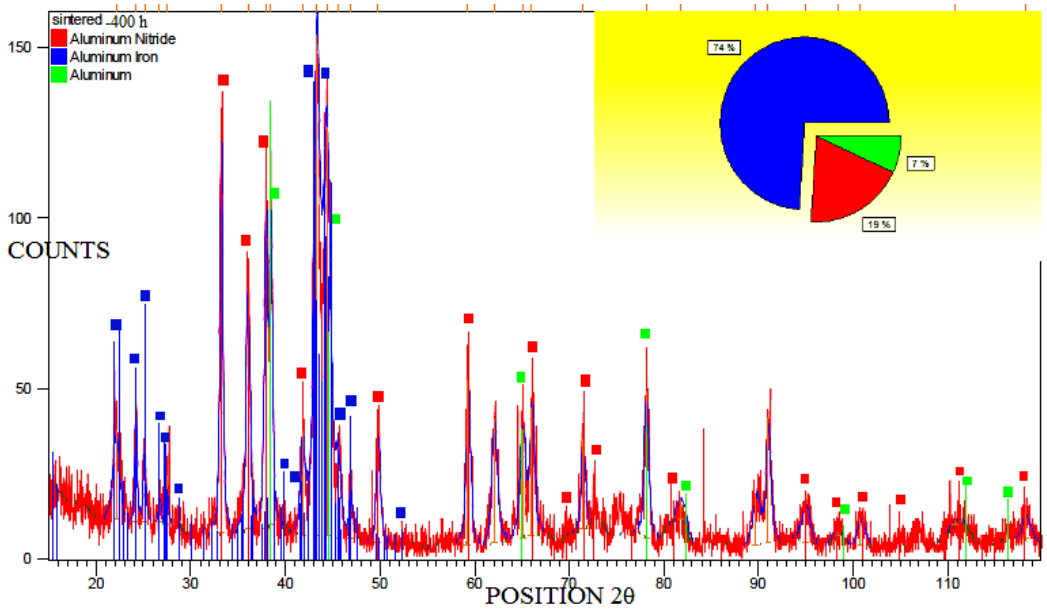

Figure 7.63 (7.55) XRD profile of sintered compact synthesized from powder ball milled for 400 hours

Table 7.26 Structural parameters of 100-h MA powder consolidated by compaction and sintering

Peak Pos. 2θ	Phase	Height (cts)	FWHM 2θ	d-spacing (Å)/'a' nm	Rel. Int. (%)/D nm/ Strain %	Matched by Ref. pattern
22.0014	Al76Fe24	18.80	1.5372	4.03676	4.72	00-038-1147
24.0692	Al76Fe24	19.54	0.3056	3.69443	4.91	00-038-1147
25.0261	Al76Fe24	33.46	0.3506	3.55531	8.40	00-038-1147
26.9543	Al76Fe24	9.97	3.5592	3.30519	2.50	00-038-1147
33.2284	Al76Fe24/ AlN	**398.18**	0.3325	2.69405	100.00	03-065-0831; 00-038-1147
36.0452	Al76Fe24/ AlN	386.11	0.3362	2.48972	96.97	03-065-0831; 00-038-1147
37.9482	Al76Fe24/ AlN/Al	335.94	0.3612	2.36912	84.37	03-065-0831; 00-038-1147; 03-065-2869
38.5171	**Al76Fe24/ AlN/Al**	**54.59**	**0.3991**	**2.33543/0.4104**	13.71/**85/0.329**	03-065-0831; 00-038-1147; 03-065-2869
41.1293	Al76Fe24	8.42	4.0000	2.19293	2.12	00-038-1147
42.9893	Al76Fe24	65.14	0.4347	2.10226	16.36	00-038-1147
44.1283	Al76Fe24/ Al	46.50	0.5709	2.05060	11.68	00-038-1147; 03-065-2869
44.6955	**Al76Fe24/ Al**	**36.48**	**0.5417**	**2.02589**	**9.16**	00-038-1147; 03-065-2869
49.8290	Al76Fe24/ AlN	117.33	0.4189	1.82854	29.47	03-065-0831; 00-038-1147

Table 7.27 Matching pattern details

Visible	Ref. Code	Score	Compound Name	Displaceme nt 2θ	Scale Factor	Chemical Formula
yes	03-065- 0831	79	Aluminum Nitride	0.000	0.990	Al N
yes	00-038- 1147	59	Aluminum Iron	-0.190	0.158	Al76.8 Fe24
yes	03-065- 2869	36	Aluminum	0.049	0.142	Al

Table 7.28 Structural parameters of 250-h MA powder consolidated by compaction and sintering

Peak Pos. 2θ	Phase	Height (cts)	FWHM 2θ	d-spacing (Å)/'a' nm	Rel. Int. (%)/D nm/ Strain %	Matched by Ref. pattern
21.8667	Al76Fe24	49.10	0.3638	4.06133	14.38	00-038-1147
22.3643	Al76Fe24	28.70	0.4913	3.97208	8.41	00-038-1147
24.1336	Al76Fe24	36.94	0.3731	3.68473	10.82	00-038-1147
25.1078	Al76Fe24	30.39	0.3803	3.54392	8.90	00-038-1147
26.6019	Al76Fe24	12.54	0.3450	3.34816	3.67	00-038-1147
27.3302	Al76Fe24	21.85	0.3996	3.26058	6.40	00-038-1147
33.2121	Al76Fe24/ AlN	341.49	0.3408	2.69534	100.00	03-065-0832; 00-038-1147
36.0215	Al76Fe24 AlN	297.81	0.3279	2.49130	87.21	03-065-0832; 00-038-1147
37.8894	Al76Fe24/ AlN/Al	261.94	0.3075	2.37267	76.71	03-065-0832; 00-038-1147; 03-065-2869
38.0873	**Al76Fe24 /AlN/Al**	**170.26**	**0.7144**	**2.36079/0.4 109**	49.86 **/20.3/0.819**	03-065-0832; 00-038-1147; 03-065-2869
43.0742	Al76Fe24	92.34	0.5309	2.09832	27.04	00-038-1147
44.2828	**Al76Fe24 /Al**	**95.64**	**0.8324**	**2.04381**	**28.01**	00-038-1147; 03-065-2869
46.8570	Al76Fe24	13.92	0.3368	1.93735	4.08	00-038-1147
49.7901	Al76Fe24/ AlN	100.91	0.3919	1.82987	29.55	03-065-0832; 00-038-1147

Table 7.29 Structural parameters of 400-h MA powder consolidated by compaction and sintering

Peak Pos. 2θ	Phase	Height (cts)	FWHM 2θ	d-spacing (Å)/'a'nm	Rel. Int. (%)/D nm/ Strain %	Matched by Ref. pattern
22.1058	Al76Fe24	25.99	0.7977	4.01793	17.69	00-038-1147
24.1780	Al76Fe24	31.91	0.3001	3.67807	21.73	00-038-1147
25.0956	Al76Fe24	20.72	0.3193	3.54561	14.11	00-038-1147
26.6872	Al76Fe24	7.07	0.3144	3.33766	4.81	00-038-1147
27.3943	Al76Fe24	14.51	0.3632	3.25309	9.88	00-038-1147
33.2040	Al76Fe24/ AlN	117.17	0.3637	2.69598	79.77	03-065-3409; 00-038-1147
36.0215	Al76Fe24/ AlN	73.34	0.4952	2.49130	49.93	03-065-3409; 00-038-1147
37.9222	Al76Fe24/ AlN/Al	97.16	0.4107	2.37069	66.15	03-065-3409; 00-038-1147; 03-065-2869
38.4587	**Al76Fe24 /AlN/Al**	**95.14**	**0.3618**	**2.33884 /0.4106**	64.78/**135.7/0. 253**	03-065-3409; 00-038-1147; 03-065-2869
41.8087	Al76Fe24	30.72	0.5817	2.15886	20.91	00-038-1147
43.2940	Al76Fe24	146.88	0.7462	2.08817	100.00	00-038-1147
44.3419	**Al76Fe24 /Al**	**120.04**	**0.9308**	**2.04122**	**81.72**	00-038-1147; 03-065-2869
45.6219	Al76Fe24	23.53	0.6538	1.98689	16.02	00-038-1147
46.8900	Al76Fe24	14.04	0.4410	1.93606	9.56	00-038-1147
49.7948	Al76Fe24/ AlN	31.70	0.4777	1.82971	21.58	03-065-3409; 00-038-1147

PUBLICATIONS

International Journal Papers:

1) Rajath Hegde, and Surendranathan A.O. 'Synthesis, characterization and annealing of mechanically alloyed nanostructured FeAl powder'; Front. Mater. Sci. 2009, 4(1): 310–318. DOI 10.1007/s11706-009-0021-4.
2) Rajath Hegde, and Surendranathan A.O. 'Thermal behaviour and magnetic properties of mechanically alloyed nanostructured Fe Al'; Journal of Metallurgy and Materials Science, Vol. 51, No. 3, July-September 2009, pp. 175-195;NML, ISSN 0972-4257.
3) Rajath Hegde, and Surendranathan A.O. 'Phase Transformation, Structural Evolution and Mechanical Property of Nanostructured FeAl as a Result of Mechanical Alloying'; ISSN 1067-8212, Russian Journal of Non-Ferrous Metals, 2009, Vol. 50, No. 5, pp. 474–484.
4) Raghavendra H., K.L. Bhat, Rajendra Udupa, and Rajath Hegde. 'Grinding Wear Behaviour of Stepped Austempered Ductile Iron as Media Material During Comminution of Iron Ore in Ball Mills'; International Conference On Advances In Materials And Processing Technologies (AMPT-2010); doi:10.1063/1.3552371; AIP Conf. Proc. January 17, 2011. Volume 1315, pp. 1341-1346.

International Conference Papers:

1) Rajath Hegde, and Surendranathan A.O. 'Magnetism, Structural and Mechanical Behavior of Transitional Bulk Nanostructured Al Alloy'; 3-7th June 2012, 13th International Conference on Al alloys; ICAA13; TMS; Wiley; Carnegie Mellon Uny; Pittsburg, Pennsylvania USA.
2) Rajath Hegde, and Surendranathan A.O. 'Synthesis and Characterization of Mechanically Alloyed Nanostructured FeAl Magnet'; 1-2 OCT 2009 International Scientific- Technical Conference on Modern Problems of Physical Metallurgy of Non-Ferrous Alloys. Department of Physical Metallurgy of Non-Ferrous Metals. State Technological University. "Moscow Institute of Steel And Alloys" (MISIS) at Moscow, Russian Federation.
3) M.M. Rajath Hegde and A.O. Surendranathan. 'Phase Transformation and Mechanical Property of Mechanically Alloyed Nanostructured FeAl'. September 14-16th 2009. The Fourth Asian Particle Technology Symposium (APT 2009) New Delhi.
4) M.M. Rajath Hegde et al. 'Ferromagnetism in compression stressed transitional bulk nanostructured $Fe_{50}Al_{50}$ alloy': Engineering asset management and infrastructure

sustainability, SMMN; Brisbane Australia; DOI; 10.1007/978-0-85729-493-7-30; Springer-Verlag London Ltd 2011.

5) M.M. Rajath Hegde and Dr A.O. Surendranathan. 'Synthesis, characterization, magnetic and mechanical properties of nanostructured FeAl alloy': Review. 9-11 August 2007. Globalization of engineering, design, R & D challenges and opportunities. IISc Bangalore India.

BIO-DATA

M. M. Rajath Hegde was born on 24 February 1962 in Muduvalli village of Tirthahalli taluck in Shimoga district of Karnataka state, India. Completed his primary, secondary and pre-university education from Sandur Residential School and composite junior college at Sandur in Bellary district of Karnataka state. Completed his bachelor's degree in Industrial production from BIET Davanagere (Mysore University) in Karnataka state and later completed Master of engineering from MSRIT Bangalore during the year 1992 in metal casting science and engineering specialisation. During 1988 to 1989 worked as apprentice engineer at MICO Bangalore and entered the teaching profession as a lecturer in the department of industrial production at JNNCE Shimoga, Karnataka in the year 1992. Joined NITK as a full time research scholar in the Department of Metallurgical and Materials Engineering in the year 2006. Selected as an overseas research student, to pursue PhD studies in the institute for technology research and innovation at Deakin University in Geelong, Australia during 2010 for a period of one year. Visited the National Technical University (MISIS) in Moscow Russian Federation for presenting a research paper in the international conference on physical metallurgy held there in 2009. Visited the Queensland university of technology, Brisbane, Australia to present a research paper at the international conference on nanostructural materials in the year 2010. Utilised the ECAP facility located in the materials department at Clayton campus of Monash University in Australia for the current research work. Visited the Synchrotron XRD and Nanofabrication centre at Melbourne in Australia during the year 2010. Currently working as associate professor in the department of mechanical engineering at JNNCE Shimoga.

Contact Address:
M.M. RAJATH HEGDE
DEPARTMENT OF MECHANICAL ENGINEERING
JNNCE, NAVULE
SHIMOGA
KARNATAKA
INDIA
TEL: 9449100306
Email id:rajathhegdemm63@gmail.com